



Norwegian University of
Science and Technology

Creep and Consolidation in Pierre Shale

Identification of how time-dependent effects
are influenced by alteration in pore fluid pH
and changes in stress conditions

Marta Laukeland Kleiven
Elisabeth Lund

Petroleum Geoscience and Engineering
Submission date: June 2016
Supervisor: Erling Fjær, IPT

Norwegian University of Science and Technology
Department of Petroleum Engineering and Applied Geophysics

Abstract

The Petroleum Safety Authority of Norway (PSA) has now acknowledged the use of shale as an annular barrier for permanent plug and abandonment (PP&A) operations in the oil industry. Shale can exhibit a natural self-sealing effect; a result from delayed deformation of the rock. It is believed that *creep* in combination with *consolidation* plays important roles in the process when shale closes in and forms a tight barrier around a well. For using shale as a permanent annular barrier it is important to comprehend how these time-dependent mechanisms are affected by externally induced parameters, like stress, temperature and chemical alterations of the pore fluid.

The purpose of this master thesis is to investigate creep characteristics and consolidation effects in Pierre shale. Two literature studies have been completed and several laboratory experiments have been carried out on small size core plugs drilled normal to the bedding plane. Axial strain-time curves have been obtained by performing uniaxial compression tests with step loading at a temperature around 30°C. The main objectives have been to identify how the creep and consolidation processes are affected by different stress levels and variations in the pore fluid pH.

Eventually, the laboratory work resulted in four successful creep experiments. The obtained data showed that Pierre shale exhibits considerable time-dependent deformation in response to applied stress. Changing the stress conditions affected the amount of deformation in periods with constant stress and it appeared like the shale demonstrated different creep behavior before and after a certain test dependent stress level. It was also seen that the temperature variation increased with extended test time for the conducted experiments and the experimental results implied that p-wave velocities are related to strain as well as stress. In addition, the creep tests indicated a correlation between p-wave velocities and temperature.

Finally, it was found that the pH value of the pore fluid had an impact on consolidation and creep properties. A lower pH value reduced the overall stiffness and strength of the samples, resulting in more consolidation. More creep deformation and increased creep rates were seen compared to a near-neutral pH environment.

Sammendrag

Petroleumstilsynet har nå erkjent bruken av skifer som en ringromsbarriere for permanent plugging- og forlatingsoperasjoner i oljeindustrien. Skifer kan utøve en naturlig selvforseglingseffekt; et resultat fra forsinket deformasjon av steinen. Det antas at *kryp* i kombinasjon med *konsolidering* spiller viktige roller i prosessen når skifer siger inn og oppretter en tett barriere rundt en brønn. For å bruke skifer som en permanent ringromsbarriere er det viktig å forstå hvordan disse tidsavhengige mekanismene er påvirket av eksterne parametere som spenning, temperatur og kjemisk forandring av porefluiden.

Hensikten med denne masteroppgaven er å undersøke krypkarakteristikker og konsolideringseffekter i Pierre skifer. To litteraturstudier er ferdigstilt og flere laboratorieforsøk har blitt utført på små kjernepluggere boret normalt på lagplanet. Aksielle deformasjon-tidskurver har blitt fremstilt ved å utføre enaksiale kompresjonstester med trinnvis lasting rundt en temperatur på 30°C. Hovedhensiktene har vært å identifisere hvordan kryp- og konsolideringsprosesser påvirkes av ulike spenningsnivå og variasjoner i porefluid pH.

Laboratoriearbeidet resulterte til slutt i fire suksessfulle krypeksperimenter. Fremstilt data viste at Pierre skifer utøver betydelig tidsavhengig deformasjon som respons av påført spenning. Forandring av spenningsbetingelser påvirket deformasjonsmengden i perioder med konstant spenning og det virket som skiferen hadde ulik kryppoppførsel før og etter et visst testavhengig spenningsnivå. Man så også at temperaturvariasjon økte med lengre testtid for eksperimentene og de eksperimentelle resultatene antydte at p-bølge hastigheter er relatert til deformasjon så vel som spenning. I tillegg indikerte kryptestene en korrelasjon mellom p-bølge hastigheter og temperatur.

Til slutt ble det funnet at pH verdien av porefluiden hadde en påvirkning på konsolidering- og krypegenskaper. En lavere pH-verdi reduserte den totale stivheten og styrken av prøvene, noe som resulterte i mer konsolidering. Mer krypdeformasjon og høyere kryprater ble observert sammenliknet med et nøytralt pH miljø.

Preface

This master thesis is the concluding work of our Master of Science degree in Petroleum Technology. It was completed at the Norwegian University of Science and Technology (NTNU) during the spring of 2016 in cooperation with SINTEF Petroleum (Trondheim, Norway).

As a preparation for the thesis, an unpublished NTNU specialization project; “Creep and consolidation effects in Pierre shale”, was conducted by the authors in the fall of 2015. The purpose of the project was to investigate and learn about time-dependent deformation in Pierre shale. In addition to theoretical studies, laboratory experiments were carried out to reveal genuine creep characteristics and consolidation effects. This master thesis is the continued work of the specialization project. New laboratory experiments and theoretical research have been performed to identify how the consolidation and creep mechanisms are affected by variation in stress conditions and alteration in the pore fluid pH value.

We want to give special thanks to our supervisor Erling Fjær for great support and advice throughout the master thesis. Also, we would like to thank Anna Stroisz, Jørn Stenebråten, Lars Erik Walle and Hans Lund for great help and guidance at the SINTEF lab.

Finally, we would like to express our gratitude to close friends and family for great support throughout these past years of studies.

Trondheim 10th of June, 2016



Marta Laukeland Kleiven



Elisabeth Lund

Table of Contents

Abstract	i
Sammendrag	iii
Preface.....	v
List of figures	xi
List of tables	xv
1 Introduction	1
1.1 Background	1
1.2 Approach.....	2
1.3 Thesis structure	3
1.4 Preceding work.....	4
2 Background theory.....	7
2.1 Brief introduction to petroleum rock mechanics	7
2.1.1 Stress and strain definitions	7
2.1.2 Relationships between stress and strain	8
2.1.2.1 Elastic behavior	8
2.1.2.2 Poroelastic behavior.....	10
2.1.2.3 Thermoelastic behavior.....	11
2.2 Rock failure	12
2.3 Time-dependent mechanisms	15
2.3.1 Creep	15
2.3.2 Consolidation.....	17
2.4 Acoustic waves	21
2.4.1 Primary waves	21
2.4.2 Influence of pore fluid, temperature and anisotropic texture	22
2.4.3 Static and dynamic moduli	23
2.5 Brief introduction to relevant chemical concepts.....	23
2.5.1 pH	24
2.5.2 Chemical weathering.....	25
2.5.3 Chemical activity	25
2.5.4 Osmosis	26
2.5.5 Ion diffusion.....	27

2.6	Shale as a rock	29
3	Literature studies	31
3.1	Descriptions of creep in shale materials	31
3.2	How reduced pore fluid pH affects creep in shale	35
3.2.1	Clay minerals in shale	35
3.2.2	Interactions between minerals and solutions.....	36
3.2.3	Chemical weathering.....	37
3.2.4	Impact of different chemical environments	38
3.2.5	CO ₂ sequestration	39
3.2.6	Summary	41
4	Preparations for laboratory work	43
4.1	Risk assessment	43
4.2	Calibration of LVDTs	43
4.3	System correction factor for acoustic measurements	43
4.4	Preparations for creep experiments.....	44
4.4.1	Estimation of expected consolidation time	44
4.4.2	Initial screening of brine and HCl mixtures	44
4.4.3	Estimation of ion diffusion time	45
4.4.3.1	By calculations.....	46
4.4.3.2	By experiment	47
4.4.3.3	Conclusion	48
4.4.4	Defining uniaxial compressive strength	48
5	Experiments and methods	51
5.1	Purpose.....	51
5.2	Core samples	51
5.3	Experimental setup.....	51
5.4	Experimental procedures	53
5.4.1	Ion diffusion experiments	53
5.4.2	UCS tests.....	54
5.4.3	Creep experiments	55
5.4.3.1	Test procedures.....	55
5.4.3.2	Loading paths	57

6	Approaches for finding the transition period between consolidation and creep dominated behaviour.....	61
6.1	Graphical approach.....	61
6.1.1	Technique for finding the best fit trendline in Excel.....	61
6.2	The Mohr-Coulomb criterion.....	63
7	Experimental results and discussion for creep experiments.....	65
7.1	Creep tests in brine.....	66
7.1.1	Core sample 346_2_15.....	66
7.1.2	Core sample 346_2_18.....	71
7.1.3	Core sample 346_2_19.....	75
7.1.4	Core sample 346_2_20.....	82
7.1.5	Core sample 346_2_23.....	99
7.2	Creep tests with reduced pore fluid pH	114
7.2.1	Core sample 346_2_21.....	114
7.2.2	Core sample 346_2_22.....	128
7.3	Comparison of the results	142
7.3.1	Common trends.....	142
7.3.2	Identification of how creep and consolidation are affected by alteration in porefluid pH and changes in stress conditions	144
7.3.2.1	pH	144
7.3.2.2	Changes in stress conditions	155
8	Potential sources of error	159
8.1	Measurement of core dimensions	159
8.2	Drying of shale samples	159
8.3	Loose grains	159
8.4	LVDTs	160
8.4.1	Calibration	160
8.4.2	Noise.....	160
8.5	Influence of room temperature.....	160
8.6	Heating element	160
8.7	Setup of the experiment.....	160
8.8	Ion diffusion time.....	161

8.9	pH meter.....	161
8.10	Equilibrium relative humidity measurements	161
9	Conclusion.....	163
10	Recommendations	165
10.1	Self-reflection.....	165
10.2	Future work.....	166
	List of abbreviations	167
	Nomenclature.....	169
	Bibliography.....	173
Appendix I.	Calculations of expected consolidation time	179
Appendix II.	Estimation of ion diffusion time	181
Appendix III.	Defining uniaxial compressive strength	183
Appendix IV.	Screening of brine and HCl mixtures.....	189
Appendix V.	Relations between elastic moduli	197
Appendix VI.	Additional tables	199
Appendix VII.	Calibration of LVDTs	203
Appendix VIII.	Calculations of system correction factor	205
Appendix IX.	Sampling rates during experiments.....	207
Appendix X.	Risk assessment	209
Appendix XI.	Pictures of core samples after creep experiments.....	211
Appendix XII.	Pictures from the unfortunate lab incident with core sample 346_2_20... 215	
Appendix XIII.	Digital attachments	217
Appendix XIV.	Additional plots – creep experiments.....	219

List of figures

Figure 2.1: Illustration of linear elastic behavior..	8
Figure 2.2: Illustration of a material suffering permanent deformation..	10
Figure 2.3: Illustration of tensile failure, shear failure and compaction failure.	13
Figure 2.4: Graphical illustration of the Mohr-Coulomb criterion in τ - σ' space.....	14
Figure 2.5: The diverse failure mechanisms illustrated in principal stress space.....	15
Figure 2.6: Stress-strain curves for an elastic material and a viscoelastic material.	16
Figure 2.7: Illustration of the different creep stages..	16
Figure 2.8: Strain vs. time for three different stress levels.....	17
Figure 2.9: Illustration of the consolidation effect.	18
Figure 2.10: Illustration of two different flow regimes.....	20
Figure 2.11: Illustration of a p-wave motion.....	21
Figure 2.12: The pH scale..	24
Figure 2.13: Osmotic pressure.	27
Figure 2.14: Diffusion of particles.	28
Figure 2.15: Cross section of Pierre shale sample saturated with oil.....	30
Figure 4.1: Illustration of core sample moving from marcol to brine.....	45
Figure 4.2: Illustration of core sample moving to a mixture of brine and hydrochloric acid. .	46
Figure 5.1: Experimental setup.	53
Figure 6.1: Best fit trendline in Excel for a log-log plot.....	62
Figure 6.2: Best fit trendline in Excel for strain versus the square root of time.....	63
Figure 7.1: Overview of creep test conducted on 346_2_15.....	66
Figure 7.2: Strain vs. time for hold period 1.	67
Figure 7.3: Estimating the transition by applying the graphical approach.....	68
Figure 7.4: Strain in conjunction with p-wave velocities for hold period 1.	69
Figure 7.5: Core sample 346_2_17 with dissolved parts after 3 weeks in brine.	71
Figure 7.6: Overview of creep test conducted on 346_2_18.....	72
Figure 7.7: Abnormal temperature variations for sample 346_2_18.....	73
Figure 7.8: Trying to predict failure for upcoming tests.	74
Figure 7.9: Overview of creep test conducted on 346_2_19.....	75
Figure 7.10: Strain vs. time for hold period 1.	76
Figure 7.11: Estimating the transition by applying the graphical approach.....	77
Figure 7.12: Temperature variations for sample 346_2_19 indicating a short circuit.	78
Figure 7.13: Strain measurements were not affected by temperature variations.....	79
Figure 7.14: P-wave velocity measurements were not affected by temperature variations..	79
Figure 7.15: Strain in conjunction with p-wave velocities for hold period 1.	80
Figure 7.16: Strain vs. time for hold period 2.	81
Figure 7.17: Overview of creep test conducted on 346_2_20.....	82
Figure 7.18: Strain in conjunction with p-wave velocities for hold period 9.	83
Figure 7.19: Strain versus time for all valid hold periods.....	84
Figure 7.20: Maximum strain for a hold period versus stress level.	84

Figure 7.21: Continuous deformation rates in the valid hold periods.....	86
Figure 7.22: Scaling the other hold periods to hold period 1 with a scaling factor s	87
Figure 7.23: P-wave velocities in the valid hold periods.....	88
Figure 7.24: P-wave velocities in the valid hold periods scaled to (0,0).	89
Figure 7.25: P-wave velocities versus deformation for the valid hold periods.	89
Figure 7.26: P-wave velocities versus deformation for the hold periods scaled to (0,0).	90
Figure 7.27: Strain versus square root of time for all valid hold periods.	91
Figure 7.28: Approximate consolidation times for different hold periods.....	92
Figure 7.29: Initial deformation versus time for all valid loading phases.....	93
Figure 7.30: $\Delta\varepsilon/\Delta\sigma$ versus stress for all valid loading phases.	94
Figure 7.31: The inverse of the initial stiffness versus stress for all valid loading phases.....	95
Figure 7.32: Relative difference in consolidation times versus stress throughout the test. ...	98
Figure 7.33: Overview of creep test conducted on 346_2_23.....	99
Figure 7.34: Strain versus time for all valid hold periods.....	100
Figure 7.35: Maximum strain for a hold period versus stress level.	101
Figure 7.36: Continuous deformation rates in the valid hold periods.....	103
Figure 7.37: Scaling the other hold periods to hold period 1 with a scaling factor s	104
Figure 7.38: P-wave velocities in the valid hold periods.....	105
Figure 7.39: P-wave velocities in the valid hold periods scaled to (0,0).	106
Figure 7.40: P-wave velocities versus deformation for the valid hold periods.	106
Figure 7.41: P-wave velocities versus deformation for the hold periods scaled to (0,0).	107
Figure 7.42: Strain versus square root of time for all valid hold periods.	108
Figure 7.43: Approximate consolidation times for different hold periods.....	109
Figure 7.44: Initial deformation versus time for all valid loading phases.....	110
Figure 7.45: $\Delta\varepsilon/\Delta\sigma$ versus stress for all valid loading phases.	111
Figure 7.46: The inverse of the initial stiffness versus stress for all valid loading phases....	111
Figure 7.47: Relative difference in consolidation times versus stress throughout the test. .	113
Figure 7.48: Overview of creep test conducted on 346_2_21.....	114
Figure 7.49: Strain versus time for all valid hold periods.....	115
Figure 7.50: Maximum strain for a hold period versus stress level.	115
Figure 7.51: Continuous deformation rates in the valid hold periods.....	117
Figure 7.52: Scaling the other hold periods down to hold period 1 with a scaling factor s . .	118
Figure 7.53: P-wave velocities in the valid hold periods.....	119
Figure 7.54: P-wave velocities in the valid hold periods scaled to (0,0).	120
Figure 7.55: P-wave velocities versus deformation for the valid hold periods.	120
Figure 7.56: P-wave velocities versus deformation for the hold periods scaled to (0,0).	121
Figure 7.57: Strain versus square root of time for all valid hold periods.	122
Figure 7.58: Approximate consolidation times for different hold periods.....	123
Figure 7.59: Initial deformation versus time for all valid loading phases.....	124
Figure 7.60: $\Delta\varepsilon/\Delta\sigma$ versus stress for all valid loading phases.	125
Figure 7.61: The inverse of the initial stiffness versus stress for all valid loading phases....	126

Figure 7.62: Relative difference in consolidation times versus stress throughout the test. .	127
Figure 7.63: Overview of creep test conducted on 346_2_22.....	128
Figure 7.64: Strain versus time for all valid hold periods.....	129
Figure 7.65: Maximum strain for a hold period versus stress level.	129
Figure 7.66: Continuous deformation rates in the valid hold periods.....	131
Figure 7.67: Scaling the other hold periods to hold period 1 with a scaling factor s.	132
Figure 7.68: P-wave velocities in the valid hold periods.....	133
Figure 7.69: P-wave velocities in the valid hold periods scaled to (0,0).	134
Figure 7.70: P-wave velocities versus deformation for the valid hold periods.	134
Figure 7.71: P-wave velocities versus deformation for the hold periods scaled to (0,0).	135
Figure 7.72: Strain versus square root of time for all valid hold periods.	136
Figure 7.73: Approximate consolidation times for different hold periods.....	137
Figure 7.74: Graphical approach applied for hold period 6.....	138
Figure 7.75: Initial deformation versus time for all valid loading phases.....	139
Figure 7.76: $\Delta\epsilon/\Delta\sigma$ versus stress for all valid loading phases.	140
Figure 7.77: The inverse of the initial stiffness versus stress for all valid loading phases....	140
Figure 7.78: Relative difference in consolidation times versus stress throughout the test. .	142
Figure 7.79: Stress and deformation for 346_2_21 versus 346_2_23.....	145
Figure 7.80: Stress and deformation for 346_2_20 versus 346_2_22.....	146
Figure 7.81: Hold periods 1-4 for 346_2_21 versus 346_2_23.....	147
Figure 7.82: Hold periods 5-8 for 346_2_21 versus 346_2_23.....	148
Figure 7.83: Hold periods 9-11 for 346_2_21 versus 346_2_23.....	148
Figure 7.84: Hold periods 1-3 for 346_2_20 versus 346_2_22.....	149
Figure 7.85: Hold periods 4-6 for 346_2_20 versus 346_2_22.....	150
Figure 7.86: Trend in average creep rates for the final 15 min of the hold periods.....	152
Figure 7.87: Obtained consolidation times for core sample 346_2_23 and 346_2_21.....	154
Figure 7.88: Obtained consolidation times for core sample 346_2_20 and 346_2_22.....	154
Figure 7.89: Deformation trends for variation in stress conditions.....	155
Figure 7.90: Decline in amount of deformation during the loading phases.....	157

Appendix II

Figure II- 1: Strain vs. time for core sample 346_2_10.	181
Figure II- 2: Strain vs. time for core sample 346_2_11.	182
Figure II- 3: Strain vs. time for core sample 346_2_14.	182

Appendix III

Figure III- 1: Stress versus time for core sample 346_2_10.	183
Figure III- 2: Core sample 346_2_10 before and after failure.....	184
Figure III- 3: Stress versus time for core sample 346_2_11.	184
Figure III- 4: Core sample 346_2_11 before and after failure.....	185
Figure III- 5: Stress versus time for core sample 346_2_14.	185
Figure III- 6: Core sample 346_2_14 before and after failure.....	186
Figure III- 7: Stress versus time for core sample 346_2_16.	186

Figure III- 8: Core sample 346_2_16 before and after failure.....	187
---	-----

Appendix IV

Figure IV- 1: Test tube 4 (15% HCl).....	191
Figure IV- 2: Test tube 3 (10% HCl).....	191
Figure IV- 3: Test tube 2 (5% HCl).....	191
Figure IV- 4: Test tube 1 (0% HCl).....	192
Figure IV- 5: Test tube 13 (0.00015625% HCl).	193
Figure IV- 6: Test tube 14 (0.00003906% HCl).	194
Figure IV- 7: Test tube 10 (0.00125% HCl).	194
Figure IV- 8: Obtained pH-values by diluting 25% HCl (aq) with 3.5wt% brine..	195
Figure IV- 9: Obtained pH-values by diluting 0.0025% HCl (aq) with 3.5wt% brine..	195

Appendix VII

Figure VII- 1: Calibration for LVDT 1	203
Figure VII- 2: Calibration for LVDT 2.....	203
Figure VII- 3: Calibration for LVDT 3.....	204

Appendix XI

Figure XI- 1: Core sample 346_2_15 after creep test.	211
Figure XI- 2: Core sample 346_2_18 after creep test.	211
Figure XI- 3: Core sample 346_2_19 after creep test.	212
Figure XI- 4: Core sample 346_2_20 after creep test.	212
Figure XI- 5: Core sample 346_2_21 after creep test.	213
Figure XI- 6: Core sample 346_2_22 after creep test.	213
Figure XI- 7: Core sample 346_2_23 after creep test.	214

Appendix XII

Figure XII- 1: A damaged heating element.....	215
Figure XII- 2: Connection point between heating element and temperature controller	215
Figure XII- 3: Melted plastic parts from the experimental setup.....	216
Figure XII- 4: Dried out core sample.....	216

Appendix XIV

Figure XIV- 1: Strain versus time for loading phase and hold period.	219
Figure XIV- 2: Maximum strain for loading phase and hold period versus stress level.	219
Figure XIV- 3: Scaling the other hold periods to hold period 1 with a scaling factor s	220
Figure XIV- 4: Strain versus time for loading phase and hold period.	220
Figure XIV- 5: Maximum strain for loading phase and hold period versus stress level.	221
Figure XIV- 6: Scaling the other hold periods to hold period 1 with a scaling factor s	221
Figure XIV- 7: Strain versus time for loading phase and hold period.	222
Figure XIV- 8: Maximum strain for loading phase and hold period versus stress level.	222
Figure XIV- 9: Scaling the other hold periods to hold period 1 with a scaling factor s	223
Figure XIV- 10: Strain versus time for loading phase and hold period.	223
Figure XIV- 11: Maximum strain for loading phase and hold period versus stress level.	224
Figure XIV- 12: Scaling the other hold periods to hold period 1 with a scaling factor s	224

List of tables

Table 2-1: Common p-wave velocities for various rock types.....	22
Table 2-2: Mechanical properties for various rocks.....	29
Table 3-1: Clay mineral composition and possible reactions with HCl.....	37
Table 7-1: Overview of test settings for each creep experiment.....	65
Table 7-2: Deformation rates for different time intervals in hold period 1.....	76
Table 7-3: Overview of deformation rates and creep phases.....	85
Table 7-4: Approximate consolidation times for different hold periods.....	91
Table 7-5: Maximum amount of strain for each loading phase.....	93
Table 7-6: Estimated values of initial stiffness for all valid loading phases.....	95
Table 7-7: How the consolidation times are affected by alteration in rock stiffness.....	97
Table 7-8: Overview of deformation rates and creep phases.....	102
Table 7-9: Approximate consolidation times for different hold periods.....	108
Table 7-10: Maximum amount of strain for each loading phase.....	110
Table 7-11: Estimated values of initial stiffness for all valid loading phases.....	112
Table 7-12: How the consolidation times are affected by alteration in rock stiffness.....	113
Table 7-13: Overview of deformation rates and creep phases.....	116
Table 7-14: Approximate consolidation times for different hold periods.....	122
Table 7-15: Maximum amount of strain for each loading phase.....	124
Table 7-16: Estimated values of initial stiffness for all valid loading phases.....	126
Table 7-17: How the consolidation times are affected by alteration in rock stiffness.....	127
Table 7-18: Overview of deformation rates and creep phases.....	131
Table 7-19: Approximate consolidation times for different hold periods.....	136
Table 7-20: Maximum amount of strain for each loading phase.....	139
Table 7-21: Estimated values of initial stiffness for all valid loading phases.....	141
Table 7-22: How the consolidation times are affected by alteration in rock stiffness.....	141
Table 7-23: Increase in initial stiffness from first to final loading phase.....	151
Table 7-24: Calculated creep rates for the final 15 min of the hold periods.....	152
Table 7-25: P-wave velocities in the beginning and at the end of the tests.....	153
Table 7-26: Stress levels for reaching steady-state creep.....	155
Table 7-27: Correlation between maximum strain and level of failure.....	157
Table 7-28: Creep phases in the last 15 min of each hold period.....	158
Appendix I	
Table I- 1: Parameters used in calculations.....	179
Appendix II	
Table II- 1: Summary of experimental settings for the ion diffusion tests.....	181
Appendix III	
Table III- 1: Summary of experimental settings for the UCS tests.....	183
Appendix IV	
Table IV- 1: Overview of amounts and measurements for test tube 1-4.....	189
Table IV- 2: Overview of amounts and measurements for test tube 5-9.....	192

Table IV- 3: Overview of amounts and measurements for test tube 10-14.	193
Appendix V	
Table V- 1: Known relations between elastic moduli.....	197
Appendix VI	
Table VI- 1: Measured data for all core samples.....	199
Table VI- 2: Mineralogy composition of Pierre shale, block 346_2.	199
Table VI- 3: Overview of the first three creep experiments.	200
Table VI- 4: Overview of the remaining creep experiments.	201
Appendix IX	
Table IX- 1: Sampling rates during ion diffusion tests.....	207
Table IX- 2: Sampling rates during UCS tests (extensions of ion diffusion tests).	207
Table IX- 3: Sampling rates during independent UCS test.	207
Table IX- 4: Sampling rates during creep experiments.	207

1 Introduction

1.1 Background

The oil industry has currently a high focus on developing new technology for PP&A operations. As several of the developed fields on the Norwegian Continental Shelf (NCS) are rapidly approaching an end simultaneously, many PP&A operations will be on the agenda for the Norwegian sector in the years to come (NPD 2014). As these operations are traditionally time consuming and expensive in today's market, the industry is in need of developing new science that will increase the efficiency and reduce the overall costs. Also, due to a recently reduced oil price and unstable petroleum market this has become utterly decisive.

The conventional way of permanently plugging a well today is to fill the inside of the casing strings with a number of cement plugs. However, this is only adequate if the sealing material behind the casing (usually casing cement) provides a required annular seal. As uncontrollable leakage outside wells represents big safety hazards, NORSOK Standard D-010 states a diverse set of requirements that must be met in order to qualify as a permanent well barrier. It is expressed that a permanent well barrier needs to be impermeable and non-shrinking, provide long term integrity, be resistant to chemicals and in addition be wetting and ductile. Also, the annular seal must have 360 degree coverage and extend over a minimum interval of 50 m (NORSOK Standard D-010, rev. June 2013). It has been confirmed that casing cement does not always fulfill these requirements, implying that the operators are left with insufficient annular barriers (Williams et al. 2009). To ensure that government regulations remain intact, one then has to go in and perform alternative and costly methods (NORSOK Standard D-010, rev. June 2013).

For some fields, it has been recognized that the formation itself has replaced casing cement as an annular barrier element by demonstrating a self-sealing effect. Creep in combination with consolidation is assumed to play important roles in the process when a formation is closing in and forming a tight barrier around a well. Creep is defined as a time-dependent deformation that can occur in materials under stress, whereas consolidation is the process where deformation occurs for a given stress increment due to excess pore pressure being slowly dissipated (Fjær et al. 2008). Even though self-sealing can be a relatively time

consuming process in the field, the formation may over time bond onto the casing and thereby form an accepted annular barrier.

The use of *shale* as an annular PP&A barrier is now acknowledged by the PSA (Williams et al. 2009). In light of the high shale zone frequency on the NCS, it is significant to further examine this rock as a barrier material. For this purpose, it is believed that shale has some benefits in comparison with cement; it is ductile, it is a natural part of the succession and it has over millions of years proven its sealing capacity by acting as cap rock for reservoirs (Sangesland et al. 2012). If this natural sealing process can be generally applied, it will eliminate a considerable portion of the work involved in creating a permanent annular barrier, implying enormous cost savings for PP&A operations. As of today, the mechanisms involved are not fully understood, and there are still no measures that may improve the likelihood of success with this method. Thus, it is vital to develop a full comprehension of how the creep and consolidation processes are affected by externally induced parameters, like temperature, stress and chemical alterations of the pore fluid. On this premise, a 3 year long project investigating shale formations as permanent annular barriers after well abandonment has been initiated by SINTEF Petroleum Research in cooperation with Forskningsrådet and five oil companies. In addition to PP&A operations, in-depth knowledge regarding creep and consolidation of shale can also be beneficial for others, including underground CO₂ storage operations. In the occurrence of a near-well leakage of CO₂ from a storage site, it is believed that if the cap rock formation is shale, it might creep towards the wellbore cement and mitigate the severity of the event.

1.2 Approach

In this thesis, the consolidation and creep processes in shale will be examined experimentally by unconfined uniaxial tests on cores samples of Pierre shale. The laboratory work aims to identify how different stress levels and alteration in the pore fluid pH value will affect these mechanisms. To achieve different pH values, the creep experiments will be conducted on core samples submerged in brine (3.5wt% $NaCl(aq)$) and for core samples submerged in a mixture of brine and hydrochloric acid ($HCl(aq)$). Furthermore, the thesis will include suitable theoretical descriptions of creep and consolidation effects and two literature studies will highlight former and relevant research on the topic.

1.3 Thesis structure

The thesis is divided into 9 main chapters:

- Chapter 2: *Background theory* presents existing and relevant theory for the thesis. In addition to introducing new content, the most significant elements of background theory from the specialization project are included here in a revised and modified version.
- Chapter 3: *Literature studies* highlights previous, relevant research and is divided into two main sections. The first section concerns studies related to creep in shale materials. This part was originally composed during the specialization project. An edited and shorter summary of the work is included here in order to provide the reader with essential insights to relevant findings within this topic. The second section attempts to involve research associated with how reduced pore fluid pH affects creep in shale. Unfortunately there have been limited studies conducted on this topic up until now, so the presented work in this section might not deal with the *exact* matter, but it rather highlights important findings. Eventually, one can draw certain speculations from these in order to recognize what to expect from the thesis' creep experiments with alternating pore fluid pH.
- Chapter 4: *Preparations for laboratory work* gives an overview of fundamental work conducted prior to working in the laboratory and before starting the creep experiments.
- Chapter 5: *Experiments and methods* presents the purpose of the lab work and describes experimental procedures, loading paths and setup.
- Chapter 6: *Approaches for finding the transition period between consolidation and creep dominated behavior* explains different methods to distinguish between a period completely dominated by consolidation and a period starting to be dominated by creep.
- Chapter 7: *Experimental results and discussion for creep experiments* shows the obtained results from the creep tests and evaluates the outcomes.
- Chapter 8: *Potential sources of error* highlights possible causes of inaccuracy that might impact final laboratory results.

- Chapter 9: *Conclusion* summarizes the most important findings and results of the thesis.
- Chapter 10: *Recommendations* presents a self-reflection section by the authors and looks into how the commenced work can be continued and potentially improved.

In addition, there are a total of 14 Excel files enclosed to the master thesis presenting obtained data and resulting graphs for all conducted experiments.

1.4 Preceding work

As previously mentioned, the specialization project “Creep and consolidation effects in Pierre Shale” was completed by the authors in the 9th semester of the Master`s degree as a preparation for this thesis. It was carried out at NTNU in cooperation with SINTEF Petroleum Research (Trondheim, Norway) and supervised by Chief Scientist Erling Fjær.

The purpose of the specialization project was to examine creep characteristics and consolidation effects in Pierre shale. Based on this, a comprehensive literature study was conducted and several laboratory investigations were carried out. Axial strain-time curves were obtained by conducting unconfined uniaxial compression tests for core samples submerged in marcol with step loading at a temperature of 40°C. To reduce the risk of permanent failure and establish the right amount of applied stress for the experiments, independent uniaxial compressive strength (UCS) tests were first run to confirm the strength of the rock. The applied load for the creep experiments was then based on 80-90% of the UCS.

The results revealed that Pierre shale exhibits considerable time-dependent deformation in response to applied stress. To distinguish between creep and consolidation dominated behavior, three different estimation methods were applied; calculations (defined in section 2.3.2, p.17), a graphical approach (explained in section 6.1, p.61) and the Mohr-Coulomb criterion (described in section 6.2, p.63). The graphical approach demonstrated that the consolidation dominated period never exceeded 4 hours in the conducted experiments. This value was consistent with the estimated consolidation time found by the calculations. The Mohr-Coulomb criterion showed a higher range of values compared to the other methods.

Overall, it was seen that temperature fluctuation increased with extended test time for the experiments. However, the temperature variation never exceeded 0.96°C which seemed to be a too low value to impact the deformation of Pierre shale. It was also observed a clear correlation between p-wave velocity and temperature. For periods with constant applied stress and a temperature variation exceeding approximately 0.80°C, increased p-wave velocities were seen for temperature drops and decreased velocities were observed for rising temperatures. When comparing samples that were drilled normal to the bedding plane with samples drilled parallel it was observed that the latter demonstrated less creep. Finally, the experimental results implied a dependency between p-wave velocities and strain for fixed stress periods.

2 Background theory

2.1 Brief introduction to petroleum rock mechanics

The aim of this introduction to petroleum rock mechanics is to present fundamental background theory in a concise manner without too many details. Time-dependent effects will be the main focus in this master thesis, but before looking into the theory behind that it is essential to present some underlying knowledge.

2.1.1 Stress and strain definitions

All solid materials, including rocks, will deform when they are subjected to stress. Generally, two stress types may act through a surface; normal stress and shear stress. Normal stress is defined as

$$\sigma = \frac{F_n}{A} \quad (2.1)$$

where F_n is the normal force acting through a surface with an area A (Fjær et al. 2008).

Shear stress is defined as

$$\tau = \frac{F_p}{A} \quad (2.2)$$

where F_p is the parallel force acting through the same surface area A . Stress can be related to surfaces in three orthogonal directions and their magnitude is determined by the orientation of the surface. Since stresses in rock mechanics are mostly compressive, the sign convention suggests that compressive stress is positive (Fjær et al. 2008).

Deformation can be seen through two types of strain; elongation and shear strain. They can both be related to surfaces in three orthogonal directions. Elongation is positive for a contraction, and is defined by

$$\varepsilon = -\frac{\Delta L}{L} \quad (2.3)$$

where L is the original distance between two particles and ΔL is the change in distance between them. Further, shear strain is defined as

$$\gamma = \frac{1}{2} \tan \psi \quad (2.4)$$

where ψ is the change in angle between two initially orthogonal directions (Fjær et al. 2008).

2.1.2 Relationships between stress and strain

There exist many different models aiming to describe the link between applied stress and resulting strain. The most recognized concepts will be briefly presented here.

2.1.2.1 Elastic behavior

Elastic behavior in rock mechanics is defined as the rocks' ability to resist and recover from deformations created by external forces. Internal forces within an elastic material will attempt to counteract a deformation caused by an external force before an equilibrium state is reached. If the external force is removed the elastic material will return to its original shape (Fjær et al. 2008).

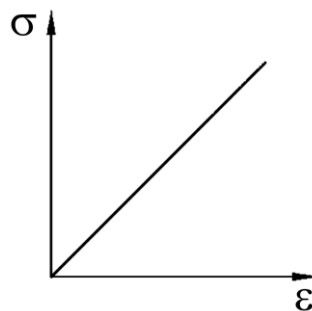


Figure 2.1: Illustration of linear elastic behavior. Modified from (Fjær et al. 2008).

To help describe the relationship between applied stress and resulting strain, several elastic parameters have been defined. Among them are:

- Young's modulus E : a measure of the stiffness of the sample, i.e. the sample's resistance against being compressed by an uniaxial stress.
- Poisson ratio ν : a measure of lateral expansion relative to longitudinal contraction.
- Bulk modulus K : a measure of the sample's resistance against hydrostatic compression.

- Shear modulus G : a measure of the sample's resistance against shear deformation.
- Uniaxial compaction modulus H
- Lamé 1st coefficient λ

When any two of the presented elastic parameters are known, the others can be calculated through identified relations given in Table V-1, Appendix V (p.197) (Fjær et al. 2008). If a material is anisotropic, the elastic parameters will vary for different directions. Due to complexity, anisotropy is often ignored in calculations of rock elasticity so one should be aware that this simplification can lead to imprecise results.

To explain elastic behavior, a variety of equations have been established. A *linear* elasticity model can generally be applied when rocks are subjected to relatively small stresses or when there are sufficiently small changes in stress. Hooke's law can be used to describe the given situation in one dimension (Fjær et al. 2008)

$$\sigma = E \cdot \varepsilon \quad (2.5)$$

This law can be extended into applicability for three dimensions. However, as most rocks behave nonlinearly when subjected to large stresses, the effectiveness of a linear elasticity model is often exceeded in practical situations. Nonlinear elasticity implies a complicated mathematical model; accordingly no further attention will be given to this here.

Finally, it might be essential to mention inelastic behavior. After reaching a certain high stress state, defined by a yield point, a transition from elastic to ductile behavior can be seen for some rocks. Ductile behavior states that the rock undergoes permanent deformation without losing the ability to support load. So after reaching the yield point, the rock will no longer return to its original state upon stress relief as it would for elastic behavior. This mechanism is illustrated in Figure 2.2. For further details, ductile behavior is modeled by the theory of plasticity (Fjær et al. 2008).

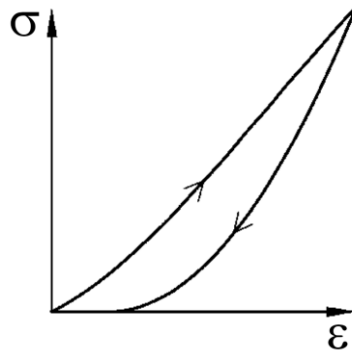


Figure 2.2: Illustration of a material suffering permanent deformation. Modified from (Fjær et al. 2008).

2.1.2.2 Poroelastic behavior

Since petroleum rocks are porous and permeable, one has to account for a potential pore fluid in the void space as well as the solid framework in the rock. A fluid will naturally influence the rocks' mechanical response; its presence adds extra terms to materials strain energy, implying that stress-strain relations will be altered (Fjær et al. 2008). The fundamental theory of poroelasticity was established by Biot and it has in the recent times been further developed by others (Detournay and Cheng 1993). To describe poroelastic behavior, new parameters have been defined in addition to the common elastic parameters (described in section 2.1.2.1, p.8). One can envision that poroelastic theory mainly revolves around two stresses; σ_{ij} (total external stress) and p_f (pore pressure) in addition to two strains; ε_{vol} (volumetric strain) and ζ (a strain parameter for the fluid part) (Holt 2013).

If the fluid is prevented from escaping the pore network, the situation is recognized as undrained. Two effects will be revealed if an external hydrostatic load compresses a porous and permeable rock in the given situation (Detournay and Cheng 1993):

1. The pore pressure will increase
2. The increased pore pressure will again induce a dilation of the rock

These connected mechanisms allocate an apparent time-dependent character to the mechanical properties of the rock. If excess pore pressure (induced by compression) is granted dissipation through diffusive mass transport, further deformation of the rock will gradually take place. When excess pore pressure is fully dissipated, the condition is characterized as drained (Detournay and Cheng 1993).

Poroelasticity is a broad research field that includes many complex equations and ideas, but one of the theories worth recognizing from this work is the *effective stress concept*. So-called effective stresses control volumetric deformation of a linear poroelastic material where the deformation is proportional to the effective stress, σ'_{ij} , rather than the total stress σ_{ij} . The effective stress is defined as (Fjær et al. 2008)

$$\sigma'_{ij} = \sigma_{ij} - \alpha p_f \quad (2.6)$$

where α is the so-called Biot coefficient. The Biot coefficient is further described in terms of

$$\alpha = 1 - \frac{K_{fr}}{K_s} \quad (2.7)$$

where K_s is the bulk modulus of the solid part of the rock and K_{fr} is the bulk modulus of the rock frame. α is defined between 0-1 and is approximately 1 for soils and soft rocks, and less than 1 for hard rocks. Interpreting equation (2.6) physically, the αp_f part is carried by the fluid while the solid framework carries the part σ'_{ij} of the total external stress σ_{ij} . Internal stresses in the solid counteract the remaining pore pressure; $(1-\alpha)p_f$ (Fjær et al. 2008).

2.1.2.3 Thermoelastic behavior

The theory of thermoelasticity considers the effect of a temperature change on the stresses and displacements in a material (Jaeger et al. 2007). It has some resemblance with the theory of poroelasticity, where the temperature portrays a similar role as the pore pressure. This matter has been discussed in detail by Norris (1992) and Geertsma (1957) among others. Regardless of the similarity, an apparent distinction between the two theories is that while the pore pressure is mostly governed by coupled equations, the temperature field is governed by the (decoupled) diffusion equation (Jaeger et al. 2007).

In a material, a temperature change often implies an expansion (by heating) or contraction (by cooling). Rocks in the subsurface, in a petroleum context, may for instance be subjected to a temperature change during production/injection in the wellbore. Under the assumption of linearity, the resulting strain from thermal effects is given by (Fjær et al. 2008)

$$\varepsilon = -\alpha_T \Delta T \quad (2.8)$$

where ΔT is the change in temperature and α_T is the coefficient of linear expansion. The minus sign indicates expansion for an increase in temperature. Further, a thermal stress will build up during the temperature change if the material is constrained;

$$\sigma = E\alpha_T \Delta T \quad (2.9)$$

Naturally, rocks are constrained to some extent in the subsurface and depending on the type of rock and its properties, thermally induced stress may be of extensive impact (Fjær et al. 2008). For instance, temperature effects that induce changes of 30 MPa or greater can be expected during injection of cold water into geothermal wells for pressure maintenance (Pruess and Bodvarsson 1984). If a rock is subjected to both a change in applied stress state and temperature, the fundamental assumption of linear thermoelasticity states that the resulting strain is the sum of the thermal strain and the stress-induced strain (Fjær et al. 2008).

2.2 Rock failure

Failure can occur when the framework of a rock is subjected to sufficiently large effective stresses. Consequently, the rock will permanently change its shape and its ability to carry loads will be reduced or lost. The level of stress that initiates failure is commonly referred to as the maximum strength of the rock. This parameter is greatly influenced by the degree of anisotropic texture (Jaeger et al. 2007). Rock failure in the petroleum industry is often the source behind serious problems such as borehole instability and solids production. These issues have been observed at many fields on the NCS; Statfjord has for instance struggled with initially tight holes that have developed into oversized boreholes due to collapse at the borehole wall (Nakken et al. 1989).

Due to its complexity, the process of rock failure is not fully comprehended even today. Regardless, several models have been established for evaluating whether or not failure will occur. Among others, *tensile failure*, *shear failure* and *compaction failure* are various failure mechanisms that have been recognized. In this section, only the most familiar models for rock failure will be acknowledged. These models represents a simplification of actual rock

behavior, and for practical applications, failure criteria's in two dimensional stress space are normally used (Fjær et al. 2008).

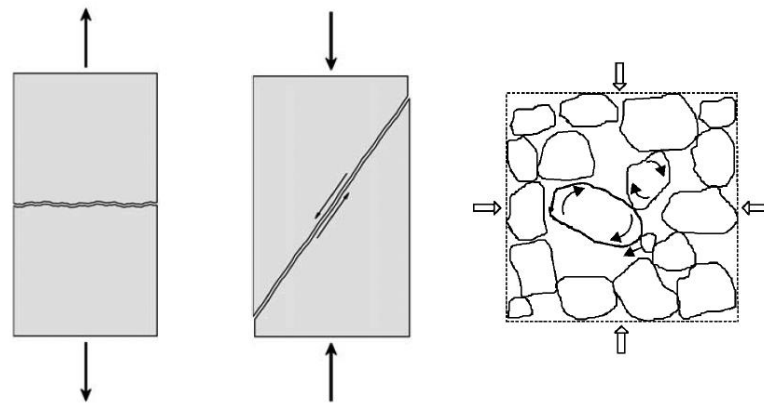


Figure 2.3: Illustration of tensile failure (left), shear failure (middle) and compaction failure (right) (Fjær et al. 2008).

Tensile failure occurs when the effective tensile stress across some plane in a rock exceeds the critical limit T_0 (tensile strength, a distinct property of the rock). Pre-existing cracks is commonly the origin for tensile fractures and the tensile failure criterion is defined as

$$\sigma' = -T_0 \quad (2.10)$$

Figure 2.3 illustrates that a rock suffering tensile failure typically originates fractures oriented more or less normal to the direction of the tensile stress (Fjær et al. 2008).

Shear failure is established when shear stress along some plane in the rock is sufficiently high. Failure normally occurs along weakness planes, and the two surfaces will move relative to each other in a frictional process (illustrated in Figure 2.3). Shear failure can be defined by Mohr's hypotheses, showing (Fjær et al. 2008)

$$|\tau_{\max}| = f(\sigma') \quad (2.11)$$

By choosing different forms of the function $f(\sigma')$ one obtains various criteria for shear failure. The Mohr-Coulomb criterion is most frequently used and it assumes that failure is controlled by only the maximum and minimum principal stress. It states that (Fjær et al. 2008)

$$\tau = S_0 + \sigma' \tan \varphi \quad (2.12)$$

where S_0 represents the cohesion of the material and φ is the friction angle. Shown graphically, shear failure is initiated when Mohr's circle touches the failure line as shown in Figure 2.4. The Mohr-Coulomb criterion can also be expressed as

$$\sigma_1' = C_0 + \sigma_3' \tan^2 \beta \quad (2.13)$$

where β is the angle for which the failure criterion is fulfilled, thus giving the orientation of the failure plane. β is defined as

$$\beta = \frac{\pi}{4} + \frac{\varphi}{2} \quad (2.14)$$

Further, C_0 is the unconfined compressional strength, given by (Fjær et al. 2008)

$$C_0 = 2S_0 \tan \beta \quad (2.15)$$

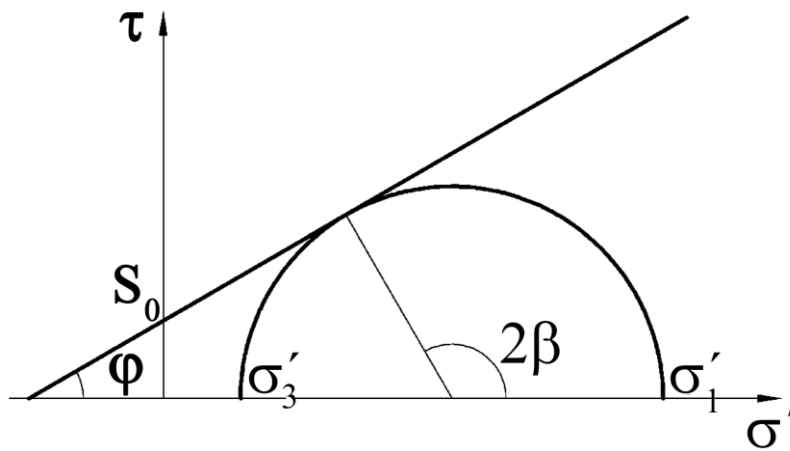


Figure 2.4: Graphical illustration of the Mohr-Coulomb criterion in τ - σ' space. Modified from (Fjær et al. 2008).

Finally, *compaction failure* is commonly observed in high porosity materials where the grain skeleton forms an open structure. Grains might get loose or break and can be pushed into the open pore space during compression, developing a closer packing of the material (Figure 2.3). Pore collapse can be initiated under pure hydrostatic loading resulting in failure due to local excessive shear forces acting through grains and grain contacts. Permanent damage of

the rock framework can occur if grains are crushed and pulled apart. Nonetheless, the rock will still be able to carry load as compaction causes a denser structure (Fjær et al. 2008).

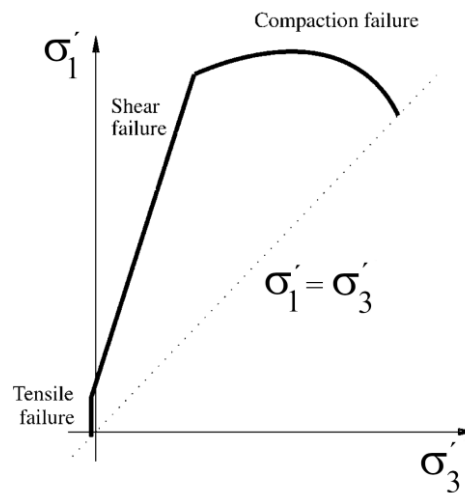


Figure 2.5: The diverse failure mechanisms illustrated in principal stress space. Modified from (Fjær et al. 2008).

2.3 Time-dependent mechanisms

As presented in section 2.1.2 (p.8) there exist several stress-strain relationships in rock mechanics. These theories all assume that deformation is an instantaneous result of the stress applied, but in addition, one also needs to acknowledge time-dependent mechanisms. When a porous material is being exerted to an external force, consolidation and creep effects can occur. Theories behind these concepts will be further explained in this section.

2.3.1 Creep

Creep is a time-dependent deformation that may occur in minerals under stress. Due to viscoelastic effects in the solid framework creep can occur in both dry and saturated rocks (Fjær et al. 2008).

A materials ability to return to its original state after stress has been applied and terminated can be characterized as the elastic part of a material (described in section 2.1.2.1, p.8). The property of the material to resist shear flow and strain linearly with time when stress is applied is defined as a viscous character. Combining these two properties results in a viscoelastic effect (Meyers and Chawla 1999). Figure 2.6 (a) illustrates how a purely elastic material behaves in a stress-strain curve. The deformation will be reversed and the material returns to its original state as the stress is removed. Figure 2.6 (b) demonstrates how the

path changes for a viscoelastic material, and the red area shows the amount of energy that is lost in a loading and unloading cycle (Meyers and Chawla 1999).

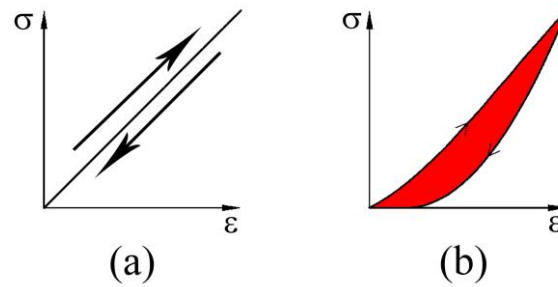


Figure 2.6: Stress-strain curves for (a) an elastic material and (b) a viscoelastic material. Modified from (Meyers and Chawla 1999).

When applied stress to a solid exceeds a yield point, it will result in an instant failure of the material (brittle fracture). For creep, as opposed to brittle fracture, a strain accumulates as a result of long-term stress and a time-delayed failure can occur. “The rate of deformation is a function of the material properties, exposure time, exposure temperature and the applied structural load” (Somiya 2013).

The creep rate is time-dependent and can be divided into the following three stages (illustrated in Figure 2.7);

- Transient stage/primary creep: Deformation rate *decreases* with time.
- Steady-state stage/secondary creep: Deformation rate is *constant* with time.
- Accelerating stage/tertiary creep: Deformation rate *increases* with time.

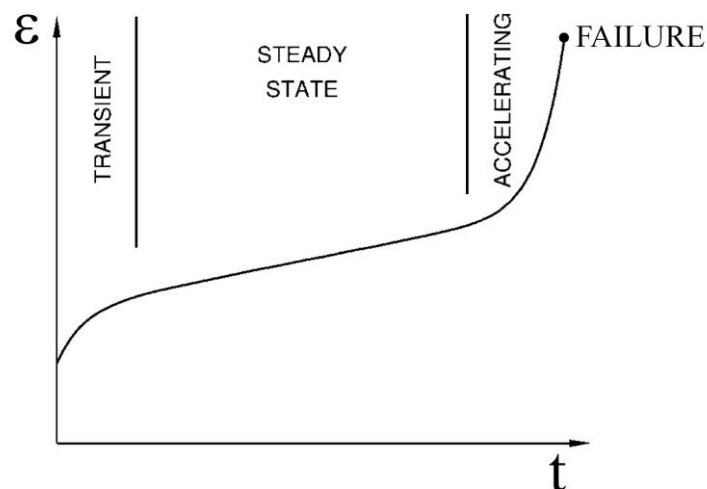


Figure 2.7: Illustration of the different creep stages. Modified from (Fjær et al. 2008).

If the applied stress is terminated in the transient stage, the deformation would be reversed and the material would return to its original state. On the contrary, reducing the stress to zero after the rock has reached steady-state or the accelerating stage would result in a permanent deformation of the rock (Olsen 2015).

As illustrated by Figure 2.8, all stages of creep will only fully develop when applying moderate stress levels to the material. Even if a rock is subjected to a load level somewhat below its ultimate strength, the steady-state creep could transition into accelerating creep and eventually failure because creep weakens the material. High levels of stress could make the rock go rapid through the transient- and steady-state phase and straight to the accelerating stage. For too low stress levels the material would stabilize after a period of transient creep (Fjær et al. 2008).

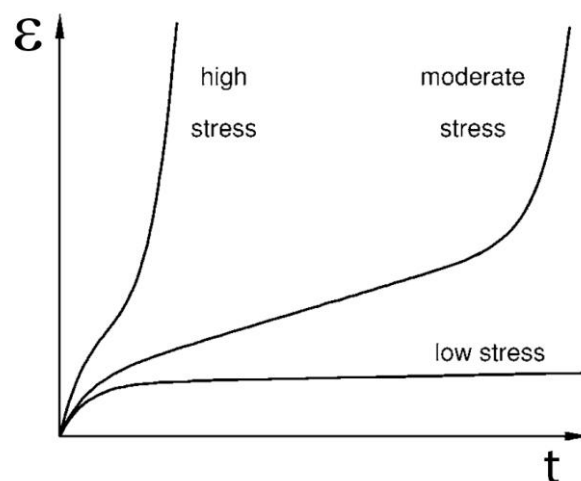


Figure 2.8: Strain vs. time for three different stress levels (Fjær et al. 2008).

2.3.2 Consolidation

While creep can occur in both dry and saturated rocks, consolidation is a time-dependent effect that can only appear for the latter condition. Consolidation develops when pore pressure from fluid inside the rock delays the deformation of the rock. “Consolidation theory describes the transient process, where pore pressure equilibrium is re-established after a change in the stress state” (Fjær et al. 2008).

A porous material that is subjected to external forces will experience a change in stress distribution. As the pores are being deformed they will initiate a compression and a flow of fluid inside the rock. Equation (2.6) (p.11) demonstrates that the effective stress on the solid

material will increase with a decreasing pore pressure, p_f , for a saturated rock. This is a result of pore pressure initially opposing the effect of the external pressure. The applied stress will gradually force the fluid out of the pores until equilibrium with the outside fluid pressure is reached. It will cause a decrease in pore pressure, and thus the effective stress on the solid will increase with time. A delayed deformation of the solid material can be seen, and the magnitude of deformation will therefore be time-dependent (Fjær et al. 2008).

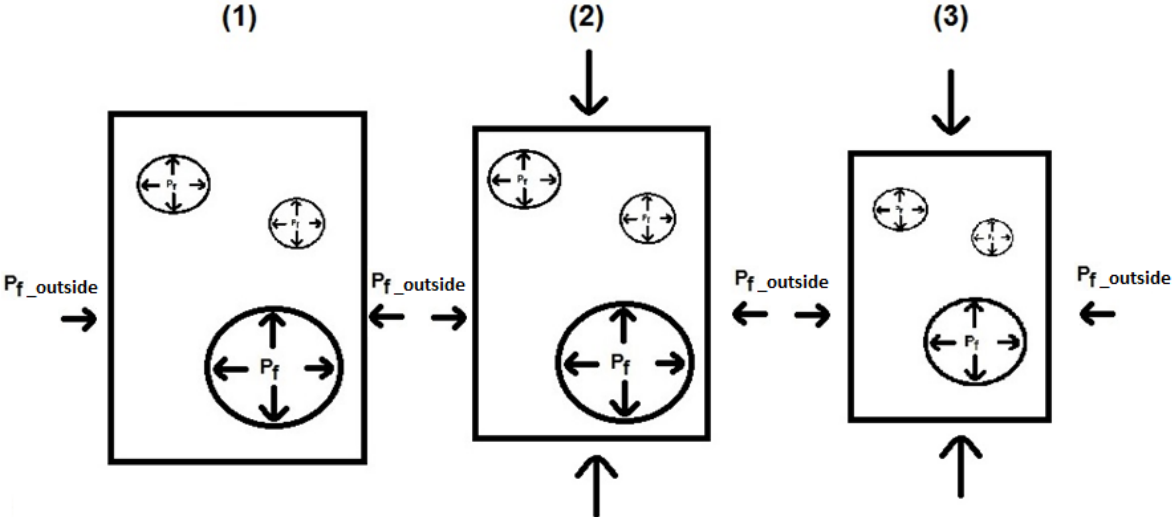


Figure 2.9: Illustration of the consolidation effect.

Figure 2.9 illustrates consolidation in a porous rock surrounded by a fluid. Step (1) shows the rock at time t_1 . Here, the pore pressure is equal to the initial pore pressure of the rock and no external pressure is present. At time t_2 the pore pressure is constant while an external stress is applied to the rock (illustrated with arrows in step (2)). This applied force induces a deformation of the solid material. At step (3) the fluid has started to flow out of the rock, resulting in a decrease of pore pressure. This causes additional deformation of the solid material until the pore pressure reaches equilibrium with the pressure from the outside fluid. The less permeable the rock is, the longer time this development will take (Jaeger et al. 2007). For a stabilized pore pressure, fluid will no longer flow out of the rock, indicating that the consolidation part has terminated. As a result, one can state that consolidation is a physical property that is strongly related to the flow of fluid inside the pores. Generally, inside a porous material, the flow Q , can be described by Darcy's law:

$$Q = -\frac{kA_c}{\eta_f} \Delta p_f \quad (2.16)$$

where k is the permeability, A_c is the cross section area, Δp_f is the pore pressure gradient and η_f is the dynamic viscosity of the fluid. Darcy's law describes a stationary flow through a porous medium for a homogenous pore pressure field and it was developed based on results from experiments of water flowing through sands (Fjær et al. 2008). Equation (2.16) demonstrates how the pore pressure gradient Δp_f induces a flow rate Q of fluid through the rock. The time it takes for the fluid to reach equilibrium will depend on the permeability of the rock, the fluid viscosity, the stress applied to the rock, the distance the fluid must flow, the cross sectional area for the flow and the pore pressure gradient. However, equation (2.16) is only applicable for stationary flow of fluid. This implies a flow where the velocity of the fluid at a particular fixed point does not change with time (illustrated in Figure 2.10a). For fluid flow inside a porous material (caused by external surrounding pressure), the flow rate will decrease as soon as pressure equilibrium is reached. Thus, the flow of fluid will be time dependent, representing a transient flow (shown in Figure 2.10b). Fjær et al. (2008) presents an equation that is more applicable for describing the transient process;

$$\frac{k}{\eta_f} \nabla^2 p_f = \frac{\partial}{\partial t} \left(\frac{1}{M} (p_f - C \varepsilon_{vol}) \right) \quad (2.17)$$

where M (Biot's M-parameter) and C (Biot's C-parameter) are additional moduli required to describe a two phase medium. Equation (2.17) shows that there is a link between the pore pressure, p_f , and the strain, ε_{vol} . For a more detailed derivation of this equation see Fjær et al. (2008), section 1.9.

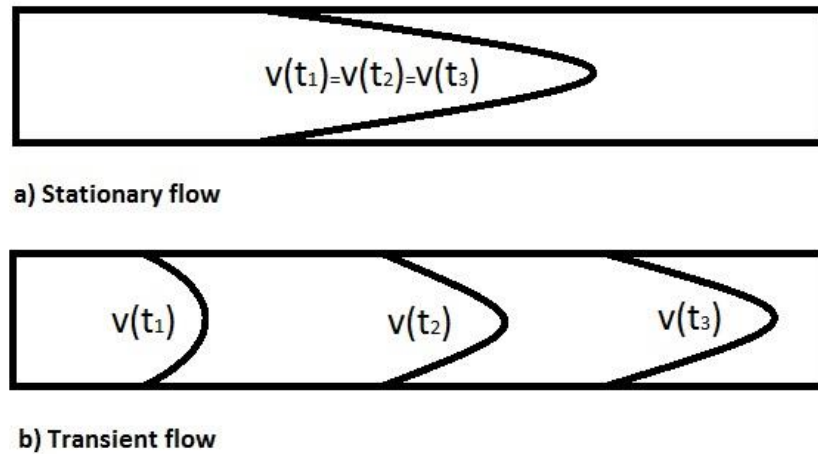


Figure 2.10: Illustration of different flow regimes: a) stationary flow and b) transient flow.

As previously mentioned, the consolidation time is dependent on the permeability of the solid material. In high permeability materials the pores will be connected and make a channel for the fluid to easily flow out of the medium. This will result in a relative rapid decrease in pore pressure as the fluid is forced out. In contrast, materials with low permeability will have a limited pathway for the fluid to flow because the pores are not sufficiently connected. Thus, the time will be longer for the fluid to escape the pores for low permeability shale compared to highly permeable sandstone. Determining the consolidation time in the rock is of interest when trying to distinguish between creep and consolidation. A rough estimate of the time it takes before the pore pressure has reached equilibrium can be made by using the following equation (Fjær et al. 2008)

$$\tau_D = \frac{l_D^2}{C_D} \quad (2.18)$$

where τ_D corresponds to the consolidation time in seconds, l_D is the pore pressure diffusion length (in this case the radius of the core) in meters and C_D is the pore pressure diffusion constant. Generally, there are several equations to choose from when estimating C_D , but one approach is given by

$$C_D \rightarrow \frac{k}{\eta_f} \left(K_{fr} + \frac{4}{3} G_{fr} \right) \quad (2.19)$$

where k is the permeability of the rock, η_f is the dynamic viscosity of the fluid, K_{fr} is the bulk modulus of the rock frame and G_{fr} is the shear modulus of the rock frame. Equation (2.19) assumes $G_{fr} \ll \frac{K_{fr}}{\phi}$ (Fjær et al. 2008).

2.4 Acoustic waves

In rock mechanics one can use acoustic waves to estimate several rock mechanical parameters. For instance, measurements of wave propagation can help distinguish between static and dynamic moduli (explained in section 2.4.3, p.23), provide correlations with rock strength and give valuable information regarding in situ stress state. In addition, acoustic measurements through core samples are often conducted in the laboratory to support interpretation of sonic logs and seismic measurements (Fjær et al. 2008).

2.4.1 Primary waves

Primary waves are one of the main acoustic wave forms. They are also commonly referred to as p-waves and involve a periodic compression of the material. It is recognized that the displacement of the medium that p-waves travels through moves parallel to the direction of the wave.

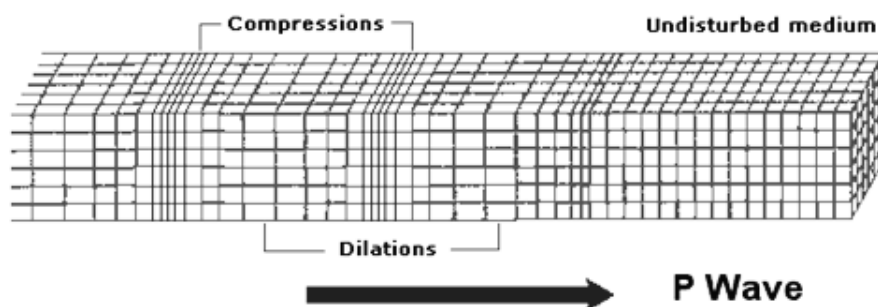


Figure 2.11: Illustration of a p-wave motion. Modified from (Rogers 2015).

By combining Newton's second law of motion and Hooke's law the p-wave velocity for a linearly elastic, homogeneous and isotropic medium can be found. Solving for parallel displacement to the wave in one direction results in

$$v_p = \sqrt{\frac{H}{\rho}} = \sqrt{\frac{K + \frac{4}{3}G}{\rho}} \quad (2.20)$$

where H is the uniaxial compaction modulus, ρ is the density of the medium, K is the bulk modulus and G is the shear modulus. To account for the fact that most rocks are usually neither linearly elastic, homogeneous nor isotropic, a more complex relation between acoustic velocities and elastic moduli has been developed (Fjær et al. 2008). More details regarding this can be found in section 2.4.3.

Table 2-1: Common p-wave velocities for various rock types. Modified from (Fjær et al. 2008).

Rock type	Density ρ [kg/m ³]	P-wave velocity [m/s]	Conditions
Shale	2300-2800	1600-4500	Saturated, various porosities
Clay	1900-2100	1500-1600	Saturated, from surface to 50 m depth
Weak shale, North Sea	1800-2300	2400-2600	Saturated, unconfined

2.4.2 Influence of pore fluid, temperature and anisotropic texture

Pore fluid in a porous material provides an extra resistance against compression, and because of this, the p-wave velocity for a saturated material can be larger than when the same material is dry. The influence of saturation depends on the ratio between the frame stiffness and the fluid modulus. Generally, the p-wave velocity for a saturated soft material (high porosity) will usually increase, while it decreases for stiff rocks. However, increased p-wave velocities can also be seen for low porosity rocks if the frame stiffness is very low. For characterizing elastic wave propagation in saturated rocks, Biot's theory may be applied (Fjær et al. 2008).

Other parameters, like temperature and anisotropy, can also affect acoustic wave propagation in rocks. With increased temperature, there is normally a slight reduction in wave velocities (Christensen 1982). Regarding anisotropic texture, one has diverse stiffness in different directions of the rock and a generalized version of the wave equation and its solution to account for this effect is presented in Fjær et al. (2008), section 5.5.

2.4.3 Static and dynamic moduli

Experiments have demonstrated that stress and strain measurements in a rock mechanical test results in different elastic moduli than those obtained from acoustic velocities and density measurements. The elastic moduli are referred to as “static moduli” and “dynamic moduli” respectively (Fjær et al. 2008). Static moduli are normally less in value than the corresponding dynamic ones. The greatest deviations can be seen for weak rocks, and depending upon the stress state the difference can be in an order of magnitude or more. Since homogeneous elastic materials have proved to acquire equal static and dynamic moduli, it is believed that the physical origin of the static-dynamic discrepancy must be related to the heterogeneous microstructure of rocks. Based on observations of weak sandstones, Fjær (1999) established a quantitative model for the relations between static and dynamic moduli;

$$K_{stat} = \frac{K_{dyn}}{1 + (P_z + 2P_r)K_{dyn}} \quad (2.21)$$

$$E_{stat} = \frac{E_{dyn}}{1 + P_z E_{dyn}} (1 - F) \quad (2.22)$$

The subscripts z and r refer to axial and radial directions in a standard triaxial test, while K_{dyn} and E_{dyn} are the dynamic bulk modulus and dynamic Young’s modulus obtained from velocity measurements. K_{stat} and E_{stat} are the corresponding static moduli obtained from the slope of the relevant stress-strain curve during initial loading in a rock mechanical test. P_i is a measure of non-elastic compliance (the inverse of stiffness) while F is a measure of the additional non-elastic deformation caused by shear loading (Fjær 1999).

2.5 Brief introduction to relevant chemical concepts

One of the main purposes of this master thesis is to identify how the consolidation and creep mechanisms are affected by alteration in pH of the pore fluid. Based on this a required introduction to some chemical concepts will be presented in this section.

2.5.1 pH

In chemistry, the acidity or alkalinity of an aqueous solution can be defined by a numeric number referred to as the pH-value. The concept of pH was first introduced in the early 1900s by the Danish bio-chemist Søren P.L. Sørensen (Sørensen 1909), and even though the exact meaning of the abbreviation has been strongly debated, it is believed by some that pH is short for “power of hydrogen” (Jensen 2004). The pH scale normally ranges from values of 0-14, where a pH of 7 represents a neutral solution, for instance pure water. Solutions with a higher value than 7 indicate bases and solutions with a lower value than 7 imply acids (Zumdahl 2009). However, in the recent years it has been shown that for very strong acids or bases, the pH value can be less than 0 or greater than 14 respectively (Lim 2006). By definition, the pH value is described by a log scale based on 10 and the concentration of H^+ ions:

$$pH = -\log[H^+] \quad (2.23)$$

As seen by equation (2.23), as $[H^+]$ increases, the pH value decreases. Theoretically, since pH is a log scale based on 10, a change of one pH unit will equal a tenfold difference in the concentration of hydrogen ions. Today, an electronic pH meter is traditionally used for measuring the pH of a solution. pH measurements are essential in many disciplines; chemical engineering, medicine, biology and environmental science among others (Zumdahl 2009). Figure 2.12 illustrates the pH values for some common substances.

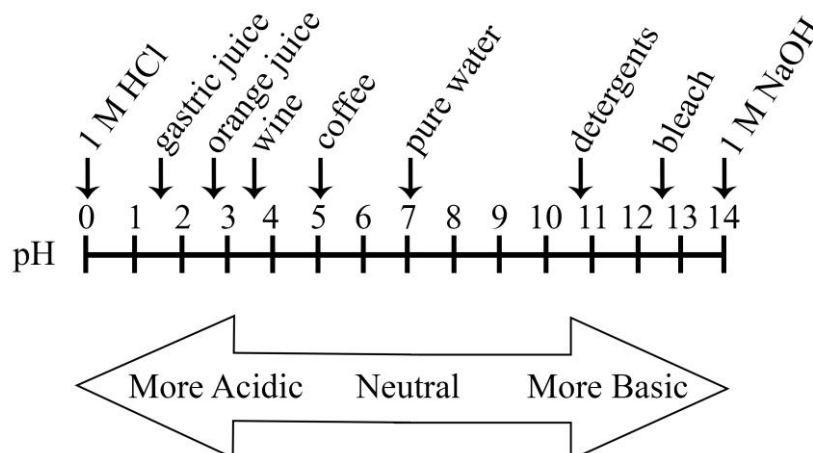


Figure 2.12: The pH scale. Modified from (Askew 2012).

2.5.2 Chemical weathering

In geology, chemical weathering is a process where rocks become chemically altered due to reactions with the surroundings. This happens because minerals in the rock adjust to approach equilibrium with near surface conditions (Birkeland 1974). The extent of disequilibrium rely on the minerals formation conditions; mineral reactivity is for instance strongly influenced by temperature (Goldich 1938). Chemical weathering can generally be divided into three main processes; oxidation, carbonation and hydrolysis. Oxidation occurs when the minerals in the rocks are exerted to oxygen. This changes the mineral composition of the rock, and thus the rocks properties. Carbonation implies that the rock reacts to carbonic acid (formed when water is combined with carbon dioxide) and it dissolves the minerals of the rock. Hydrolysis is a process caused by water exposure. Water makes the rock less resistant to weathering, and changes its minerals sizes and chemical composition (Mamo 2016). Further, common minerals, precipitated from or dissolved in an aqueous phase can be distinguished into those who are inert and those who are relatively reactive. Minerals with simple stoichiometry, like calcite, are much more likely to reach solubility equilibrium than those who have a complex stoichiometry (Olabode and Radonjic 2014).

2.5.3 Chemical activity

In a simplified manner, chemical activity can be interpreted as a measure of the “effective concentration” of specie in a mixture. In practice, the chemical activity is frequently used as described and this can be valid for some cases, but since chemical activity is influenced by its surroundings, implying that the concentration and the activity can be significantly different, “effective concentration” is not a precise term. A more accurate characterization is to use chemical activity to specify equilibrium constants. The chemical activity a_A of component A is defined as the product of the activity coefficient f_A and the molar concentration of a given ion, denoted as x_A ;

$$a_A = x_A \cdot f_A \quad (2.24)$$

a_A is a dimensionless quantity, but dependent on choices of standard state for the species. The activity coefficient f_A is defined from 0 to 1, and is commonly used in thermodynamics as a measure of how much a mixture of substances deviates from ideal behavior. In an ideal

mixture there will be no microscopic interactions between the chemical species, and these mixtures will have an activity coefficient of 1. f_A will decrease as there is an increase in concentration of charged ions that are present in the solution (deviating from an ideal solution). If the solutions ionic strengths are known one can find the activity coefficient in tables and compute the activity (Egeland 2015). Generally, the chemical activity of a solution can be used to calculate the pH-value or the solubility of the solution (Atkins and De Paula 2006).

2.5.4 Osmosis

The physical phenomenon osmosis was introduced in 1854 by Thomas Graham, but it was not thoroughly studied until Wilhelm Pfeffer examined it closer in 1877. Osmosis is defined as the resultant movement of water through a semi-permeable membrane caused by a difference in osmotic pressure across the membrane. By definition, this membrane is a selective membrane which only allows for passage of water, and not ions or solute molecules. Due to a difference in concentration of a solute across the membrane an osmotic pressure, π , builds up and acts as a driving force for water flow through the membrane. The water will flow towards the higher concentration of the solute. The osmotic pressure is defined as (Cath and Childress 2006)

$$\pi = \rho gh \quad (2.25)$$

where g is the gravity constant, ρ is the density of the fluid and h is the difference in height of the columns on each side of the membrane, illustrated in Figure 2.13. When the osmotic pressure has stabilized there will be no net flow of water through the membrane. Adding additional solute to one of the columns in Figure 2.13 will alter the osmotic pressure and a new flow of water will be initiated. This effect can be avoided if one adds solute such that the concentration on each side of the membrane is constant (Cath and Childress 2006).

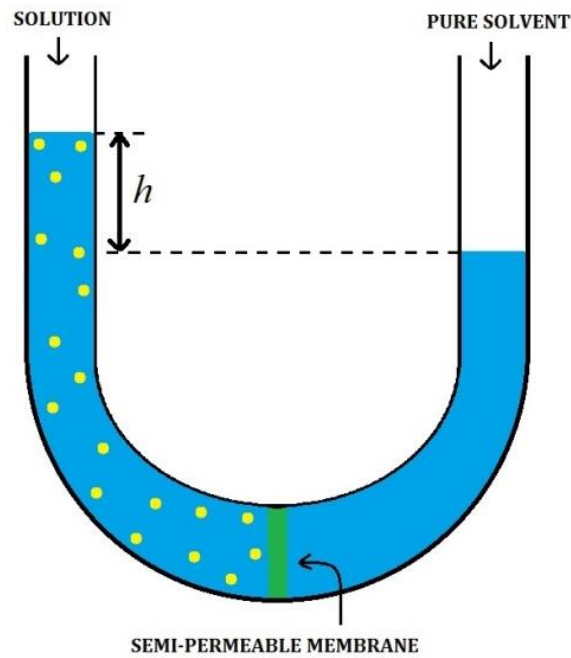


Figure 2.13: Osmotic pressure caused by water movement through a semi-permeable membrane. Modified from (Hillewaert 2007).

Some rocks, such as shales, are relatively sensitive to exposure of different fluids. Thus, osmosis is an important mechanism to comprehend as it can drastically change the characteristics of a rock (Lal 1999).

2.5.5 Ion diffusion

Ion diffusion is the migration of ions and molecules in a fluid/gas due to a gradient of pressure, temperature or concentration. For a concentration gradient the molecules and ions will move from a region of high concentration to low concentration. A simple explanation of this concept is illustrated in Figure 2.14 where the molecules diffuse from a high concentration to a low concentration. Although it looks like the molecules are evenly distributed and there is no diffusion in Figure 2.14 B, the net flux differs from zero.

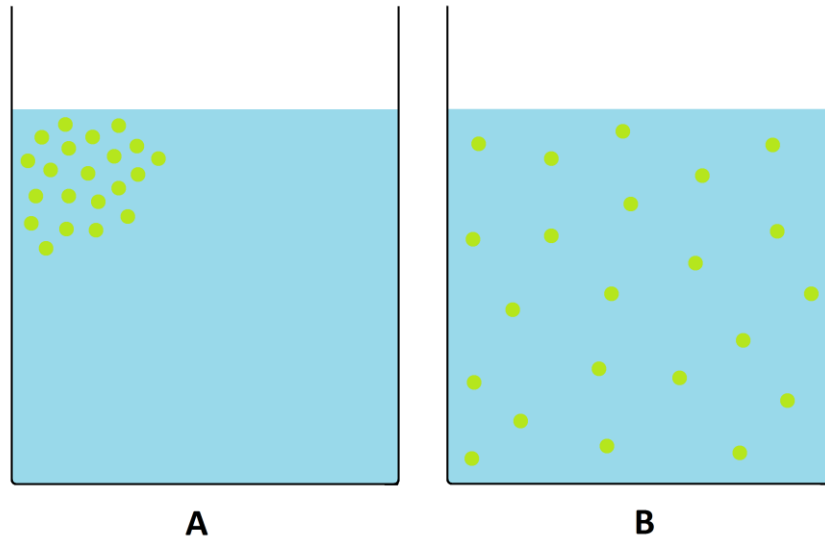


Figure 2.14: Diffusion of particles shown as a result of a concentration gradient in the fluid. A: Particles are added to the water. B: Particles are evenly distributed after some time due to diffusion. Modified from (Pool 2008).

Diffusion is a spontaneous and random movement of particles that results in an evenly distributed concentration in a specified volume after a given time. The force that represents the spontaneous tendency of the molecules to disperse is defined as (Atkins and De Paula 2006):

$$F_m = -\left(\frac{\partial\mu}{\partial x}\right)_{P,T} \quad (2.26)$$

where μ is the chemical potential, x is the position of the ion, P is the pressure and T is the temperature. The diffusion rate is dependent on several other parameters, such as (Muniz and Abildsnes 2009):

- the relationship between volume and surface area of the molecule; as this ratio increases the rate of diffusion will increase.
- the length of the diffusion path; a decrease in diffusion path will give a higher diffusion rate.
- difference in concentration in the fluid/gas; a greater difference in concentration will increase the rate of diffusion.
- the size of the molecules; a small molecule will diffuse faster than a larger one.

To determine diffusion rates, a diffusion coefficient has been determined experimentally for several species pair and can be found in physical handbooks (Samson et al. 2003).

Since porous materials can contain different fluids, these fluids can alter the properties of the material if it is reactive. As this master thesis handles a sensitive rock such as shale, this is an important mechanism to comprehend. The movement of ions in solution is highly dependent on the ion charge, so the movement will naturally depend on the presence of other ions. In addition to reactions among ions within the fluid, the ions present on the surface of the pores can also react with the ions in the pore fluid. This can further result in an alteration in the surface properties of the pores (Samson et al. 2003).

2.6 Shale as a rock

Shale is a type of clastic sedimentary rock with extensive presence of clay minerals. For a rock to be defined as shale the clay content should exceed 40% (Fjær et al. 2008). Kaolinite, smectite, chlorite and illite are some of the most frequent clay mineral groups present (Skalle 2014). Thus, there is a high probability to find many variations and diverse compositions within shale. However, the key characteristics are often similar; low permeability, fine-grained, large negatively charged surface areas and anisotropic texture. Still, the elastic shale properties highly depend on the dominant clay mineral and the absorbed or bound water present within the minerals and on the mineral surfaces (Fjær et al. 2008). Consequently, there exists a large variation in mechanical properties for shale. Shale formations are known, depending on lithology and in-situ stress conditions, to be capable of creep. This is a property of the rock that can be applicable in many areas of different industries. Shale is often put into a category on the borderline between hard soils and weak rocks. Its typical strength characteristics are analogous to rocks, while lithology wise they are similar to clay soil (Nakken et al. 1989). Due to the former, shale will in this thesis be treated as a rock.

Table 2-2: Mechanical properties for various rocks (Fjær et al. 2008).

Rock type	Density ρ [kg/m ³]	Young's modulus E [GPa]	Poisson ratio ν [-]	Unconfined compressive strength C_0 [MPa]
Shale	2300-2800	0,4-70	0-0,30	2-250
Clay	1900-2100	0,06-0,15	~0,40	0,2-0,5
Pierre shale I	2370-2390	0,77-1,12	0,35-0,37	7,5-13,9

Since shale makes up approximately 75% of all sedimentary rocks by volume, the probability to interact with it is high during the various stages of exploration, drilling and production in the petroleum industry (Mese and Tutuncu 1996).

In this master thesis all laboratory work will revolve around Pierre shale. The Pierre shale is commonly found in the North West part of the US and it is an Upper Cretaceous marine shale (Fooks and Dusseault 1996). It was first acknowledged by Meek and Hayden in 1862 and named due to its existence near Fort Pierre on the Missouri River in South Dakota (Schultz et al. 1980). They described the rock as a dark-gray shale containing fossils and veins and seams of gypsum. It is fairly easy to recover large amounts of the Pierre shale since it is usually not buried too deeply. Due to this, and its similarity in mineralogy to many other shales encountered during deep borehole drilling, it is an ideal shale to investigate further in the lab (Fooks and Dusseault 1996).

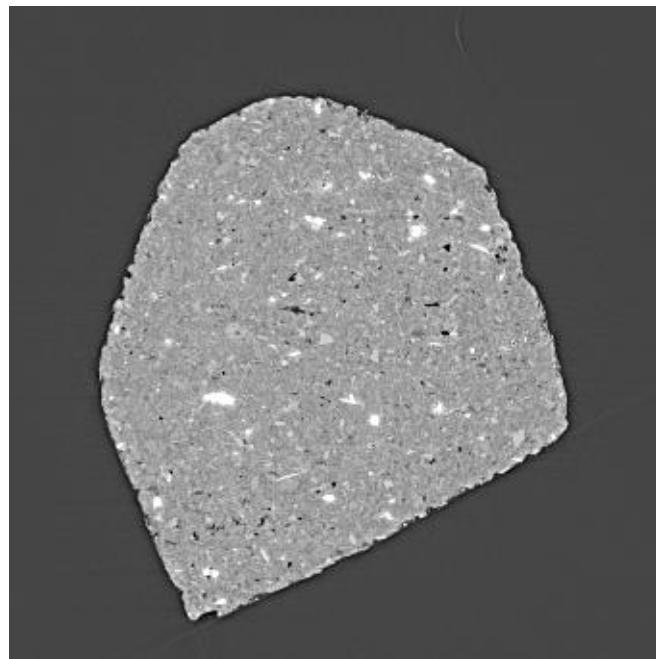


Figure 2.15: Cross section of Pierre shale sample saturated with oil (provided by SINTEF Petroleum 2016).

3 Literature studies

As mentioned earlier (section 1.4, p.4), a rather comprehensive literature study on descriptions of creep in shale materials was conducted in the authors' specialization project. A shorter summary of this is included here to provide the reader with essential insights to previous findings within this topic. In addition, a new literature study has been carried out to gain knowledge of how reduced pore fluid pH affects creep in shale. This topic is relevant for the laboratory work in the thesis.

3.1 Descriptions of creep in shale materials

The properties of shale as a rock have over the past years been thoroughly investigated. In addition to being a potential annular barrier for PP&A operations and possibly mitigating near-well leakage from underground CO₂ storage sites, many shale reservoirs have been discovered and evolved all over the world in the recent times. With a high desire to optimally develop these fields, an increased focus on examining shale has risen. As a result of this, several have gained interest in further exploring the creep phenomenon of this rock. Knowledge of time-dependent deformation behavior of shale is also essential to others than the petroleum industry. For instance, this kind of expertise is fundamental for design and construction of underground structures like tunnels (Lo and Lee 1990) and mines (Mishra and Verma 2015). In this section some of the previous research conducted on creep in shale materials will be highlighted and presented in a historical order.

Already in the 70s, Cogan (1976) presented results from triaxial creep experiments conducted on shale. His results showed that the consolidation phase varied with the amount of axial stress applied to a sample. For low axial stresses, the consolidation part continued into the secondary stage of creep, while for a high axial stress, it was immediately terminated. Cogan's (1976) experiments also demonstrated how consolidation retards the creep phase. Two separate creep rates were observed for samples with the same creep stress ratio. A sample that was exposed to a low confining pressure experienced a reduced creep rate compared to a sample that was exposed to a higher confining pressure. In addition, his results postulated that the primary creep stage period was highly dependent on the axial load applied to the sample. For a test performed with low axial stress, he observed a near to non-existing primary creep stage, while a higher axial load under the same

confining pressure resulted in a noticeable increase in time for the primary creep stage. Overall, Cogan was one of the first in the modern times who demonstrated that shale exhibits considerable time-dependent deformation (Cogan 1976).

Two years later, Chong et al. (1978) performed uniaxial tests to investigate how creep behavior was affected by different stress levels and organic/mineral content in oil shale samples. The results showed that the samples' mechanical properties under creep tests were strongly influenced by various stress levels and the volumetric organic content. It was also observed that the creep mechanism was insignificantly affected by dolomite contents. Eventually, the authors developed a rheological model for creep behavior of oil shale as a function of organic content and stress level (Chong et al. 1978).

A few years later, Chu and Chang (1980) investigated how elevated temperatures affected the creep and strength of oil shale. The overall results from uniaxial tests showed that creep behavior, rock strength and mechanical properties of oil shale were very sensitive to temperatures and stress levels. They observed that the ultimate strength of the samples decreased substantially with temperature increase. Also, it was demonstrated that creep deformation entered tertiary creep and eventually failure under a sufficiently high temperature or large stress. In addition, the creep strain rate was seen to increase with time in a secondary and tertiary creep state for raised stress and/or temperature, and the tertiary creep life was found to be dependent upon secondary creep strain rate. Eventually, Chu and Chang (1980) developed a generalized rheological Kelvin model to predict primary and secondary creep of oil shale for various stresses and temperatures (Chu and Chang 1980).

Later, Rongzun et al. (1987) investigated creep characteristics of shale samples with different water content, and utilized the obtained results to analyze loadings on oil well casings. In the test program, the authors considered stress level and water content exclusively as important parameters. Ultimately, the acquired test data was fitted to two different modified non-linear models (Maxwell and Burger's). Overall, the final results demonstrated that increased water content in shale produced a higher formation creep loading, hence raising the possibility for casing collapse (Rongzun et al. 1987).

In the early 90s, Savage and Braddock (1991) carried out an extensive testing program to determine the mechanical properties of Pierre shale. The authors conducted hydrostatic

consolidation tests with different confining pressures. Their results illustrated how pore pressure supports solid material as long as the fluid is not drained from the pores inside the rock. Overall, a model was developed that had the ability to estimate the time variation of the volumetric strain, pore pressure and a number of material properties of Pierre shale (Savage and Braddock 1991).

A few years later, Horsrud et al. (1994) performed laboratory studies to examine time-dependent borehole stability during drilling in shale. Their results demonstrated that as a consequence of low permeability in shale, consolidation effects may act on a time scale of days and can contribute to delayed failure. It was found that the permeability of shale was proportional to this time scale. Also, the authors concluded that creep effects cannot be entirely ignored as a contribution to stability problems. It was demonstrated that creep can contribute to stability problems in younger, normally consolidated shale (Horsrud et al. 1994).

In the millennium, Liu and Zhou (2000) conducted a great amount of experiments to examine how creep behavior altered with diverse confining pressures and water content. They also analyzed how the failure mode changed with the same parameters. Their results demonstrated that there was a significant link between failure strength parameters and the water content. Liu and Zhou (2000) observed that increased water content resulted in decreased rock failure strength, and thus the rock collapsed faster. This confirmed the findings of Rongzun et al. (1987). In shale, clay minerals absorb water which changes their inner structure and reduce the strength. Thus, increased water content accelerates creep deformation. For uniaxial creep tests with identical water content, all of the failures resulted in shear failures. However, when the confining pressure was increased, the failure mode switched from shear failure to fracture failure (Liu and Zhou 2000).

Some years later, Chang and Zoback (2008) conducted hydrostatic pressure creep experiments on room-dried unconsolidated shale samples. Their results demonstrated significant creep strain when stress was applied to the shale. The authors observed that if the deformation was restricted to the size of the pores, the creep did not level off as anticipated. This implied that creep could be seen as an inherent property of the dry matrix of the shale. When comparing strain above and below a certain level (30 MPa), the results

showed a slight different behavior for the shale. An increase in strain was seen when the pressure was raised up to 30 MPa, while the strain decreased when the pressure had passed this level. Studies showed that this was due to the stiffening effect of the shale. Overall, the experiments revealed that shale exhibits time-dependent creep, and the authors developed a theoretical model based on power law to describe the behavior of the rock (Chang and Zoback 2008).

A couple of years later, Sone and Zoback (2010) investigated creep in shale gas reservoir rocks with different carbonate and clay content. The authors observed that the samples containing more carbonate seemed to creep less. Also, the results implied that the creep mechanism was not dependent on confining pressure. Finally, a link between strength of the samples and clay content was found; increased clay content showed a decrease in strength of the samples (Sone and Zoback 2010).

In 2012, Li and Ghassemi (2012) performed several uniaxial and multi-stage triaxial creep tests on shale. Results from the experiments showed that stiffer shale (less clay) creeps less under the same ambient conditions and stress state as shale with higher clay- and organic material content. The uniaxial creep tests also demonstrated a stress threshold for steady-state creep and the shale sample would only exhibit steady-state creep exclusively above this stress level. Strain-time curves below this threshold had a flat end. The authors also demonstrated that under the same stress level at a certain time, higher confining pressures increased the magnitude of creep strain. Eventually, it was found that an empirical power law function of stress and time could best predict the creep deformation (Li and Ghassemi 2012).

Two years later, Sone and Zoback (2014) completed an extensive study on time-dependent deformational properties of shale gas reservoir rocks. Their experiments demonstrated that all samples showed time-dependent deformation. However, the most distinct creep behavior was found for rocks with the greatest clay- and organic content. This observation coincides with previous findings from Li and Ghassemi (2012). A significant variation in the strain response was observed for samples from different reservoirs, and it was also observed an increased creep effect for cores drilled perpendicular to the bedding plane compared to

the samples drilled parallel. Further, a correlation between creep rate and dryness was found; a decrease in creep rate was seen for oven-dried samples compared to room dried.

Sone and Zoback (2014) also observed that creep rate and strain response were independent of the confining pressure, and that strain response was approximately proportional to the applied axial differential load. In addition their results showed that the parallel direction to the applied differential load exhibited the most time-dependent strain. The authors concluded that the time-dependent behavior of the reported shale could be modeled as an empirical power-law function of time (Sone and Zoback 2014).

Finally, in recent research from 2015 Villamor and Ghazanfari (2015) examined creep behavior of rocks from shale gas reservoirs. Their results demonstrated that creep behavior was significant in all the samples, and creep strain was found to be proportional to the deviatoric stress. The authors also observed that creep strain in the axial direction was higher than in the radial direction. Eventually, a developed power-law strain-time model by Ghassemi & Suarez-Rivera (2012) showed close agreement with the experimental and analytical results of the creep behavior in these studies (Villamor & Ghazanfari 2015).

3.2 How reduced pore fluid pH affects creep in shale

Up until today, there has been limited research conducted on how alteration of the pore fluid pH will affect the creep phenomena in shale. Also, several interdisciplinary fields, including chemistry, geology and rock mechanics are involved in regards to this topic, which makes it somewhat complex. Due to shortage of applicable literature, the work that will be presented here might not deal with the *exact* topic. However, it still presents and highlights some relevant findings from several studies that one can eventually draw certain speculations from.

3.2.1 Clay minerals in shale

As a sedimentary rock, the pore system in shale is usually lined or filled with a variety of different clay minerals. Understanding the structure of these minerals and the implications that they might have on the shale itself is significant. In 1981, Almon and Davies (1981) presented detailed knowledge regarding the chemistry of clays. Overall, clay minerals are fine-grained and may be divided into four main groups; kaolinities, smectites, illites and

chlorites. The different groups have their own specific chemical composition, but even so, each individual group can contain up to several members itself that may also show differences in chemical structures within the group. Thus, the reaction rate between clays and fluids and the degree of sensitivity to different fluids may vary considerably both between groups as well as within a single group. In a petroleum context, there are several potential problems related to fluid interaction with clays during various well operations. Smectite is water-sensitive and can swell in the presence of fresh water while chlorite is extremely sensitive to acid (dissolves readily in dilute $HCl(aq)$) and can cause precipitation of secondary iron compounds. Illite is recognized for increasing pore tortuosity and kaolinite is associated with migration-of-fines problems (Almon and Davies 1981).

3.2.2 Interactions between minerals and solutions

When it comes to shale, or any other rock for that matter, one aspect that can be significant to look into is research related to how minerals in the rock interact with other minerals or solutions. Generally, clay minerals consist of small platy or rod like crystals, and because of this atomic structure, a high surface-area to volume ratio is obtained. Due to the large surface areas, clay minerals tend to react rapid and stronger with fluids introduced into a sedimentary rock compared to quartz, feldspar etc. (Almon and Davies 1981). In shale for instance, clay minerals make the rock easily deformable with a potential to creep, while the presence of quartz gives the rock a reasonably high mechanical strength (Olabode and Radonjic 2014).

In regards to clay minerals interaction with $HCl(aq)$, kaolinite does not react severely to acid and is more or less stable from a chemical point of view since it is a hydrated aluminosilicate. However, both smectite and illite appear to react slightly with $HCl(aq)$, and chlorite is extremely sensitive to it (Almon and Davies 1981). Considering other minerals, carbonates are soluble in low pH while quartz/feldspar are more stable, but they will react at very low acidic environments which can for instance impact the sealing integrity of shale (Olabode and Radonjic 2014).

Table 3-1: Clay mineral composition and possible reactions with HCl. Modified from (Almon and Davies 1981).

Clay Mineral	Important elements in composition	Reaction with HCl	Comment
Kaolinite	Al Si O H	Slight/Small	May be stable
Illite	K Al Si O H	Slight	May dissolve
Smectite	Na Mg Ca Al Si O H	Slight	May swell
Chlorite	Mg Fe Al Si O H	High	Dissolves

In 2006, Wang et al. (2006), performed a molecular dynamic computer simulation study of the interaction of liquid water with five ideal minerals. Various mineral surfaces will affect the chemical properties, structure and dynamical behavior of interfacial water in different ways. Overall, the conducted research presented a detailed and comprehensive understanding of how mineral substrate structure and composition affect the molecular-scale structure and properties of interfacial water. For a given mineral, by modifying the substrate surface, properties and structure of the interfacial water can be affected by bulk properties (for instance pH) of the near-surface aqueous solutions. At high (approximately 12) and low (approximately 2) pH-values on the water-quartz interface, the structure of the interfacial water molecules are well ordered (yields spectroscopic features like ice-quartz interfaces), while for intermediate pH-values the surface water is projected to be less ordered. Thus, one can speculate that a medium pH-value of the pore fluid will potentially cause a high creep deformation whereas high and low pH-values will be unfavorable for the creep mechanism (Wang et al. 2006).

3.2.3 Chemical weathering

Theory concerning chemical weathering is previously described in section 2.5.2 (p.25). When it comes to studying this process, Steward and Cripps (1983) showed in the early 80s that weathering reduces the strength of the rock. The authors performed experiments on Edale shale (a dark grey, thinly bedded mudstone of Namurian age) and concluded that weathering solutions “attacks” fresh shale and makes it weaker. Consequently, chemical weathering can cause significant alteration in the engineering properties of a rock. For shale, the mineralogical composition and oxygenated water will influence this process. Two different reactions occur when minerals are exposed to a weathering process; 1) interlayer cation exchange, which is a rapid process, and 2) an attempt to reach clay equilibrium with

relative low ionic strength solutions (Steward and Cripps 1983). Later, it has been shown that low pH solutions enhance chemical weathering through hydrolysis of clays and feldspars in the absence of buffering minerals such as carbonates (Chigira and Oyama 1999).

In 2000, Petsch et al. (2000) studied how ancient sedimentary organic matter in shale responded to chemical weathering. Results showed from 60 to nearly 100% loss in total organic content (TOC) due to weathering. The authors concluded that the extent of weathering is limited by a combination of the exposure of the rock to oxidizing surface waters and the rate of physical erosion and exposure of the rock. The type of organic matter in the tested outcrops did not influence the process (Petsch et al. 2000).

3.2.4 Impact of different chemical environments

It can also be relevant to consider research related to rocks consisting of clay minerals and their behavior in different chemical environments. Shale may upon exposure to different chemical conditions, deteriorate and deform (Tuttle and Breit 2009). In 2015, Wu and Sharma (2015) presented their study on how acid dissolution changes the petrophysical properties, microstructure and pore structures of shale. A shale with high carbonate content (24 wt%), the Bakken shale, was used in the investigations. It mainly consisted of quartz, illite, dolomite and calcite. Among other experiments, acid solubility tests and a field-emission scanning electron microscope (FE-SEM) were used to examine pre-and post-acidized shale samples. The obtained results showed that microstructure changes were strongly dependent on mineral distribution; relative inert minerals such as quartz and organic matter remained mostly structurally stable whereas carbonates dissolved and developed channels and/or cavities in the samples. Also, in an acidized shale matrix, significant increase in permeability and porosity were measured and acidizing was also seen to reduce the overall hardness of the shale (Wu and Sharma 2015).

Furthermore, back in 1992, Chermak (1992) performed batch reactor experiments at different temperatures on Opalinus shale to investigate the effect of high pH solutions on the shale mineralogy over a time period of 40 days. The results showed a significant change in the mineralogy of the shale and the general sequence of observed reaction products were precipitation of analcime, vermiculite precipitation and eventually Na-rectorite precipitation. Initial minerals that were found reactive included quartz, kaolinite and chlorite. These results

showed similarity to other low pH and higher temperature studies on shale. The main difference found was that reaction rates in high pH environments were much faster than in low pH solutions (Chermak 1992).

In the 60s, Mungan (1965) investigated how changes in pH of the pore fluid could affect the permeability in a couple of rocks, including Berea sandstone. The samples consisted of the following clay minerals; kaolinite, illite, chlorite and interlayered illite. Permeability reduction has generally been associated with swelling of clay minerals. Swelling leads to blocking of the free pore space and some clay minerals, such as smectite, have the ability to expand many times its original volume. The author performed permeability tests on extracted and non-extracted reservoir cores at both room and reservoir temperatures. Fluids were pumped through the cores at constant volumetric rate. To examine the effect of changes in pH to the permeability, four different cases were considered; adding acid (HCl) to the fluid and adding three different alkalines (KOH , NH_4OH and $NaOH$). The results illustrated a clear reduction in permeability due to the additives, especially for $NaOH$. Mungan (1965) concluded that the primary cause of permeability reduction was blockage of pore passages by dispersed particles. Particles dissolved due to the flow of acidic or alkaline solutions and entered the pore spaces, consequently blocking small channels inside the rock. Since the tests were performed on cores containing non-expandable clays or specimens that were essentially free of clays, the author proved that permeability reduction can also be caused by changes in pH and not exclusively by swelling. He also found that the extent of permeability reduction depended on temperature (Mungan 1965).

3.2.5 CO_2 sequestration

One research field that might give relevant information on how reduced pore fluid pH affects shale or creep is CO_2 sequestration. As a potential solution to limit climate change, it has today become accepted to mitigate the increase of CO_2 in the atmosphere by capturing it and storing it in the subsurface. It is common to inject it into deep rock formations such as sandstone reservoirs capped by shale. One of the effects of CO_2 exposure is pH reduction of the fluid diffusing into the pores of the rock. A relevant study related to this subject from 2010 presents Hangx et al. (2010) conducting uniaxial compaction creep experiments on granular aggregates of quartz and Ca-bearing feldspar. The objective of the tests was to

examine the effects on creep due to CO_2 injection. Creep effects generally depend on several factors, and the effect of pore fluid pH was only one of the elements that the authors studied in detail. The tests were run under both wet and dry conditions, and the pore fluid pH was altered by addition of acidic and alkaline additives and by CO_2 injection. For the quartz experiments, the pH-value was altered from 2.8-12.4. The results showed that the pH of the pore fluid had a significant impact on the amount of creep of the samples, as well as the creep rate. Reduced pH showed less creep and lower creep rates compared to near-neutral pH environments. This coincides with the speculations based on Wang et al. (2006). In contrast, alkaline pore fluids ($pH > 7$) enhanced creep and creep rates compared to near-neutral fluids. Also, increased creep was seen for wet conditions compared to lab dry material. For the feldspar experiments, at room temperature, creep strain decreased with increasing pH in the pH range of 2.8-5.5, and remained more or less constant between pH 5.5 and 11. At reservoir conditions (80°C, 36 MPa effective stress) creep strain and creep rates generally increased with greater solution pH and slightly with enhanced salinity. The acceleration of creep with increasing pH and salinity might be connected to enhanced stress corrosion cracking. In comparison to near-neutral solutions, addition of CO_2 inhibited creep or decelerated it strongly at room temperature as well as reservoir conditions. This agrees with the speculations based on Wang et al. (2006). Also for the feldspar samples, creep was enhanced by adding aqueous pore fluid compared to lab dry material (Hangx et al. 2010).

Further, in 2013, Olabode and Radonjic (2013) investigated geochemical interaction of shale cap rock with aqueous CO_2 flooding (acidic fluid transport). The objective of the experiments was to examine shale cap rock integrity in CO_2 sequestration technology. Crushed shale samples of known mineralogy from the Pottsville Formation in Alabama (USA) were used in a flooding period of approximately 3 months. It is known that the mineralogical composition of shale cap rock can impact its ability to seal effectively, and the samples used in these tests consisted of mainly quartz, feldspar and (bulk) clay. Eventually, the results from the experiments postulated that petrophysical properties can be affected by shale/ CO_2 -brine interaction under dynamic conditions. It was showed that rock properties of shale can be significantly altered on a nano-scale. For instance the naturally low permeability

in shale may be changed, thus the cap rock integrity with respect to permeability can be influenced (Olabode and Radonjic 2013).

Similarly, in 2015, Balashov et al. (2015) carried out a comprehensive study to understand how shale interacts with CO_2 during sequestration. The mineralogy of the tested shale resembled black shale from the Marcellus formation mainly consisting of quartz, illite and chlorite. A reactive diffusion model was used to simulate the transport of CO_2 in a subsurface sandstone reservoir capped by the shale. From the results, the authors concluded with a prediction that shale with higher content of Mg, Ca and Fe ions (e.g. more chlorite or smectite) will more likely self-seal after injection of CO_2 than other shale with less content of these cations (Balashov et al. 2015).

3.2.6 Summary

Overall, from the presented research in this section, one may predict that reduced pore fluid pH will decrease creep and creep rates compared to near-neutral environments. Depending on mineral composition of the shale, one must expect that some of the minerals (especially chlorite) will potentially react with added acid, and the degree of chemical weathering will depend on the acid concentration and strength in addition to the exposure time. Chemical weathering will weaken the rock and change the shale's properties, thus it is significant to keep this impact to a minimum. Finally, since the creep tests in this thesis will have a reduced pH environment, the reaction rates will most likely be low compared to a potential high pH solution.

4 Preparations for laboratory work

4.1 Risk assessment

Conducting a risk assessment is a necessary task before performing any experiments in the laboratory. The objective of the assessment is for the participants to determine the potential hazards associated with the experiments, evaluate the level of risk involved and get an overall picture of what to expect from the upcoming assignments.

Prior to starting the laboratory work in this master thesis, the potential hazards related to the experiments were identified and the risks associated with these were evaluated. To reduce the risk of potential dangerous situations for people and/or equipment, countermeasures to the hazards were also suggested. Since some of the experiments involved handling of corrosive acid, it was in particular significant for the participants to understand the implications and learn how to show caution. A risk assessment form given by SINTEF was filled out, and reviewed/signed by the research manager at the laboratory. The final risk assessment can be found in Appendix X (p.209).

4.2 Calibration of LVDTs

Before the experiments could start essential equipment needed calibration. To calibrate the LVDTs (linear variable differential transformers) a digital Mitutoyo micrometer was used in accordance with the CatMan software. Results of the calibrations can be found in Appendix VII (p.203).

4.3 System correction factor for acoustic measurements

To establish a system correction factor for acoustic measurements, p-waves were sent through a dummy sample of PEEK (Polyether ether ketone). The time it took for the waves to travel from the acoustic transmitter to the receiver was recorded by the software Aptrans. Since one should only use the travel time through the core itself when calculating p-wave velocities for a specimen, the delay through the system must be subtracted. It is optimal to use PEEK as a dummy sample because the wave velocity through this material is already known. Thus, the delay through the system is easily recognized, and a system correction

factor can be established. This parameter was estimated to the value of 14.18 μs (procedure for the calculations can be found in Appendix VIII, p.205).

4.4 Preparations for creep experiments

As previously mentioned, the creep experiments were going to be conducted in a near to neutral pH environment (brine) and later with reduced pore fluid pH (mixture of brine and acid). Certain necessary measures had to be finalized to prepare for this.

4.4.1 Estimation of expected consolidation time

An estimation of the expected consolidation time in Pierre shale was calculated as a preparation for the creep experiments. By completing this task, one got an indication of what to anticipate for the samples and could use this as a starting point when proposing a loading path for the upcoming tests. However, it was important to keep in mind that this approach only provided a rough approximation. By using given parameters for Pierre shale, the consolidation time was estimated to be 40.5 min (0.68 hours). For details regarding the calculations, see Appendix I (p.179).

4.4.2 Initial screening of brine and HCl mixtures

For the creep experiments with reduced pH, it was determined that the fluid surrounding the core samples should be a mixture of 3.5wt% $\text{NaCl}(aq)$ and $\text{HCl}(aq)$. Before selecting the optimal blend, it was significant to acknowledge which $\text{HCl}(aq)$ concentration would provide a sufficient pH reduction in the pore fluid. Obtaining “a sufficient pH reduction” was not aimed at a specific pH-value, but rather targeted to finding something that assumingly would adequately affect the creep of the samples while at the same time not deviate too much from the chemical activity of 3.5wt% $\text{NaCl}(aq)$. In addition, it was believed that the overall amount of $\text{HCl}(aq)$ should be kept to a minimum to avoid dissolution of clay minerals and thus prevent or minimize weathering of the Pierre shale.

An initial screening of brine and HCl mixtures was arranged in the lab where several test tubes were prepared with 3.5wt% $\text{NaCl}(aq)$ and varying acid concentrations in room temperature. A pH measurement was performed with a digital pH meter and the solutions chemical activity was calculated based on a measurement by a relative humidity sensor.

Small samples of Pierre shale (approximately 1 inch in diameter and 0.4 inch in length) were put in some of the tubes and the system was monitored for 3-4 days to reveal potential weathering. Eventually, the screening showed that a solution consisting of brine and 0.00125% $HCl(aq)$ resulted in a pH of 3.14 and the solution had a chemical activity close to initial brine (deviation of 0.4). Overall, it was considered as the best fit for performing the creep experiments with reduced pH. Details about the screening process and the obtained results can be found in Appendix IV (p.189).

4.4.3 Estimation of ion diffusion time

As described in section 2.5.5 (p.27), ion diffusion is the migration of ions and molecules in a fluid/gas due to a gradient of pressure, temperature or concentration. The laboratory work in this master thesis concerns two main ionic diffusion processes, foremost as a result of concentration diversity;

1. Moving core samples from marcol to brine; core samples of Pierre shale were directly submerged in marcol after preparations, but prior to the creep experiments in brine they were immersed in 3.5wt% $NaCl(aq)$.

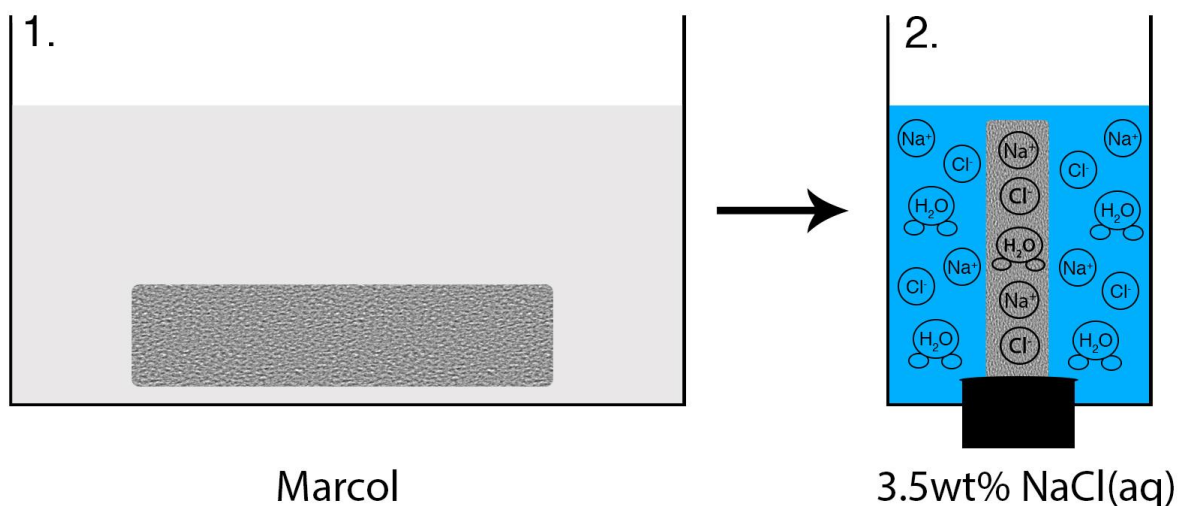


Figure 4.1: Illustration of core sample moving from marcol to brine.

2. Moving core samples from marcol to a mixture of brine and $HCl(aq)$; before the core samples were used in the creep experiments with reduced pore fluid pH they were placed in a mixed solution of 3.5wt% $NaCl(aq)$ and $HCl(aq)$.

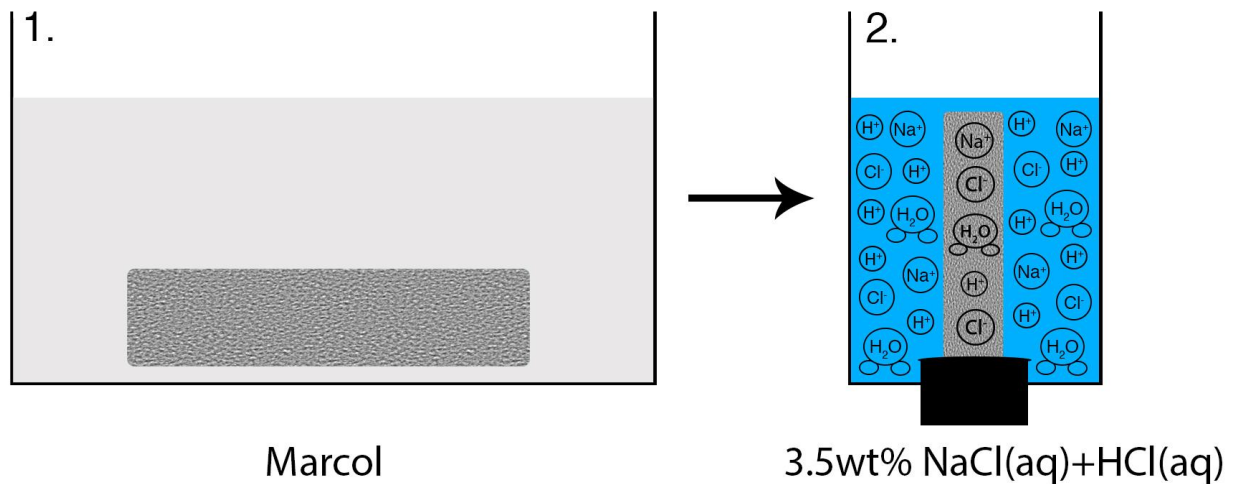


Figure 4.2: Illustration of core sample moving from marcol to a mixture of brine and hydrochloric acid.

To achieve an overall chemical equilibrium of ions within the systems it was significant to let the ion diffusion processes complete before proceeding with the creep experiments. There are several ways of estimating how long the core samples had to be submerged in the new solutions to ensure successful diffusion processes, and two different methods will be presented here.

4.4.3.1 By calculations

Calculations can be used to roughly predict the ion diffusion time τ_I . It is defined by

$$\tau_I = \frac{l_I^2}{C_I} \quad (4.1)$$

where C_I is the ion diffusion coefficient and l_I is the ion diffusion length (in this case the core radius). It is possible to use the calculated pore pressure diffusion constant C_D from estimation of the expected consolidation time (Appendix I, p. 179), and then assume that C_I is approximately a magnitude of 10^{-2} less in value. This assumption is based on experimental experience from the SINTEF lab and even though it does not provide an exact value, it is still a valid approach for estimating this parameter. By following this method, it is important to keep in mind that it is hard to know exactly how much the pore pressure diffusion constant itself will be affected when the core samples are moved from one fluid to another. For instance, pH alteration in the mixed solution of brine and $HCl(aq)$ might influence the

permeability of the shale, thus adjusting the overall magnitude of C_D which again will directly influence C_I . Still, as a rough starting point one can assume that the potential changes will be negligible and presume that C_D will be the same before and after the samples are submerged in different fluids. If that is the case, based on the calculations of C_D (Appendix I, p.179) and application of the SINTEF lab assumption, the time it takes before an overall chemical equilibrium of ions is established within the systems will be

$$\tau_I = \frac{0.0127^2}{6.63 \cdot 10^{-10} \frac{m^2}{s}} = 243273 \text{ s} \approx \underline{\underline{2.8 \text{ days}}} \quad (4.2)$$

4.4.3.2 By experiment

In addition to, and as a verification of the estimated ion diffusion time found by calculations, an ion diffusion experiment was performed. The procedure involved placing a core sample of Pierre shale in a container filled with 3.5wt% $NaCl(aq)$. A small amount of stress (0.5 MPa) was then applied to the setup (just enough to keep the system steady) and the strain was recorded. Before the experiment started, the core sample was initially submerged in marcol. Replacing this fluid with brine in the container caused ion diffusion due to a concentration gradient. Two counteracting processes occurred; swelling from the brine and compaction due to the applied stress from the load frame. This directly affects the measured strain, so when the LVDTs are eventually showing stable deformation, one can assume an overall chemical equilibrium of ions within the system, implying successful ion diffusion. Running this test at 30°C resulted in an ion diffusion time of approximately 12 hours (see Figure II-1 in Appendix II, p.181). The same experiment was then repeated to verify the results. The second test showed a stabilization time around 15 hours (see Figure II-2 in Appendix II, p.182). It is significant to keep in mind that this approach only provides an approximation. Ideally, to increase accuracy in the measurements, one should have put the core sample inside a container filled with marcol, applied a small stress and set the desired temperature. Then the system should have stabilized before draining out the marcol and replacing it with brine without physically touching the experimental setup. To achieve this one needs a container fit for drainage and pumping of fluids. In lack of such a container, a time period of approximately 20 min passed from the sample was put in brine until the LVDTs started

recording the deformation. This lag was caused by the fact that the experimental setup required some adjustments after the brine was poured into the container before the experiment could start.

The same experiment was also performed on a core sample of Pierre shale submerged in a mixture of 3.5wt% $NaCl(aq)$ and $HCl(aq)$. Overall, the solution had a concentration of 0.00125% $HCl(aq)$ and a pH value of 3.14. The results showed a stabilization time period of 14 hours (see Figure II-3 in Appendix II, p.182). More details and data from all the ion diffusion experiments can be found in Appendix II (p.181).

4.4.3.3 Conclusion

As the described methods showed, the ion diffusion time ranged from 12 hours to 2.8 days. The calculations only provided a rough estimate indicating an overall idea of what time one could expect, while the experiments were performed under appropriate conditions implying more reliable results. Thus, it was determined to leave the shale samples submerged in the desired new solution for a minimum of 24 hours prior to all creep experiments to ensure a successful ion diffusion process.

4.4.4 Defining uniaxial compressive strength

To reduce the chance of premature failure in the creep tests, it was essential to define the compressional strength of Pierre shale. As extensions of the ion diffusion experiments described in section 4.4.3.2, UCS tests were performed. Applying load until failure for a sample submerged in brine showed an uniaxial compressive strength of 9.2 MPa (see Figure III-1 in Appendix III, p.183). An identical, second UCS test was run to confirm that the first shale sample was not an anomaly. These results revealed the exact same value; 9.2 MPa (see Figure III-3 in Appendix III, p.184). Both UCS tests were performed at 30°C. It is ideal to perform the creep experiments at the same temperature because compressive strengths can be highly sensitive to temperature variations (Chu and Chang 1980).

For a sample submerged in a mixture of brine and $HCl(aq)$, the results showed an UCS of 7.7 MPa (see Figure III-5 in Appendix III, p.185). It was natural to obtain a lower value in this case since the surrounding fluid contained acid, which could imply a possible weakening of

the sample due to chemical weathering. This speculation coincides with previous research conducted by Steward and Cripps (1983) and Chigira and Oyama (1999).

After establishing that the samples (all drilled with 0 degrees to the bedding plane) could fail at 9.2 MPa in brine and 7.7 MPa in a mixture of brine and $HCl(aq)$, these values were used as a basis for selecting the proper stresses to apply when first proposing a loading path for the creep tests. Overall, Table III-1 (Appendix III, p.183) summarizes the experimental settings for each UCS test.

5 Experiments and methods

5.1 Purpose

In this master thesis, there have been conducted ion diffusion experiments, UCS tests and creep experiments. The aim of the ion diffusion experiments was to find the required time period for establishing chemical equilibrium of ions after moving a sample from one fluid to another. Further, the UCS tests were performed to reveal the strength of the core samples. In regards to the creep experiments, their purpose was to reveal genuine creep characteristics of the samples in addition to consolidation effects, and show how different stress levels and reduced pore fluid pH affected these mechanisms.

5.2 Core samples

Core samples of Pierre shale were used for all experiments. Every core was drilled with 0 degrees to the bedding plane, and its dimensions were approximately 1 inch (25 mm) in diameter and 2 inch (52 mm) in length. The Pierre shale had been acquired from a quarry in Colorado, and its mineralogy composition consisted of mainly chlorite, illite, smectite and quartz. Details obtained from fine analysis of the mineralogy can be found in Table VI-2, Appendix VI (p.199).

To measure the cores, a sliding caliper was used. The diameter of all core samples was measured at 3 distinctive heights; top, center and bottom. At each height, the diameter was measured twice; in the original position and then rotated 90 degrees, resulting in 6 measurements in total. The length of the core samples was measured at two points 90 degrees apart. Eventually, the average values were found for all dimensions. The cores were also weighed (wet) and photographed before and after the experiments. All obtained values for the core samples are presented in Table VI-1, Appendix VI (p.199).

5.3 Experimental setup

All experiments were performed with a 10 kN MTS electromechanical load frame, implying a maximum applied stress of approximately 20 MPa for the 1 inch in diameter core samples. The UCS tests proved that less than half of that value was required for the creep experiments. All test procedures were implemented in the software TestWorks4, and recorded data from the load frame was obtained here. A specimen was submerged in brine

or a mixture of brine and $HCl(aq)$ (depending on the conducted experiment) inside a container positioned between two pistons. Two tests (core sample 346_2_10 and 346_2_11) were run with an aluminum container from the specialization project while a newly made copper container was used for the rest of the experiments. The latter was introduced to the experimental setup to avoid potential reactions between hydrochloric acid and aluminum. Three LVDTs were mounted around the upper piston with a 120 degrees spacing. The LVDTs were connected to a computer, and the software CatMan recorded all axial deformations. An acoustic transmitter was located in the top piston and a receiver was placed in the opposing piston. The acoustic transmitter and receiver were connected to an amplifier and data logger, and acoustic waves were recorded by the software Aptrans. Four temperature sensors were put inside the container at different height levels to register temperature variations in the fluid surrounding the core during tests. In addition, the room temperature was measured. The software PicoLog recorded all temperature measurements. The container itself was coated with thermal conductive silicon foil, a heating element, Armaflex (isolating material) and tape able to withstand heat up to 95°C. A temperature sensor was placed between the thermal conductive silicon foil and the heating element. The temperature sensor was connected to a temperature controller regulating the heating element. All tests were run at approximately 30°C and the overall aim with using a heating element was to provide a close to constant temperature around the core during experiments by overriding a potential varying room temperature. Figure 5.1 shows a picture of the experimental setup for the experiments.

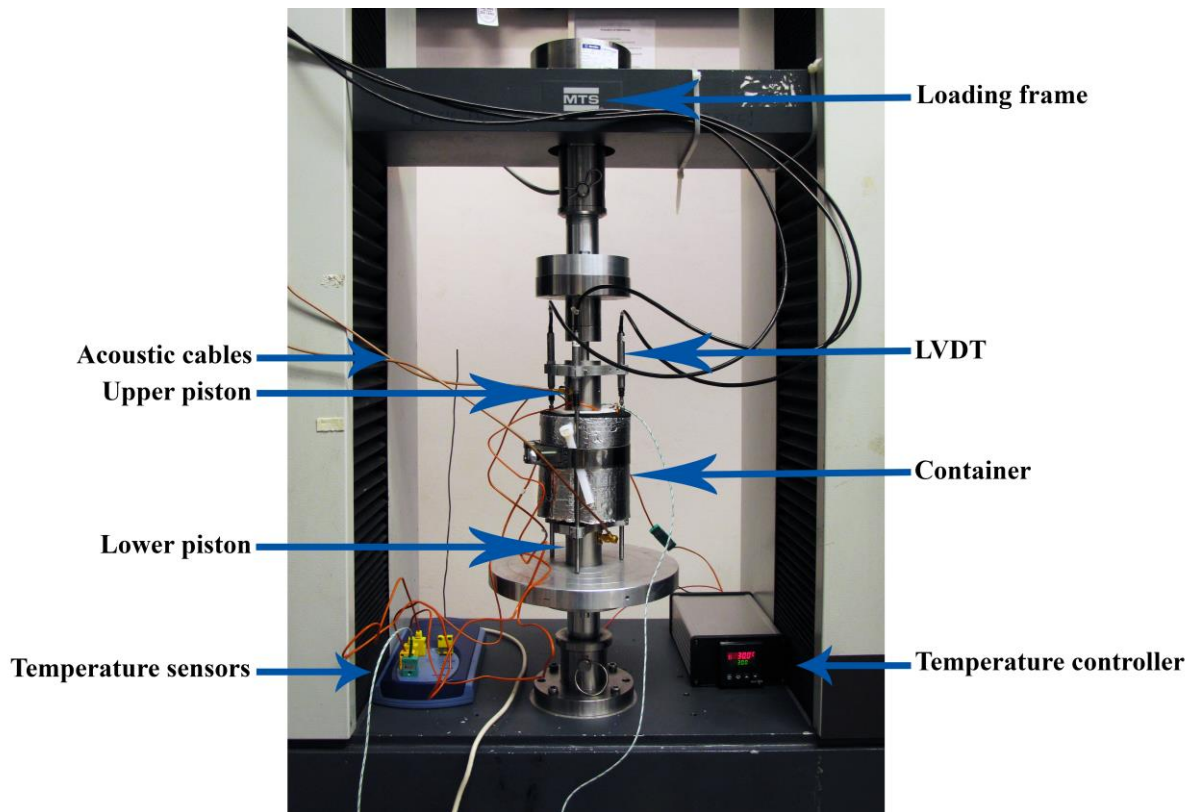


Figure 5.1: Experimental setup.

5.4 Experimental procedures

All test procedures were implemented into TestWorks4 and run automatically. Appendix IX (p.207) summarizes the used sampling rates for the different experiments.

5.4.1 Ion diffusion experiments

Three ion diffusion tests were performed to recognize the required time period for achieving an overall chemical equilibrium of ions within a system. For the first two tests a sample was submerged in brine while the last one was submerged in a mixture of brine and $HCl(aq)$. The general procedure for the experiments was to apply load with a pre-determined speed up to 0.5 MPa and wait until the deformation was stable (explained in section 4.4.3.2, p.47). A more detailed description is listed below:

1. Remove the film around the core sample with a scalpel.
2. Measure the dimensions of the specimen and weigh it. Take photos.
3. Set up the temperature sensors and connect the acoustic sensors.

4. Restart computer. Prepare software's for the experiment; Testworks4, CatMan, Picolog and Aprans.
5. Move the core sample from marcol and put it inside the container. Submerge it with the desired new fluid. Put the upper piston on top of the core and connect the LVDTs.
6. Align the container to the center of the load frame to achieve an even stress distribution across the core sample.
7. Pre-load 70 N with the load frame on the setup.
8. Adjust LVDTs and zero them in the CatMan software. Test acoustic sensor.
9. Set temperature for 30°C on temperature controller.
10. Start all software's on the computer for recording. Note the time difference in which the software's are started. The test will run automatically according to the pre-defined procedure entered in TestWorks4, and the equipment will be undisturbed for the rest of the experiment.

5.4.2 UCS tests

A total of four UCS tests were run to establish unconfined compressive strengths of the Pierre samples. The first three UCS experiments were all extensions of ion diffusion tests, so after achieving stable deformation, load was applied with a pre-determined speed until failure of the cores. A description of the procedure is listed below:

1. Wait to achieve stable deformation in the ion diffusion test.
2. Adjust TestWorks4 to start a pre-defined UCS procedure.
3. The test will run automatically, and the equipment will be undisturbed for the rest of the experiment.
4. Take photos of the core sample after failure.

The last UCS test was run on a sample that had been submerged in brine for 24 hours prior to the test and kept in a heating cabinet at 30°C. Afterwards a load was applied with a pre-determined speed until failure of the core sample. The reason for running this test is explained in section 7.1.1 (p.66). The following procedure describes the experiment in more detail:

1. Remove the film around the core sample with a scalpel.
2. Measure the dimensions of the specimen and weigh it. Take photos.

3. Submerge the specimen in brine and keep it in a heating cabinet at 30°C for 24 hours.
4. Place a PEEK sample inside the container, fill it with brine and heat it up to 30°C with the temperature controller. Put a small load on the system and let it stabilize for approximately 2 hours.
5. Restart computer. Prepare software's for the experiment; Testworks4, CatMan, Picolog and Aptrans.
6. Remove the PEEK sample from the container and replace it with the core sample from the heating cabinet. Put the upper piston on top of the core and connect the LVDTs. Install the temperature sensors and connect the acoustic cables.
7. Align the container to the center of the load frame to achieve an even stress distribution across the core sample. Pre-load 70 N with the load frame on the setup.
8. Adjust LVDTs and zero them in the CatMan software. Test acoustic sensor.
9. Start all software's on the computer for recording. Note the time difference in which the software's are started. The test will run automatically according to the pre-defined procedure entered in TestWorks4, and the equipment will be undisturbed for the rest of the experiment.
10. Take photos of the core sample after failure.

5.4.3 Creep experiments

Seven creep tests were run in total; five on cores submerged in brine and two on cores submerged in a mixture of brine and $HCl(aq)$.

5.4.3.1 Test procedures

Initially, the general procedure for the creep experiments was to keep a sample submerged in the desired fluid for 24 hours inside a heating cabinet at 30°C, then apply load with a pre-determined speed until reaching 80-90% of the UCS, let it consolidate/creep for 48 hours, re-load closer to failure and then finally further consolidation/creep for 48 hours. Due to poor results, this procedure was revised during the testing period and the loading path was adjusted accordingly. For details regarding what was actually run for each core sample in the creep tests, see Table 7-1 (p.65). Even though the initial, general description for the creep experiments is similar to the last run UCS test, it is still listed:

Test procedure 1

1. Remove the film around the core sample with a scalpel.
2. Measure the dimensions of the specimen and weigh it. Take photos.
3. Submerge the specimen in the desired fluid and keep it in a heating cabinet at 30°C for 24 hours.
4. Place a PEEK sample inside the container, fill it with brine and heat it up to 30°C with the temperature controller. Put a small load on the system and let it stabilize for approximately 2 hours.
5. Restart computer. Prepare software's for the experiment; Testworks4, CatMan, Picolog and Aprans.
6. Remove the PEEK sample from the container and replace it with the core sample from the heating cabinet. Put the upper piston on top of the core and connect the LVDTs. Install the temperature sensors and connect the acoustic cables.
7. Align the container to the center of the load frame to achieve an even stress distribution across the core sample. Pre-load 70 N with the load frame on the setup.
8. Adjust LVDTs and zero them in the CatMan software. Test acoustic sensor.
9. Start all software's on the computer for recording. Note the time difference in which the software's are started. The test will run automatically according to the pre-defined procedure entered in TestWorks4, and the equipment will be undisturbed for the rest of the experiment.
10. Take photos of the core sample after the creep test.

As mentioned, this test procedure was later revised (explained more in section 7.1.1, p.66).

The following text describes the new procedure in more detail:

Test procedure 2

1. Remove the film around the core sample with a scalpel.
2. Measure the dimensions of the specimen and weigh it. Take photos.
3. Set up the temperature sensors and connect the acoustic sensors.
4. Restart computer. Prepare software's for the experiment; Testworks4, CatMan, Picolog and Aprans.

5. Move the core sample from marcol and put it inside the container. Submerge it with the desired new fluid. Put the upper piston on top of the core and connect the LVDTs.
6. Align the container to the center of the load frame to achieve an even stress distribution across the core sample.
7. Pre-load 70 N with the load frame on the setup.
8. Adjust LVDTs and zero them in the CatMan software. Test acoustic sensor.
9. Set temperature for 30°C on temperature controller.
10. Start all software's on the computer for recording. Note the time difference in which the software's are started. The test will run automatically according to the pre-defined procedure entered in TestWorks4, and the equipment will be undisturbed for the rest of the experiment.
11. Take photos of the core sample after the creep test.

5.4.3.2 Loading paths

The loading path used for each creep experiment is summarized in Table 7-1 (p.65).

Creep tests in brine

Loading path 1

Based on results from the UCS tests in brine, the following initial loading path was proposed for the creep experiments:

1. Load up to 7.8 MPa over a time period of 7.8 hours (1 MPa/hr).
2. Hold stress, let consolidate and creep for 2 days.
3. Load up to 8.3 MPa over a time period of 5 min (0.1 MPa/min).
4. Hold stress, let consolidate and creep for 2 days.

The first creep test in brine was run as proposed.

Loading path 2

Because of poor results in the first creep test (described in section 7.1.1, p.66) a new test procedure (Test procedure 2) was developed. Due to this a new step in the experiment had to be incorporated into the start of the loading path.

1. Load up to 0.5 MPa and hold stress for 24 hours to complete ion diffusion.

2. Start creep test by loading up to 7.8 MPa over a time period of 7.8 hours (1 MPa/hr).
3. Hold stress, let consolidate and creep for 2 days.
4. Load up to 8.3 MPa over a time period of 5 min (0.1 MPa/min).
5. Hold stress, let consolidate and creep for 2 days.

The second creep test in brine was run as suggested.

Loading path 3

Due to poor results in the second creep test (described in section 7.1.2, p.71), it was in cooperation with the supervisor determined to lower the stresses in the hold periods to make sure of a greater creep data collection. The following loading path was proposed:

1. Load up to 0.5 MPa and hold stress for 24 hours to complete ion diffusion.
2. Start creep test by loading up to 5.2 MPa over a time period of 5.2 hours (1 MPa/hr).
3. Hold stress, let consolidate and creep for 2 days.
4. Load up to 5.7 MPa over a time period of 5 min (0.1 MPa/min).
5. Hold stress, let consolidate and creep for 5 hours.
6. Reduce the stress to 5.2 MPa over a time period of 5 min (0.1 MPa/min).
7. Hold stress, let consolidate and creep for 2 hours.
8. Load up to 6 MPa over a time period of 8 min (0.1 MPa/min).
9. Hold stress, let consolidate and creep for 2 hours.
10. Load until failure (1 MPa/hr).

The third creep experiment in brine was performed as described above.

Loading path 4

Later, a final optimized loading path was suggested to *ensure* that a complete set of creep data was obtained:

1. Load up to 0.5 MPa and hold stress for 24 hours to complete ion diffusion.
2. Start creep test by loading up to 1.0 MPa over a time period of 5 minutes (0.1 MPa/min).
3. Hold stress, let consolidate and creep for 4 hours.

4. Continue to increase load stepwise with 0.5 MPa (approximate running speed 0.1 MPa/min) until failure. Hold stress, let consolidate and creep for 4 hours at each step.

The fourth and fifth creep experiment in brine was performed as planned.

Creep tests with reduced pore fluid pH

Based on results from the creep tests in brine, it was suggested to also run Loading path 4 for the creep experiments with reduced pore fluid pH.

6 Approaches for finding the transition period between consolidation and creep dominated behaviour

Distinguishing between consolidation effects and creep characteristics is essential when studying time-dependent deformation. It can be challenging to predict the transition period between the mechanisms accurately, but there are several approaches one can use to estimate it. Two main methods are described in this chapter and one of them is later utilized on obtained experimental data.

6.1 Graphical approach

One of the methods for identifying the transition between a period completely dominated by consolidation and a period starting to be dominated by creep is the graphical approach. When displaying measured strain from a hold period on a log-log plot, and there are two separate ongoing processes, a distinctive change in slope of the graph can be expected at some point. Adding two linear trendlines to the data set will result in an intersection point between them, theoretically representing the transition. However, a lot of uncertainty is related to this process; the positioning of the trendlines will highly affect the final results, and one cannot even be 100% certain that the second trendline should be linear. Even though the doubt with this method is high, the approach is still valid and works as a way to estimate the changeover from consolidation to creep dominated behavior.

6.1.1 Technique for finding the best fit trendline in Excel

The described procedure below can be used to find the “correct” angle of inclination and positioning for the trendlines in Excel:

1. Select a small segment in the beginning/end of a graph displaying measured strain from a hold period on a log-log plot.
2. To find an estimate of the line, use the trendline function in Excel.
3. Save the R^2 value for this fitting.
4. Use the same starting point and repeat the same procedure (point 1-3) several times with increasingly larger segments of the graph.

- The “correct” angle of inclination and position for the trendline will be given by the fitting of the largest segment of the graph before the R^2 value starts dropping noticeably.

Due to observed deviations, the selection criterion for stopping was set to $R^2 \geq 0.990$. Figure 6.1 illustrates the concept further.

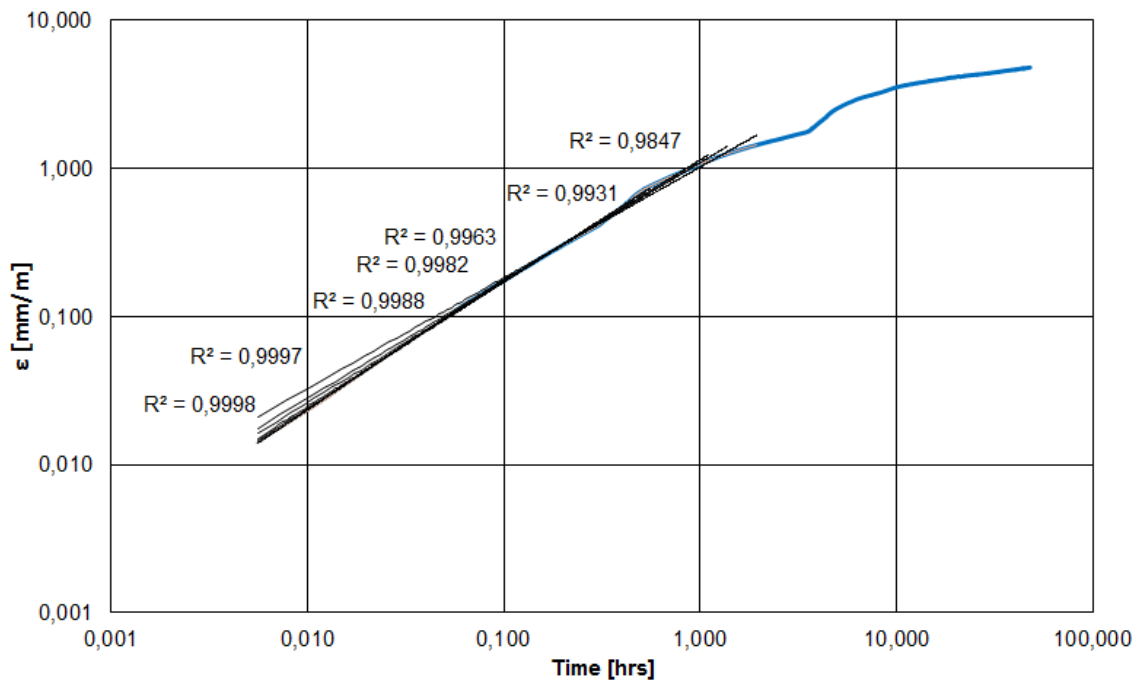


Figure 6.1: Illustration of how to select the first best fit trendline in Excel for a log-log plot.

A similar approach can also be used on a plot displaying strain versus the square root of time. In this case, only one trendline is added for the data points and the consolidation dominated period is assumed to end when the curve starts deviating from the straight line and adapt a more curve like shape. The selection criterion for stopping the trendline was set to $R^2 \geq 0.998$. Figure 6.2 illustrates the idea further.

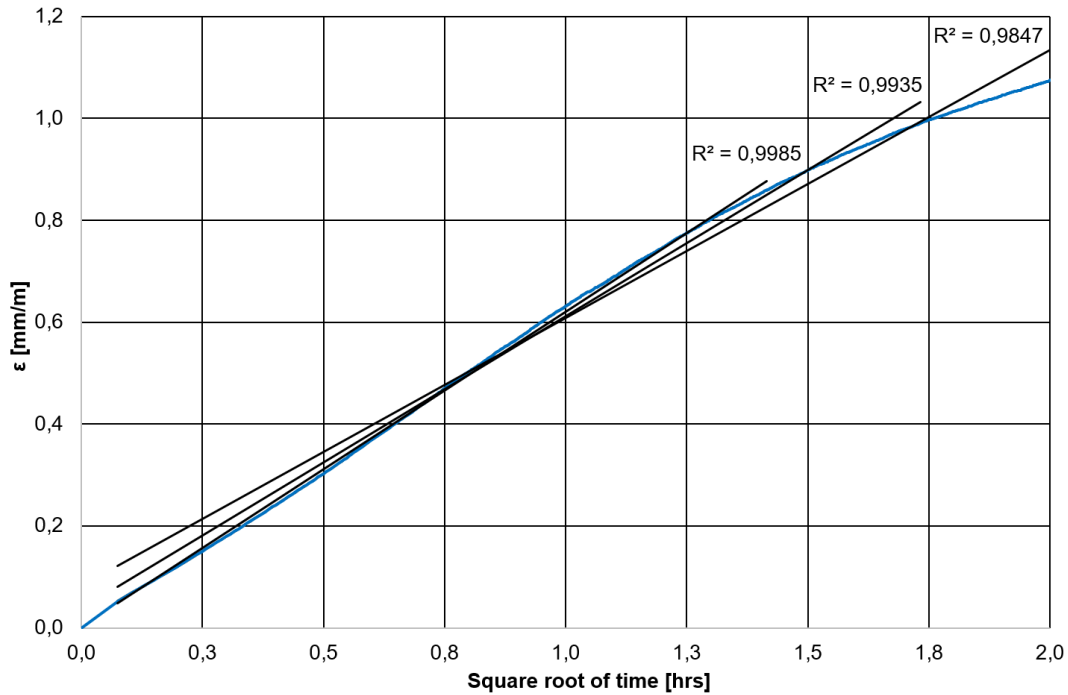


Figure 6.2: Illustration of how to select the best fit trendline in Excel for a plot displaying strain versus the square root of time.

6.2 The Mohr-Coulomb criterion

An alternative method for estimating the transition period between the mechanisms is to determine the consolidation time τ_D . This approach was used in the authors' specialization project, but since its results deviated from the other applied methods (section 1.4, p.4), it was decided to only mention the procedure here and not include it in the final discussions.

In regards to the procedure of the method itself, the consolidation time τ_D can be calculated by using the change in pore pressure and applying the Mohr-Coulomb criterion;

$$\sigma_1 - p_f = C_0 + (\sigma_3 - p_f) \times \tan^2(\beta) \quad (6.1)$$

where σ_1 represents the axial peak stress at hold period 1, $\sigma_3 = 0$ (unconfined test), C_0 is the uniaxial compressional strength, p_f is the pore pressure and β is the failure angle.

Solving equation (6.1) for p_f and applying $\sigma_3 = 0$ results in

$$p_f = \frac{C_0 - \sigma_1}{\tan^2(\beta) - 1} \quad (6.2)$$

It is significant to mention that σ_1 for this equation should be gathered from creep experiments, and not UCS tests. This implies that the actual σ_1 (at failure) is most likely higher than the σ_1 (axial peak stress at hold period 1) chosen to calculate p_f in equation (6.2). This will naturally impact final outcomes and result in a too high estimated consolidation time (equation (6.5)). Thus, different and higher values for σ_1 should be applied to account for this uncertainty in the estimations.

Further, the estimated p_f from equation (6.2) can be used in the following equation given by the supervisor;

$$\Delta p_f = \frac{B}{3} \frac{\Delta \sigma_1}{\Delta t} \int_0^{\Delta t} e^{-(\Delta t - t')/t} dt' = \frac{B}{3} \frac{\Delta \sigma_1}{\Delta t} \tau_D (1 - e^{-\Delta t/t}) \quad (6.3)$$

where B is the Skempton parameter, representing the saturation degree of the soil (= 0 for dry soils and = 1 for saturated soils) (NPTEL 2015). Equation (6.3) assumes an increase in stress with constant rate. The last term becomes so small that it can be neglected, resulting in a simplified version

$$\Delta p_f = \frac{B}{3} \frac{\Delta \sigma_1}{\Delta t} \tau_D \quad (6.4)$$

where $\frac{\Delta \sigma_1}{\Delta t}$ is the loading rate up to a hold period. Finally, re-arranging gives an expression for the consolidation time

$$\tau_D = \frac{3}{B} \times \Delta p_f \times \frac{1}{\frac{\Delta \sigma_1}{\Delta t}} \quad (6.5)$$

7 Experimental results and discussion for creep experiments

As previously mentioned, a total of seven creep tests have been conducted. A short summary of the results from the experiments are presented in the table below. Five of the tests were performed on samples submerged in brine, while the remaining were run on samples submerged in a mixture of brine and $HCl(aq)$. All experiments were conducted on samples drilled normal to the bedding plane at 30°C to override room temperature variations. As later described in this chapter, there was a lot of trial and error in the lab before a successful procedure and loading path could finally be established. For most of the tests, the first 24 hours involved a stabilization period to avoid steel expansion/contraction of the equipment due to temperature and most importantly; completing the ion diffusion process before startup of the creep experiment itself. Table 7-1 gives an overview of the test settings for each performed experiment while Table VI-3 and Table VI-4 (Appendix VI, pp.200-201) present more detailed descriptions. Also, pictures of the core samples after the creep tests are included in Appendix XI (p.211). Eventually, the lab work resulted in a total of four successful creep experiments. In this chapter, only the most significant graphs are featured and discussed, however, additional charts can be found in Appendix XIV (p.219) and a full collection is provided in the enclosed Excel files.

Table 7-1: Overview of test settings for each creep experiment.

Core sample [#]	Test procedure [#]	Loading path [#]	Fluid submerged in	Comment
346_2_15	1	1	Brine	Sample failed after 1.56 hours on loading level 1 (7.8 MPa)
346_2_18	2	2	Brine	Sample failed <i>before</i> reaching loading level 1 (7.8 MPa) at 6.3 MPa
346_2_19	2	3	Brine	Sample failed after 1.89 hours on loading level 2 (5.7 MPa)
346_2_20	2	4	Brine	Successful test, failure on loading level 10 (5.5 MPa)
346_2_21	2	4	Mixture of brine and HCl	Successful test, failure on loading level 12 (6.5 MPa)
346_2_22	2	4	Mixture of brine and HCl	Successful test, failure on loading level 7 (4.0 MPa)
346_2_23	2	4	Brine	Successful test, failure on loading level 13 (7.0 MPa)

The specific test procedures and loading paths are fully described in section 5.4.3.1 (p.55) and 5.4.3.2 (p.57) respectively.

7.1 Creep tests in brine

All creep tests in brine used a solution of 3.5wt% $NaCl(aq)$ as the fluid surrounding the core samples. The fluid itself had a pH value of 7.31 and a chemical activity of 0.942.

7.1.1 Core sample 346_2_15

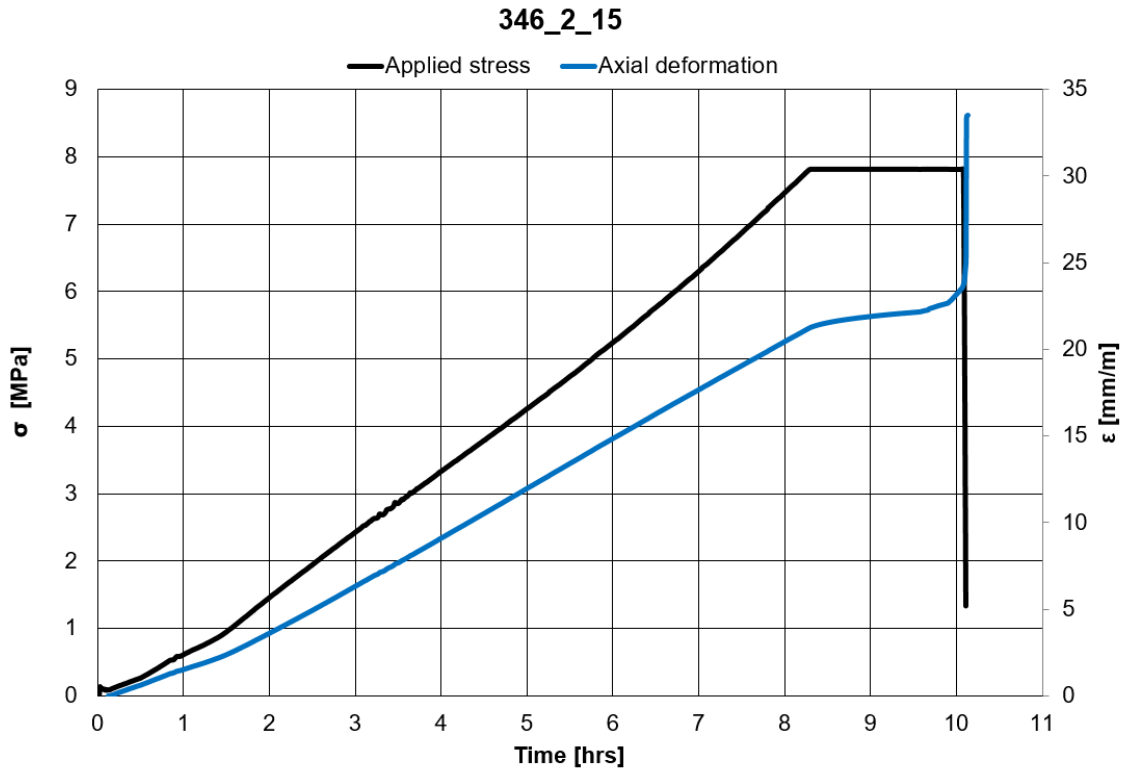


Figure 7.1: Overview of creep test conducted on 346_2_15.

The first creep test in brine ran successfully until an unwanted failure occurred after 1.56 hours on load level 1 (7.8 MPa). The previously conducted UCS tests had indicated that the sample strength should be as high as 9.2 MPa, but naturally there can be some variation in strength between different cores. However, the sample appeared fragile and was already starting to dissolve slightly when it was put into the container before start-up of the experiment. This was after spending 24 hours in brine inside a heating cabinet at 30°C. Thus, it was believed that these preparation measures might have been the main cause behind the early failure. Overall, the maximum temperature variation during the test was 0.37°C.

346_2_15
Hold period 1

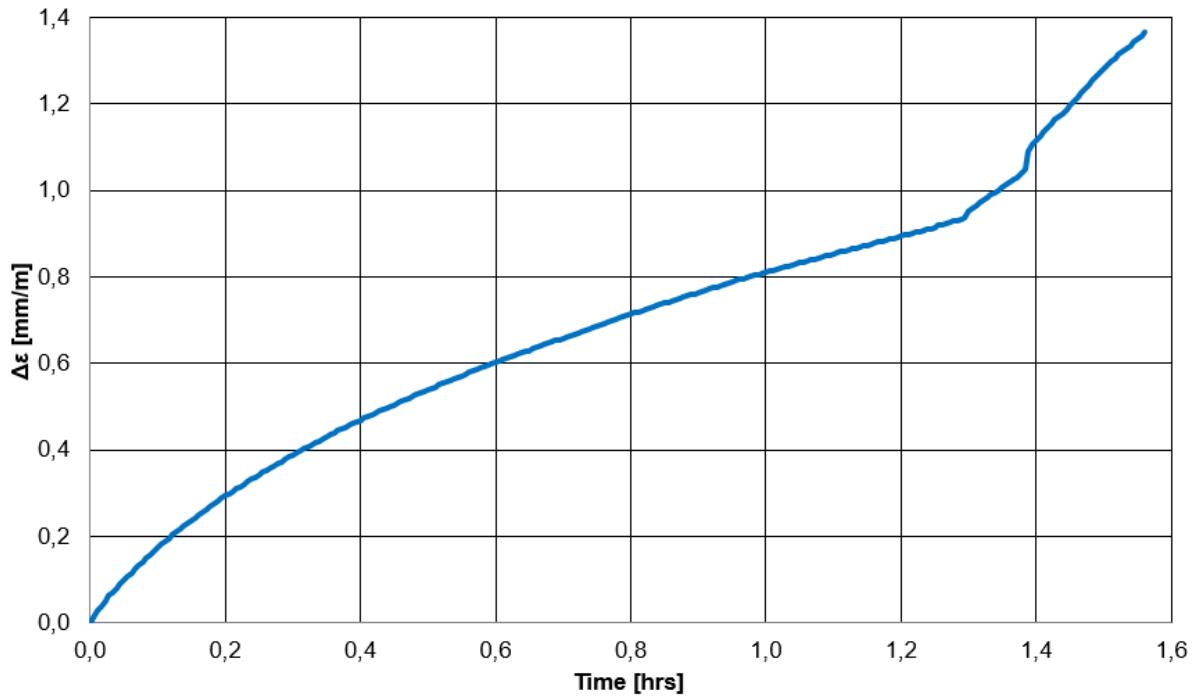


Figure 7.2: Strain vs. time for hold period 1.

Studying hold period 1, Figure 7.2 indicates a transient creep stage in the beginning while accelerated creep is initiated from approximately 1.3 hours resulting in failure 15 min later. The reason for this rapid failure is most likely that load level 1 (7.8 MPa) was too close to the sample's maximum strength after spending 24 hours in brine prior to the experiment. Also, creep in general weakens the rock so this can be considered as a natural development. Consequently, no steady-state creep stage could be observed.

By using the graphical approach (described in section 6.1, p.61), one can try to distinguish between consolidation- and creep dominated behavior. When investigating the deformation on log scales for this sample, it is clear that the time period is too short for finding a distinct transition between the mechanisms. Figure 7.3 shows that only one trendline fits the measured data, indicating that the creep *dominating* period has not yet been fully initiated.

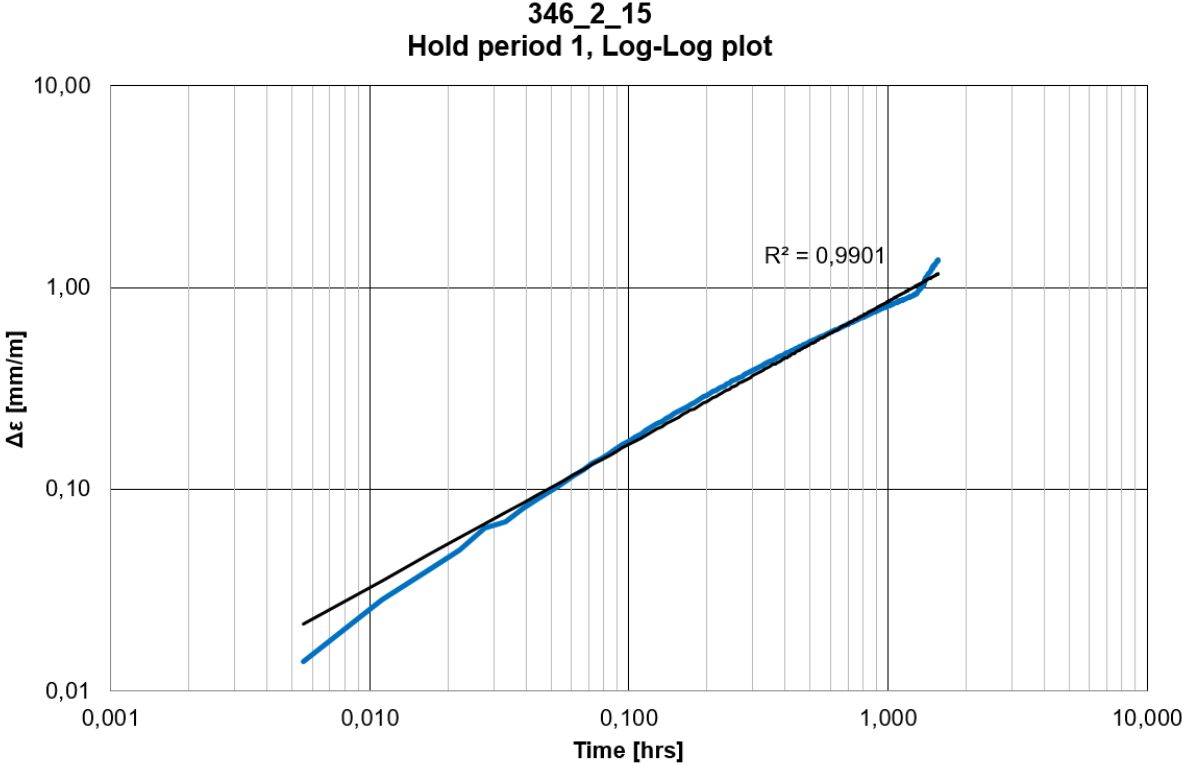


Figure 7.3: An attempt to estimate the transition between creep and consolidation dominated behavior by applying the graphical approach.

For all creep tests, acoustic waves were sent along the vertical axis of the cores. P-wave velocities were then calculated by the following formula;

$$v_p = \frac{L(t)}{\Delta t} \tag{7.1}$$

where $L(t)$ is the time-dependent length of the core (deformation subtracted by the original length of the core) and Δt is the travel time of the wave through the core. The latter parameter was obtained by subtracting a system correction factor from the total wave travel time. The system correction factor was acquired by measuring acoustics through a PEEK reference sample (see Appendix VIII, p.205, for calculations).

In general, p-wave velocities typically increase with increasing stress (Fjær 2006). This is somewhat expected since the rock becomes stiffer when applied stress leads to cracks closing and grain contacts escalating (Fjær et al. 2008). Consequently, one should expect that hold periods have constant velocities. However, by investigating the p-wave velocities for hold period 1 (Figure 7.4), one can observe that the velocities are not constant, thereby indicating that they are dependent on other factors than applied stress exclusively. As one can observe, the p-wave velocities increase simultaneously with the deformation. This coincides with obtained results by Fjær (2006), showing that velocities are related to strain as well as stress. Overall, the obtained p-wave velocities are within the range of expected values for shale (Table 2-1, p.22).

The maximum temperature variation in hold period 1 was measured to 0.04°C; a more or less constant value. As Figure 7.4 shows, no abnormal behavior was seen for deformation or velocities measurements, thus a variation of 0.04°C is assumed to be too low for affecting these parameters.

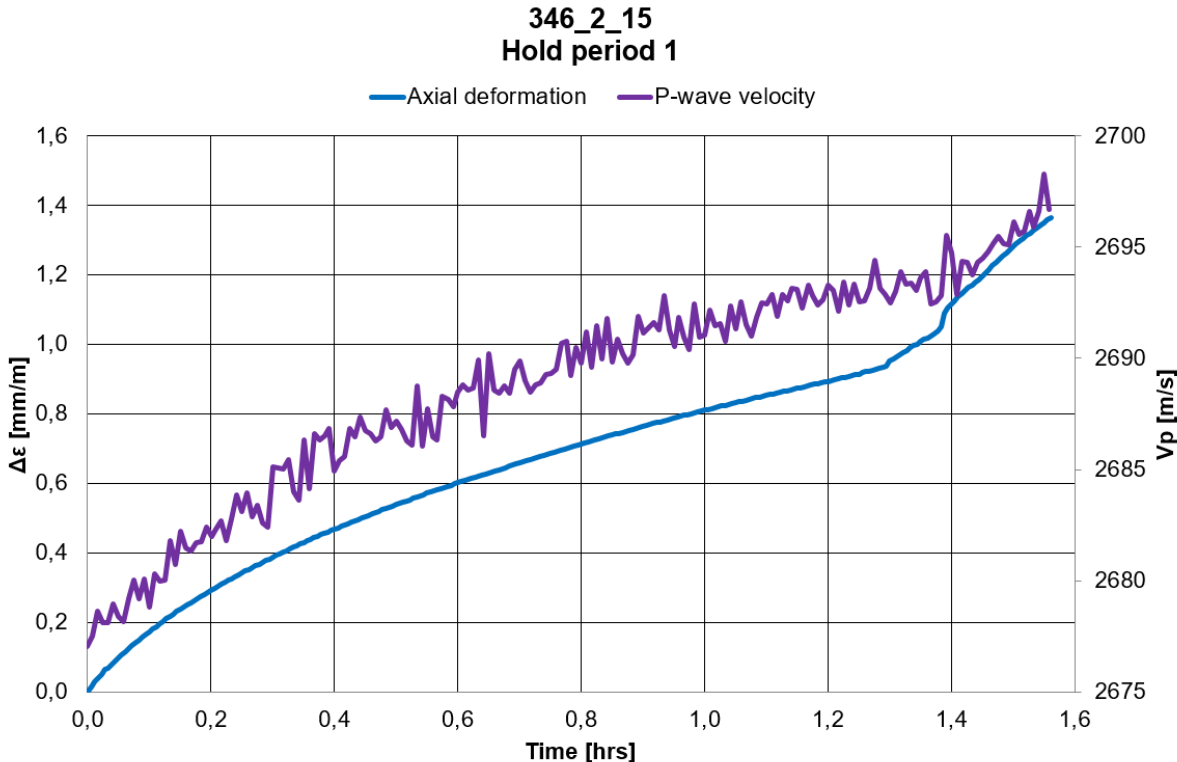


Figure 7.4: Strain in conjunction with p-wave velocities for hold period 1.

Since the sample failed after only 1.56 hours in hold period 1 and considering that it appeared fragile/dissolved after spending 24 hours in brine inside a heating cabinet, it was

decided to investigate how one could potentially obtain more measured creep data for upcoming tests. The previously conducted UCS tests showed 9.2 MPa in maximum strength and were performed as extensions of ion diffusion tests (i.e. the UCS test started after the core had been held at 0.5 MPa for approximately 24 hours). Since the creep experiment was performed under different conditions (24 hours in brine + heating cabinet prior to start-up), it was believed that 9.2 MPa was too high and not applicable as an indication of sample strength. Based on this, it was decided to run a new, independent UCS test that would instead resemble the conditions of the creep experiment procedure (Test procedure 1, p.56). Thus, a UCS test was performed on a sample (346_2_16) that had been put in brine inside the heating cabinet at 30°C for 24 hours prior to the test. When running the new UCS test, the sample had an unexpectedly early failure at 3.6 MPa; approximately 60% less in value than the previous UCS tests. The reason for this low value is believed linked to the way shale expands when it absorbs fluid. Due to clay minerals with large surface-areas, a sample of Pierre shale will naturally soak up as much fluid as possible when submerged in brine, expand significantly and drastically change its own properties. If one studies the picture of core 346_2_16 after failure (Figure III-8, Appendix III, p.187), one can observe that big pieces of rock have fallen off, which may indicate that the sample initially had small cracks that expanded drastically when the sample absorbed brine resulting in an overall weaker sample. This coincides with the obtained results of Liu and Zhou (2000) showing that when clay minerals in shale absorb water, their inner structure changes and reduces the strength of the rock. A severe weakening of shale due to brine was later confirmed after core sample 346_2_17 had been submerged in the fluid for approximately 3 weeks inside the heating cabinet. Figure 7.5 shows a sample with clearly dissolved parts. Obviously, it was clear that running the creep tests after cores had been submerged in brine inside a heating cabinet was not optimal for obtaining successful results. Thus, it was concluded that one should modify Test procedure 1 before running the next test.

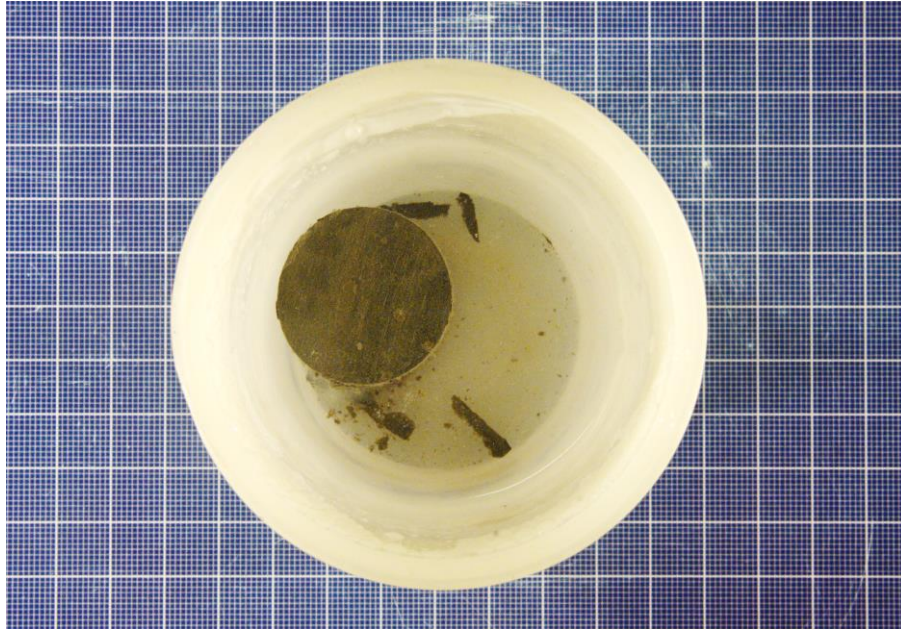


Figure 7.5: Core sample 346_2_17 with dissolved parts after 3 weeks in brine.

7.1.2 Core sample 346_2_18

Test procedure 2 was determined based on shale's ability to absorb fluid. To avoid extensive absorption of brine in the shale one can either increase the salt concentration of the surrounding fluid or have some load on the sample while introducing the brine. The Pierre shale was recovered from an outcrop in Colorado and it naturally had an initial salt concentration in the pore space. When it was exposed to brine in the lab with a different salt content, water moved from low to high salt concentration due to osmosis (the concept of osmosis is explained in section 2.5.4, p.26). With equal/higher salt concentration in the surrounding fluid compared to the initial pore fluid, no net flow of water will occur in the sample, and thus a reduced expansion effect is obtained. Analogously, by keeping a load on the sample when brine is introduced, as in the ion diffusion tests, one avoids unlimited expansion. For Test procedure 2 it was decided to resemble the ion diffusion test procedure (load on sample) because this was the most convenient solution and one would then have a "reliable" UCS value to relate to (9.2 MPa). Increasing the salt concentration would have caused more adjustments, as 3.5wt% $NaCl(aq)$ was the concentration previously used to mix the appropriate amount of brine and acid to reduce the pore fluid pH in some of the upcoming creep experiments. By maintaining this salt concentration the already mixed solutions could still be applicable for later tests.

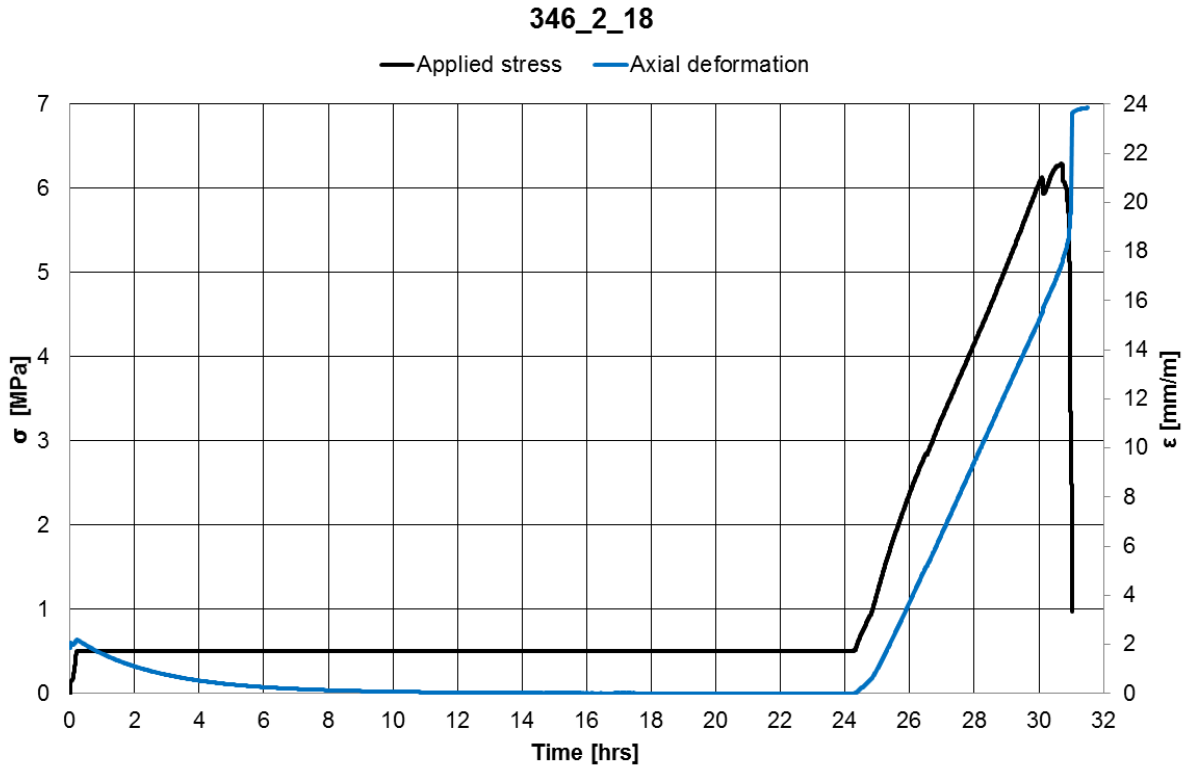


Figure 7.6: Overview of creep test conducted on 346_2_18.

This creep test was the first where the sample had not been submerged in brine inside a heating cabinet before start-up. The aim of the first 24 hours of the test at 0.5 MPa was to complete the ion diffusion process and stabilize the system, so the creep test itself begins after this point. As Figure 7.6 shows, there is a decrease in deformation in the beginning of the test which indicates swelling of the sample due to brine. This is natural since the shale sample contains approximately 20% smectite (Table VI-2, Appendix VI, p.199), a clay mineral known to have the ability to expand many times its original volume (Mungan 1965). By including a stabilization period of 24 hours, the swelling effect is neutralized prior to starting the creep test.

Further, Figure 7.6 demonstrates that the sample failed before reaching loading level 1 (7.8 MPa) at 6.3 MPa. Since a countermeasure against rock weakening was implemented in Test procedure 2 (a small load was applied in the beginning of the test to prevent unlimited absorption of brine), this early failure was highly unexpected. The reason for this rapid failure is unknown. Low running speed could potentially have initiated creep during the loading phase resulting in weakening of the rock. However, when comparing the running speed for this sample with 346_2_15 (who reached loading level 1), there is no distinct

deviation (see Table VI-3 in Appendix VI, p.200), thus this is not believed to be the cause behind it. Most likely, the reason for this early failure might be due to variation of strength within the core samples.

Studying the overall temperature measurements revealed abnormal behavior during the test. As Figure 7.7 demonstrates, the average fluid temperature of the surrounding fluid is not constant at 30°C, but highly fluctuating. An unusual variation is also observed for the room temperature. Because this irregular trend was only detected for temperature data and no other measured parameters (strain is showed to have a normal development in Figure 7.6), it was believed that the origin of the problem had to be linked to the thermocouple data logger itself (connection point for the temperature sensors). Thus, it was concluded to replace this device with a new one for upcoming tests.

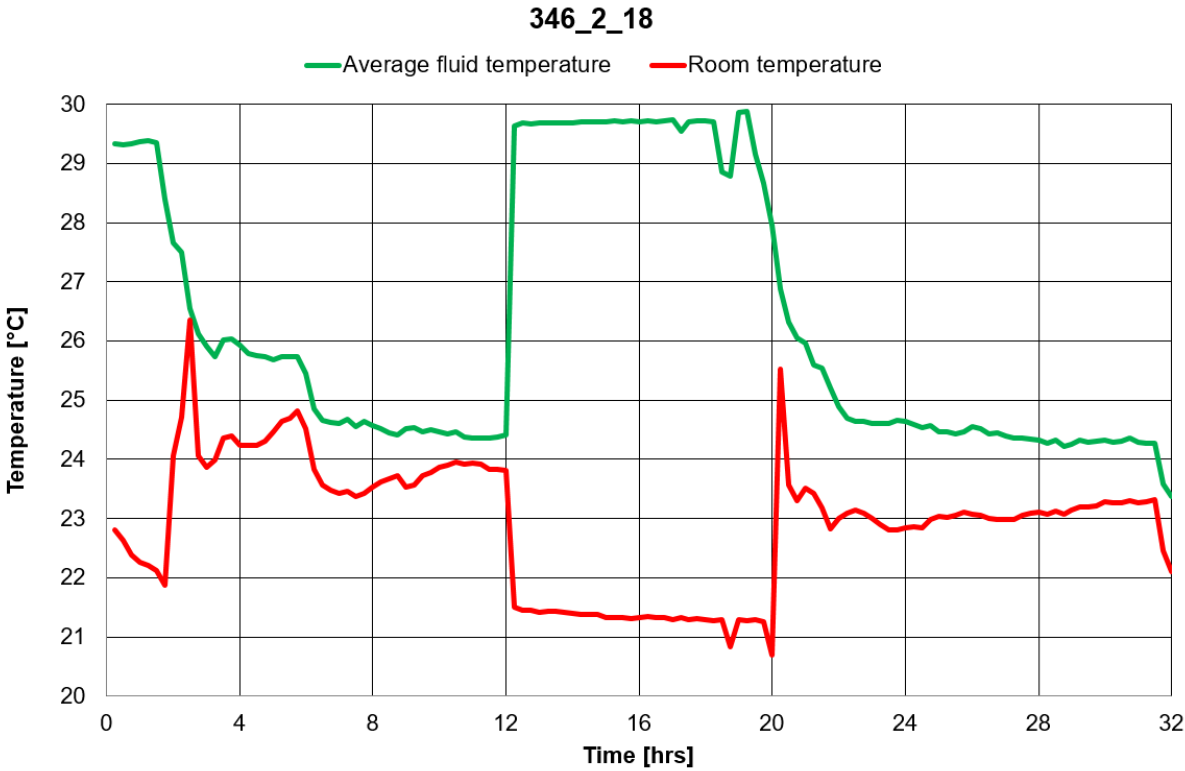


Figure 7.7: Abnormal temperature variations for sample 346_2_18.

Because this sample never reached loading level 1, limited data of relevancy was obtained from this test and thus no further attention will be given. Due to these poor results it was in cooperation with the supervisor determined to lower the stresses in the hold periods for the upcoming tests to ensure a greater collection of creep data. To see if one was able to discover a repeating pattern indicating when samples had failed in previous creep tests,

stress was plotted against strain for samples run in the specialization project in addition to recent samples (346_2_15 and 346_2_18). Figure 7.8 shows the results, but no clear correlation between the different samples could be found. Eventually, it was suggested to run the upcoming tests with a loading path similar to the one used in the specialization project (Loading path 3, as described in section 5.4.3.2, p.57).

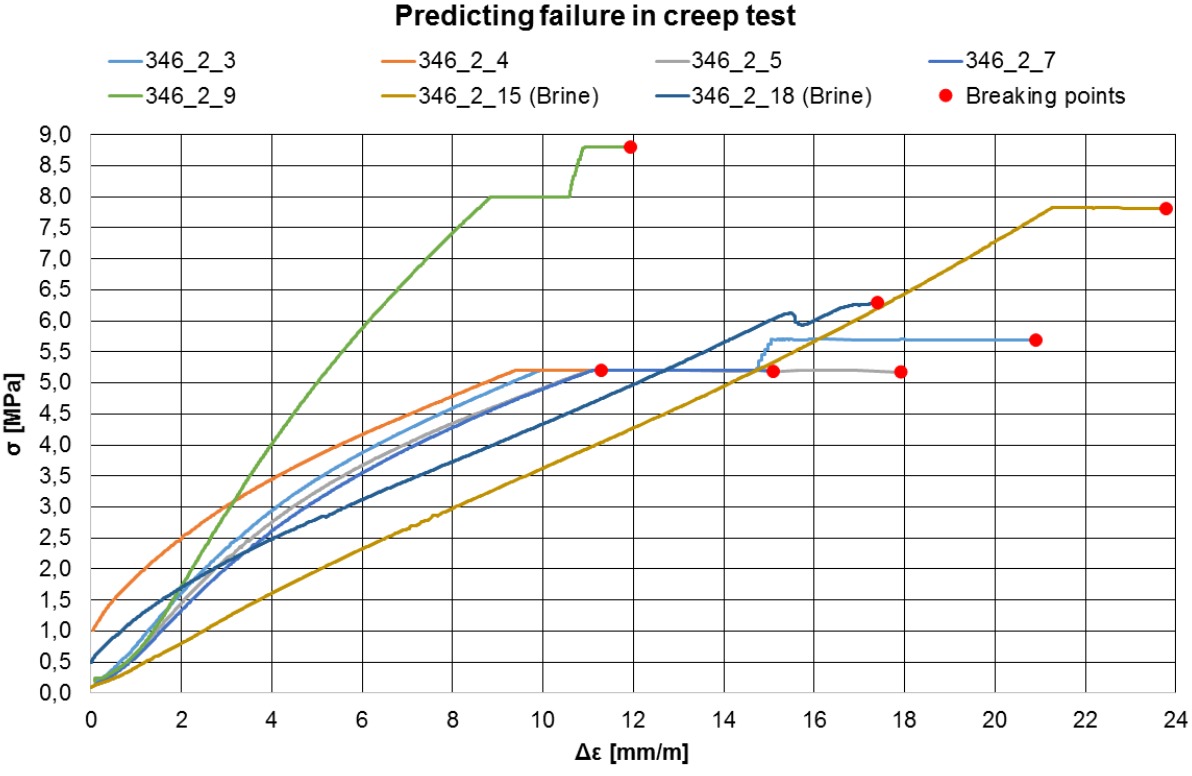


Figure 7.8: Trying to predict failure for upcoming tests by studying previously conducted creep experiments.

7.1.3 Core sample 346_2_19

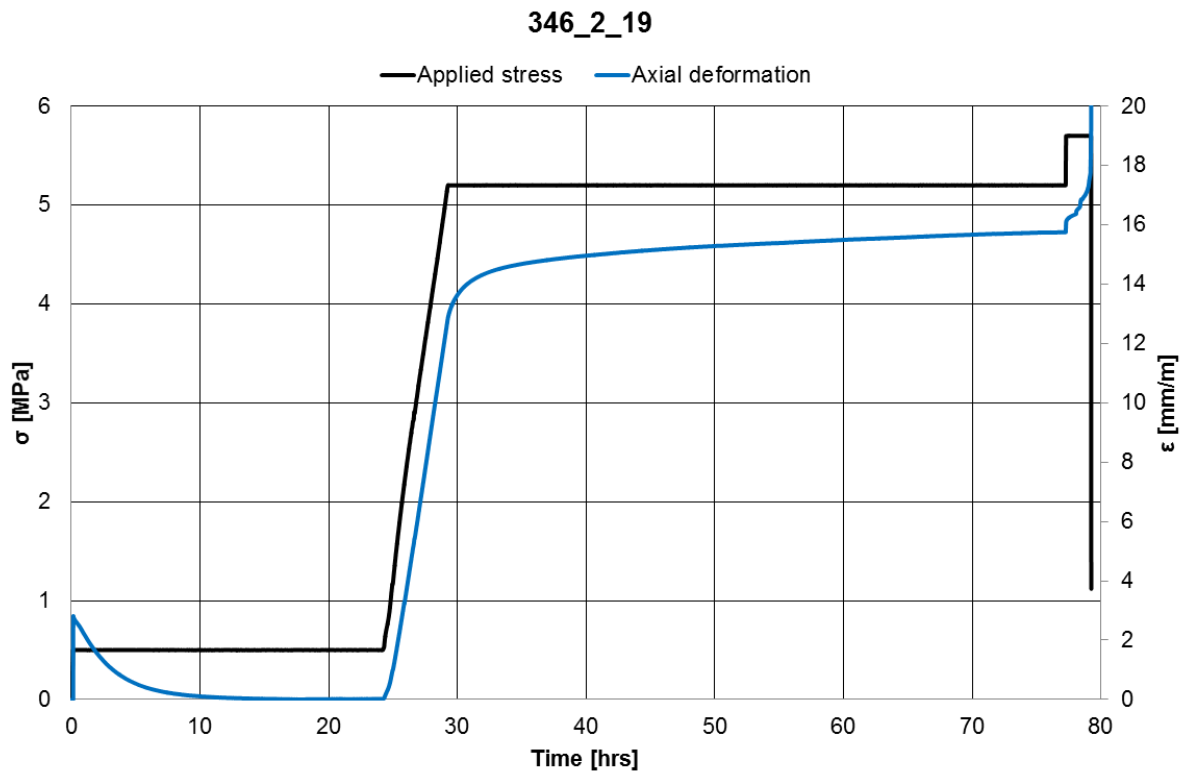


Figure 7.9: Overview of creep test conducted on 346_2_19.

The third creep test in brine ran successfully until an unwanted failure occurred after 1.89 hours in the second hold period (5.7 MPa). As mentioned for previous samples, it is believed that an early, unwanted failure could be explained by variation of strength within the core samples. Also, by studying the running speed from hold period 1 to hold period 2, it was discovered that the actual running speed deviated from the desired running speed. When implementing the test procedure in TestWorks4, the aim was to achieve a running speed of 0.1 MPa/min between the two hold periods. However, looking at the results afterwards revealed an actual running speed of 0.3 MPa/min. This implied a loading phase of 1.8 min instead of the preferred time period of 5 min. Since the sample had already been creeping for 48 hours in hold period 1, implying weakening of the rock, the rapid loading might have been too fast for the sample to withstand; resulting in failure.

346_2_19
Hold period 1

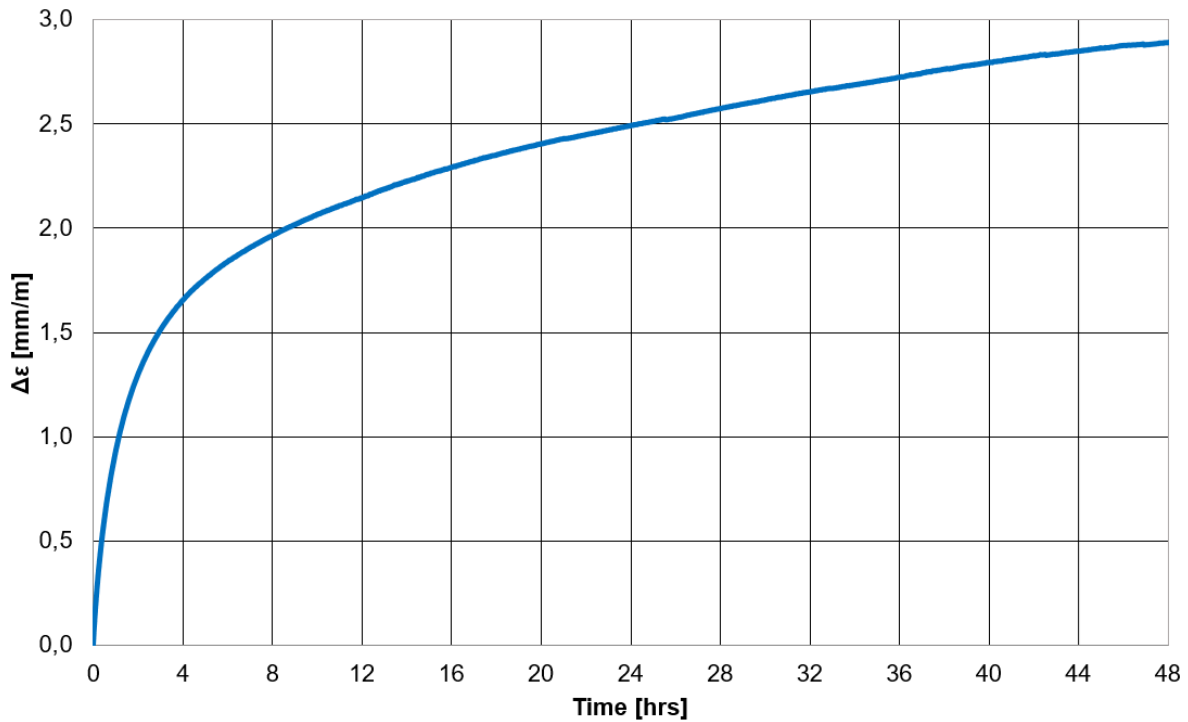


Figure 7.10: Strain vs. time for hold period 1.

When investigating strain in the first hold period, one can observe the two first stages of creep; transient and steady-state. The latter period starts after approximately 16 hours, indicating that transient creep is dominant for the first 1/3rd of the hold period. This is confirmed in Table 7-2 showing a transition between decreasing and more or less constant rates before and after this time. No accelerated creep is seen. This is logical since the sample did not approach failure in the given time interval.

Table 7-2: Deformation rates for different time intervals in hold period 1.

Time in hold period	First 4 hrs	First 8 hrs	First 12 hrs	First 16 hrs	Last 28 hrs	Last 24 hrs	Last 20 hrs	Last 16 hrs	Last 12 hrs	Last 8 hrs	Last 4 hrs
Deformation rate [(mm/m)/hrs]	0,414	0,246	0,179	0,143	0,017	0,017	0,016	0,015	0,014	0,012	0,011

Looking at log scales, the transition between consolidation- and creep dominated behavior occurs at approximately 1.5 hours into the hold period (Figure 7.11).

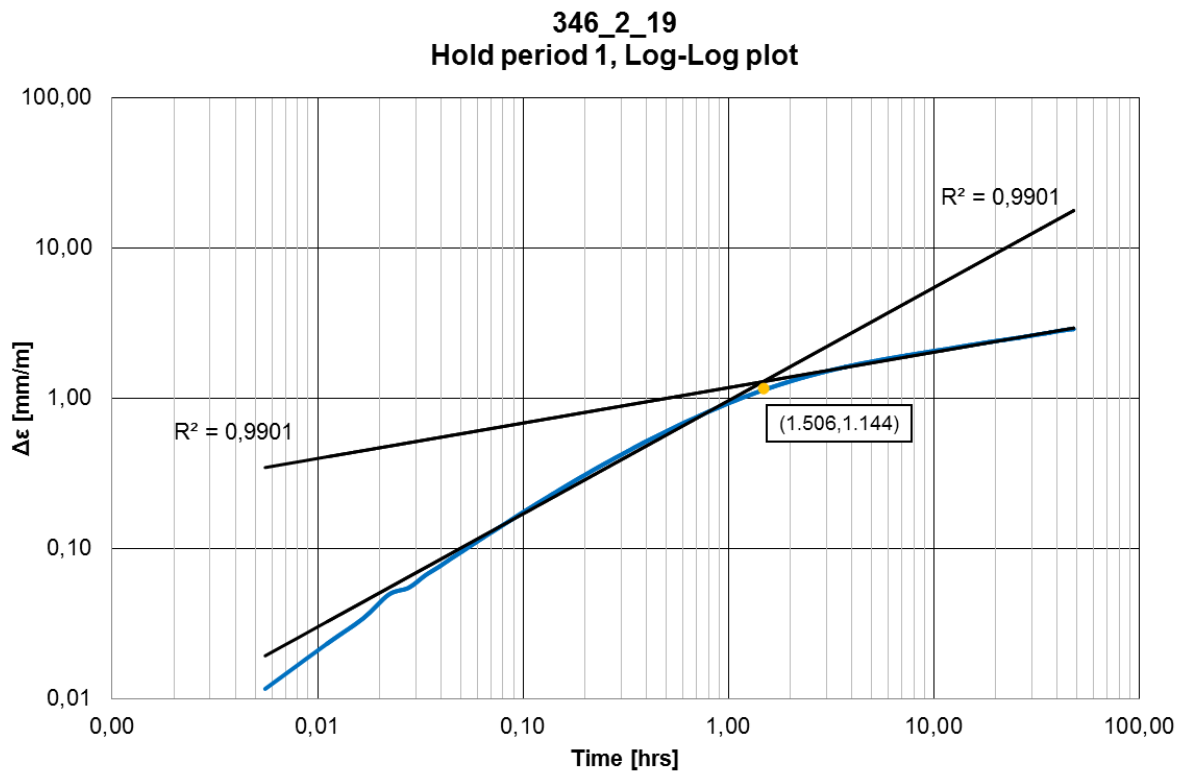


Figure 7.11: Estimated transition between creep and consolidation dominated behavior by applying the graphical approach.

Studying the temperature measurements it once again, like for core sample 346_2_18, indicated strange behavior. As Figure 7.12 shows there is no correspondence between the different thermocouples after approximately 18.5 hours. They are supposed to measure the same temperature, but the variation behind this point is extreme. The presented graph illustrates a typical short-circuiting. Thus, all temperature measurements after 18.5 hours had to be discarded. This was unfortunate, but based on how well the temperature controller had worked in creep test 346_2_15 (a temperature variation of 0.37°C) and in the first 18.5 hours of this test (a temperature variation of 0.25°C), one can assume that the actual temperature in the surrounding fluid was more or less constant around 30°C during the whole test. Even if there is no actual temperature data to back up this statement, the assumption is more or less confirmed as measurements of the other parameters were unaffected (Figure 7.13 and Figure 7.14). Also, a room temperature of 241°C in the lab (Figure 7.12) is highly unlikely. When investigating the reason behind the abnormal

measurements, a solution was not found until after the next test had completed (core sample 346_2_20). It was then established that the thermocouples measuring the fluid temperature inside the container had absorbed brine due to capillary suction and directed the fluid into the temperature data logger causing a short circuit. Looking back, this was probably also the reason behind the irregular temperature measurements for core sample 346_2_18.

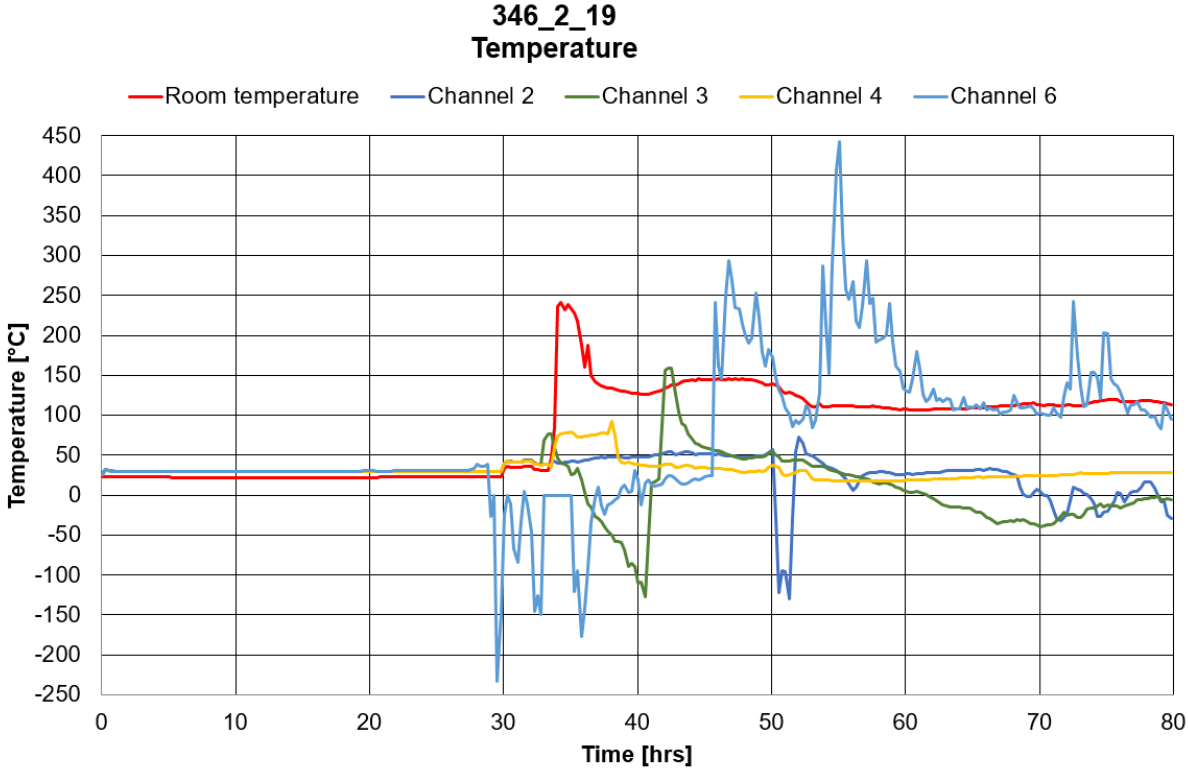


Figure 7.12: Temperature variations for sample 346_2_19 indicating a short circuit.

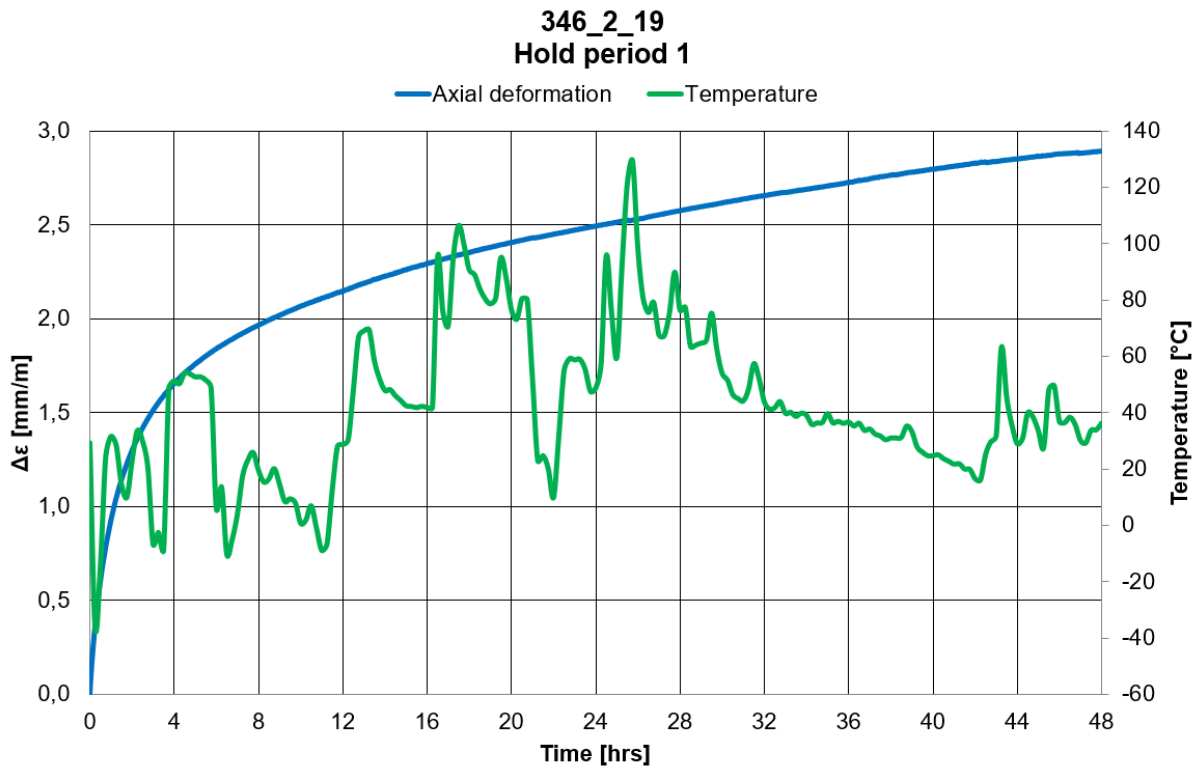


Figure 7.13: Strain measurements were not affected by the recorded temperature variations.

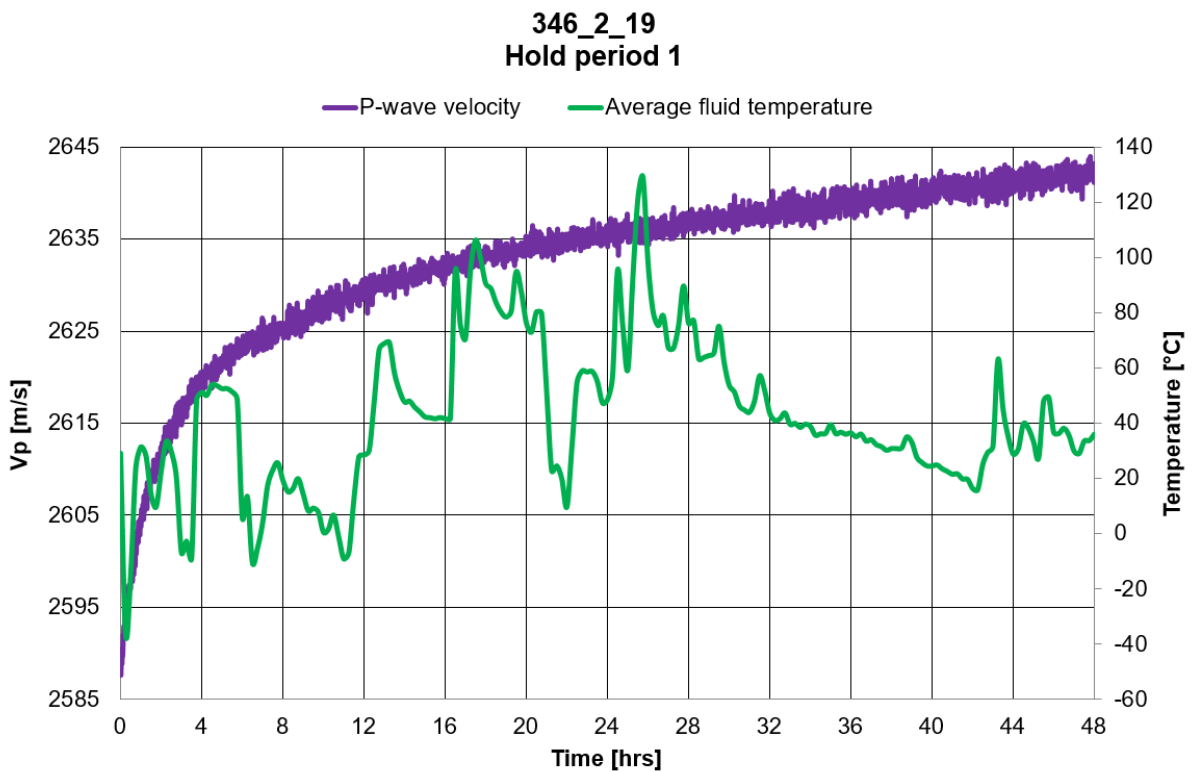


Figure 7.14: P-wave velocity measurements were not affected by the recorded temperature variations.

By investigating the p-wave velocities for hold period 1, the trend found for sample 346_2_15 was confirmed; the velocities increase simultaneously with the strain in the hold period instead of being constant (Figure 7.15). Unfortunately, due to lack of valid temperature measurements for this time period, no analysis in regards to temperature variation in conjunction with p-wave velocities could be conducted.

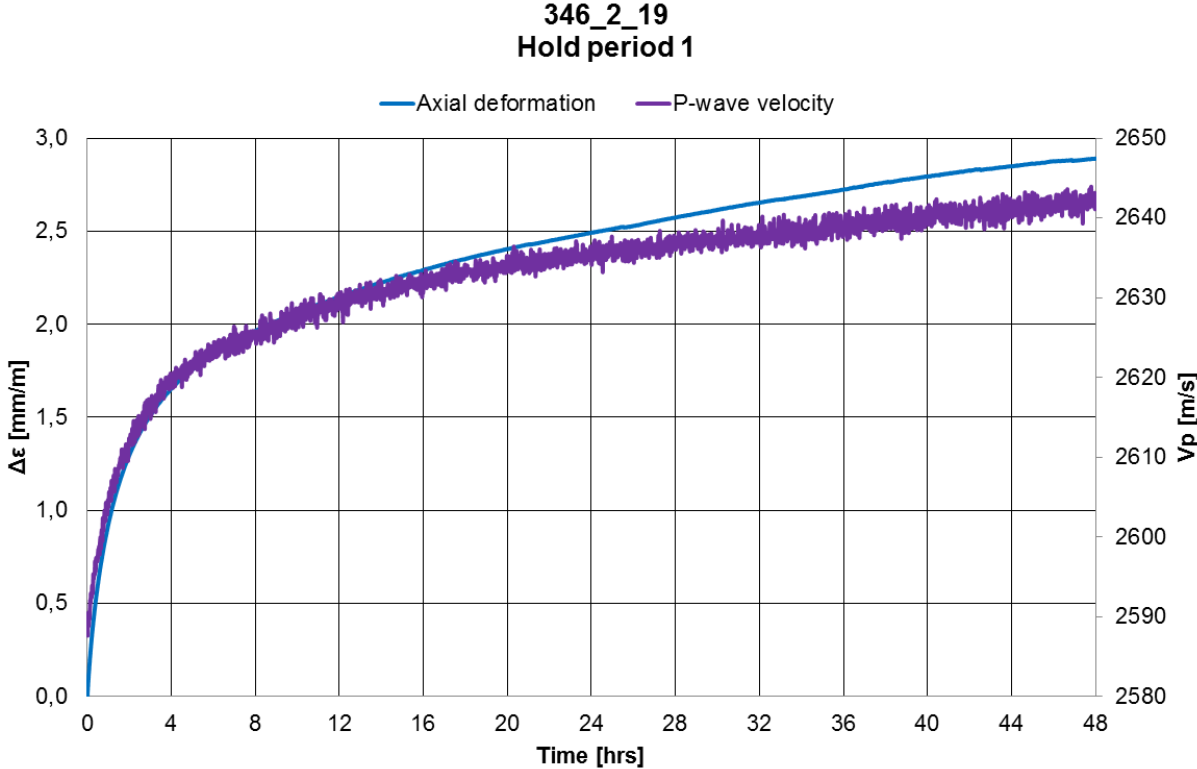


Figure 7.15: Strain in conjunction with p-wave velocities for hold period 1.

As previously described, the sample failed after a short time in hold period 2. Figure 7.16 indicates that accelerated creep is initiated from approximately 0.78 hours, and the sample fails after 1.89 hours. Based on this, very limit data was obtained from hold period 2, thus no further attention will be given.

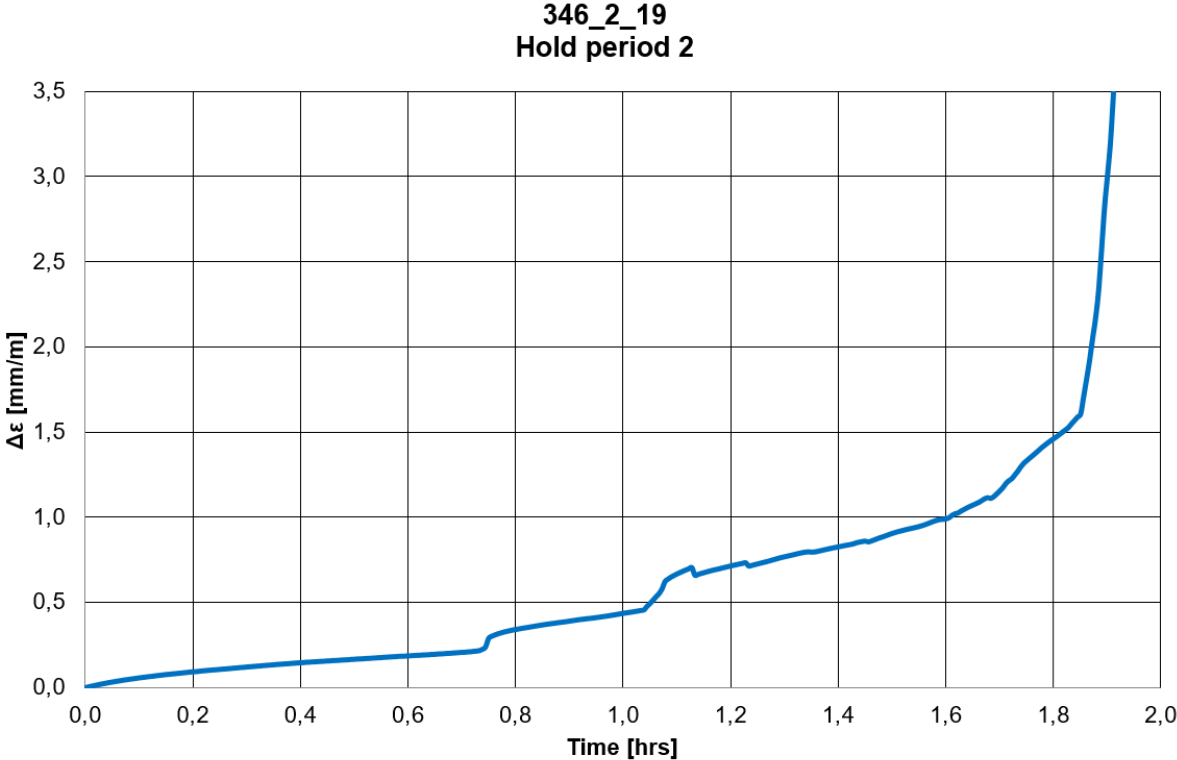


Figure 7.16: Strain vs. time for hold period 2.

When evaluating this creep test as a whole, one had acquired a great amount of creep data for hold period 1, but unfortunately the sample failed early in hold period 2. To ensure complete sets of creep measurements for upcoming tests, it was decided to optimize the loading path once again (to Loading path 4). Instead of trying to predict which loading levels one should collect creep data from and in addition avoid early, unwanted failures, it was suggested to frequently (every 4 hours) increase load stepwise with 0.5 MPa until failure.

7.1.4 Core sample 346_2_20

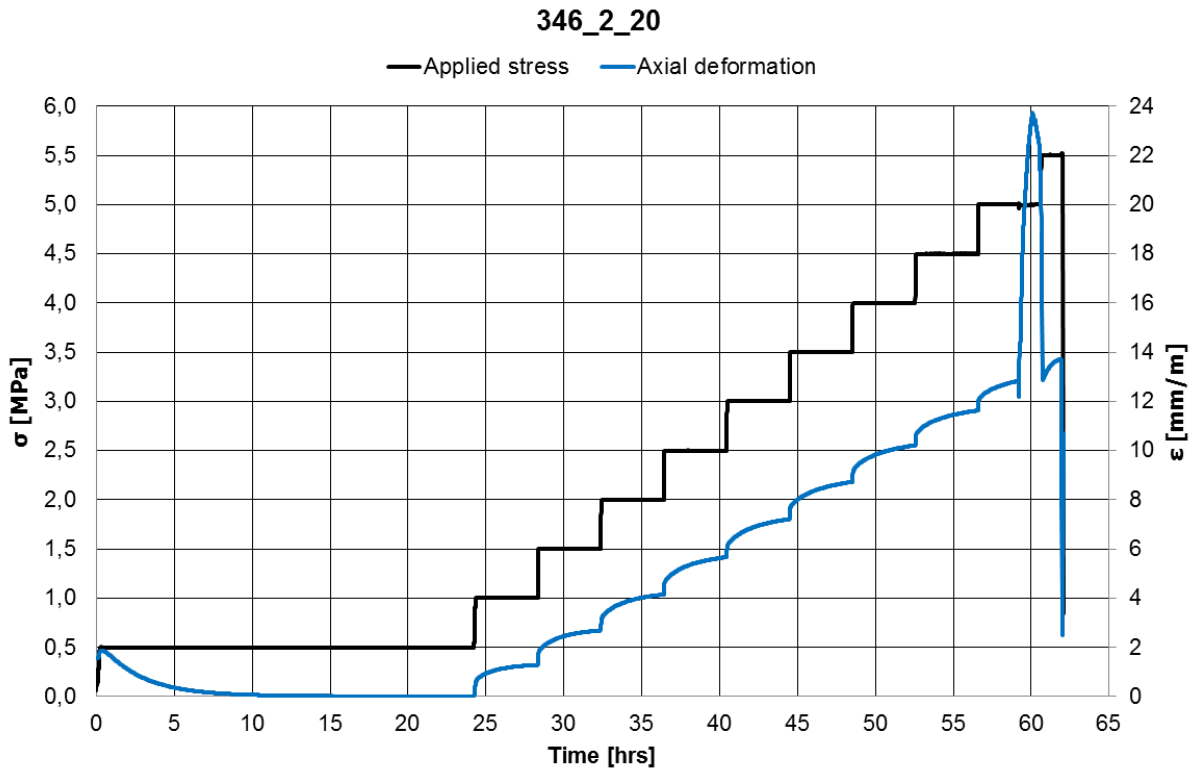


Figure 7.17: Overview of creep test conducted on 346_2_20.

The fourth creep experiment in brine was performed without temperature measurements. After the thermocouple data logger was damaged in the previous test, there were none available at the lab while a new one was ordered. Overall, the test went successfully up to 10 load levels after completing ion diffusion for 24 hours. Failure of the sample occurred 1.4 hours into hold period 10, at 5.5 MPa. However, as Figure 7.17 demonstrates, an abnormal deformation developed in hold period 9 at 5.0 MPa. Studying this irregular behavior in conjunction with p-wave velocities in Figure 7.18, shows that the p-wave velocities have a significant drop simultaneously as the strain rises. It is believed that this unusual behavior is related to an unfortunate incident that happened in the lab at the end of the test (described later, p.98), causing a sudden and enormous temperature increase. Thus, due to invalid data at the end of the test, the final two hold periods will not be included for further discussion.

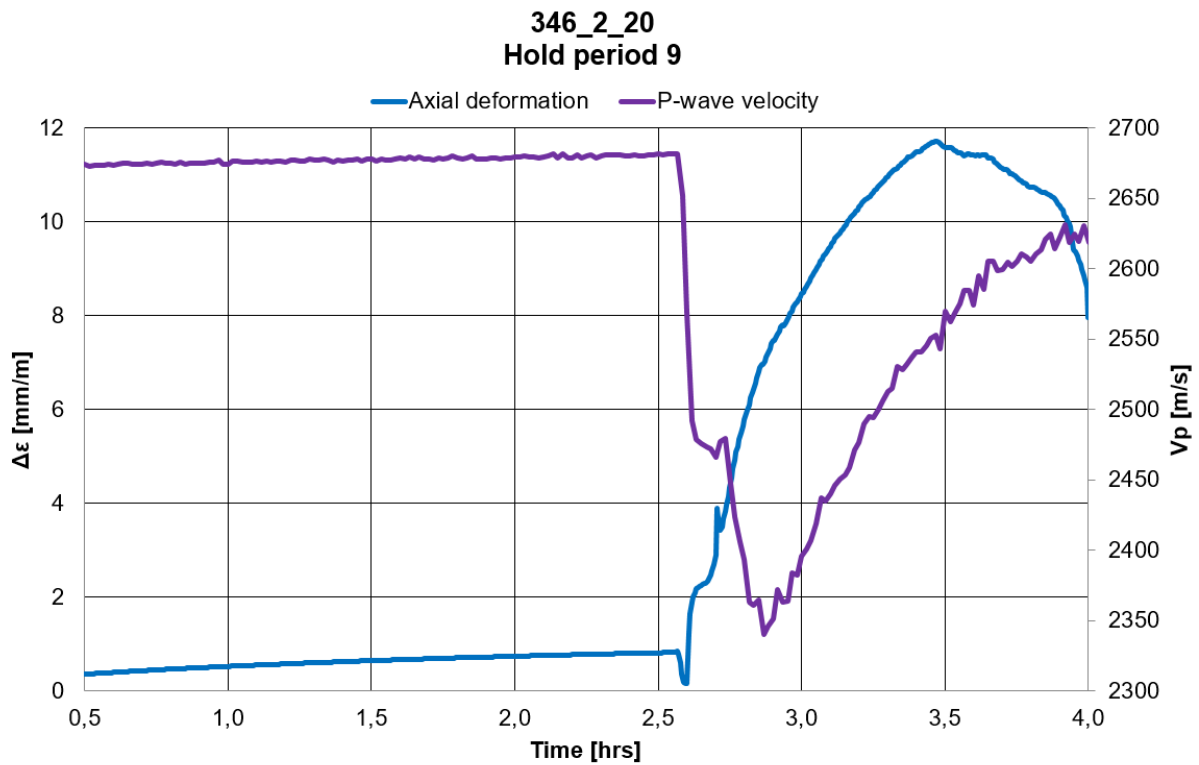


Figure 7.18: Strain in conjunction with p-wave velocities for hold period 9.

As already mentioned, there was unfortunately no temperature data obtained from this test, but based on previous experiments one can assume that the temperature of the fluid surrounding the sample was more or less constant around 30°C for the first 8 hold periods. However, one should keep in mind that the time duration of this test was extended compared to previous ones. As described in section 1.4 (p.4), the experiments conducted in the specialization project showed that temperature variation increased with extended test time. Thus, this sample might have been exposed to a more pronounced, but not severe, temperature variation than the previous samples.

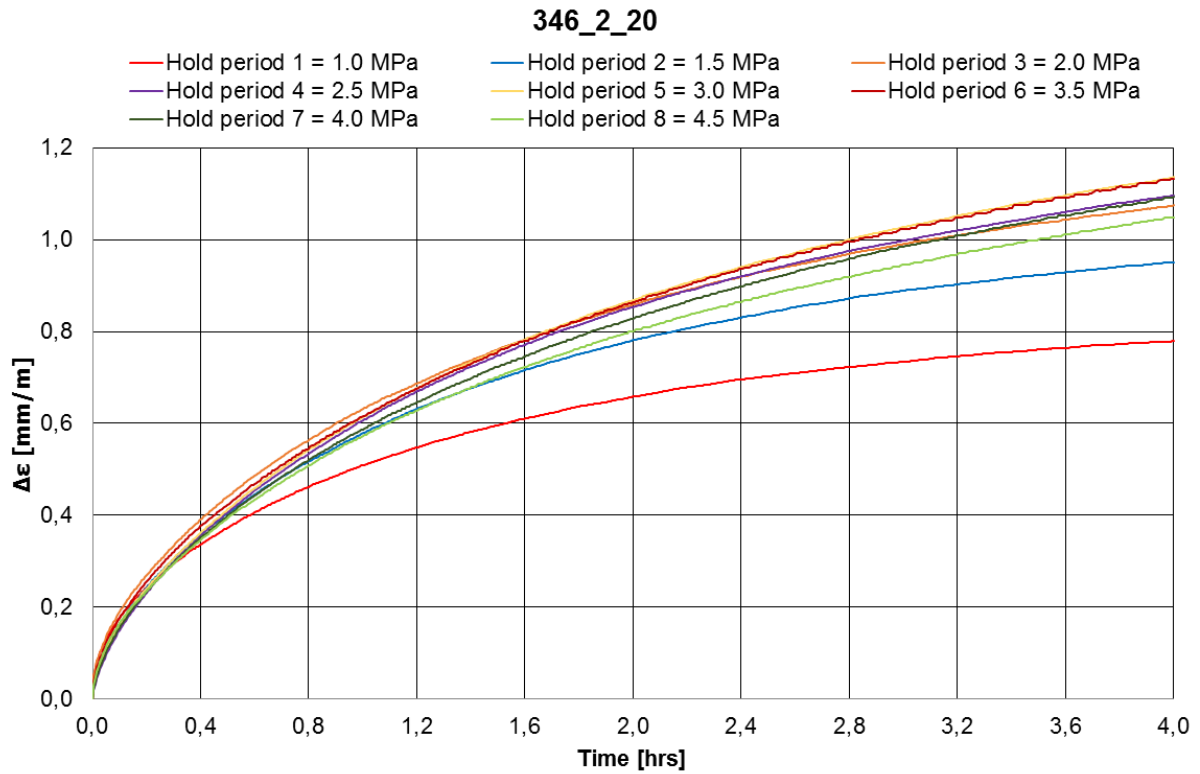


Figure 7.19: Strain versus time for all valid hold periods.

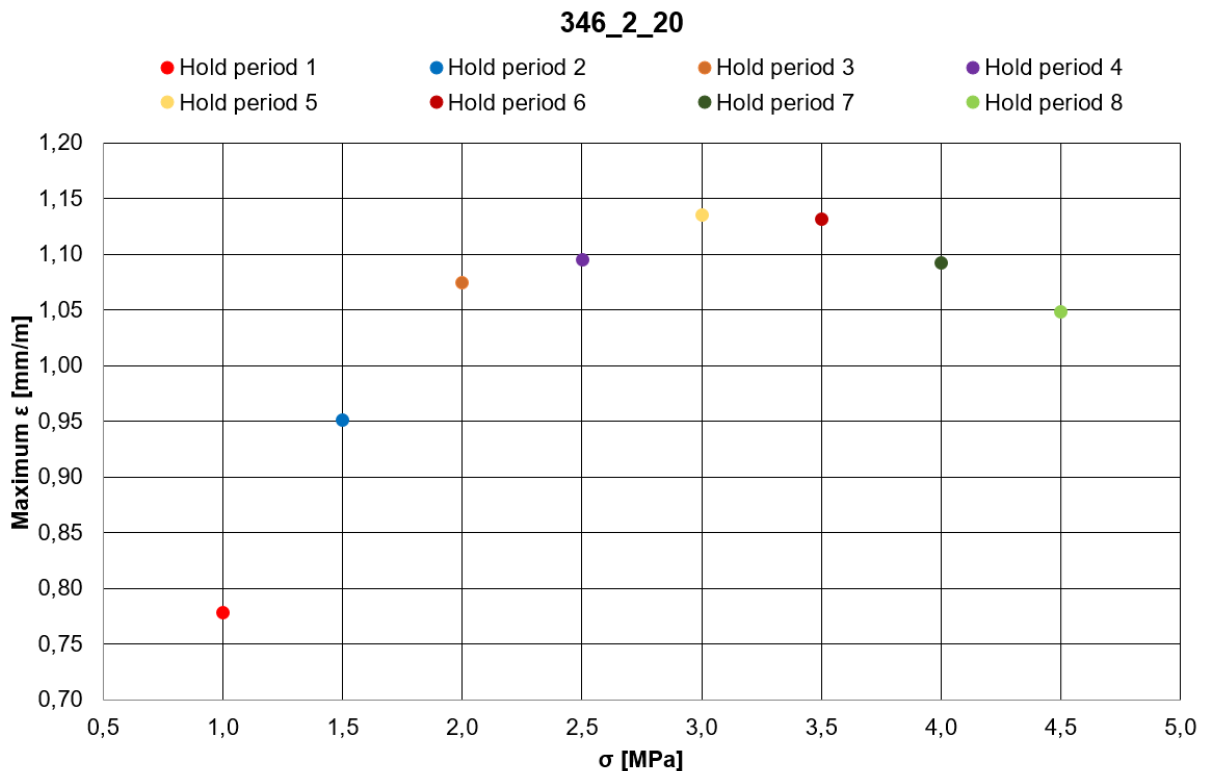


Figure 7.20: Maximum strain for a hold period versus stress level.

Figure 7.19 shows the obtained strain for all valid hold periods scaled to the same reference point (0,0). As one can observe, the amount of strain increases with load for the first 5 hold

periods, but from hold period 6 and onwards, a decrease in deformation occurs. This is even more clearly illustrated in Figure 7.20, showing maximum strain for a hold period versus stress level.

Comparing the slopes of the curves (equivalent to the deformation rates) in Figure 7.19 for certain time intervals (Table 7-3), shows that period 1 and 2 have the lowest deformation rates among all at the end. This is clearly illustrated in Figure 7.19 where the remaining hold periods have steeper curves in the end in contrast to period 1 and 2. For these low load levels it appears like the deformation is approaching stable behavior after a period of transient creep. This is consistent with the theory illustrated in Figure 2.8 (section 2.3.1, p.17). Based on the low and stable deformation rates, the same figure indicates that the shift from *low* to *moderate* stress levels for this sample occurs in the transition between 1.5 MPa (hold period 2) and 2.0 MPa (hold period 3). Further, it seems like there might be a stress threshold (2.0 MPa) for reaching steady-state creep. Generally, finding a stress threshold for this creep phase agrees with research of Li and Ghassemi (2012). As Table 7-3 demonstrates, the deformation rates are not constant for hold period 4 and 5 at the end implying that these are still in transient creep phase. This suggests that 4 hours might be a too short time period to initiate the other phases of creep for these load levels. However, the deformation rates for hold period 6, 7 and 8 are more or less constant the last 30 min, indicating that creep has reached steady-state phase.

Table 7-3: Overview of deformation rates and creep phases at the end of the hold periods.

Hold period	Load [MPa]	Interval [hrs]						Creep phase at the end of hold period*
		0,0-1,0	1,0-2,0	2,0-3,0	3,0-3,5	3,5-3,75	3,75-4,0	
		Deformation rate [(mm/m)/hrs]						
1	1,0	0,509	0,149	0,076	0,055	0,040	0,031	Stable
2	1,5	0,579	0,202	0,108	0,067	0,061	0,054	Stable
3	2,0	0,631	0,227	0,132	0,091	0,077	0,078	Steady-state
4	2,5	0,606	0,247	0,145	0,105	0,098	0,082	Transient
5	3,0	0,613	0,255	0,159	0,117	0,107	0,093	Transient
6	3,5	0,615	0,249	0,159	0,119	0,096	0,101	Steady-state
7	4,0	0,586	0,241	0,157	0,114	0,103	0,099	Steady-state
8	4,5	0,572	0,229	0,144	0,108	0,101	0,098	Steady-state

*To distinguish between transient and steady-state creep phase at the end of a hold period, a threshold value, T_{cp} , representing the difference between the last two time intervals, was set for $T_{cp} \leq 0.01$. An increase in deformation rate between the last two time intervals exceeding the established T_{cp} was used to define accelerating creep.

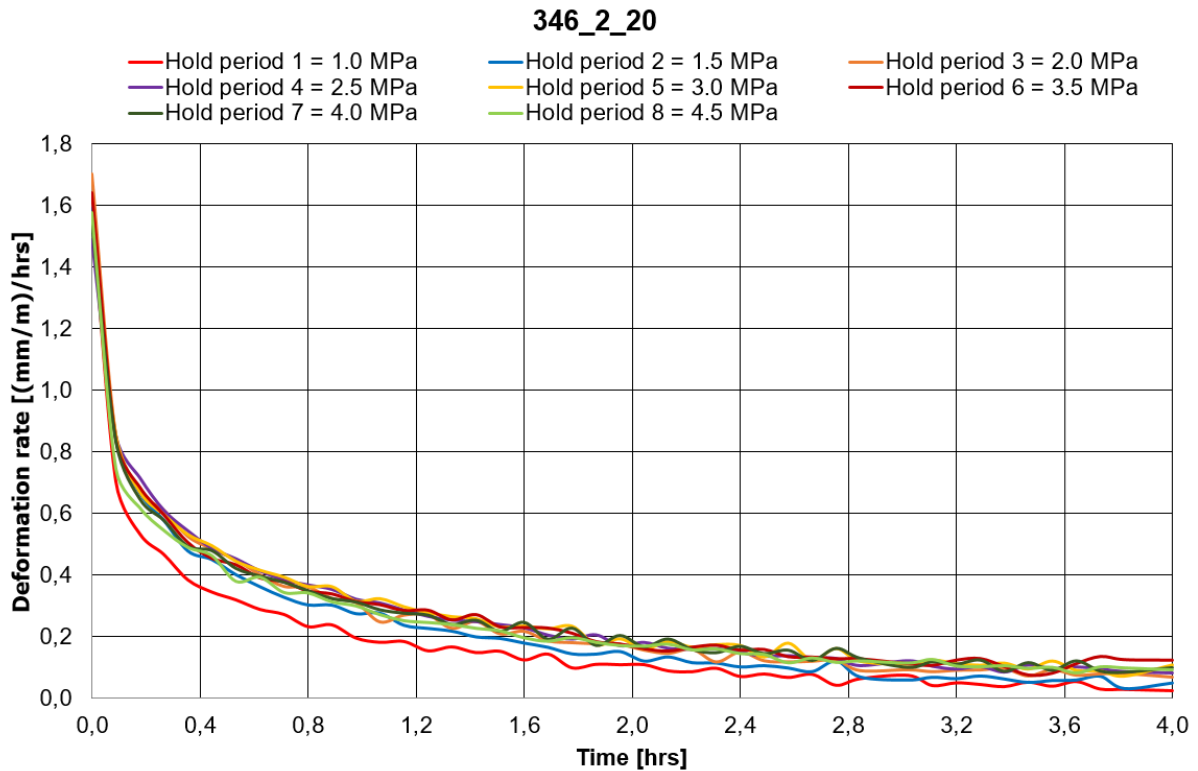


Figure 7.21: Continuous deformation rates in the valid hold periods.

Figure 7.21 presents continuous deformation rates for the hold periods. A noticeable decrease in deformation rate is observed in the start of all periods, confirming transient creep phase. Later, the decline is more subtle before stable rates occur for most of them. Generally, one should anticipate higher deformation rates for increased stress. However, in this test, only the two first hold periods follows this expectation by standing out with the lowest rates while the other periods blend more or less together. Overall, the sequence of the curves is as expected based on Figure 7.20 and the small difference among the last six hold periods might be due to the consolidation effect.

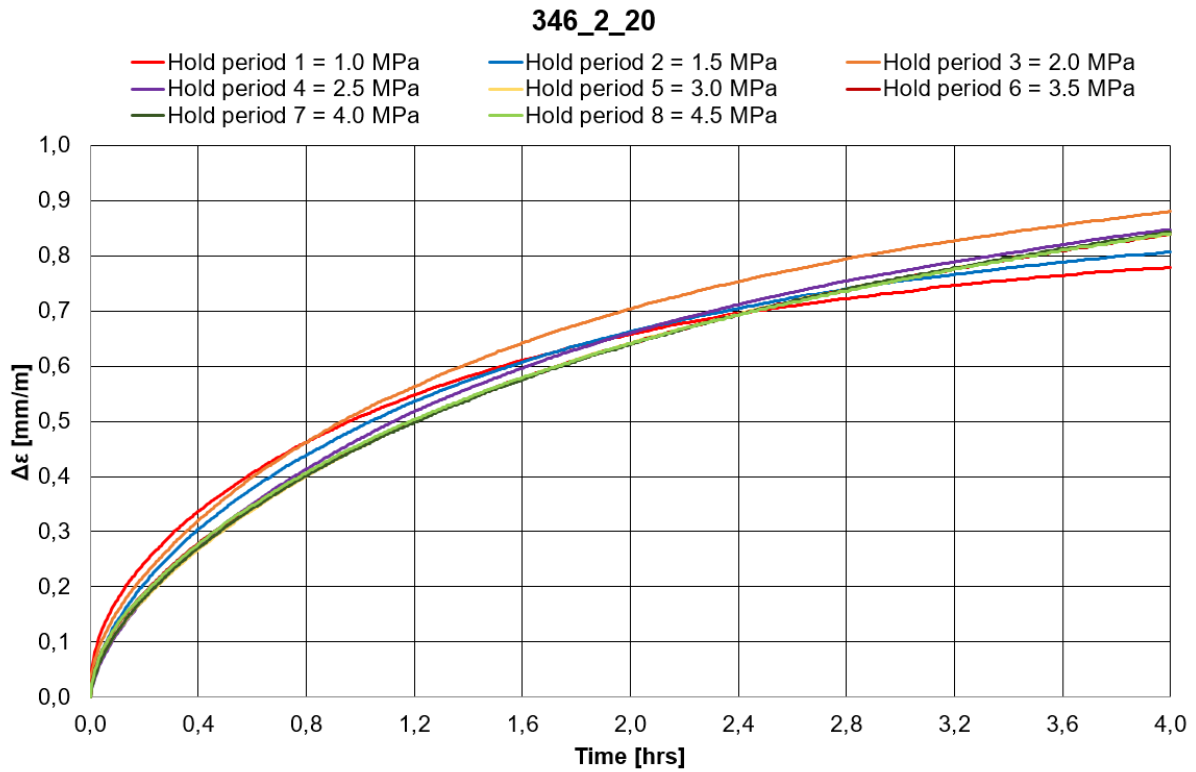


Figure 7.22: An attempt to scale the other hold periods down to hold period 1 with a scaling factor s .

Figure 7.22 presents an attempt to scale the other hold periods down to a reference, hold period 1, by using a scaling factor s . Since the shapes of the curves differ for the hold periods, it illustrates that the variation in deformation between them is not only dependent on an amplitude factor. This is consistent with the fact that the hold periods have varying deformation rates compared to each other. As consolidation and creep are two processes with different time dependencies, it is natural that the curves of the hold periods can have varying shapes dependent on when the two mechanisms are dominating.

346_2_20

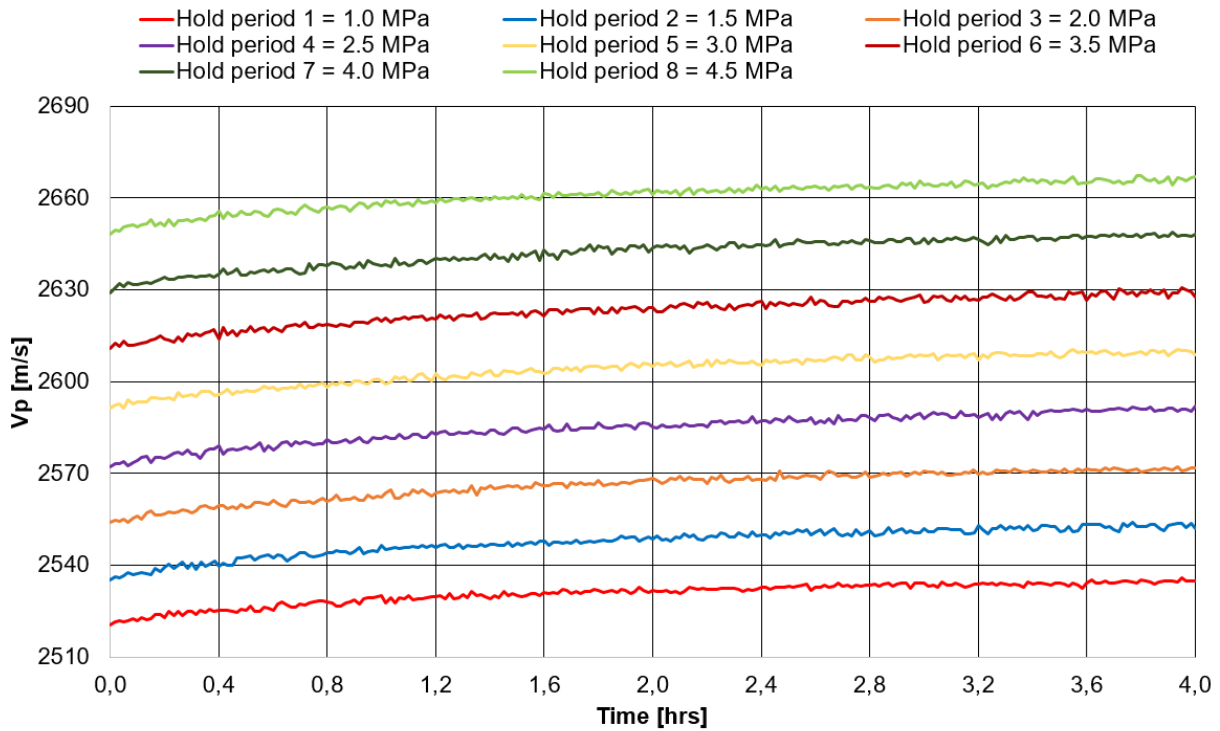


Figure 7.23: P-wave velocities in the valid hold periods.

By investigating p-wave velocities for the hold periods (Figure 7.23), one can observe that the magnitude of the velocities increases with stress level. However, the p-wave velocities are not constant for periods with fixed stress (Figure 7.24), they increase with time, implying a direct correspondence between velocities and strain. In addition, looking at velocities versus deformation for the hold periods (Figure 7.25) indicate an almost linear dependency between p-wave velocities and strain. This is later confirmed in Figure 7.26 (the same plot as Figure 7.25, only scaled to (0,0)), and suggests that velocities in the hold periods are more or less a linear function of deformation. Overall, based on this discussion, one can assume that p-wave velocities are related to strain as well as stress. This coincides with findings for previous tests.

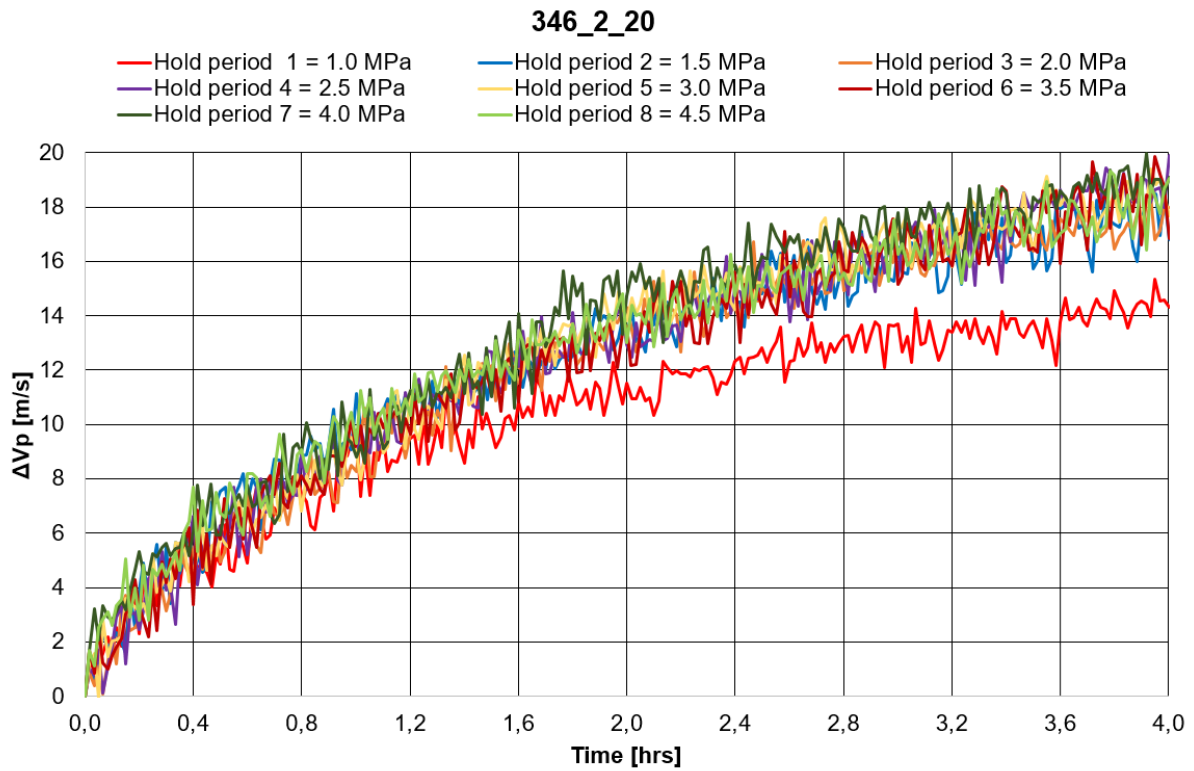


Figure 7.24: P-wave velocities in the valid hold periods scaled to (0,0).

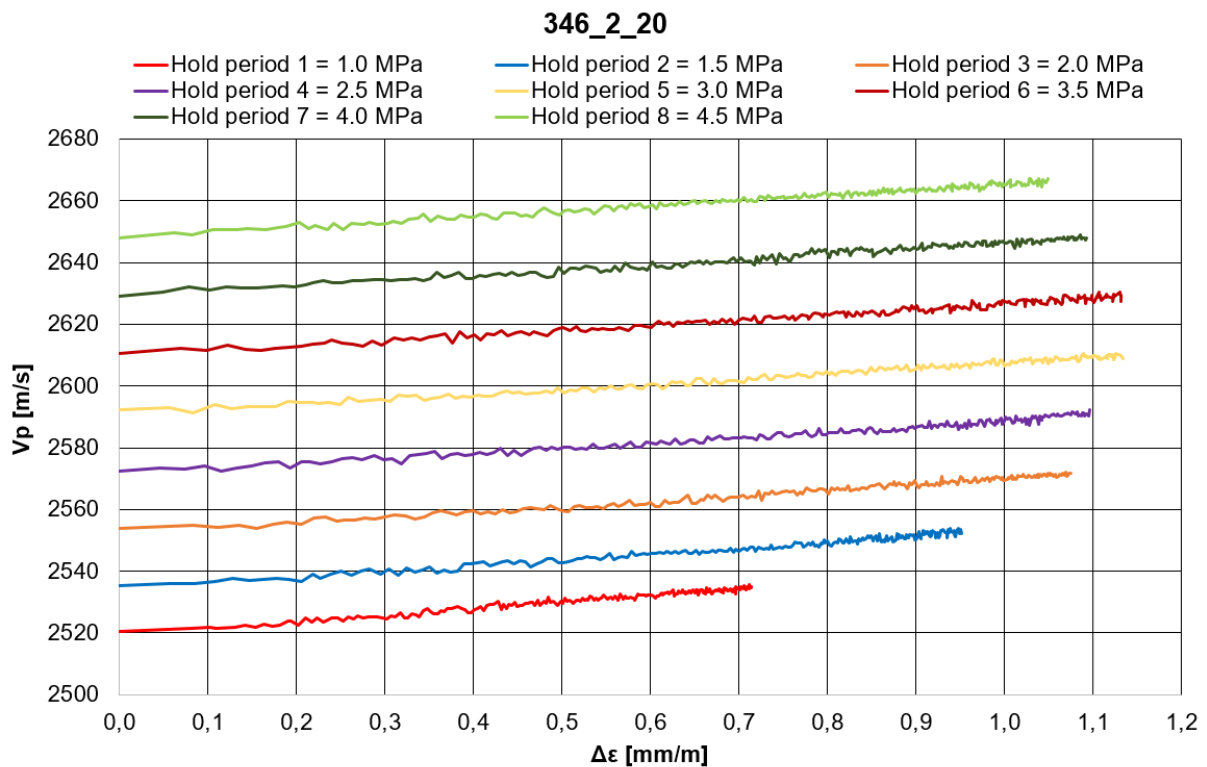


Figure 7.25: P-wave velocities versus deformation for the valid hold periods.

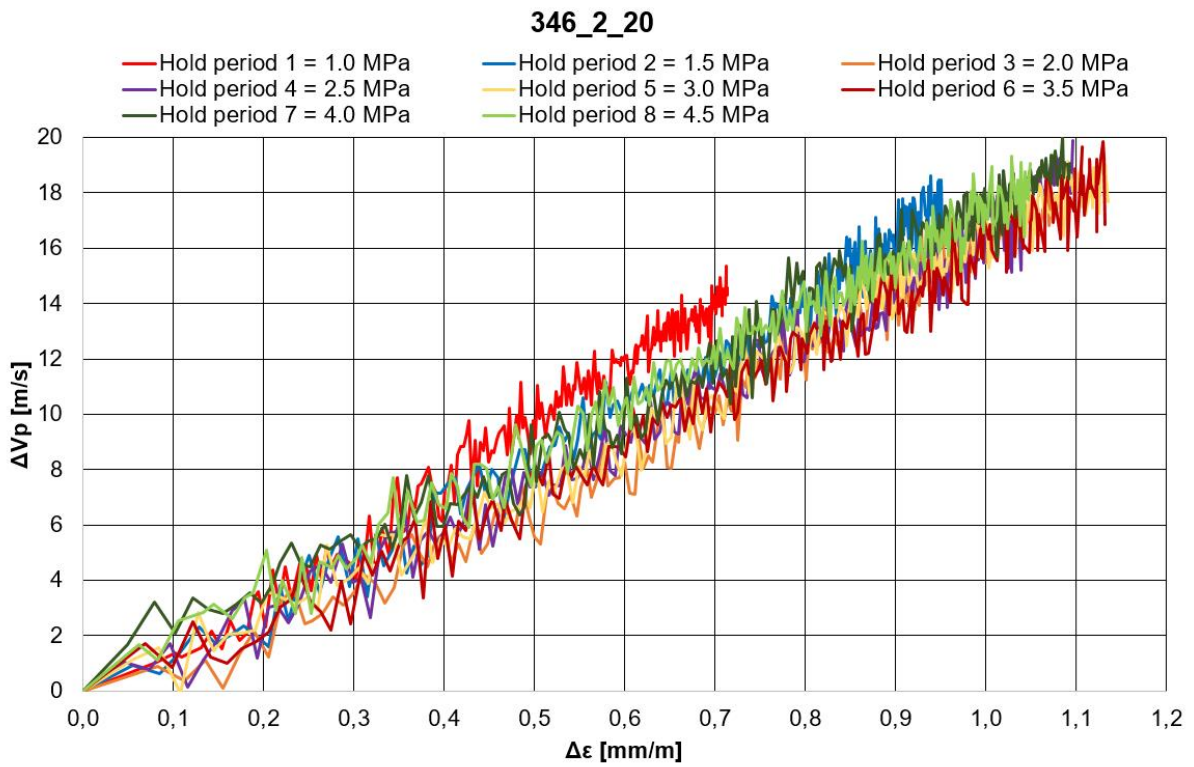


Figure 7.26: P-wave velocities versus deformation for the valid hold periods scaled to (0,0).

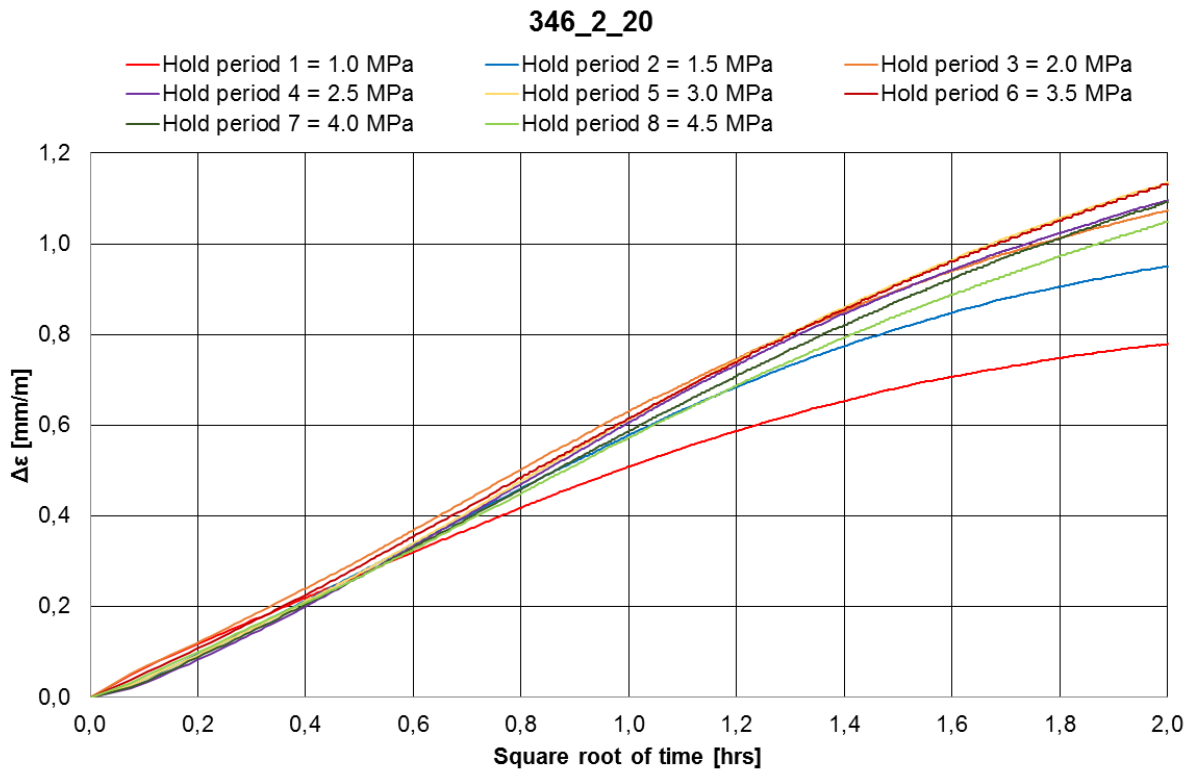


Figure 7.27: Strain versus square root of time for all valid hold periods.

Studying deformation versus the square root of time (Figure 7.27) may indicate when the consolidation process has terminated. By applying the graphical approach described in section 6.1 (p.61) one can extract the approximate time for when consolidation ends in the different hold periods. The results are presented in Table 7-4 and Figure 7.28, and shows that the parameter ranges from 1.5-2.5 hours.

Table 7-4: Approximate consolidation times, τ_D , for different hold periods.

Hold period	Load [MPa]	Square root of time [hrs]	τ_D [hrs]
1	1,0	1,240	1,538
2	1,5	1,254	1,573
3	2,0	1,358	1,844
4	2,5	1,432	2,051
5	3,0	1,518	2,304
6	3,5	1,565	2,449
7	4,0	1,551	2,406
8	4,5	1,531	2,344

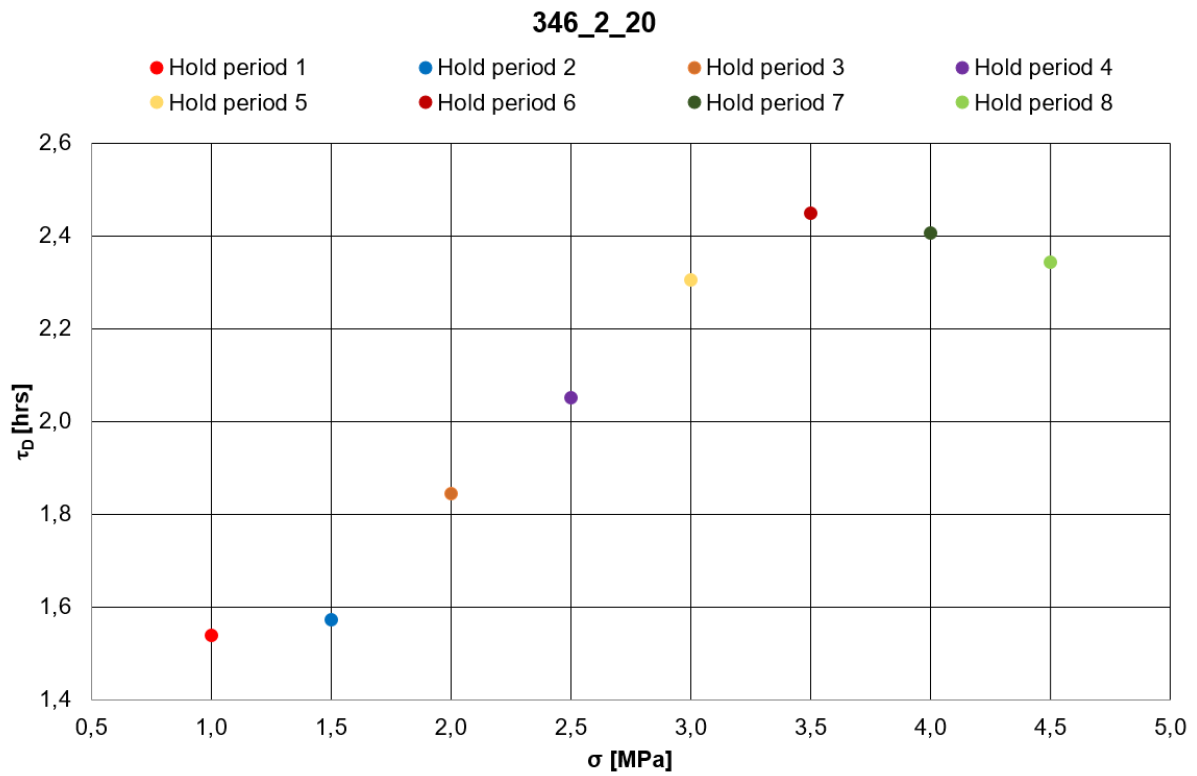


Figure 7.28: Approximate consolidation times for different hold periods.

Figure 7.28 demonstrates that the consolidation time increases more or less linearly up to hold period 6 before it declines. The fact that the consolidation phase varies with the amount of axial stress applied to a sample agrees with Cogan (1976).

346_2_20

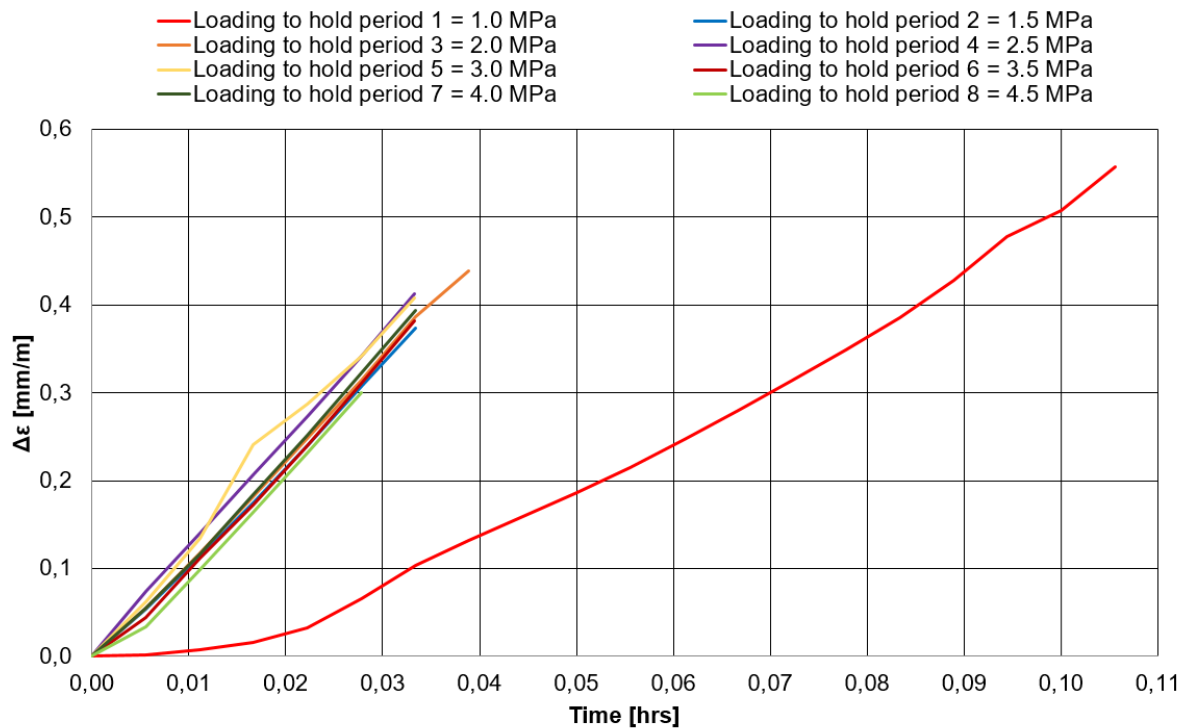


Figure 7.29: Initial deformation versus time for all valid loading phases.

By looking at the strain for the *loading phases* (Figure 7.29), one can observe a deviation in shape of the deformation curve for loading phase 1 compared to the others. Since the connection between the core and the pistons might not be optimal in the beginning of a test this can be considered as normal behavior. Once the load increases and a good connection is established, one can see a more or less expected behavior for the remaining loading phases. For each loading phase the stress increases with 0.5 MPa, and the figure illustrates that the amount of initial deformation differs for the phases. As shown in Table 7-5 the overall trend shows decreased strain for increased load.

Table 7-5: Maximum amount of strain for each loading phase.

	346_2_20							
Loading phase	1	2	3	4	5	6	7	8
σ [MPa]	0,5-1,0	1,0-1,5	1,5-2,0	2,0-2,5	2,5-3,0	3,0-3,5	3,5-4,0	4,0-4,5
ϵ [mm/m]	0,557	0,374	0,439	0,413	0,409	0,382	0,394	0,300

Further, the slopes of the curves in a $\frac{\Delta\varepsilon}{\Delta\sigma}$ versus σ plot (Figure 7.30) for the loading phases will represent a stiffness feature of the shale. Due to loading in only one direction, the slope can be characterized as the inverse of the initial Young's modulus; $1/E_{initial}$. Figure 7.31 shows the described parameter, and one can observe a close to linear decline throughout the test. The corresponding values of $E_{initial}$ for the different loading phases are presented in Table 7-6.

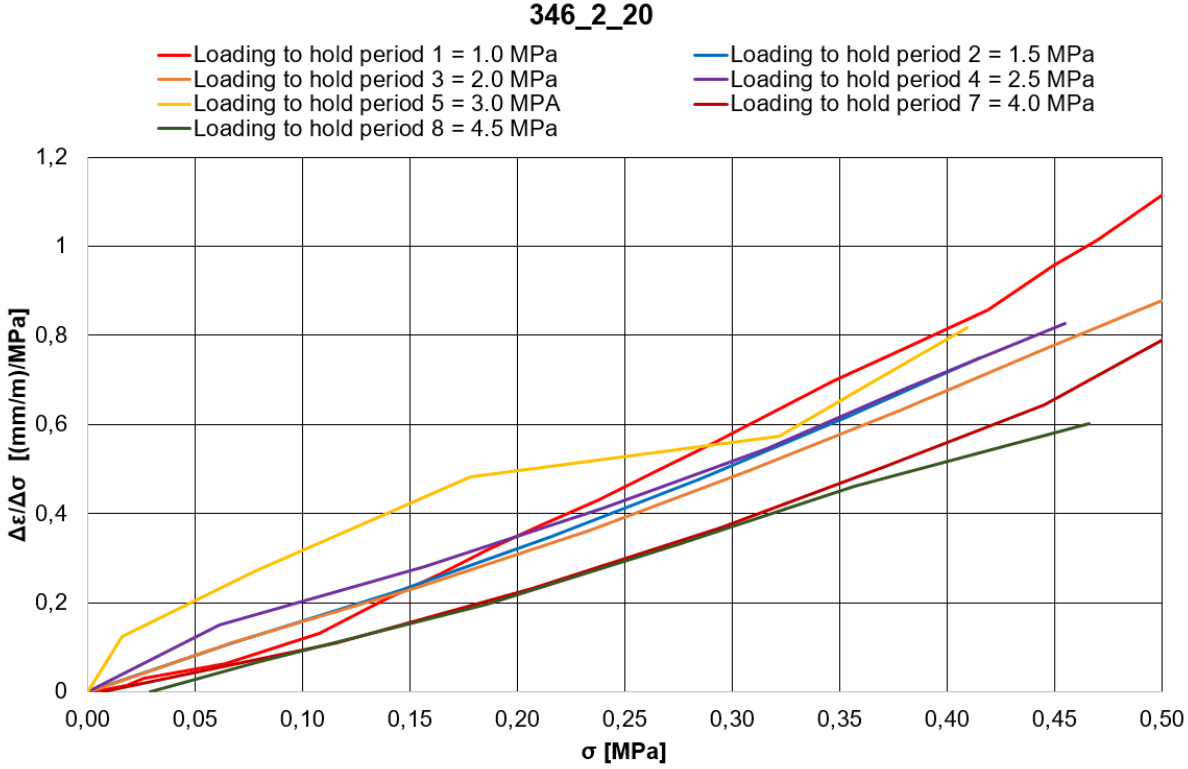


Figure 7.30: $\Delta\varepsilon/\Delta\sigma$ versus stress for all valid loading phases.

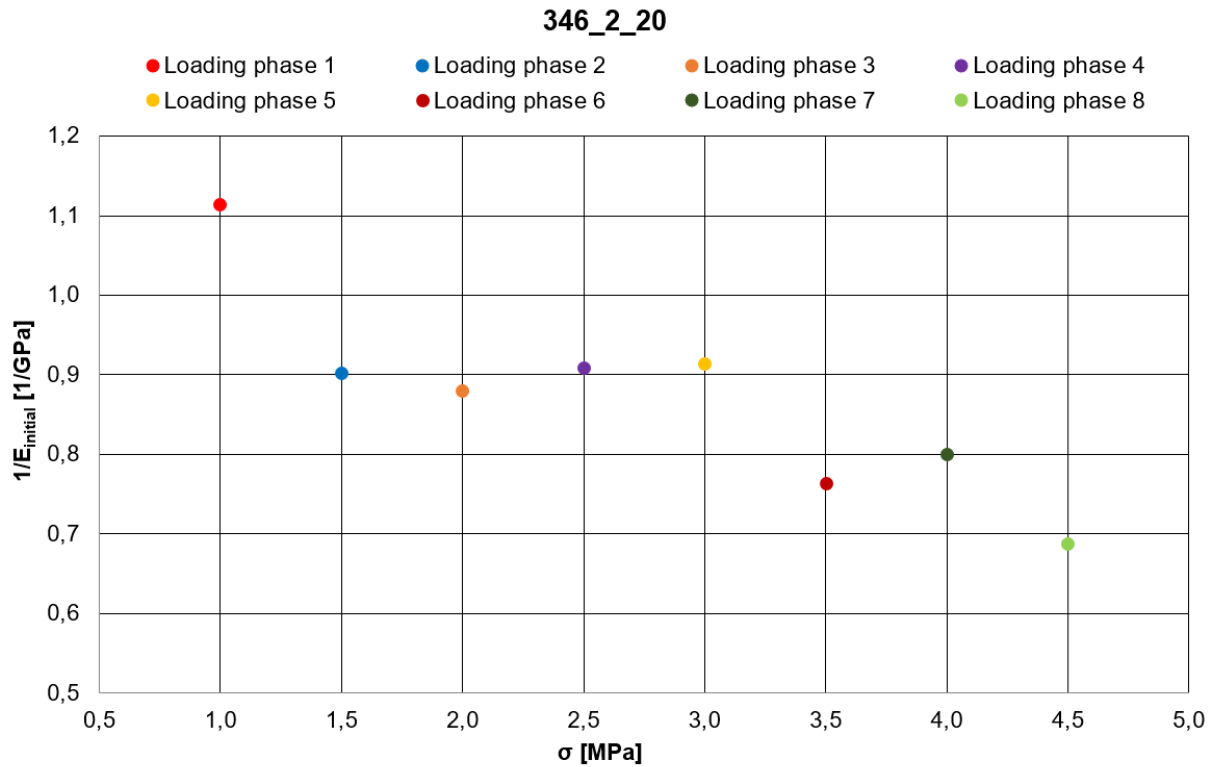


Figure 7.31: The inverse of the initial stiffness versus stress for all valid loading phases.

Table 7-6: Estimated values of initial stiffness for all valid loading phases.

Loading phase	$E_{initial}$ [GPa]
1	0,898
2	1,109
3	1,137
4	1,101
5	1,094
6	1,309
7	1,250
8	1,454

As the table shows, one can observe that the sample becomes stiffer throughout the test. The sample has increased approximately 38% in initial stiffness at the end compared to the beginning. This is looked upon as a natural development since applied stress causes escalation of grain contacts and cracks to close (Fjær et al. 2008). By using the obtained values of $E_{initial}$, one can further investigate how the consolidation time, τ_D , possibly is affected by alteration in the rocks' stiffness. As previously defined in section 2.3.2 (p.17),

$$\tau_D = \frac{l_D^2}{C_D} \quad (7.2)$$

Additionally, C_D is given by

$$C_D \rightarrow \frac{k}{\eta_f} \left(K_{fr} + \frac{4}{3} G_{fr} \right) \quad (7.3)$$

As one can see, the permeability k , the dynamic viscosity of the fluid η_f and the shear- and bulk modulus of the rock frame, G_{fr} and K_{fr} , directly influence the consolidation time. If one assumes that $E_{initial}$ is equivalent to the shear- and bulk modulus of the rock frame, one can investigate how C_D will change for different stiffness values;

$$C_D = \frac{k}{\eta_f} E_{initial} \quad (7.4)$$

Further, η_f is a parameter dependent on temperature, and since the temperature was assumed more or less constant during the test, one can presume this to be constant as well. It can be difficult to accurately predict how the permeability k will change for the loading phases throughout the test, but one can *estimate* the variation in this parameter by using the Carman-Kozeny equation. The equation is defined as (Dullien 1992)

$$k = \frac{\phi^3}{k_0 (L_e / L)^2 (1 - \phi)^2 S_A^2} \quad (7.5)$$

where ϕ is the porosity, k_0 is a shape factor, $(L_e / L)^2$ is the hydraulic “tortuosity factor” and S_A is the specific surface area based on the solid’s volume. Further, to obtain an impression of how the permeability varies, a simplified version where one assumes most of the parameters to be constant can be used

$$k = C \cdot \frac{\phi^3}{(1 - \phi)^2} \quad (7.6)$$

Also, to find the change in porosity between the loading phases, a modified version of Hooke’s law assuming infinite grain stiffness (only change in the pore volume) can be applied

$$\Delta\phi = -(1-\phi_{i-1})\Delta\varepsilon_z(1-2\nu) \quad (7.7)$$

where $\Delta\varepsilon_z$ is the vertical change in deformation during a loading phase and ν is Poisson ratio. Initially, the porosity of Pierre shale 346_2 is 20.8%, and Poisson ratio was assumed to be 0.7 (given by the supervisor). The results from using the equations above are presented in Table 7-7.

Table 7-7: Investigation of how the consolidation times are possibly affected by alteration in rock stiffness.

346_2_20							
Loading phase	$\Delta\varepsilon_z$	$\Delta\Phi$	Φ_{new}	k	E_{initial}	C_D	Relative τ_D
1	0,0006	0,00018	0,208	0,0143	0,898	12,84	1,00
2	0,0004	0,00012	0,208	0,0143	1,109	15,83	0,81
3	0,0004	0,00014	0,208	0,0142	1,137	16,19	0,79
4	0,0004	0,00013	0,207	0,0142	1,101	15,64	0,82
5	0,0004	0,00013	0,207	0,0142	1,094	15,51	0,83
6	0,0004	0,00012	0,207	0,0141	1,309	18,52	0,69
7	0,0004	0,00013	0,207	0,0141	1,250	17,65	0,73
8	0,0003	0,00010	0,207	0,0141	1,454	20,50	0,63

The results show that while initial stiffness increases throughout the test, the permeability decreases slightly. Consequently, the overall trend is that C_D increases and the consolidation time decreases. By looking at the relative difference in τ_D for the test (Figure 7.32), one can observe a declining trend. This analogy does not agree with the obtained trend for consolidation times found by using the graphical approach on a square root of time plot (Table 7-4 and Figure 7.28, p.91-92). However, one has to keep in mind that both approaches are based on different assumptions and simplifications that could potentially lead to deviating outcomes.

346_2_20

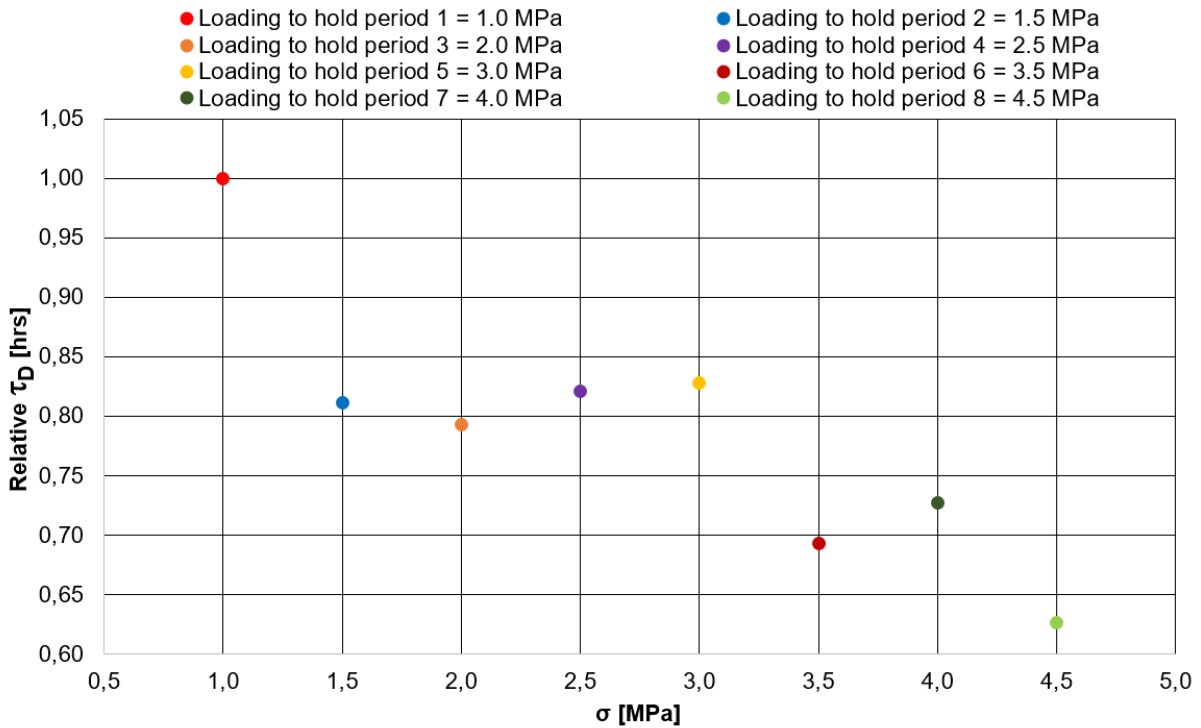


Figure 7.32: Relative difference in consolidation times versus stress throughout the test.

Finally, as mentioned earlier, an unfortunate incident took place at the end of this test. Smoke evolved from the experimental setup and set off the fire alarm. Investigating the cause afterwards showed that the thermocouple connected to the temperature controller (regulating the heating element) had most likely absorbed brine due to capillary suction and directed the fluid into the connection point between the thermocouple and the temperature controller. This affected the thermocouple and made it dysfunctional causing it to send wrong measurements to the temperature controller. Even if the temperature was actually 30°C, it most likely reported a much lower value. This resulted in continuous heat supply from the heating element trying to reach 30°C, but when it never got the recognition from the thermocouple it ended in an overheating and assumingly temperatures over 100°C (plastic melted). Some equipment in the experimental setup was damaged, but luckily, all measured data from the experiment was saved. Pictures from the incident can be found in Appendix XII (p.215).

Before the next test could start, countermeasures had to be implemented to avoid a similar incident and new equipment had to be acquired. To avoid capillary suction it was decided to

place the temperature controller and the thermocouple data logger at a somewhat elevated height in the experimental setup. Also, the new thermocouples used were molded indicating no chance for fluid flow inside the cables. Furthermore, a safety regulation was implemented into the temperature controller. An additional temperature sensor was placed at the same position as the thermocouple regulating the temperature controller to confirm its readings, causing the device to shut down if it measured a temperature above 33°C.

Overall, this test procedure (#4) and loading path (#4) resulted in a great collection of measured data for analysis. Based on this it was decided to proceed with the same approach for all upcoming creep experiments.

7.1.5 Core sample 346_2_23

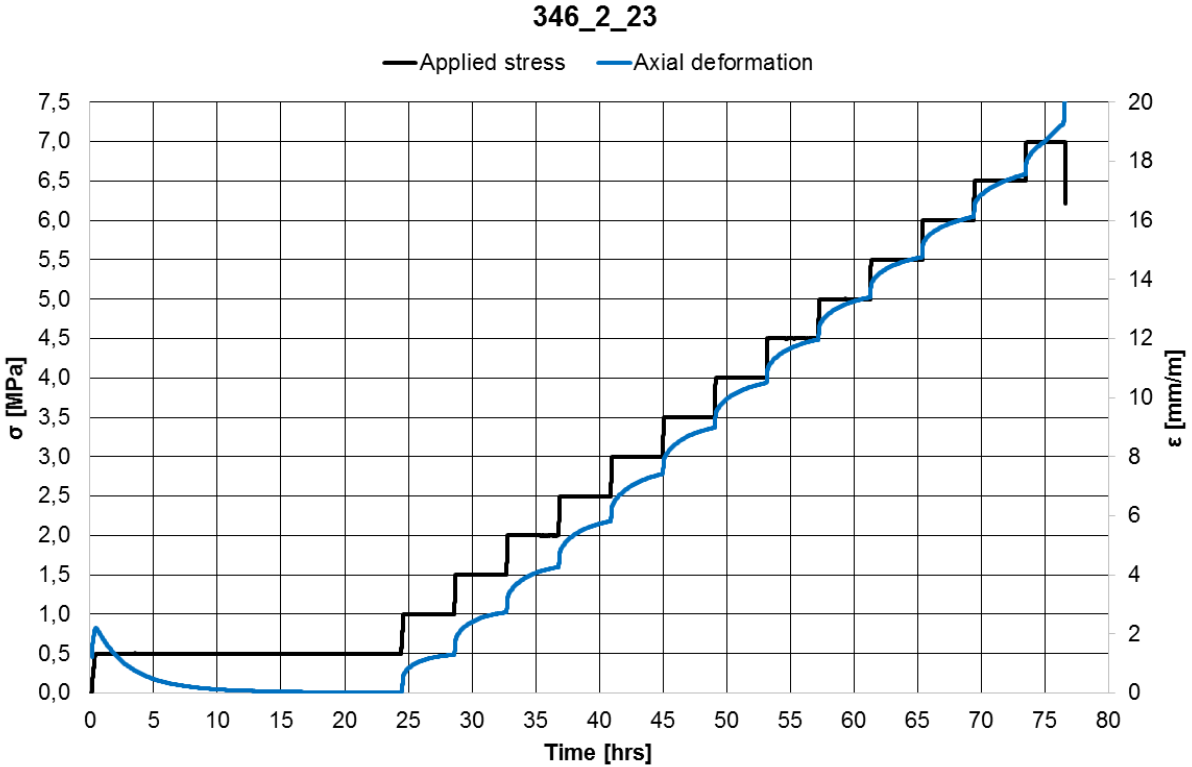


Figure 7.33: Overview of creep test conducted on 346_2_23.

The final creep test in brine ran successfully up to 13 load levels after completing ion diffusion for 24 hours. Failure of the sample occurred 3.10 hours after reaching 7.0 MPa, hence, only the first 12 hold periods are included for further discussion. The desired temperature for running the experiment was 30°C, but the results of the test showed an actual temperature around 28°C. The temperature controller had not functioned properly

for the past two tests (346_2_21, p.114 and 346_2_22, p.128), and even after small adjustments it was still not working optimally. However, it was an improvement from the last experiment (346_2_22); now showing only 2°C deviation from 30°C compared to 5°C. Overall, the maximum temperature variation during this creep test was 0.98°C.

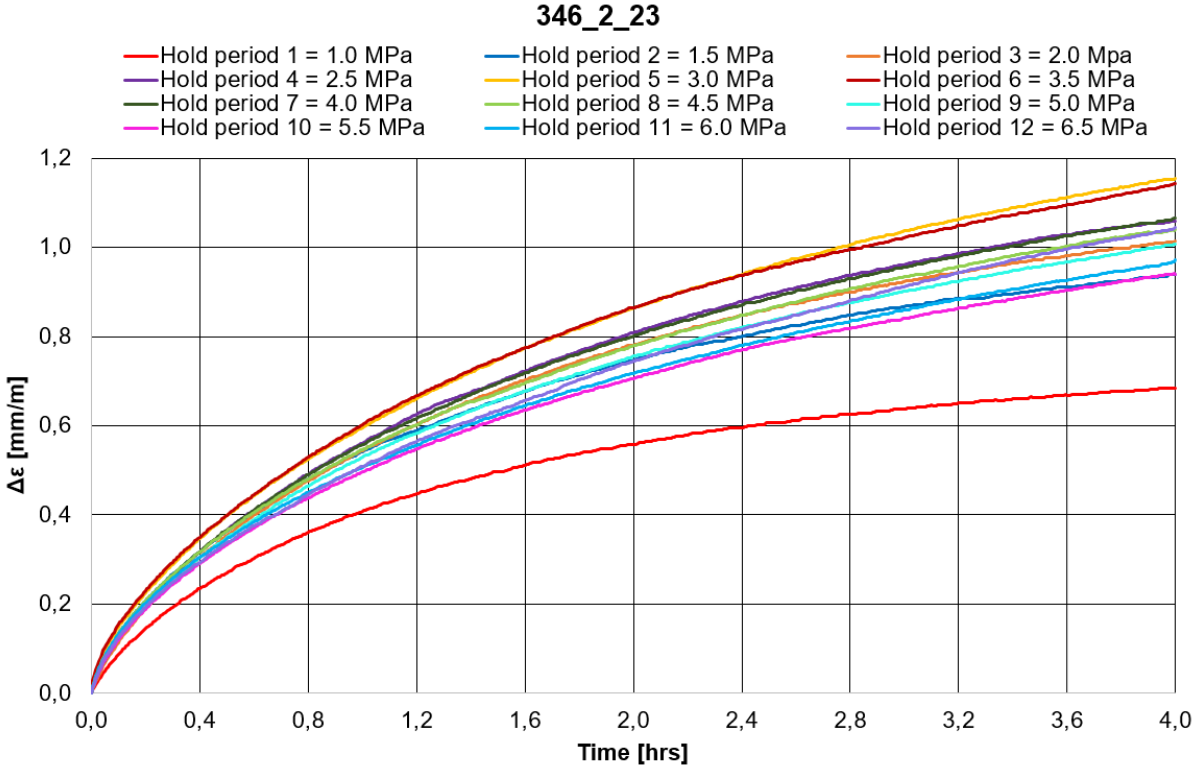


Figure 7.34: Strain versus time for all valid hold periods.

346_2_23

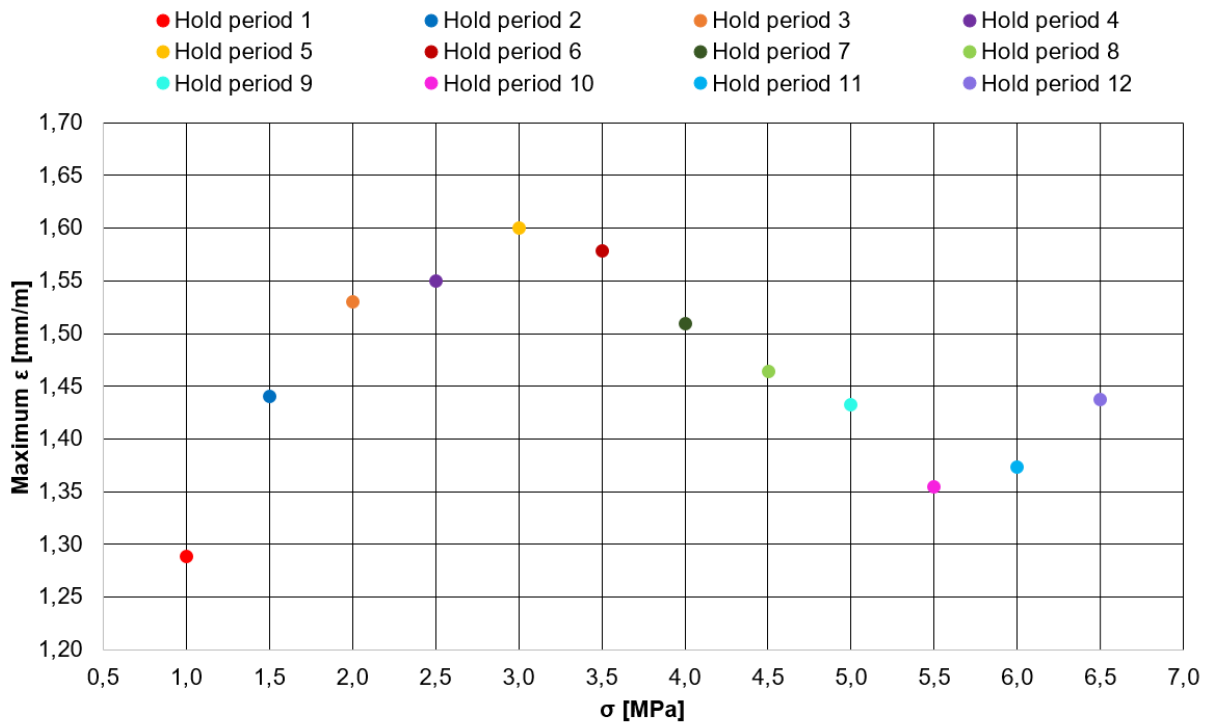


Figure 7.35: Maximum strain for a hold period versus stress level.

Obtained strain for all valid hold periods scaled to the same reference point (0,0) is presented in Figure 7.34. The amount of deformation increases with load for the first 5 hold periods, then declines for the following 5 before it eventually rises again for the remaining two. This is clearly illustrated in Figure 7.35, showing maximum strain for a hold period versus stress level. Since the duration of this particular test was relatively long, it could potentially give a good indication of Pierre shales' overall deformation trend in brine for Loading path 4 (p.58).

Looking at hold period 1 in Figure 7.34 and its deformation rates for certain time intervals in Table 7-8, demonstrates that it approaches stable behavior at the end. This is analogous with previous findings for low stresses. Further, it implies that the transition between *low* and *moderate* stress levels occurs somewhere between 1.0 MPa and 1.5 MPa. The latter stress level also seems to be the threshold value for reaching steady-state creep. As Table 7-8 shows, hold period 2 and 3, together with number 7, 9 and 12, reaches steady-state creep phase at the end. Further, a decreasing deformation rate is seen at the end of hold period 4, 5, 8 and 10 indicating transient creep phases. There is no defined creep phase in Table 7-8 at the end of hold period 6 and 11. Based on their deformation rates at the end, the creep

phases should have been defined as accelerating, but since their following periods are not accelerating it is highly unlikely that the relevant periods have entered this phase. This assumption is consistent with established theory showing that accelerating creep phase is the last stage before failure of a rock (Figure 2.7, p.16).

Table 7-8: Overview of deformation rates and creep phases at the end of the hold periods.

Hold period	Load [MPa]	Interval [hrs]						Creep phase at the end of hold period*
		0,0-1,0	1,0-2,0	2,0-3,0	3,0-3,5	3,5-3,75	3,75-4,0	
		Deformation rate [(mm/m)/hrs]						
1	1,0	0,408	0,150	0,080	0,051	0,047	0,038	Stable
2	1,5	0,543	0,204	0,121	0,076	0,071	0,064	Steady-state
3	2,0	0,545	0,237	0,143	0,097	0,086	0,078	Steady-state
4	2,5	0,561	0,247	0,152	0,119	0,085	0,066	Transient
5	3,0	0,596	0,269	0,172	0,127	0,115	0,097	Transient
6	3,5	0,602	0,263	0,157	0,123	0,111	0,126	-
7	4,0	0,557	0,245	0,153	0,118	0,104	0,100	Steady-state
8	4,5	0,547	0,233	0,154	0,117	0,106	0,083	Transient
9	5,0	0,530	0,226	0,146	0,109	0,103	0,099	Steady-state
10	5,5	0,497	0,210	0,134	0,107	0,098	0,085	Transient
11	6,0	0,506	0,212	0,141	0,118	0,100	0,114	-
12	6,5	0,509	0,236	0,167	0,144	0,121	0,119	Steady-state

*To distinguish between transient and steady-state creep phase at the end of a hold period, a threshold value, T_{cp} , representing the difference between the last two time intervals, was set for $T_{cp} \leq 0.01$. An increase in deformation rate between the last two time intervals exceeding the established T_{cp} was used to define accelerating creep.

346_2_23

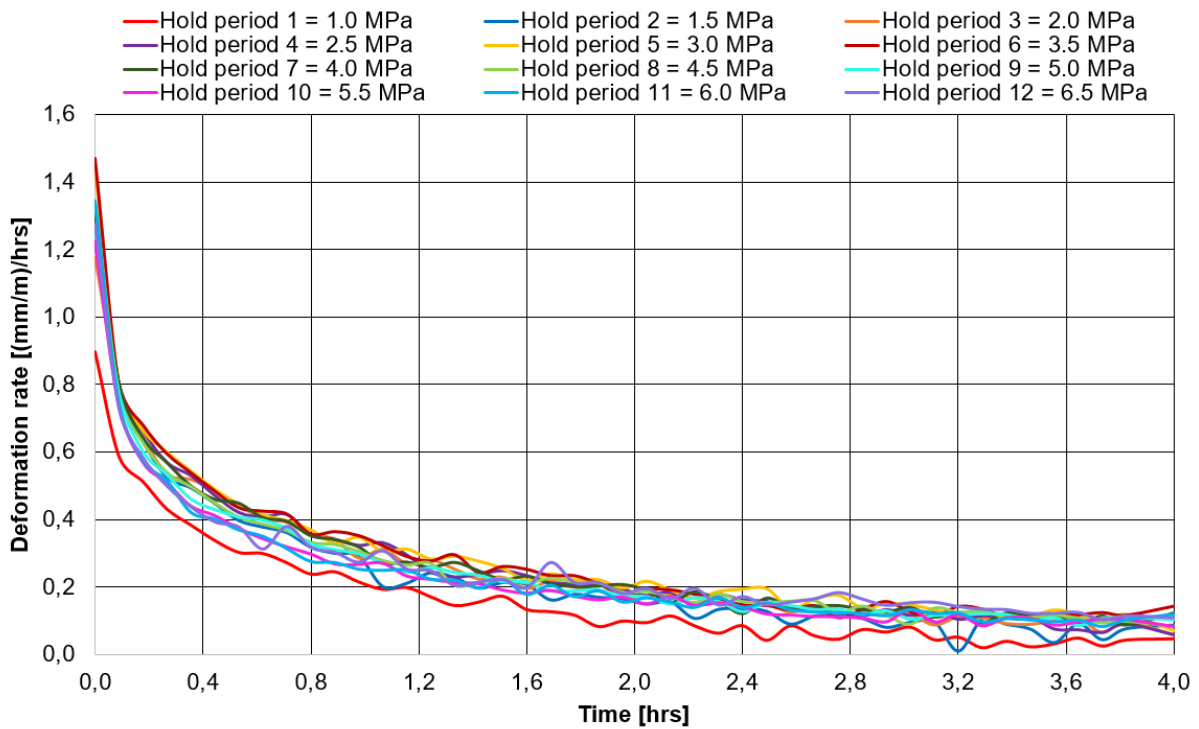


Figure 7.36: Continuous deformation rates in the valid hold periods.

Studying continuous deformation rates for the hold periods in Figure 7.36 illustrates a decreasing trend in the beginning of all periods, similar to the previous sample. Eventually, the decline is more subtle before stable rates occur for most of them. Only the first hold period stands out with the lowest rates while the other periods blend more or less together. The latter contradicts the theoretical expectation of higher deformation rates with increased stress. As mentioned earlier, the small variation might be caused by a consolidation dominating effect.

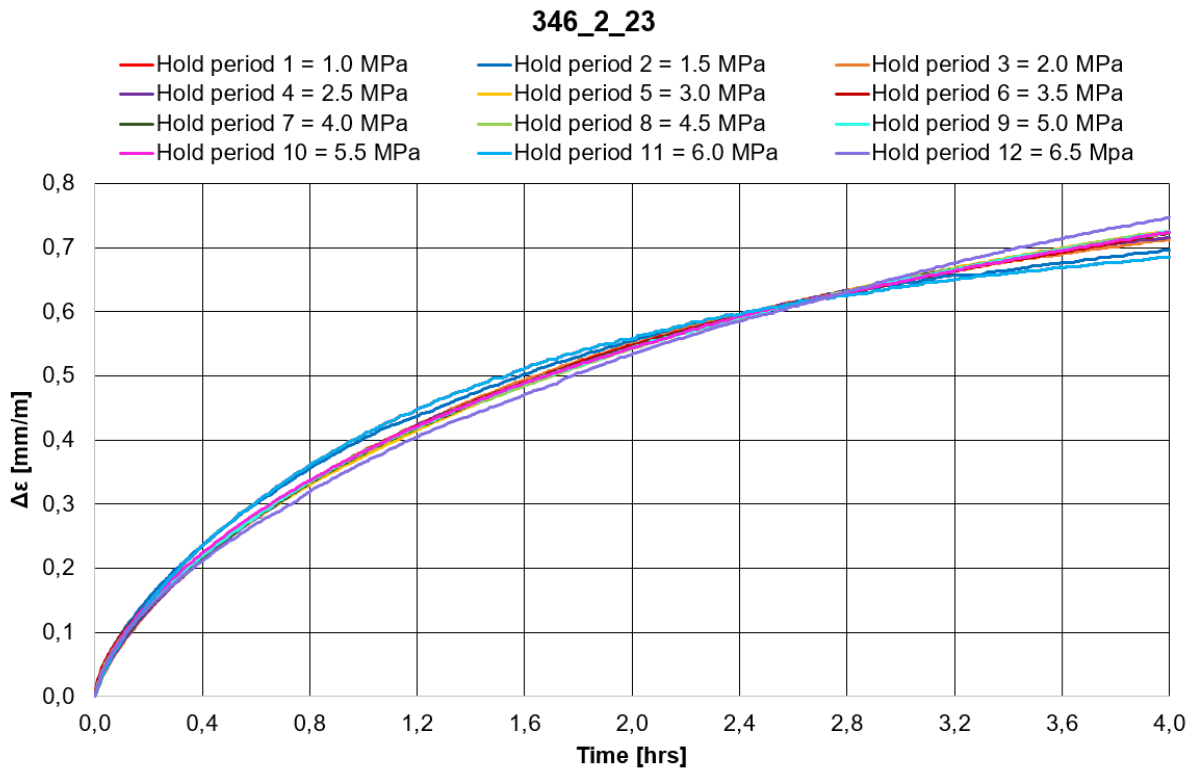


Figure 7.37: Attempt to scale the other hold periods down to hold period 1 with a scaling factor s .

Figure 7.37 presents the other hold periods scaled down to hold period 1 with a scaling factor s . Similar to the previous creep test in brine (346_2_20), one can observe that the shape of the curves vary for the hold periods. This indicates that the difference in deformation between them is not only dependent on an amplitude factor, but also affected by which time-dependent process that dominates; consolidation or creep.

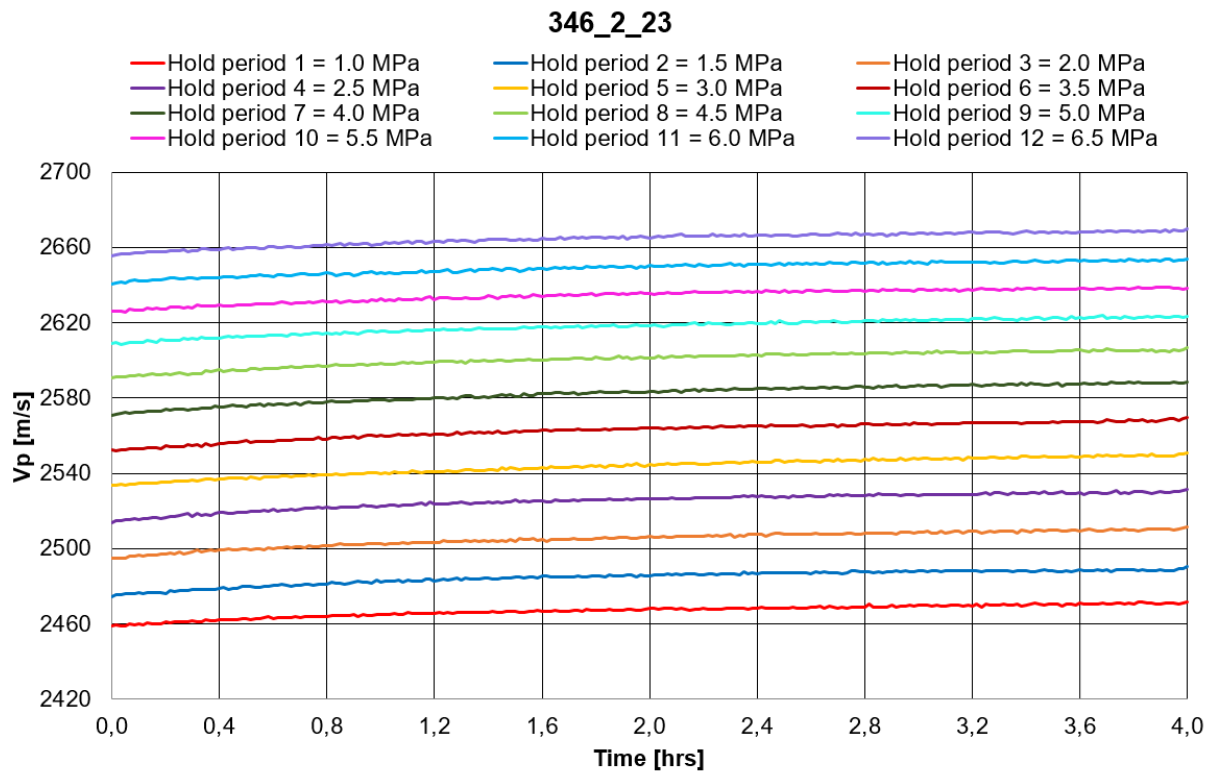
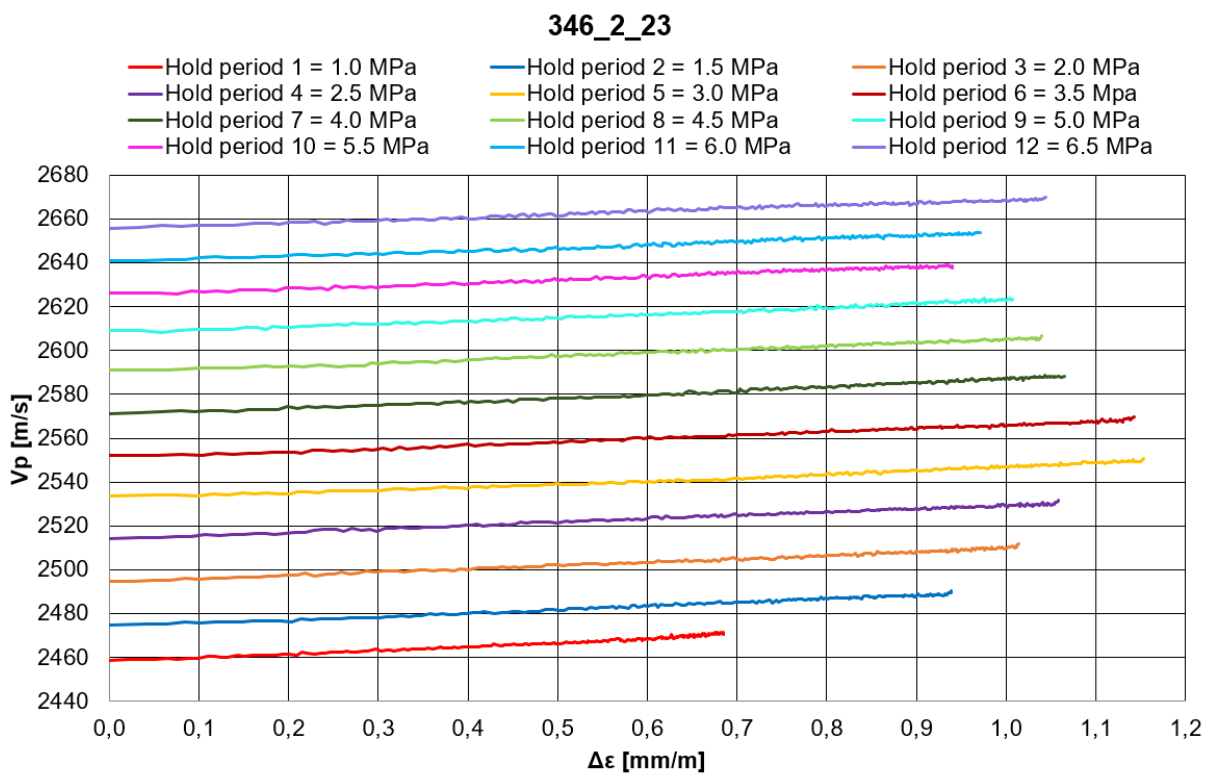
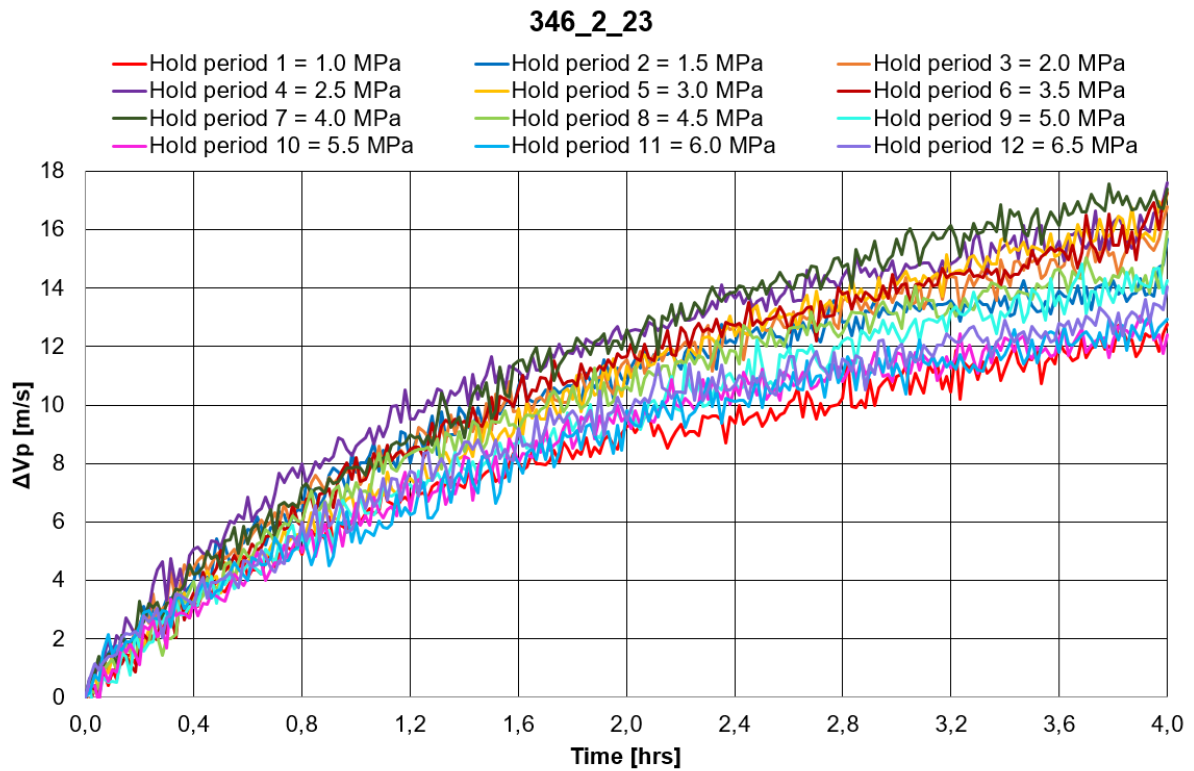


Figure 7.38: P-wave velocities in the valid hold periods.

Investigating p-wave velocities in the valid hold periods confirm the exact same trends as found for the previous sample in brine (346_2_20);

- the magnitude of the velocities rises with stress level (Figure 7.38)
- velocities increases with time for all hold periods (Figure 7.39)
- there is a close to linear dependency between p-wave velocities and strain in the periods with constant stress (Figure 7.40 and Figure 7.41)

Based on all this, one can assume that stress is not the only parameter affecting the p-wave velocities, it seems like strain is also a factor with significant impact.



346_2_23

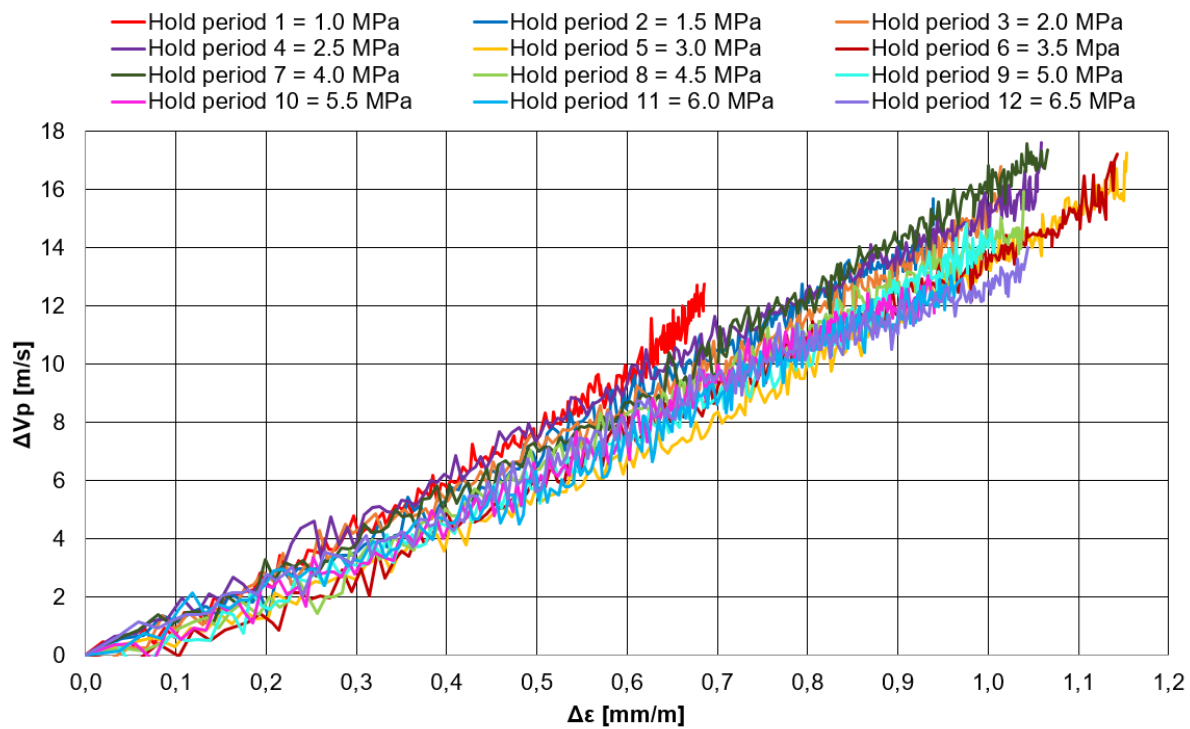


Figure 7.41: P-wave velocities versus deformation for the valid hold periods scaled to (0,0).

346_2_23

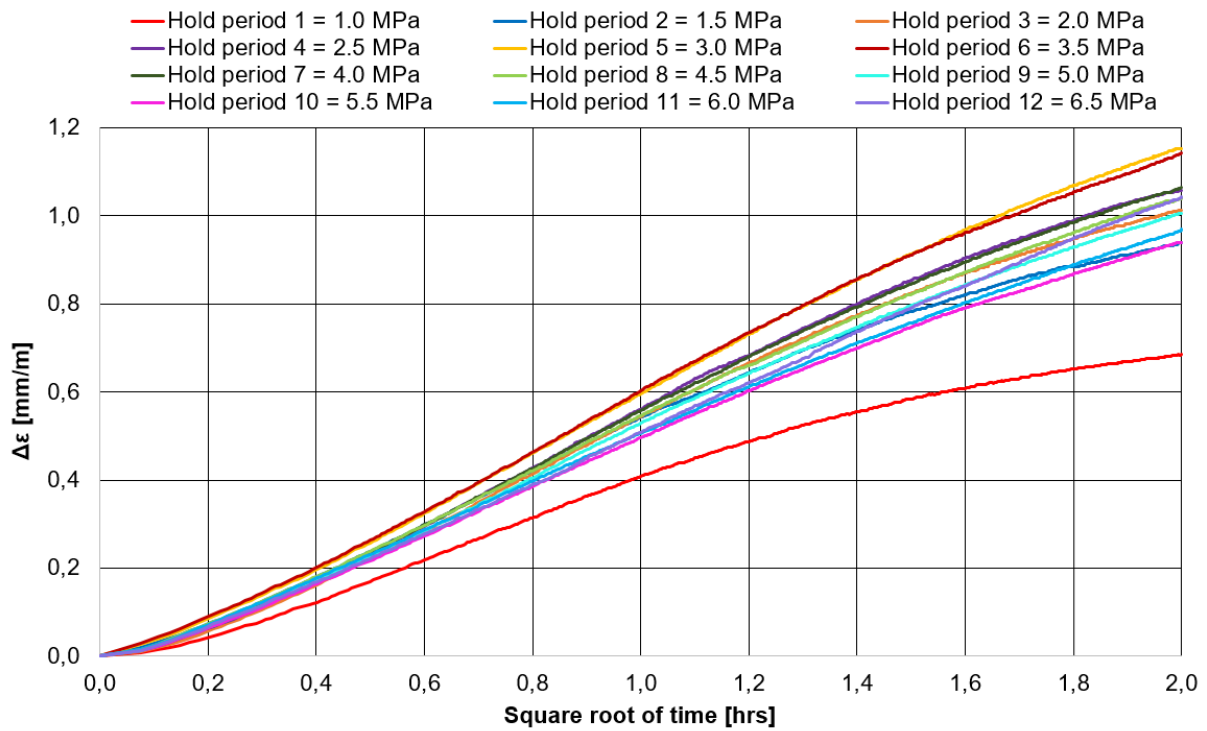


Figure 7.42: Strain versus square root of time for all valid hold periods.

Further, the graphical approach was applied on the obtained data in Figure 7.42 to acquire approximate consolidation times for the different hold periods. The results are presented in Table 7-9 and Figure 7.43, showing that the parameter ranges from 1.4-3.7 hours.

Table 7-9: Approximate consolidation times, τ_D , for different hold periods.

Hold period	Load [MPa]	Square root of time [hrs]	τ_D [hrs]
1	1,0	1,211	1,467
2	1,5	1,308	1,711
3	2,0	1,457	2,123
4	2,5	1,485	2,205
5	3,0	1,657	2,746
6	3,5	1,537	2,362
7	4,0	1,533	2,350
8	4,5	1,599	2,557
9	5,0	1,538	2,365
10	5,5	1,574	2,477
11	6,0	1,616	2,611
12	6,5	1,913	3,660

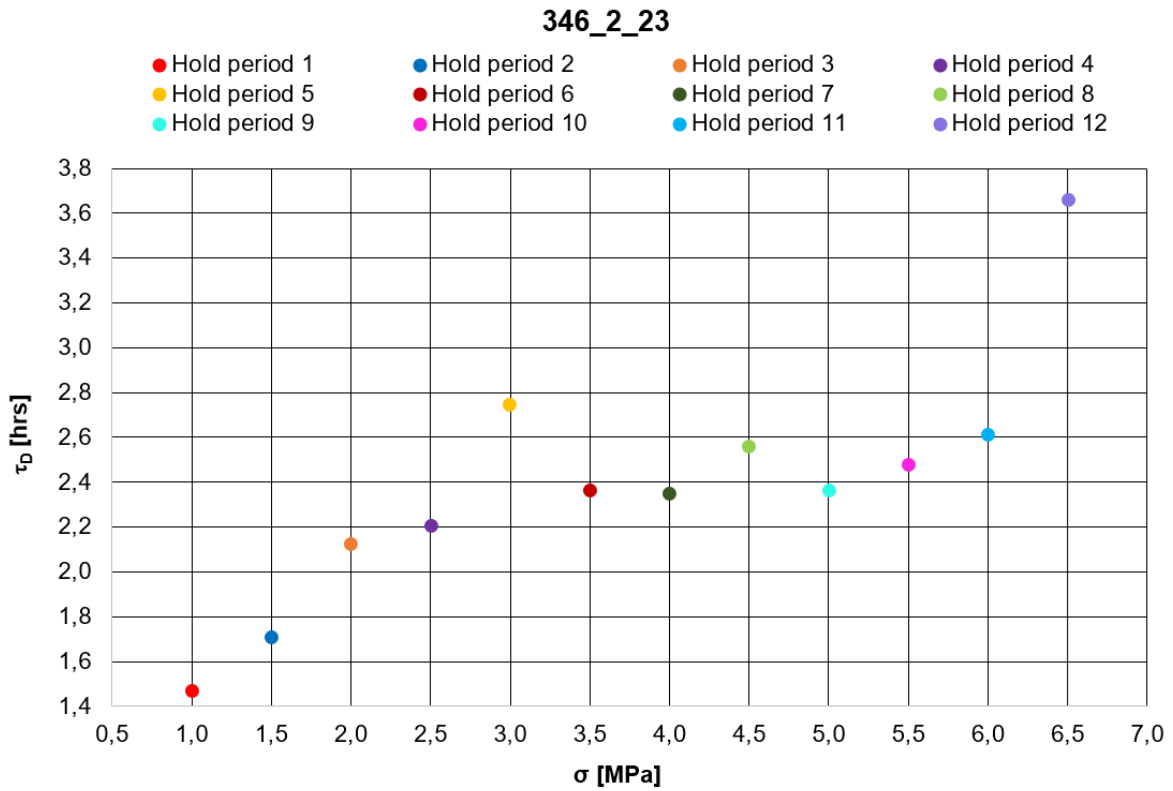


Figure 7.43: Approximate consolidation times for different hold periods.

Figure 7.43 demonstrates the approximate consolidation time for each stress level. As can be seen, it increases more or less linearly up to hold period 5 (with the exception of period 4), before it declines slightly and then rises again at the end.

346_2_23

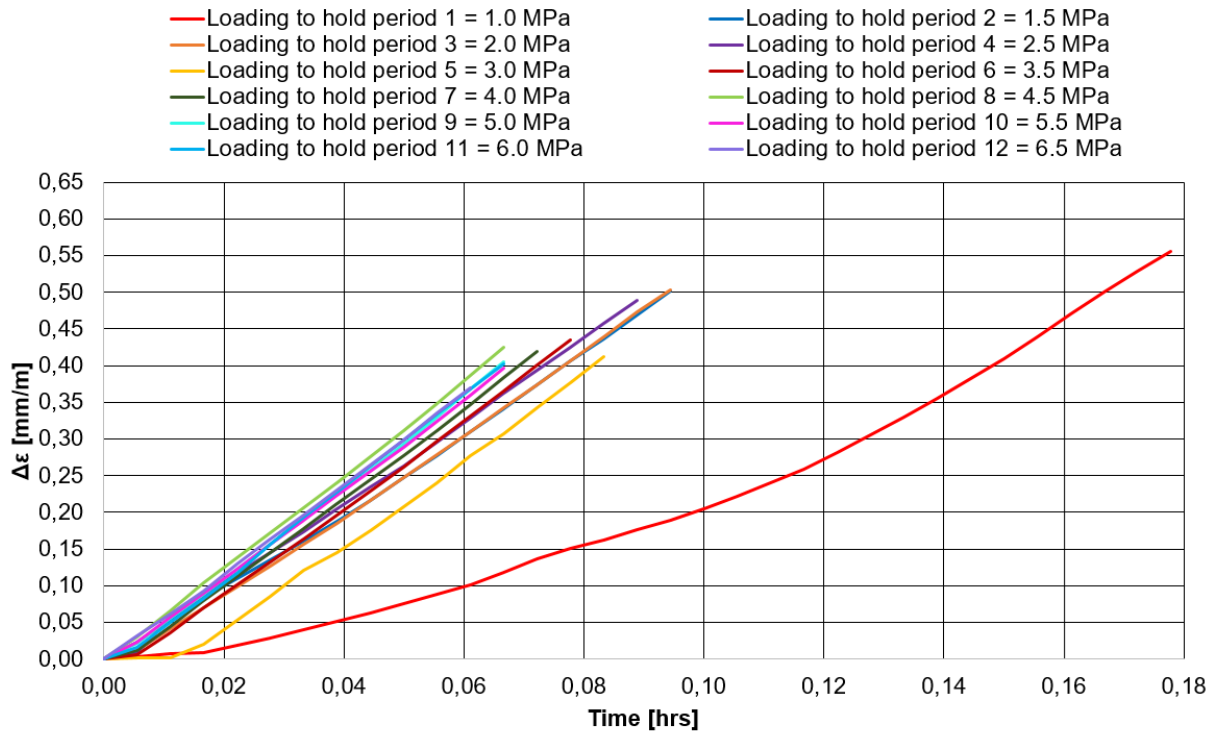


Figure 7.44: Initial deformation versus time for all valid loading phases.

Investigating strain for the *loading phases* (Figure 7.44) demonstrates the same findings as for the previous creep test in brine (346_2_20); the first phase stands out with a different shape of deformation curve compared to the others. One can observe that the amount of initial deformation varies for the different loading phases and the overall trend appears to be more or less that the amount of initial deformation decreases for increased stress level (Table 7-10).

Table 7-10: Maximum amount of strain for each loading phase.

346_2_23												
Loading phase	1	2	3	4	5	6	7	8	9	10	11	12
σ [MPa]	0,5-1,0	1,0-1,5	1,5-2,0	2,0-2,5	2,5-3,0	3,0-3,5	3,5-4,0	4,0-4,5	4,5-5,0	5,0-5,5	5,5-6,0	6,0-6,5
ϵ [mm/m]	0,556	0,502	0,503	0,489	0,413	0,435	0,420	0,424	0,405	0,396	0,402	0,370

To examine the variation in the rocks' stiffness, Figure 7.46, presenting $1/E_{initial}$ for the different loading phases versus σ , was used. The figure indicates a more or less linear decline in $1/E_{initial}$ throughout the test, implying an increase in the corresponding values of $E_{initial}$ (Table 7-11). The values of $1/E_{initial}$ were found by calculating the slopes of the curves in Figure 7.45.

346_2_23

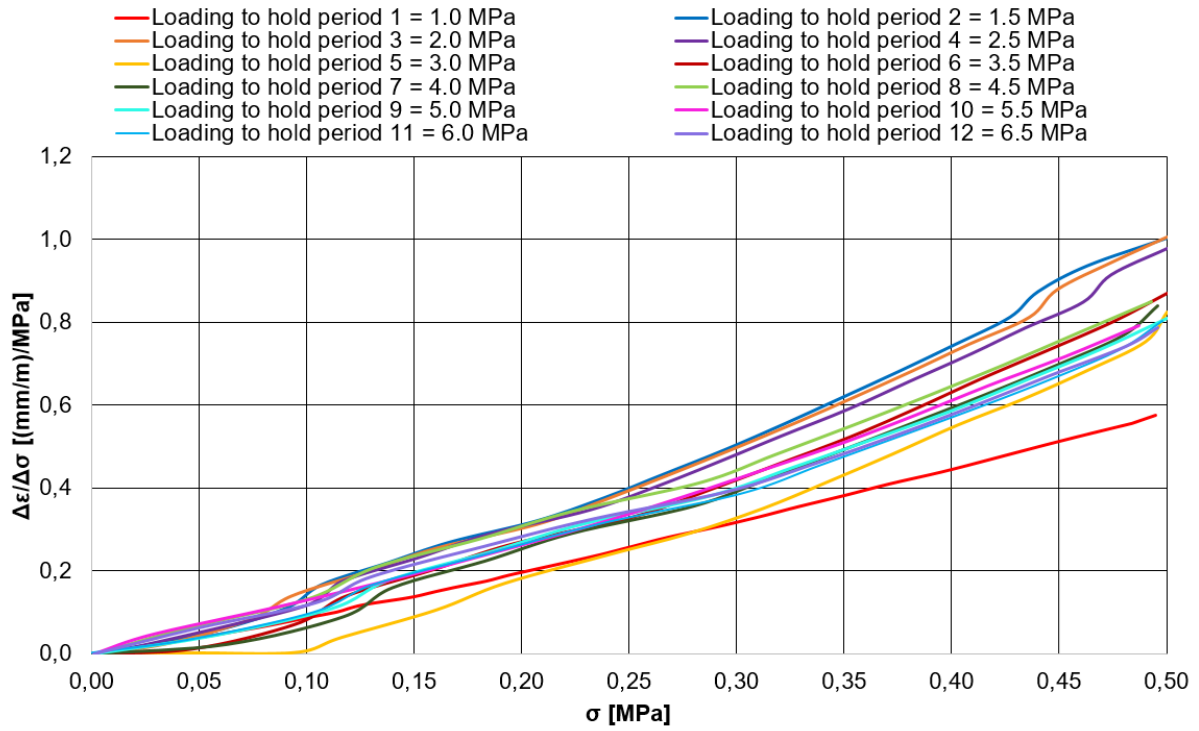


Figure 7.45: $\Delta\varepsilon/\Delta\sigma$ versus stress for all valid loading phases.

346_2_23

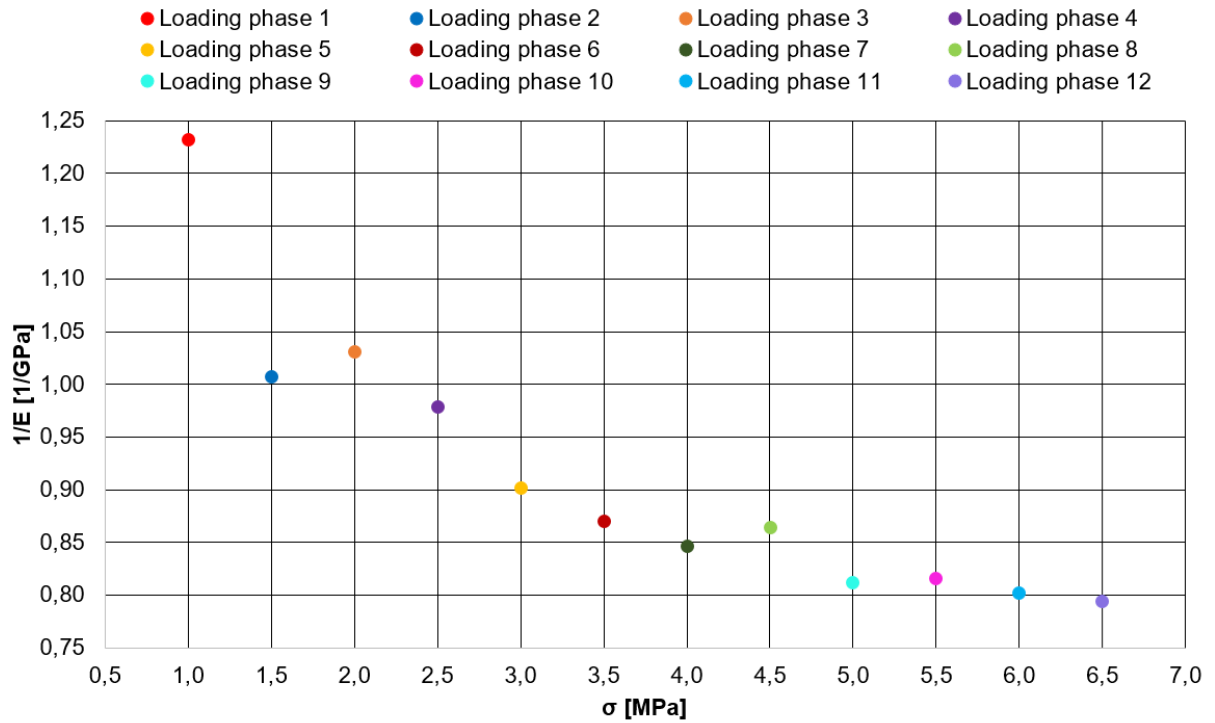


Figure 7.46: The inverse of the initial stiffness versus stress for all valid loading phases.

Table 7-11: Estimated values of initial stiffness for all valid loading phases.

Loading phase	$E_{initial}$ [GPa]
1	0,811
2	0,992
3	0,970
4	1,022
5	1,109
6	1,149
7	1,181
8	1,157
9	1,232
10	1,226
11	1,246
12	1,259

By looking at the results in Table 7-11, one can observe that the sample naturally becomes stiffer throughout the test. Compared to the first loading phase, the samples' initial stiffness has increased approximately 36% at the end. This is similar to the trend seen for the previous experiment in brine (346_2_20).

To further study how the consolidation times are possibly affected by variation in the rocks' stiffness, the values of $E_{initial}$ was used in combination with equations (7.2) to (7.7) (pp.96-97). The initial porosity and Poisson ratio of Pierre shale was set to 20.8% and 0.7 respectively, and the dynamic viscosity of the fluid η_f was assumed constant. Table 7-12 shows the obtained results.

Table 7-12: Investigation of how the consolidation times are possibly affected by alteration in rock stiffness.

346_2_23							
Loading phase	$\Delta\varepsilon_z$	$\Delta\Phi$	Φ_{new}	k	$E_{initial}$	C_D	Relative τ_D
1	0,0006	0,00019	0,208	0,0143	0,811	11,60	1,00
2	0,0005	0,00016	0,208	0,0143	0,992	14,15	0,82
3	0,0005	0,00016	0,207	0,0142	0,970	13,79	0,84
4	0,0005	0,00016	0,207	0,0142	1,022	14,50	0,80
5	0,0004	0,00014	0,207	0,0142	1,109	15,69	0,74
6	0,0004	0,00014	0,207	0,0141	1,149	16,22	0,72
7	0,0004	0,00013	0,207	0,0141	1,181	16,64	0,70
8	0,0004	0,00013	0,207	0,0141	1,157	16,26	0,71
9	0,0004	0,00013	0,207	0,0140	1,232	17,27	0,67
10	0,0004	0,00013	0,207	0,0140	1,226	17,15	0,68
11	0,0004	0,00013	0,206	0,0140	1,246	17,40	0,67
12	0,0004	0,00012	0,206	0,0139	1,259	17,54	0,66

As the results shows, while initial stiffness increases throughout the test the permeability decreases slightly. Accordingly, C_D increases and the consolidation time decreases. By looking at the relative difference in τ_D for the test (Figure 7.47), one once again observes a declining trend as found for the previous test in brine (346_2_20).

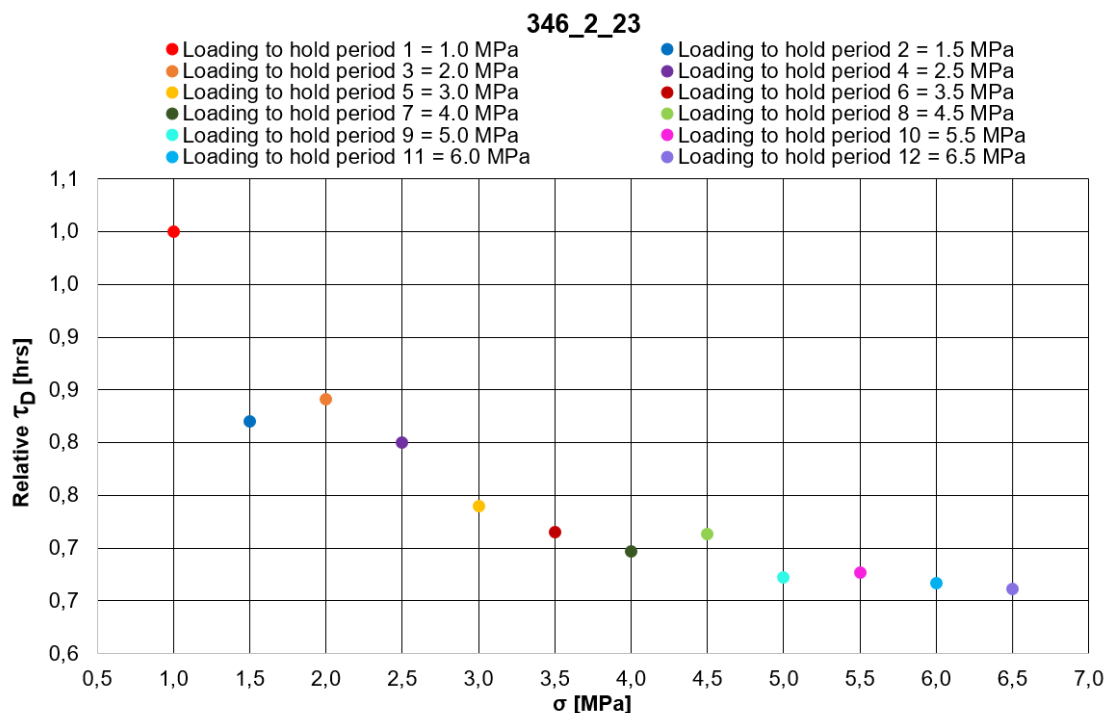


Figure 7.47: Relative difference in consolidation times versus stress throughout the test.

7.2 Creep tests with reduced pore fluid pH

Both creep tests with reduced pore fluid pH used a mixture of 3.5wt% $NaCl(aq)$ and 0.00125% $HCl(aq)$ as the fluid surrounding the core samples. The fluid itself had a pH value of 3.14 and a chemical activity of 0.938.

7.2.1 Core sample 346_2_21

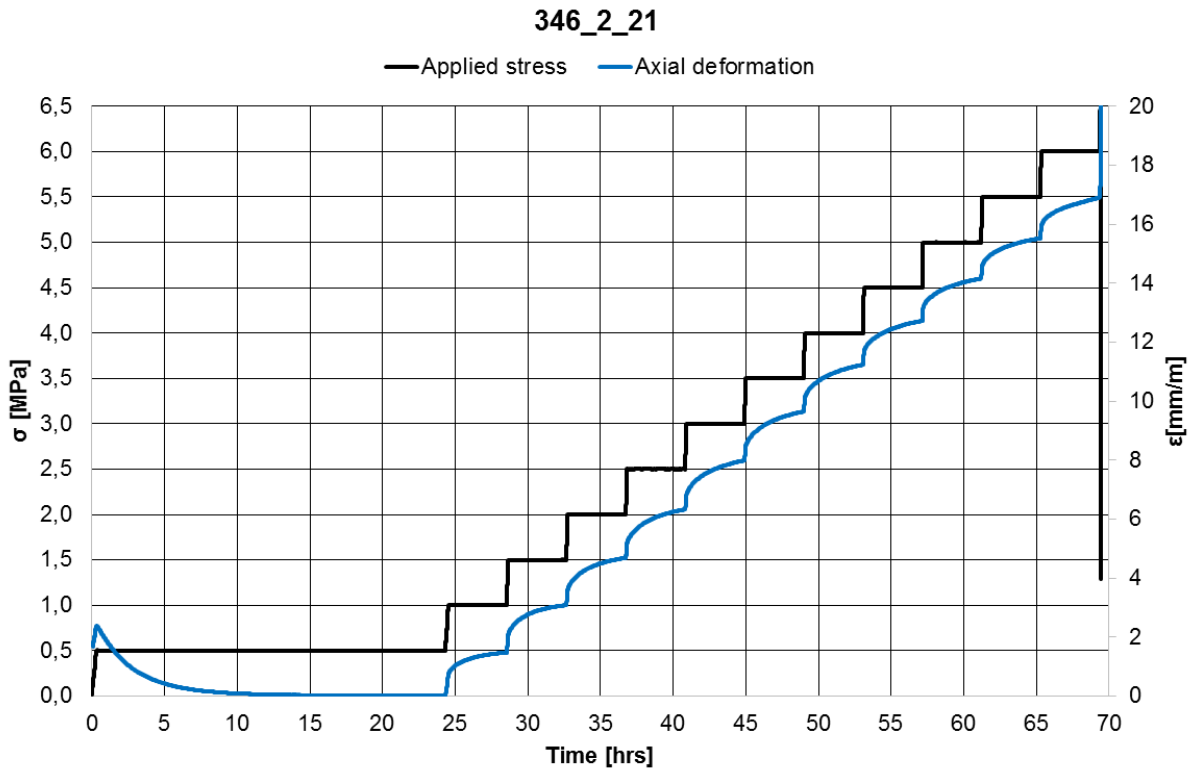


Figure 7.48: Overview of creep test conducted on 346_2_21.

The first creep test in a mixture of brine and $HCl(aq)$ ran successfully up to 12 load levels after completing ion diffusion for 24 hours. Failure of the sample occurred immediately after loading to 6.5 MPa. Thus, only the first 11 hold periods are included for further discussion. Due to a damaged temperature controller in 346_2_20, a new and modified device was installed for this test. Initially, the temperature controller was set for 30°C, but the results showed an actual temperature around 27°C, which was not optimal. This was 3°C below the desired temperature, and probably caused by the new temperature installation. Overall, the maximum temperature variation during the creep test was 0.83°C.

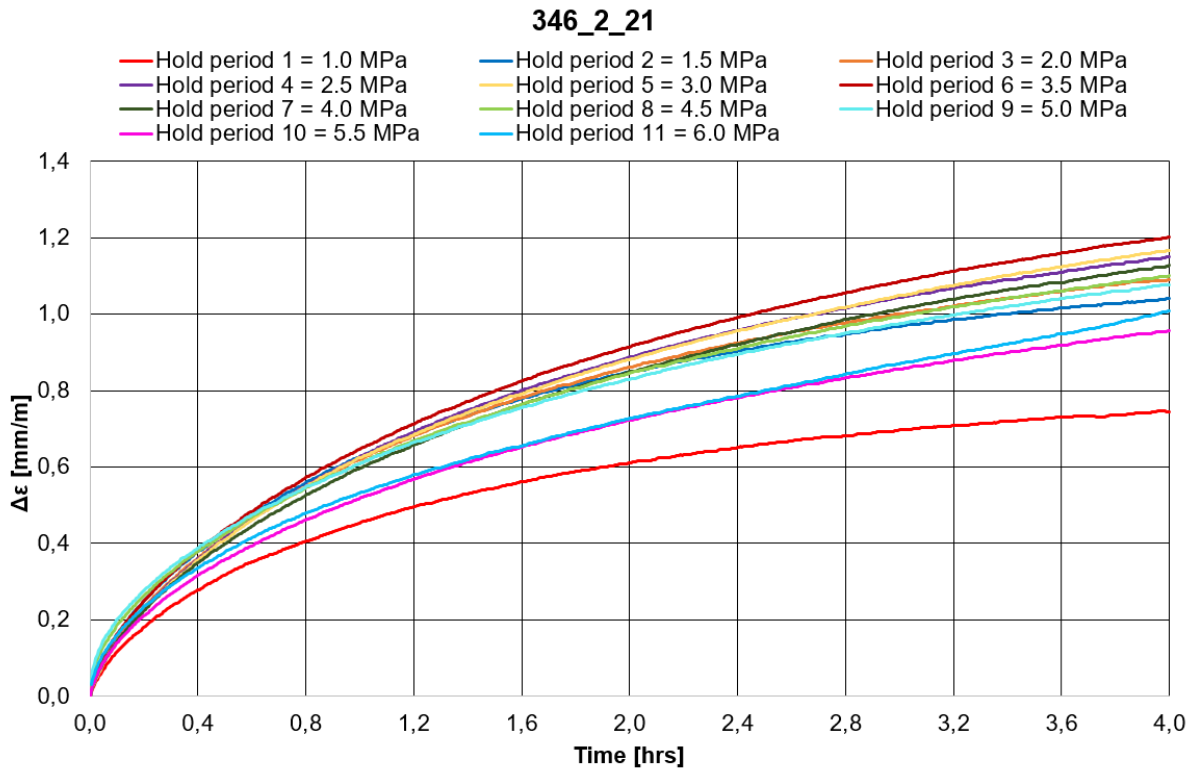


Figure 7.49: Strain versus time for all valid hold periods.

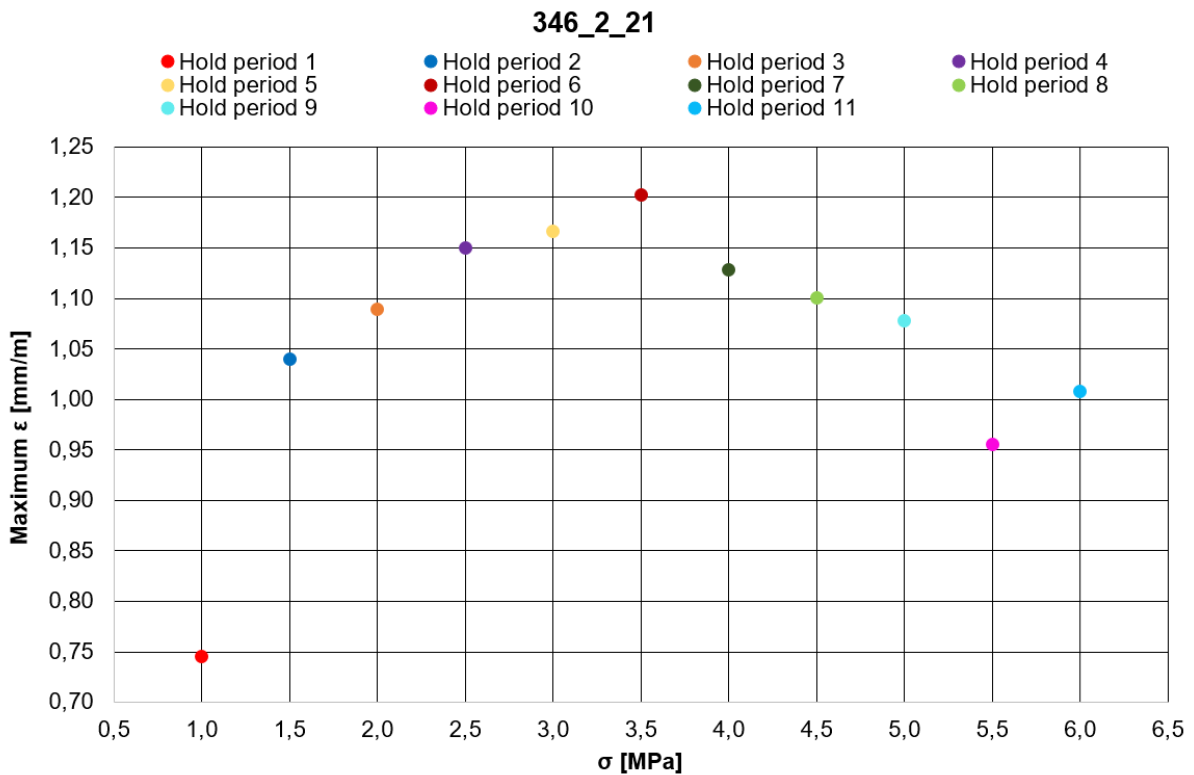


Figure 7.50: Maximum strain for a hold period versus stress level.

By investigating obtained strain for all valid hold periods scaled to the same reference point (0,0) (Figure 7.49), one can observe that the amount of strain increases with load for the first 6 hold periods, decreases for the following 5 and then rises again for the last period before failure. Figure 7.50 illustrates this more clearly by showing maximum strain for a hold period versus stress.

Comparing the deformation rates in Figure 7.51 for certain time intervals (Table 7-13), shows that the low load levels in hold period 1 and 2 approaches stable behavior after a period of transient creep. This agrees with previous findings for low stresses and causes the transition from *low* to *moderate* stress levels for the sample to occur somewhere between 1.5 MPa and 2.0 MPa. Further, the threshold for reaching steady-state creep seems to be 2.5 MPa. As Table 7-13 demonstrates, the deformation rates varies for hold period 3, 5 and 6 at the end implying that these are still in transient creep phase. This indicates that 4 hours might be a too short time period to initiate the other phases of creep for these load levels. The deformation rates for hold period 4, 7, 8, 9 and 10 are more or less constant the last 30 min, suggesting that the creep phase has transitioned from transient to steady-state. For hold period 11, the deformation rate increases with time at the end, implying accelerating creep phase. Eventually, this lead to failure of the sample only minutes later.

Table 7-13: Overview of deformation rates and creep phases at the end of the hold periods.

Hold period	Load [MPa]	Interval [hrs]						Creep phase at the end of hold period*
		0,0-1,0	1,0-2,0	2,0-3,0	3,0-3,5	3,5-3,75	3,75-4,0	
		Deformation rate [(mm/m)/hrs]						
1	1,0	0,454	0,157	0,086	0,055	-	0,058	Stable
2	1,5	0,626	0,224	0,118	0,079	0,065	0,066	Stable
3	2,0	0,619	0,242	0,139	0,098	0,089	0,070	Transient
4	2,5	0,627	0,260	0,157	0,112	0,103	0,100	Steady-state
5	3,0	0,624	0,257	0,168	0,125	0,119	0,102	Transient
6	3,5	0,647	0,267	0,171	0,125	0,121	0,098	Transient
7	4,0	0,597	0,253	0,164	0,121	0,107	0,111	Steady-state
8	4,5	0,609	0,236	0,148	0,119	0,093	0,098	Steady-state
9	5,0	0,609	0,221	0,145	0,110	0,095	0,096	Steady-state
10	5,5	0,518	0,205	0,134	0,107	0,095	0,089	Steady-state
11	6,0	0,532	0,196	0,143	0,128	0,136	0,159	Accelerating

*To distinguish between transient and steady-state creep phase at the end of a hold period, a threshold value, T_{cp} , representing the difference between the last two time intervals, was set for $T_{cp} \leq 0.01$. An increase in deformation rate between the last two time intervals exceeding the established T_{cp} was used to define accelerating creep.

346_2_21

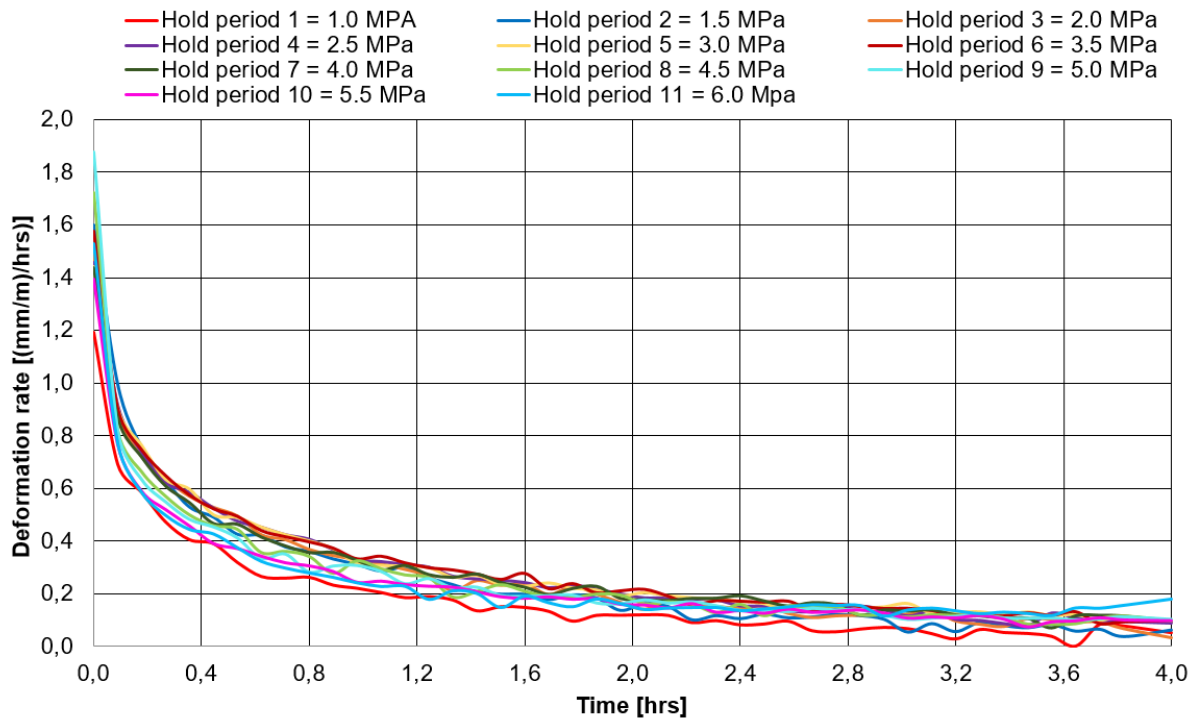


Figure 7.51: Continuous deformation rates in the valid hold periods.

Looking at continuous deformation rates for the hold periods in Figure 7.51 shows a decreasing trend in the beginning of all hold periods, confirming transient creep phase. Later, the decline is more subtle before stable rates occur for most of them. Generally, the overall variation between the curves in this test is small. One typically assumes that increased stress results in higher deformation rates, but as seen here, the first hold period is the only one who adapts to that philosophy. The remaining periods blend more or less together and the reason behind this might be caused by a consolidation dominating effect. Finally, hold period 11 stands out at the end with a sudden increase in deformation rate compared to the others due to accelerated creep phase.

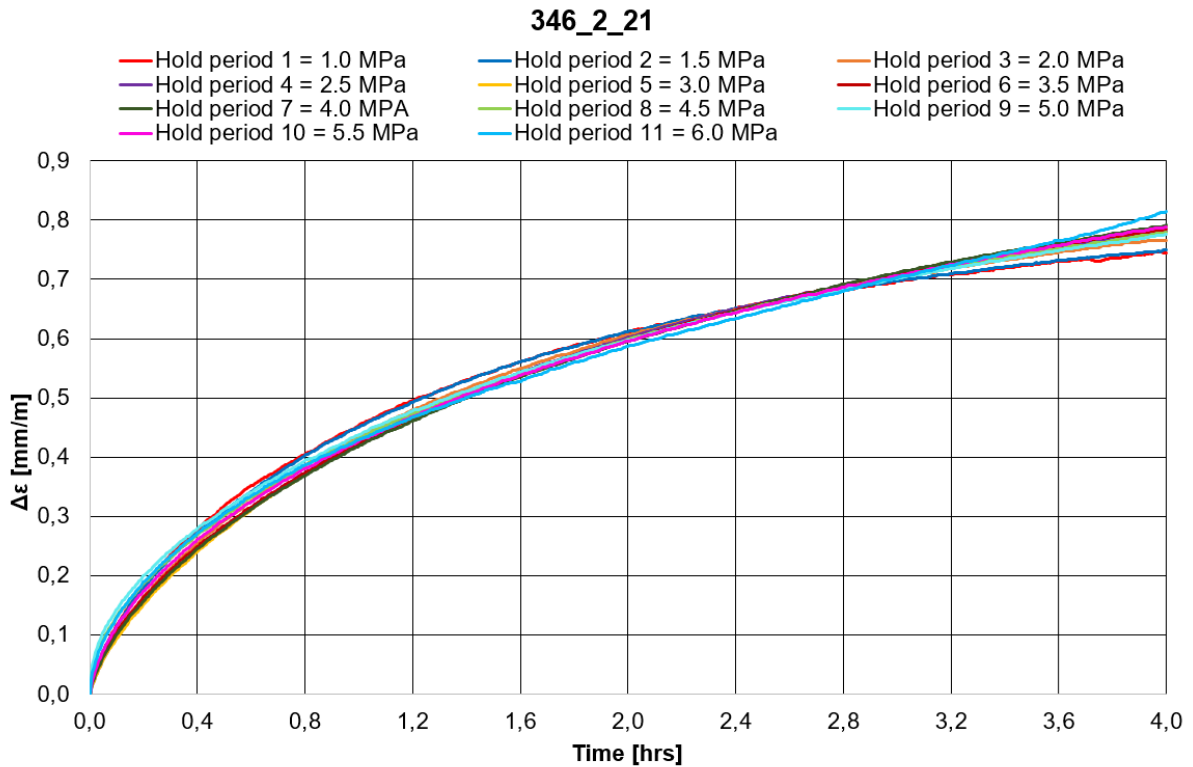
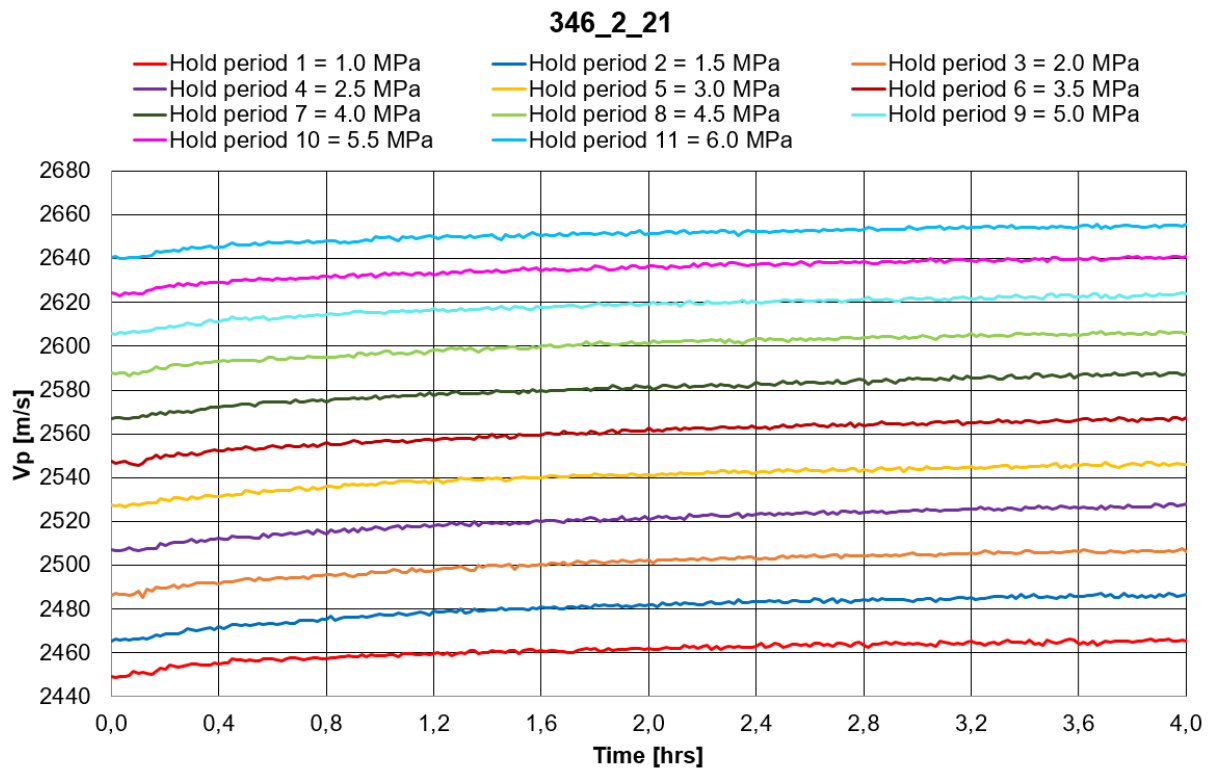
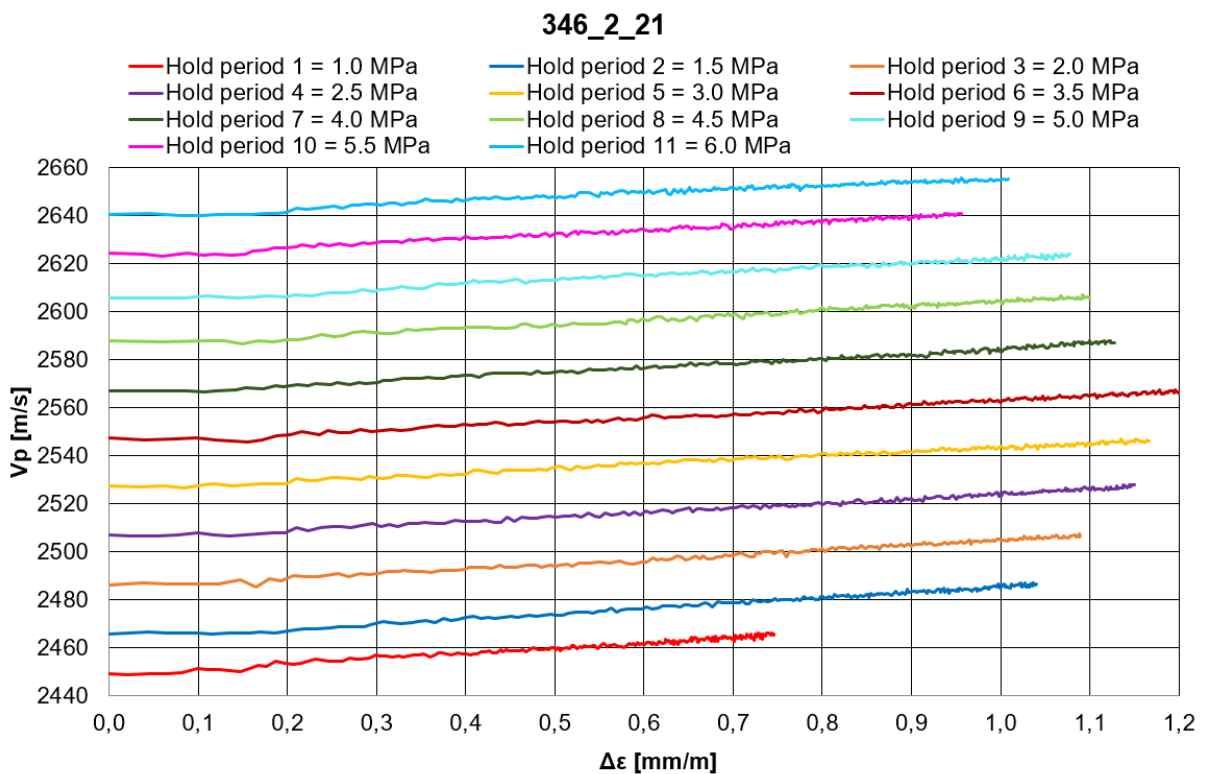
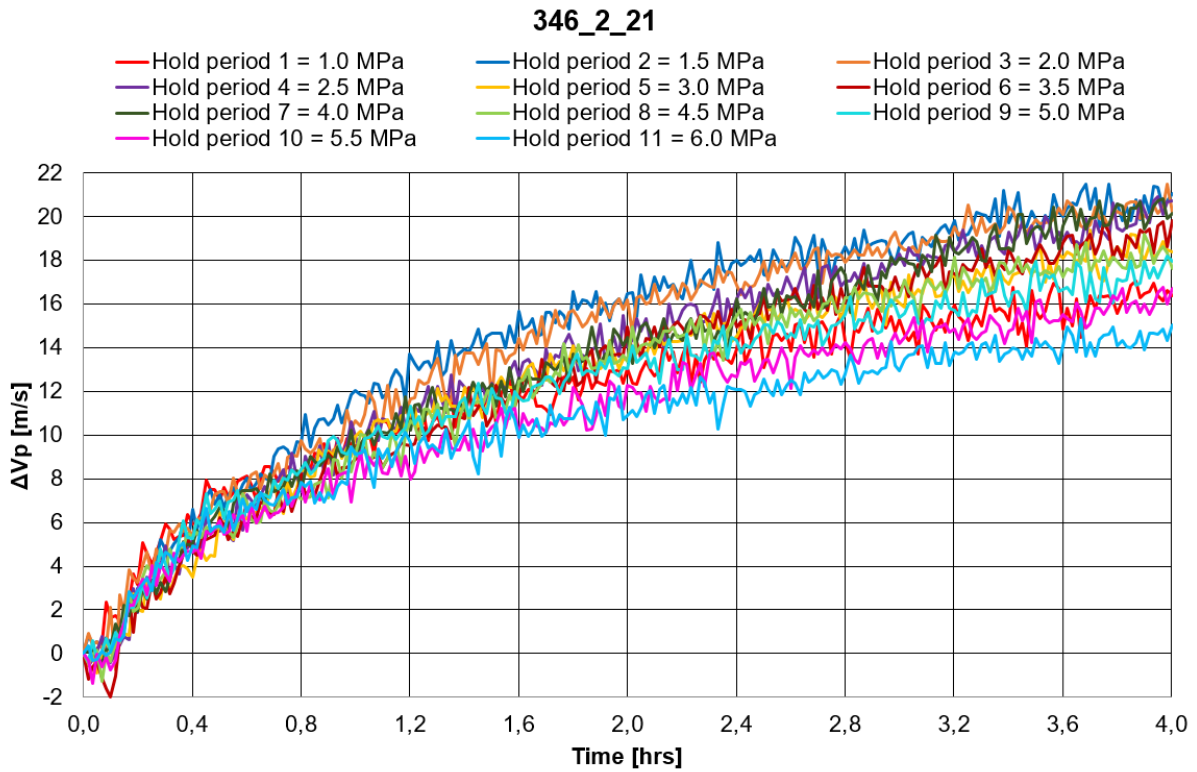


Figure 7.52: Attempt to scale the other hold periods down to hold period 1 with a scaling factor s .

Scaling the other hold periods down to hold period 1 with a scaling factor s , demonstrates that the shape of the curves are somewhat similar for most parts of the time interval. This illustrates that the difference in deformation between them is mainly dependent on an amplitude factor. Further, these observations suggest that consolidation and creep are roughly dominating for the same periods in the different hold periods.



Looking at the p-wave velocities for all valid hold periods (Figure 7.53) shows that the magnitude of the velocities increases with applied stress. Further, by investigating the p-wave velocities scaled to the same reference point (0,0) (Figure 7.54), it can be seen that velocities increase with time in the hold periods. Also, a close to linear dependency between p-wave velocities and deformation can be observed when studying Figure 7.55. This is later confirmed in Figure 7.56 (the same plot as Figure 7.55, only scaled to (0,0)), implying that the velocities are more or less a linear function of strain in the hold periods. This is consistent with previous findings and indicates that p-wave velocities are sensitive to strain as well as stress.



346_2_21

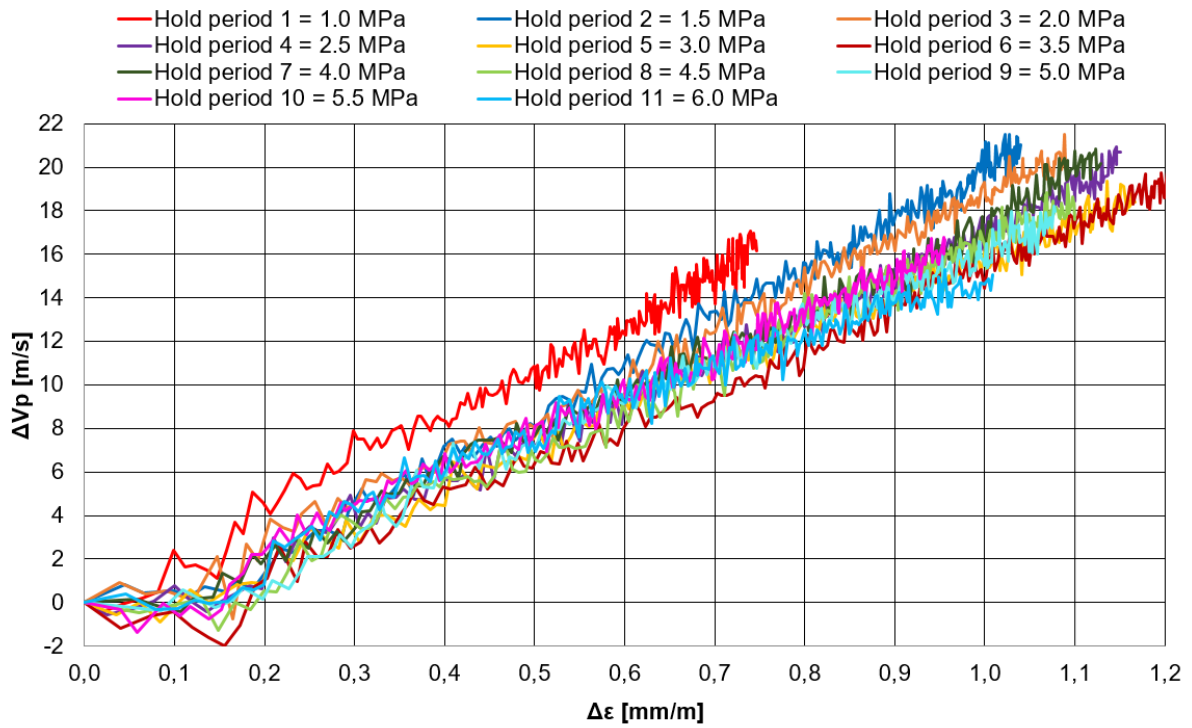
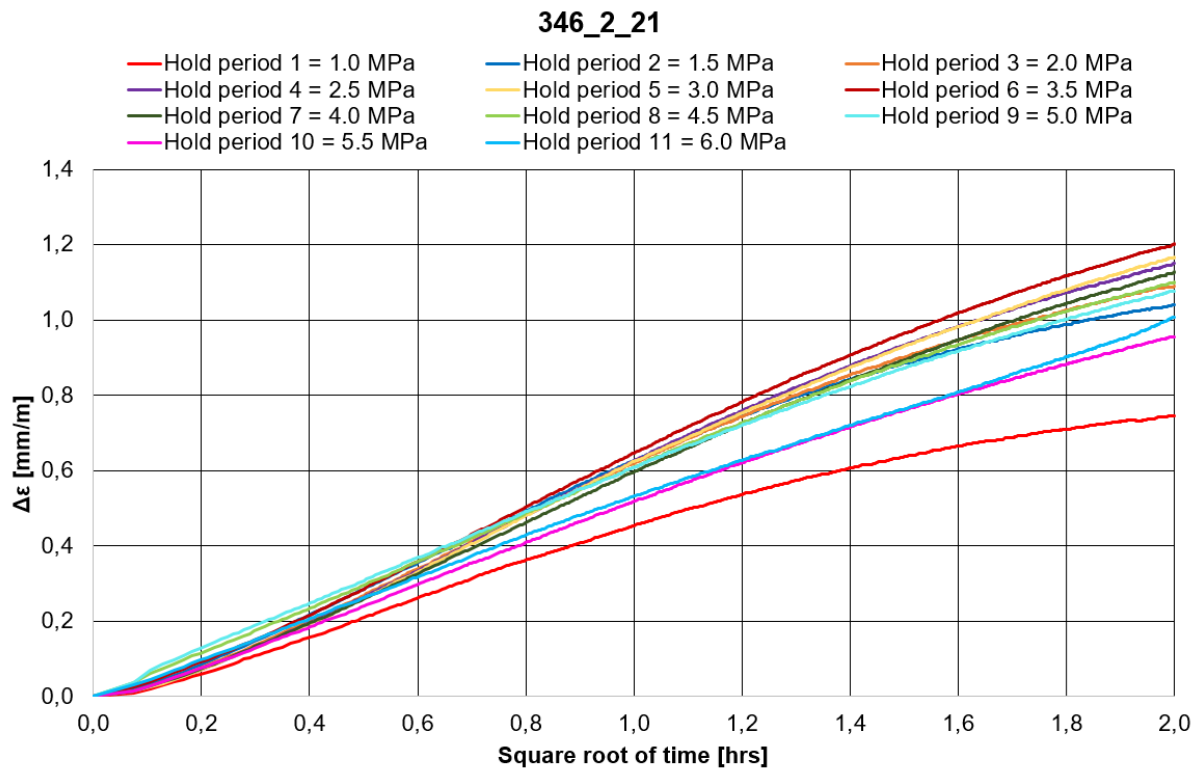


Figure 7.56: P-wave velocities versus deformation for the valid hold periods scaled to (0,0).



Furthermore, the approximate consolidation times for the different hold periods were found by applying the graphical approach. The results are presented in Table 7-14 and Figure 7.58, and shows that the parameter ranges from 1.2-2.3 hours.

Table 7-14: Approximate consolidation times, τ_D , for different hold periods.

Hold period	Load [MPa]	Square root of time [hrs]	τ_D [hrs]
1	1,0	1,108	1,228
2	1,5	1,227	1,506
3	2,0	1,267	1,605
4	2,5	1,352	1,828
5	3,0	1,386	1,921
6	3,5	1,420	2,016
7	4,0	1,476	2,179
8	4,5	1,502	2,256
9	5,0	1,491	2,223
10	5,5	1,493	2,229
11	6,0	1,436	2,062

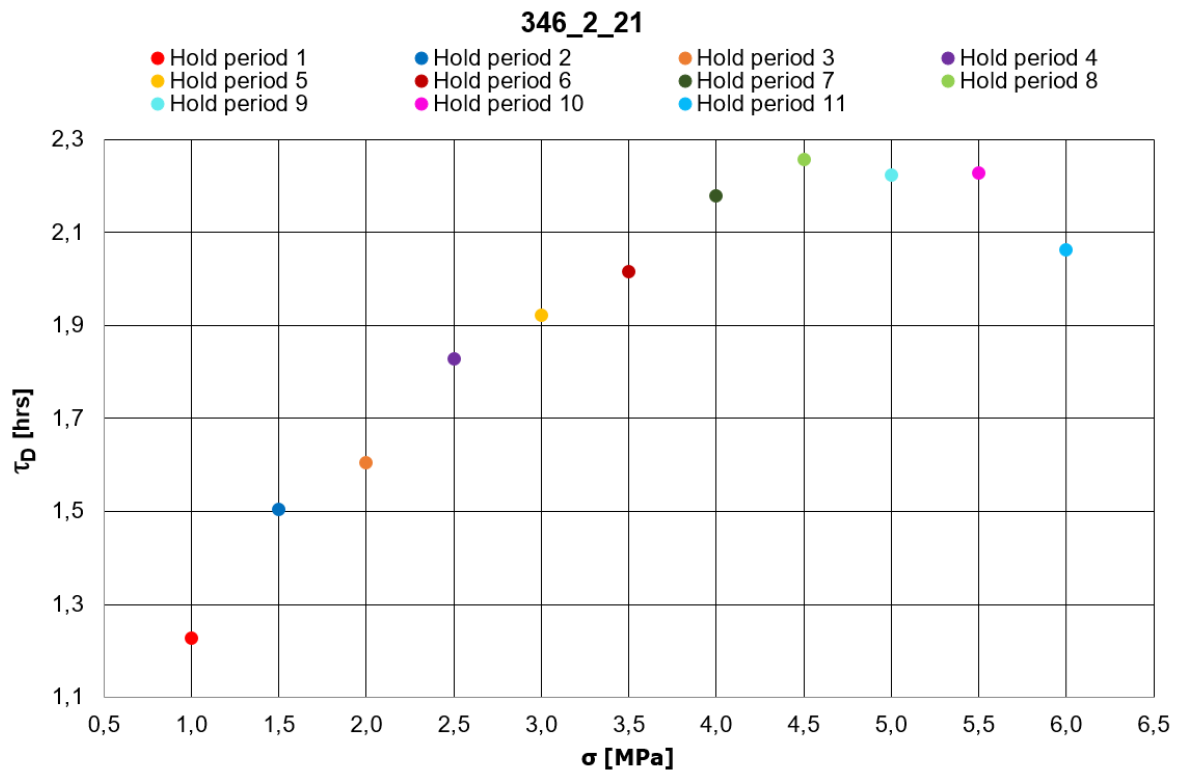


Figure 7.58: Approximate consolidation times for different hold periods.

Figure 7.58 demonstrates that the consolidation time increases more or less linearly up to hold period 8 before it declines.

346_2_21

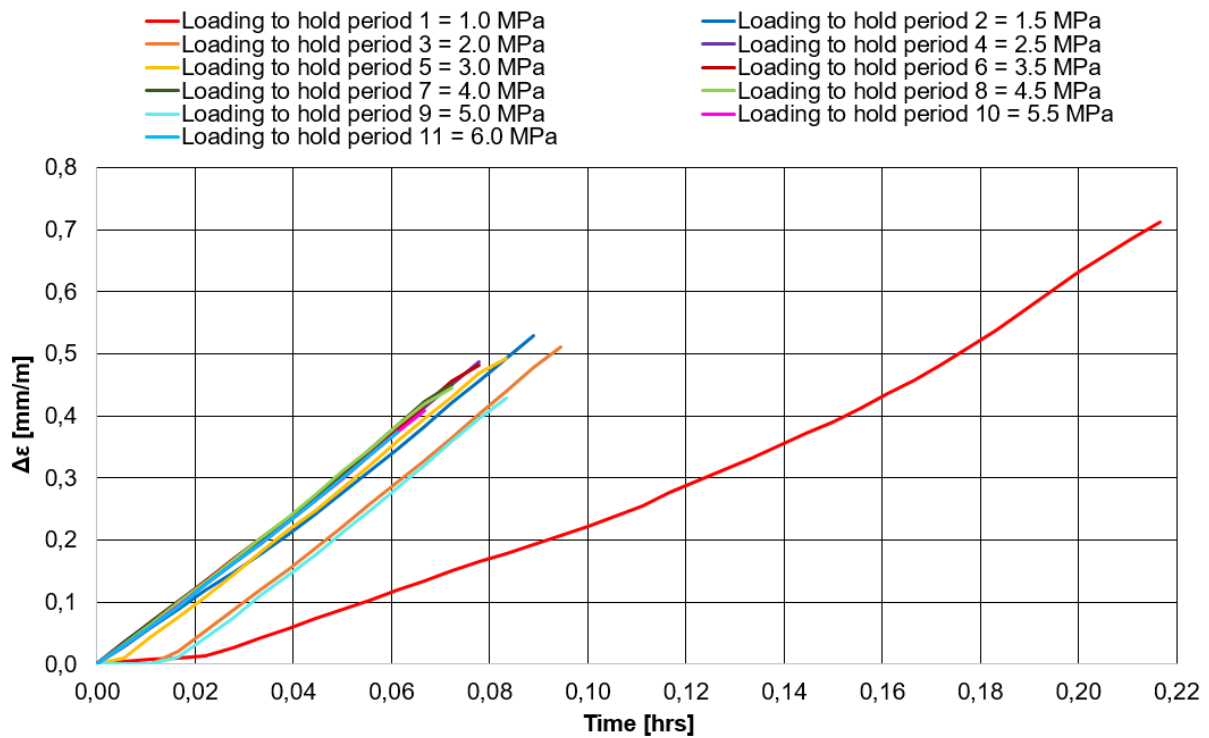


Figure 7.59: Initial deformation versus time for all valid loading phases.

By examining strain for the *loading phases* (Figure 7.59) one observes that most of the curves have similar behavior while the first one stands out. As previously mentioned, in the beginning of a test, the connection between the pistons and the core might not be optimal, resulting in a deviating curve. Overall, each loading phase represents an increase in stress of 0.5 MPa. The figure illustrates that the amount of initial deformation varies for the different loading phases and the overall trend seems to indicate decreasing deformation with increased stress level (Table 7-15).

Table 7-15: Maximum amount of strain for each loading phase.

	346_2_21										
Loading phase	1	2	3	4	5	6	7	8	9	10	11
σ [MPa]	0,5-1,0	1,0-1,5	1,5-2,0	2,0-2,5	2,5-3,0	3,0-3,5	3,5-4,0	4,0-4,5	4,5-5,0	5,0-5,5	5,5-6,0
ϵ [mm/m]	0,711	0,530	0,478	0,487	0,492	0,481	0,450	0,445	0,428	0,408	0,374

To study how the rocks' stiffness changed throughout the test, $1/E_{initial}$ was plotted versus σ for the different loading phases (Figure 7.61). One can observe a more or less linear reduction in the graph, indicating increasing values of the equivalent $E_{initial}$ (Table 7-16). The numbers for $1/E_{initial}$ were found by estimating the slopes of the curves in Figure 7.60.

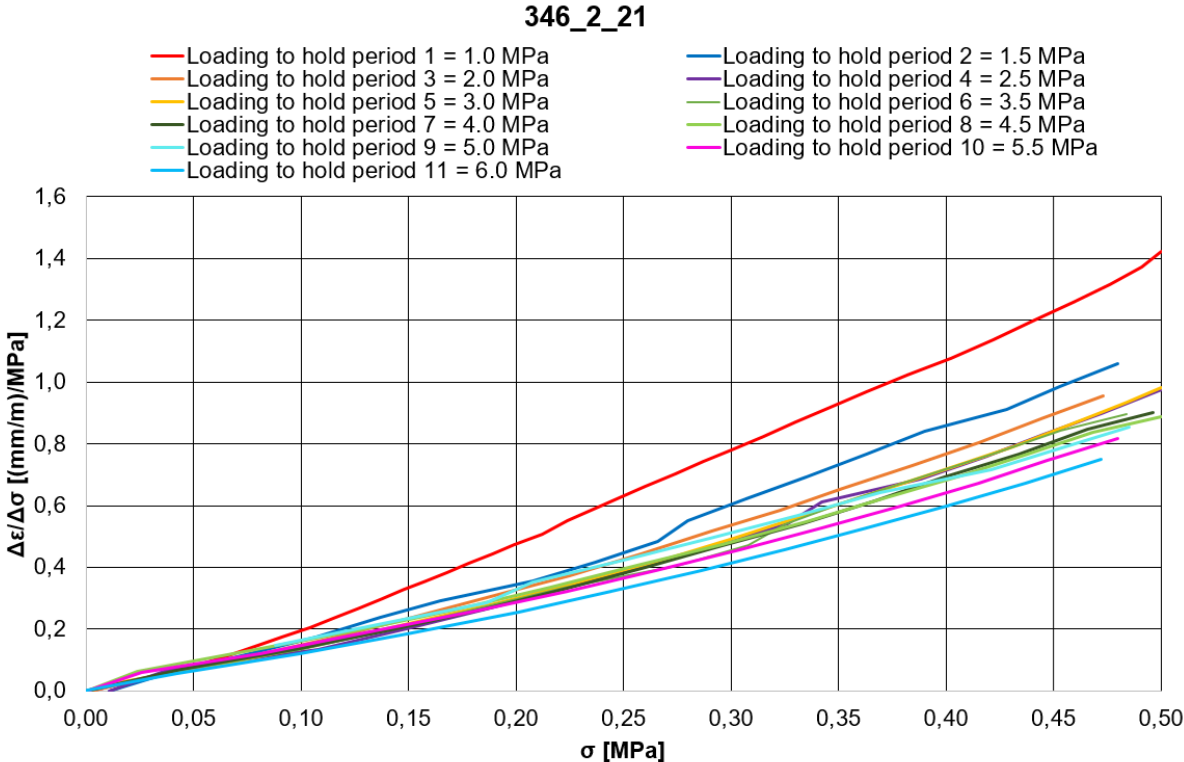


Figure 7.60: $\Delta\varepsilon/\Delta\sigma$ versus stress for all valid loading phases.

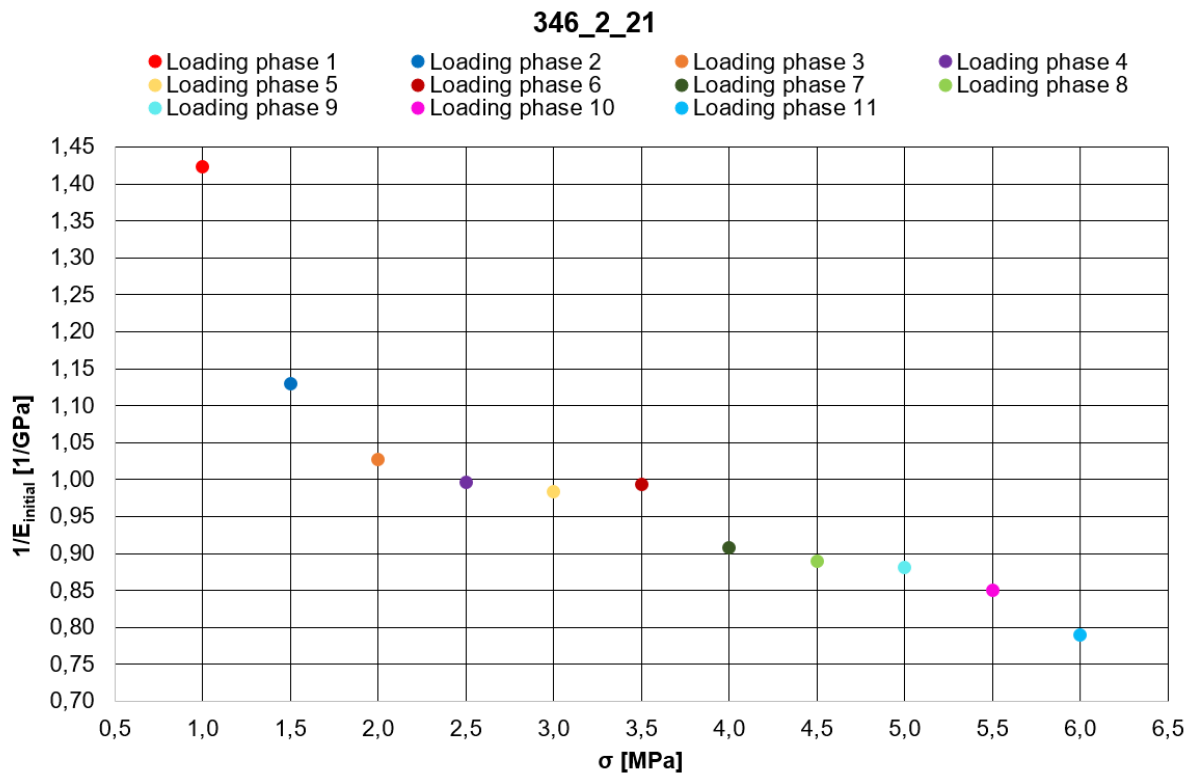


Figure 7.61: The inverse of the initial stiffness versus stress for all valid loading phases.

Table 7-16: Estimated values of initial stiffness for all valid loading phases.

Loading phase	$E_{initial}$ [GPa]
1	0,703
2	0,885
3	0,974
4	1,016
5	1,016
6	1,006
7	1,101
8	1,124
9	1,134
10	1,176
11	1,266

As the results in Table 7-16 shows, the sample becomes stiffer throughout the test. Its initial stiffness has increased approximately 44% in the final loading phase compared to the first. Subsequently, the values of $E_{initial}$ was used in combination with equations (7.2) to (7.7) (pp.96-97) for reviewing how the consolidation times are possibly affected by the change in the rocks' stiffness. As for previous tests, the initial porosity of Pierre shale 346_2 was set to

20.8%, Poisson ratio was assumed to be 0.7 (given by the supervisor) and the dynamic viscosity of the fluid was presumed constant. Table 7-17 presents the obtained results.

Table 7-17: Investigation of how the consolidation times are possibly affected by alteration in rock stiffness.

346_2_21							
Loading phase	$\Delta\epsilon_z$	$\Delta\Phi$	Φ_{new}	k	$E_{initial}$	C_D	Relative τ_D
1	0,0007	0,00023	0,208	0,0143	0,703	10,04	1,00
2	0,0005	0,00017	0,208	0,0143	0,885	12,61	0,80
3	0,0005	0,00016	0,207	0,0142	0,974	13,84	0,73
4	0,0005	0,00015	0,207	0,0142	1,004	14,23	0,71
5	0,0005	0,00016	0,207	0,0141	1,016	14,37	0,70
6	0,0005	0,00015	0,207	0,0141	1,006	14,19	0,71
7	0,0005	0,00014	0,207	0,0141	1,101	15,49	0,65
8	0,0004	0,00014	0,207	0,0140	1,124	15,78	0,64
9	0,0004	0,00014	0,207	0,0140	1,134	15,87	0,63
10	0,0004	0,00013	0,206	0,0140	1,176	16,43	0,61
11	0,0004	0,00012	0,206	0,0139	1,266	17,65	0,57

The table reveals similar trends as discussed for 346_2_20 and 346_2_23, resulting in overall decreasing consolidation times throughout the test. Consequently, looking at the relative difference in τ_D for the test (Figure 7.62), demonstrates a declining trend.

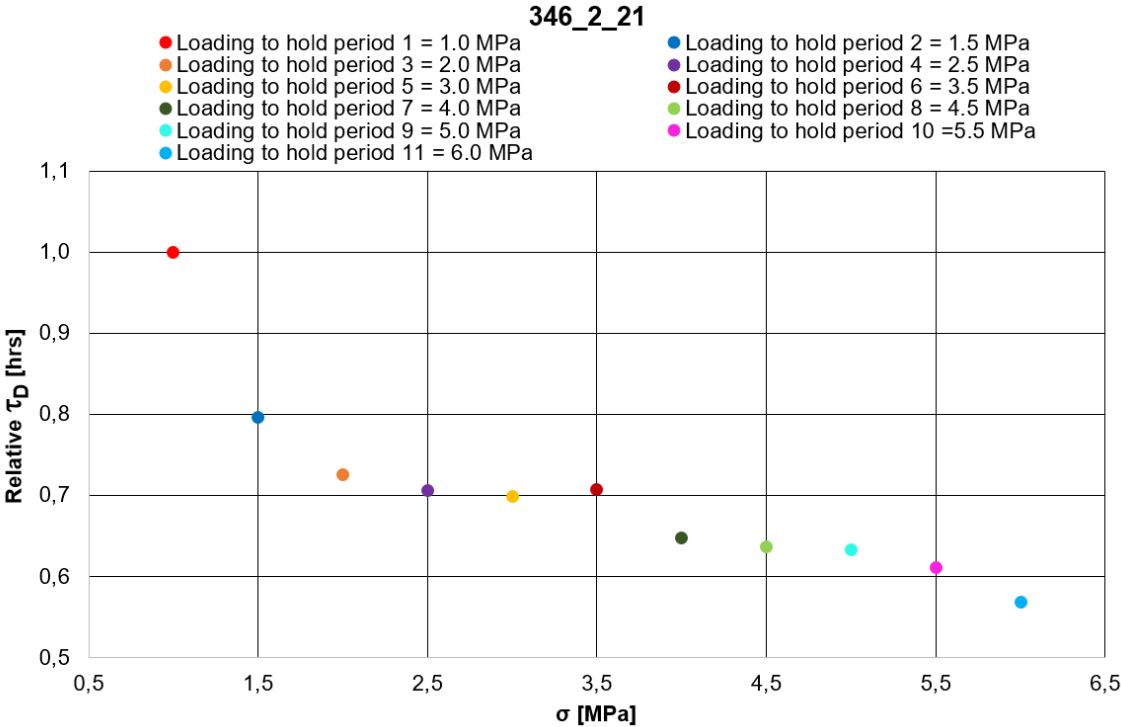


Figure 7.62: Relative difference in consolidation times versus stress throughout the test.

7.2.2 Core sample 346_2_22

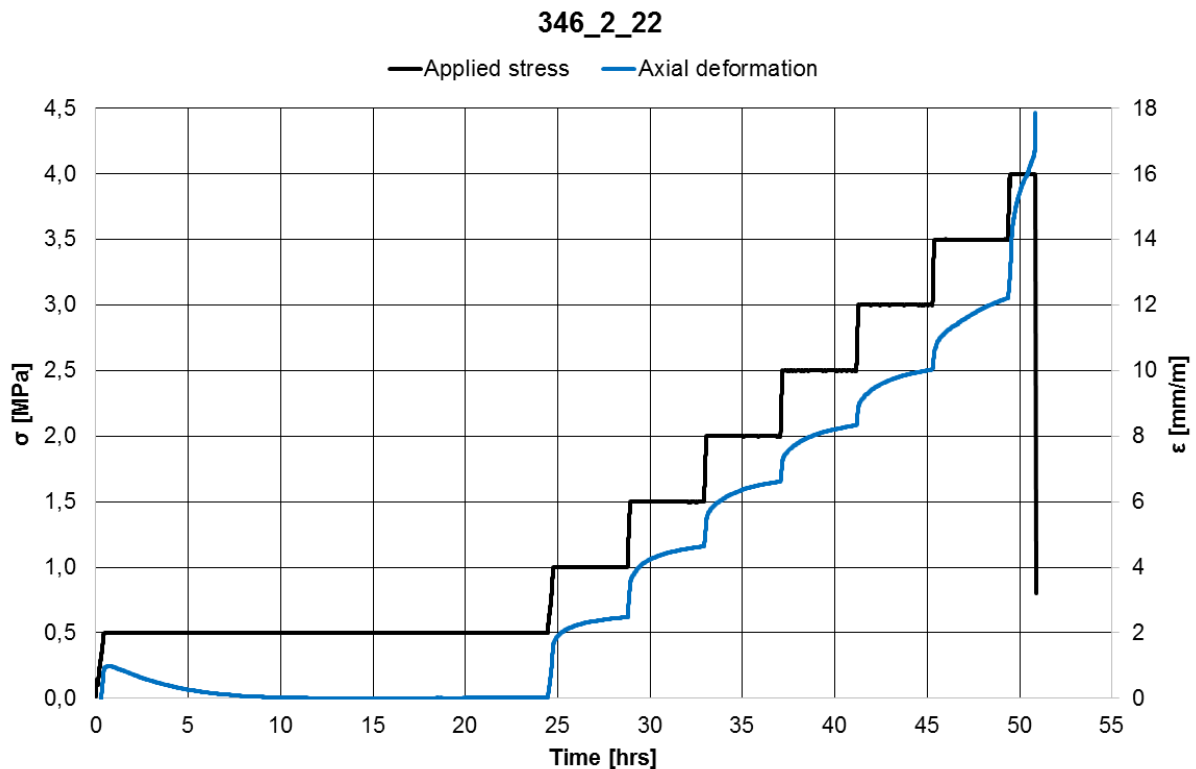


Figure 7.63: Overview of creep test conducted on 346_2_22.

After ion diffusion for 24 hours, the second and final creep test in a mixture of brine and $HCl(aq)$ completed 6 load levels before reaching failure 1.36 hours into load level 7 (4.0 MPa). Thus, the final hold period is not included for further discussion. The reason for an early failure might be due to variations within the samples or there can be other explanations. When cleaning up after the test had finished, it was discovered that all of the fluid surrounding the core had leaked out of the container. It was believed that this leak had happened in conjunction with failure of the sample, but if it occurred during the test itself, it might have been the actual reason for why it failed early. If the specimen was no longer submerged in any fluid at all it would have easily dried out implying an overall weakening of the rock. To avoid potential leakage in the upcoming test 346_2_23, a more robust O-ring was acquired for sealing the lower part of the experimental setup.

Due to a 3°C deviation between the actual temperature and the desired temperature for the previous creep experiment (346_2_21), it was decided to set the temperature controller for 33°C, aiming to obtain an actual temperature of 30°C. However, the results of the test instead showed a temperature around 25°C. This was not optimal, and it is unknown why

the temperature controller did not function properly. Overall, the maximum temperature variation during the creep experiment was 0.47°C.

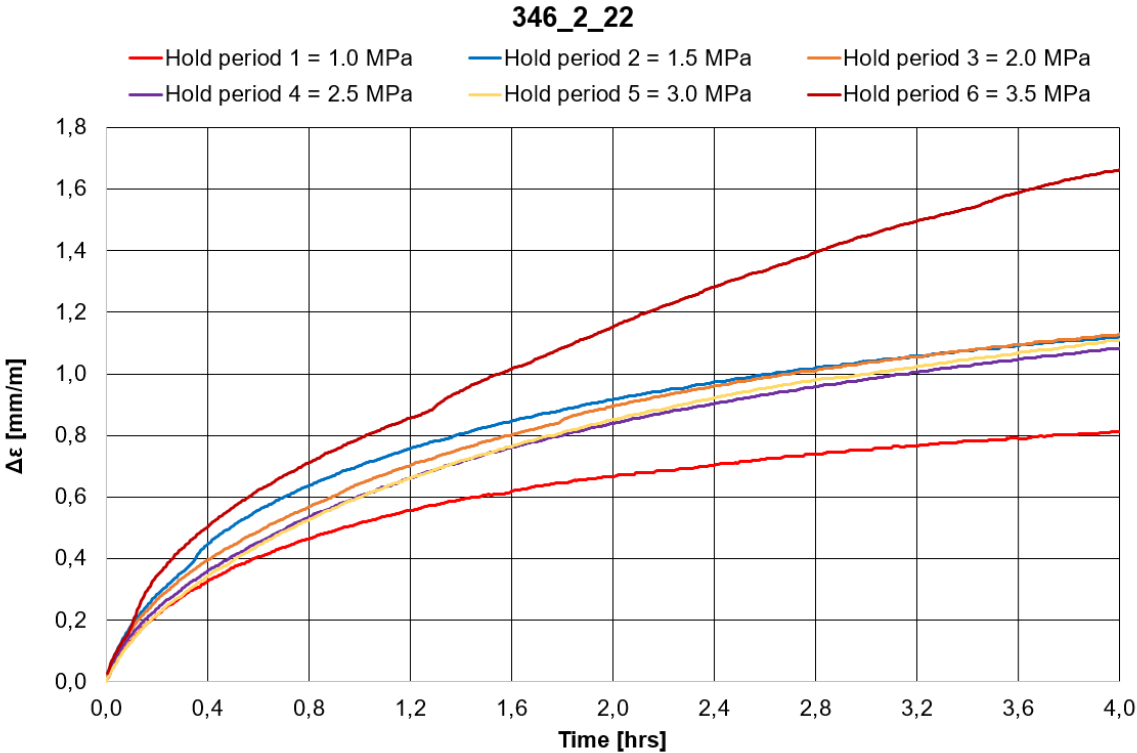


Figure 7.64: Strain versus time for all valid hold periods.

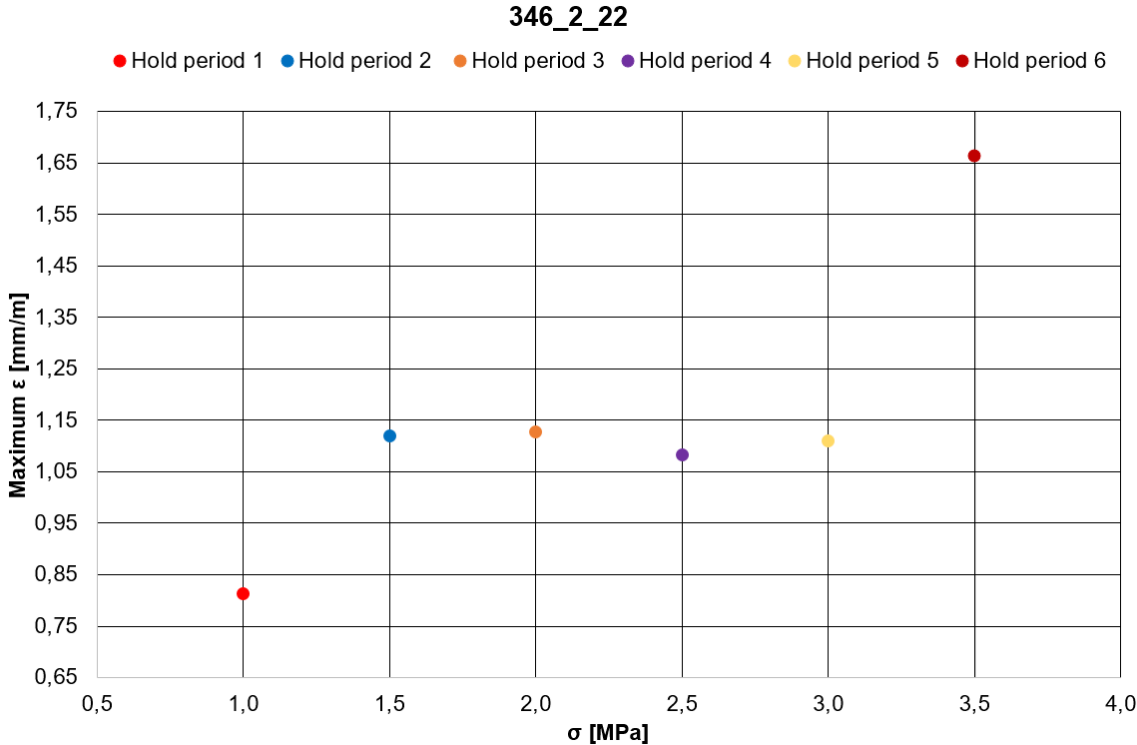


Figure 7.65: Maximum strain for a hold period versus stress level.

By looking at obtained strain for all valid hold periods scaled to the same reference point (0,0) (Figure 7.64), one can observe that the amount of strain increases with load for the first 3 hold periods, decreases for hold period 4 and then rises again for the remaining two. This is more clearly illustrated in Figure 7.65, showing maximum strain for a hold period versus stress level. Hold period 6 stands out with much higher deformation than the others and a potential reason for this could be the fact that this is the period right before failure. Also, when studying hold period 1, 2, 3 and 6 closely in Figure 7.64, small cave-ins can be observed in the curves. This can potentially be explained by crushing of grains in the beginning of a test. Later, for hold period 6, one can assume that the cave-in originates from development of a small crack, causing higher loads in the surrounding area and an overall weakening the rock. This is logical since the sample reached failure early in the next period.

Investigating the deformation rates in Figure 7.66 for certain time intervals (Table 7-18), shows that hold period 1 and 2 are in transient creep phase. Since none of the first hold periods approaches stable behavior, it is impossible to accurately predict the transition between *low* and *moderate* stress levels for this sample. However, the threshold for reaching steady-state creep seems to be 2.0 MPa. As Table 7-18 demonstrates, the deformation rates for hold period 3 and 4 are more or less constant the last 30 min, implying that the creep phase has transitioned from transient to steady-state. The deformation rate increases with time at the end for hold period 5, indicating accelerating creep phase. There is no defined creep phase in Table 7-18 at the end of hold period 6. Naturally, since this period is a continuation of the previous, the creep phase should be accelerating. However, as Figure 7.66 illustrates, the deformation rates for period 6 fluctuate highly through the whole period with a random dip at the end. Thus, the obtained values at the end of the hold period are not representative for the creep phase and should not be used to define it.

Table 7-18: Overview of deformation rates and creep phases at the end of the hold periods.

Hold period	Load [MPa]	Interval [hrs]						Creep phase at the end of hold period*
		0,0-1,0	1,0-2,0	2,0-3,0	3,0-3,5	3,5-3,75	3,75-4,0	
		Deformation rate [(mm/m)/hrs]						
1	1,0	0,515	0,151	0,086	0,066	0,071	0,046	Transient
2	1,5	0,702	0,215	0,124	0,084	0,085	0,060	Transient
3	2,0	0,643	0,253	0,140	0,102	0,085	0,075	Steady-state
4	2,5	0,603	0,236	0,142	0,110	0,092	0,092	Steady-state
5	3,0	0,598	0,253	0,147	0,112	0,103	0,119	Accelerating
6	3,5	0,790	0,363	0,296	0,231	0,226	0,168	-

*To distinguish between transient and steady-state creep phase at the end of a hold period, a threshold value, T_{cp} , representing the difference between the last two time intervals, was set for $T_{cp} \leq 0.01$. An increase in deformation rate between the last two time intervals exceeding the established T_{cp} was used to define accelerating creep.

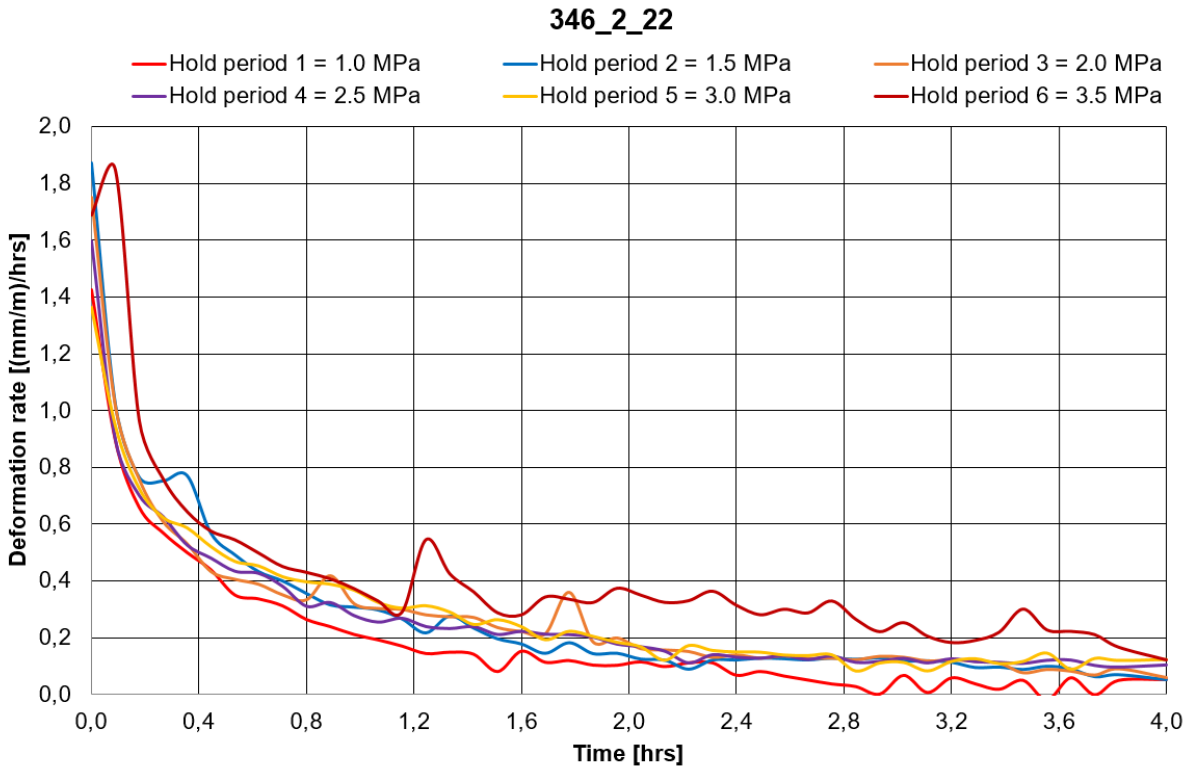


Figure 7.66: Continuous deformation rates in the valid hold periods.

A decreasing trend in the beginning of all hold periods can be observed when studying continuous deformation rates. Later, more stable rates occur for most of them. Hold period 6 stands out with a highly fluctuating graph compared to the others which might be caused by the cave-in after 1.2 hours as explained earlier. Overall, the first hold period has the lowest rates, while the last period has the highest. This coincides with the expectation of

increased deformation rates for higher levels of stress. The remaining periods blend more or less together, and the small variation might be due to a consolidation dominating effect.

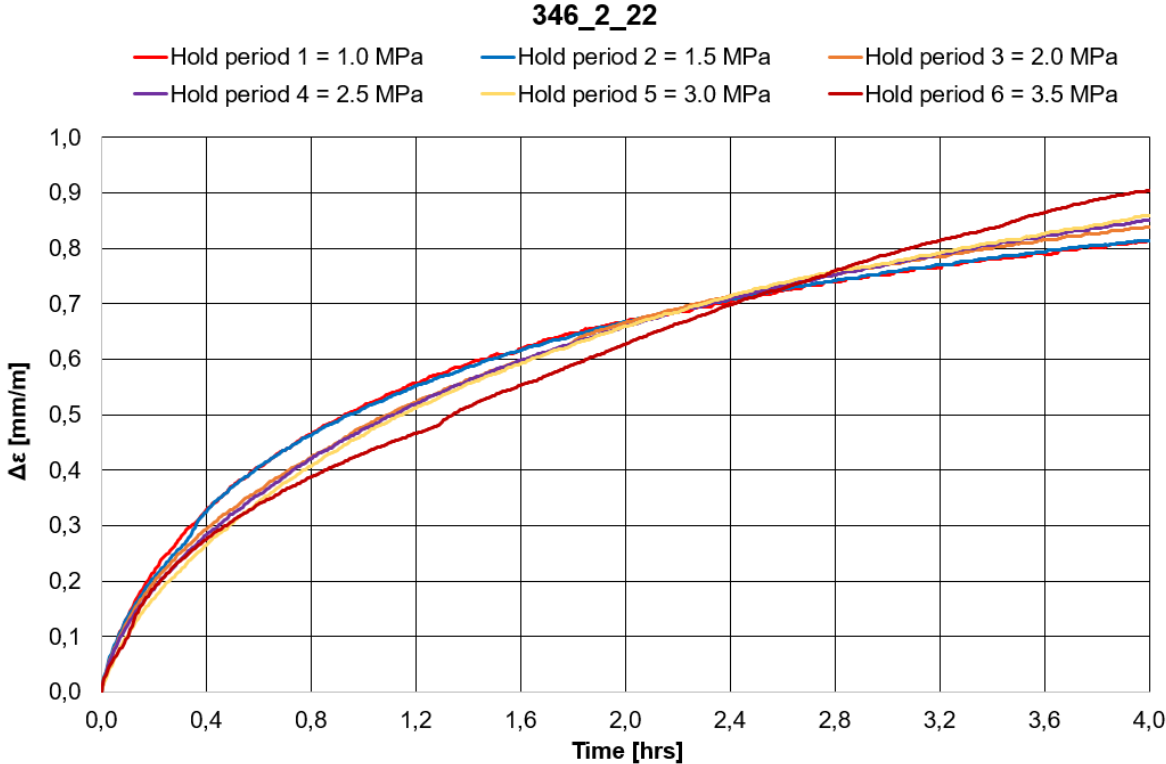


Figure 7.67: Attempt to scale the other hold periods down to hold period 1 with a scaling factor s .

By scaling the other hold periods down to period 1 with a scaling factor s , one can observe that the shape of the curves differ for the hold periods. This implies that the variation in deformation between them is not only dependent on an amplitude factor, but also affected by *when* consolidation and *when* creep is the dominating effect.

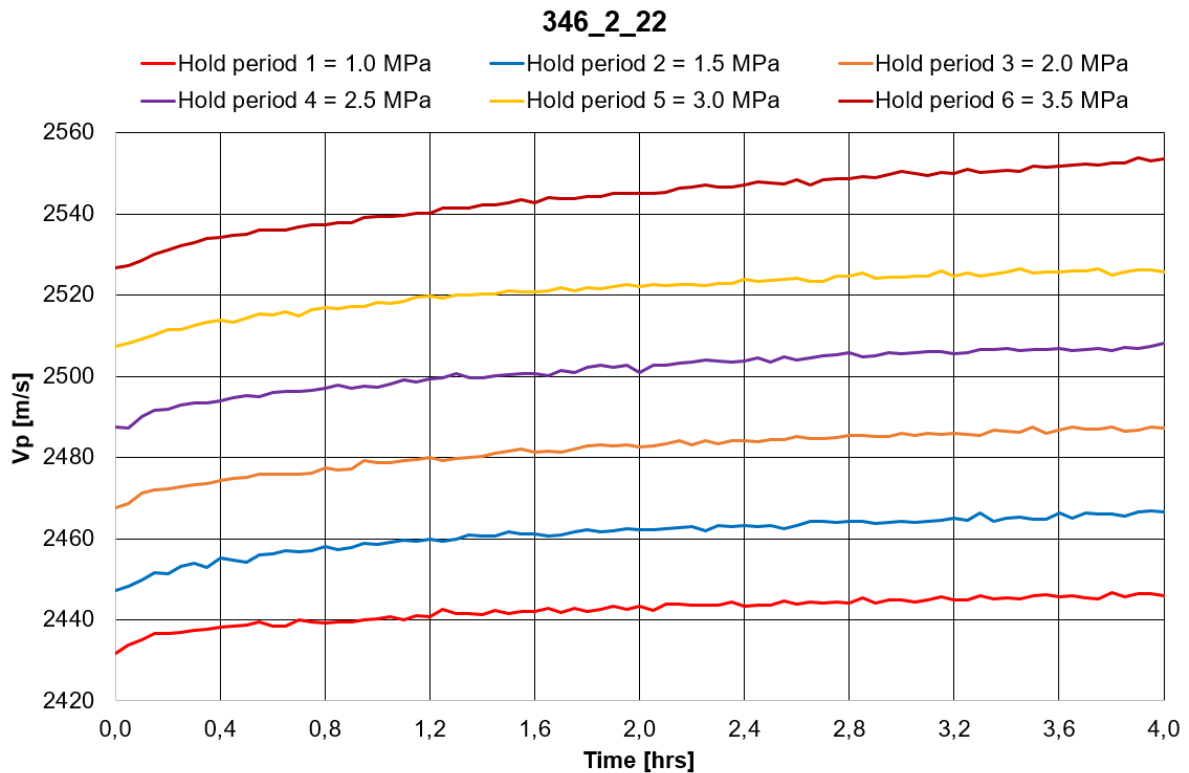


Figure 7.68: P-wave velocities in the valid hold periods.

Investigating p-wave velocities show, as similar to all previous tests, that the magnitude of the velocities increases with applied stress (Figure 7.68). Also, looking at the p-wave velocities scaled to the same reference point (0,0) (Figure 7.69), reveals that velocities are not constant with time in all hold periods, they increase, indicating a correspondence between the p-wave velocities and strain. The first and last period stands out with smaller and larger increase in velocities compared to the others. When studying Figure 7.70, it seems like there is a linear dependency between p-wave velocities and deformation. This is later confirmed in Figure 7.71 (the same plot as Figure 7.70, only scaled to (0,0)), and suggests that the velocities are more or less a linear function of strain in the hold periods. All speculations above acknowledge that p-wave velocities are most likely dependent upon strain as well as stress.

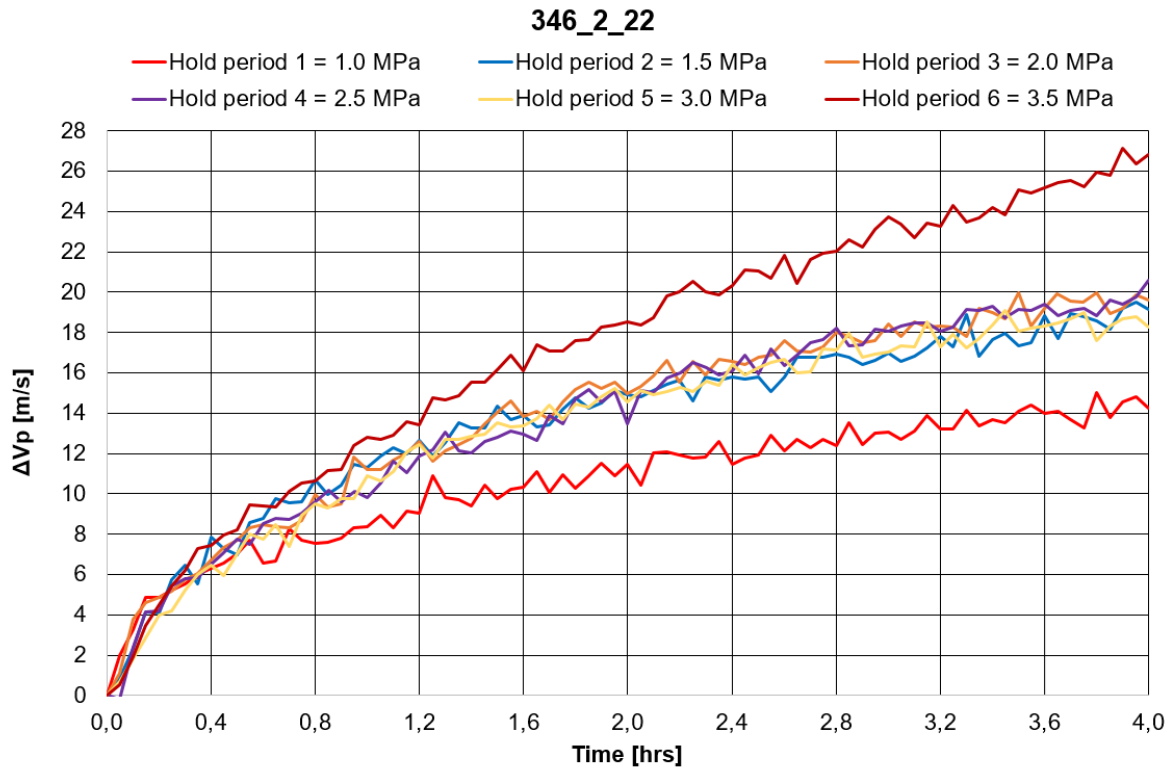


Figure 7.69: P-wave velocities in the valid hold periods scaled to (0,0).

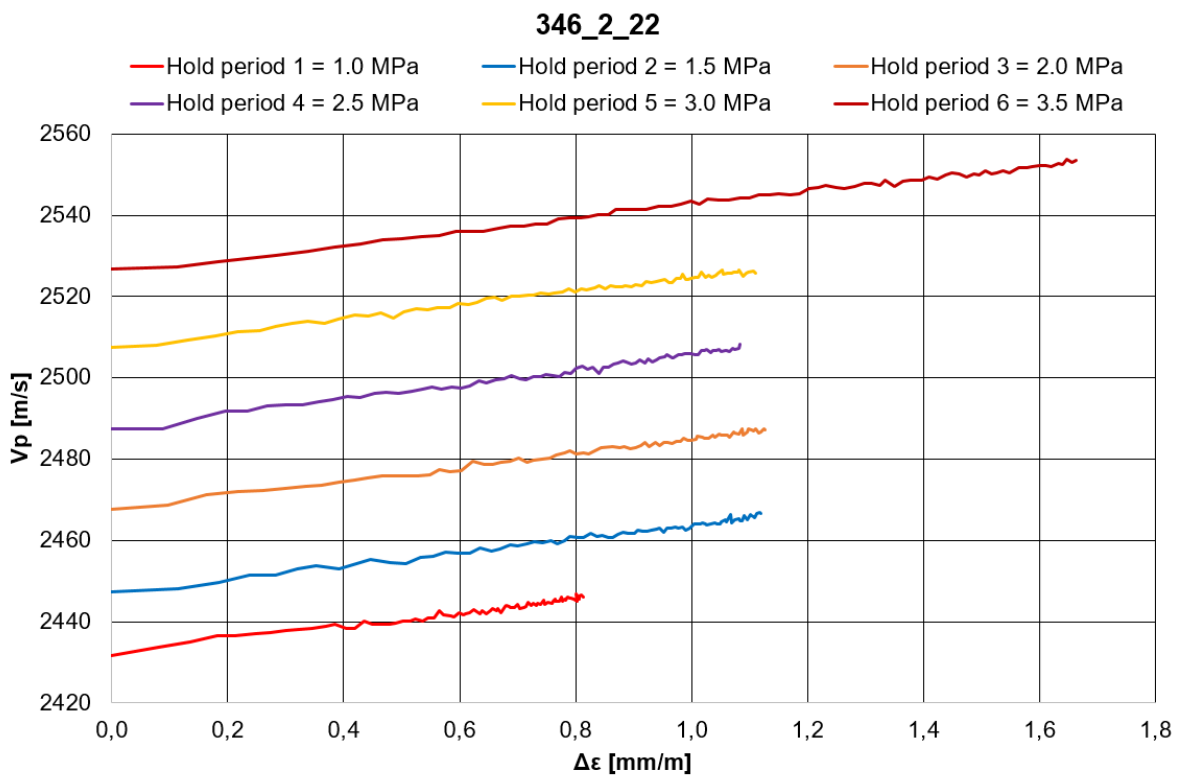


Figure 7.70: P-wave velocities versus deformation for the valid hold periods.

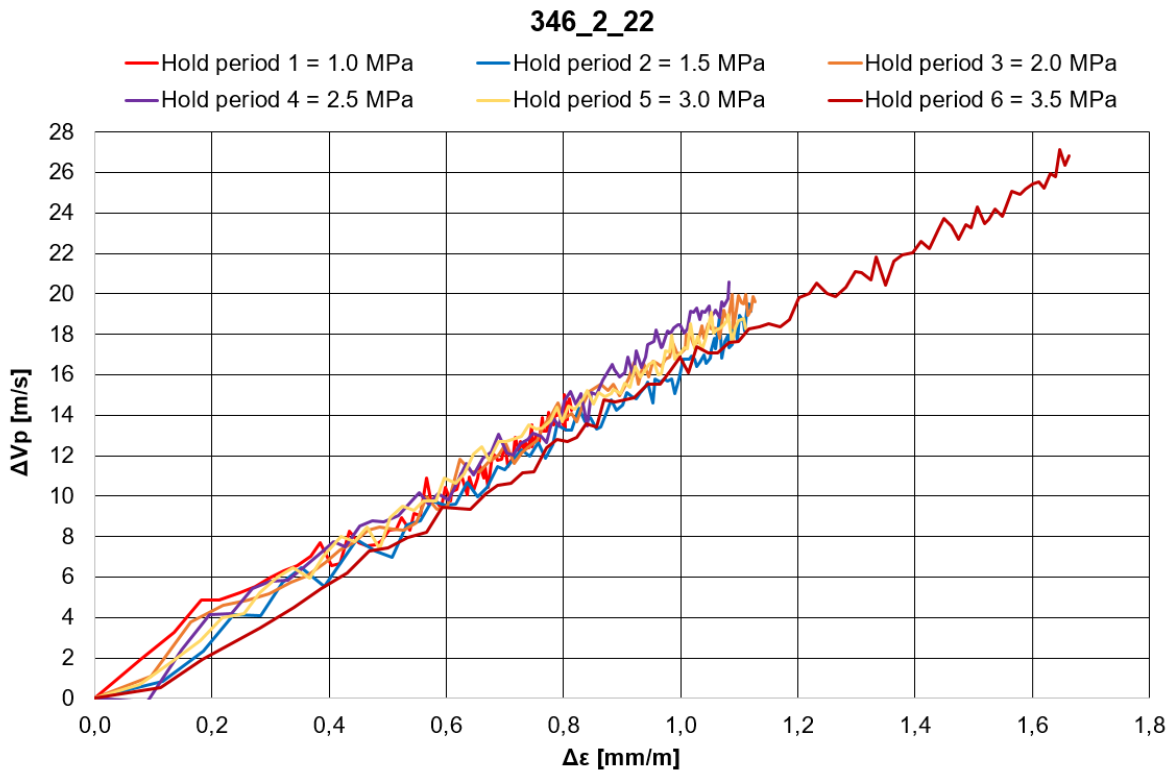


Figure 7.71: P-wave velocities versus deformation for the valid hold periods scaled to (0,0).

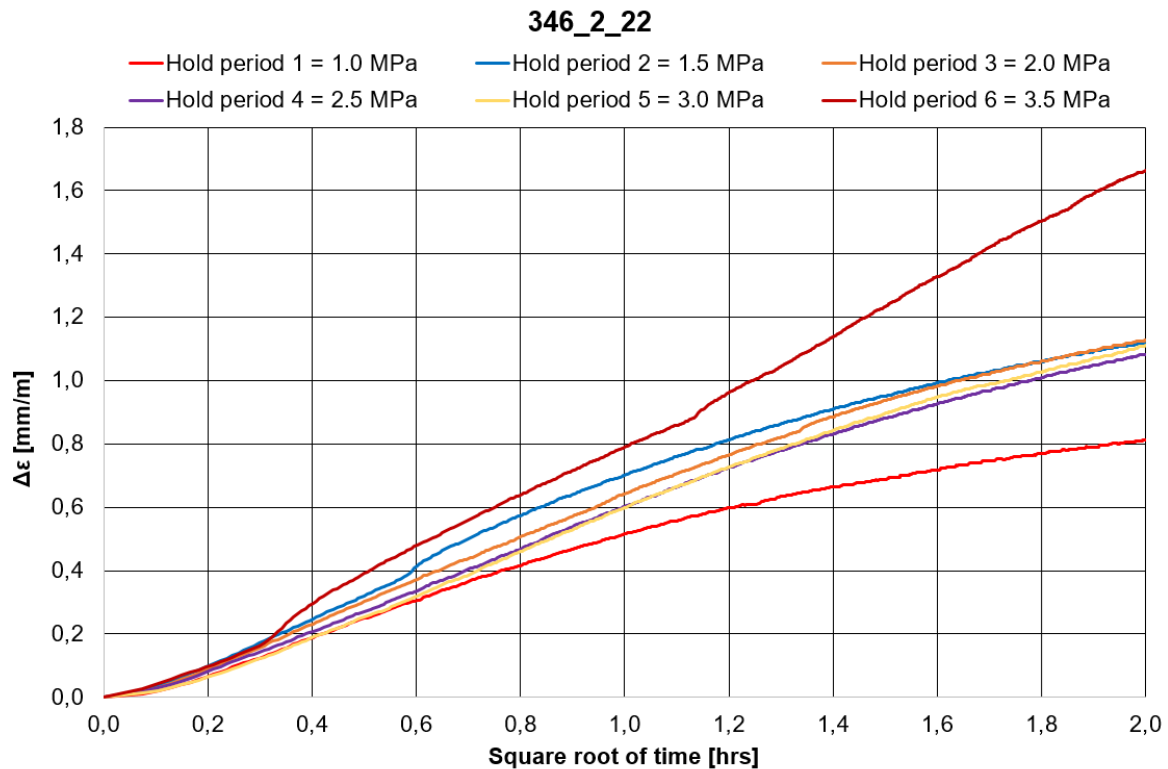


Figure 7.72: Strain versus square root of time for all valid hold periods.

By applying the graphical approach on the obtained data in Figure 7.72, the approximate consolidation times for the different hold periods were estimated. Table 7-19, in addition to Figure 7.73, presents the results and shows that the parameter ranges from 0.8-4.0 hours.

Table 7-19: Approximate consolidation times, τ_D , for different hold periods.

Hold period	Load [MPa]	Square root of time [hrs]	τ_D [hrs]
1	1,0	0,922	0,850
2	1,5	1,276	1,628
3	2,0	1,449	2,100
4	2,5	1,354	1,833
5	3,0	1,443	2,082
6	3,5	2,000	4,000

346_2_22

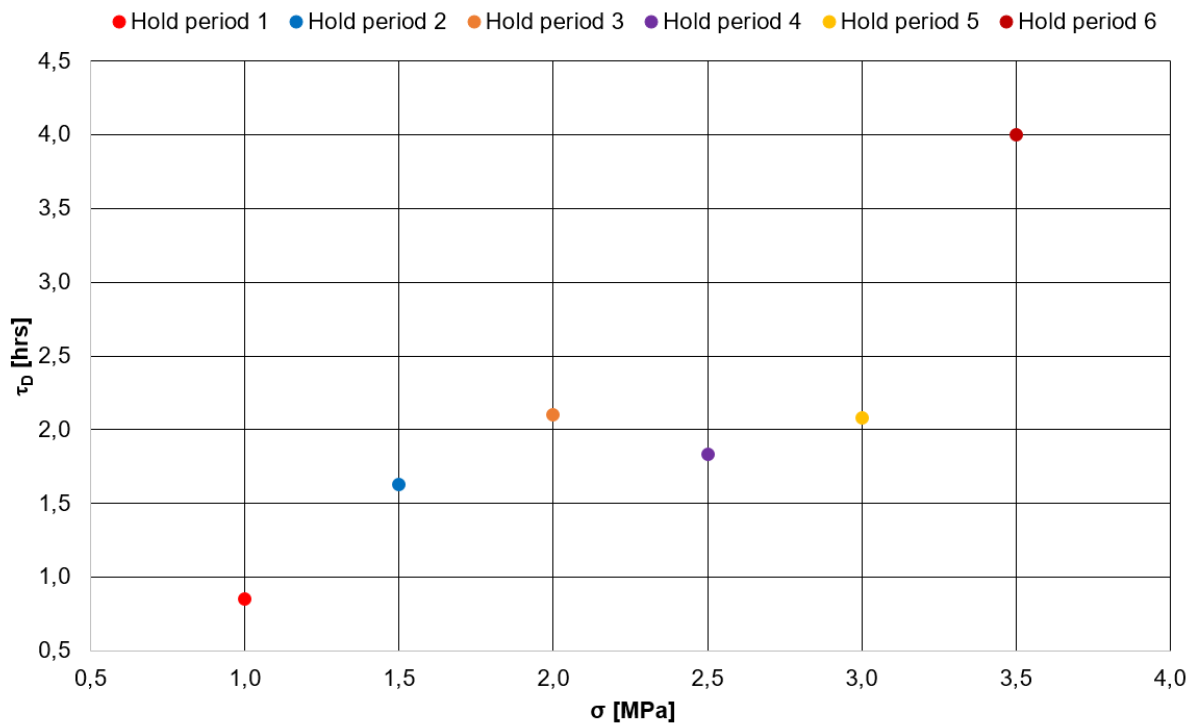


Figure 7.73: Approximate consolidation times for different hold periods.

Figure 7.73 demonstrates that the consolidation time increases more or less linearly up to hold period 3 before it declines. As one can observe, the consolidation time for hold period 6 extends through the whole period of constant stress (4 hours). This is highly uncertain, and the accelerating creep phase in combination with the cave-in mentioned earlier is believed to be the genuine reasons for obtaining a straight line in a square root of time plot through the entire time period (Figure 7.74). Applying the graphical approach in this case, is most likely not a good method for finding the *actual* consolidation time.

346_2_22

— Hold period 6 = 3.5 MPa

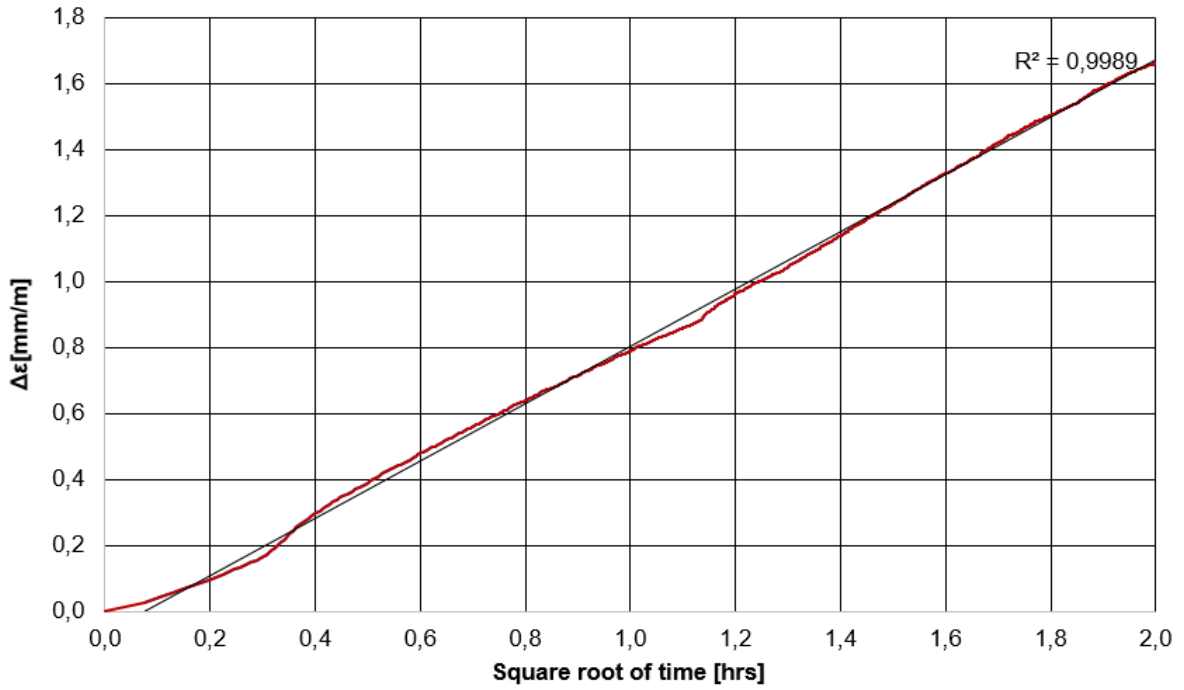


Figure 7.74: Graphical approach applied for hold period 6.

346_2_22

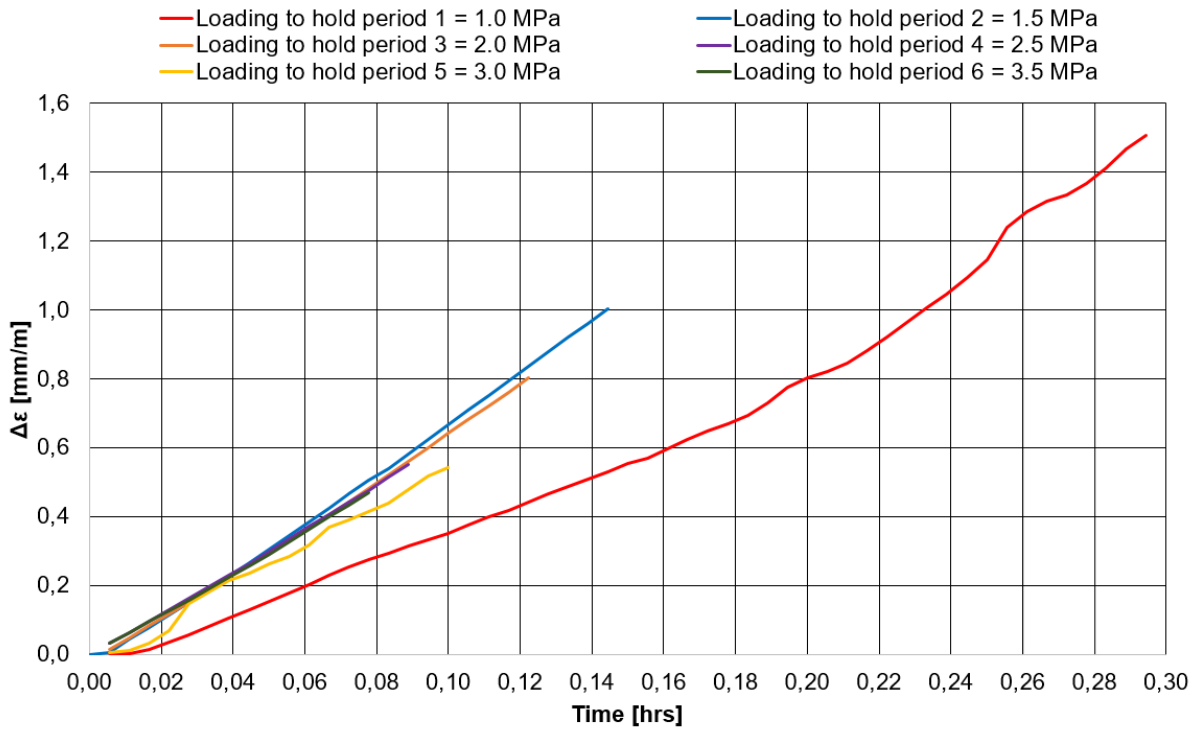


Figure 7.75: Initial deformation versus time for all valid loading phases.

Studying strain for the *loading phases* (Figure 7.75) demonstrates the same trend as found for the previous creep tests;

- the first phase stands out due to a not optimal connection between the core and the pistons
- remaining loading phases have more or less similar behavior
- the overall trend seems to indicate decreasing amount of initial deformation with increased stress level (Table 7-20)

Table 7-20: Maximum amount of strain for each loading phase.

	346_2_22					
Loading phase	1	2	3	4	5	6
σ [MPa]	0,5-1,0	1,0-1,5	1,5-2,0	2,0-2,5	2,5-3,0	3,0-3,5
ϵ [mm/m]	1,505	1,033	0,816	0,517	0,545	0,438

To investigate the variation in rock stiffness throughout the test, $1/E_{initial}$ for the different loading phases was plotted versus σ (Figure 7.77). The figure shows a close to linear reduction in the parameter, indicating increasing values of the corresponding $E_{initial}$ (Table

7-21). The values of $1/E_{initial}$ were found by calculating the slopes of the curves in Figure 7.76.

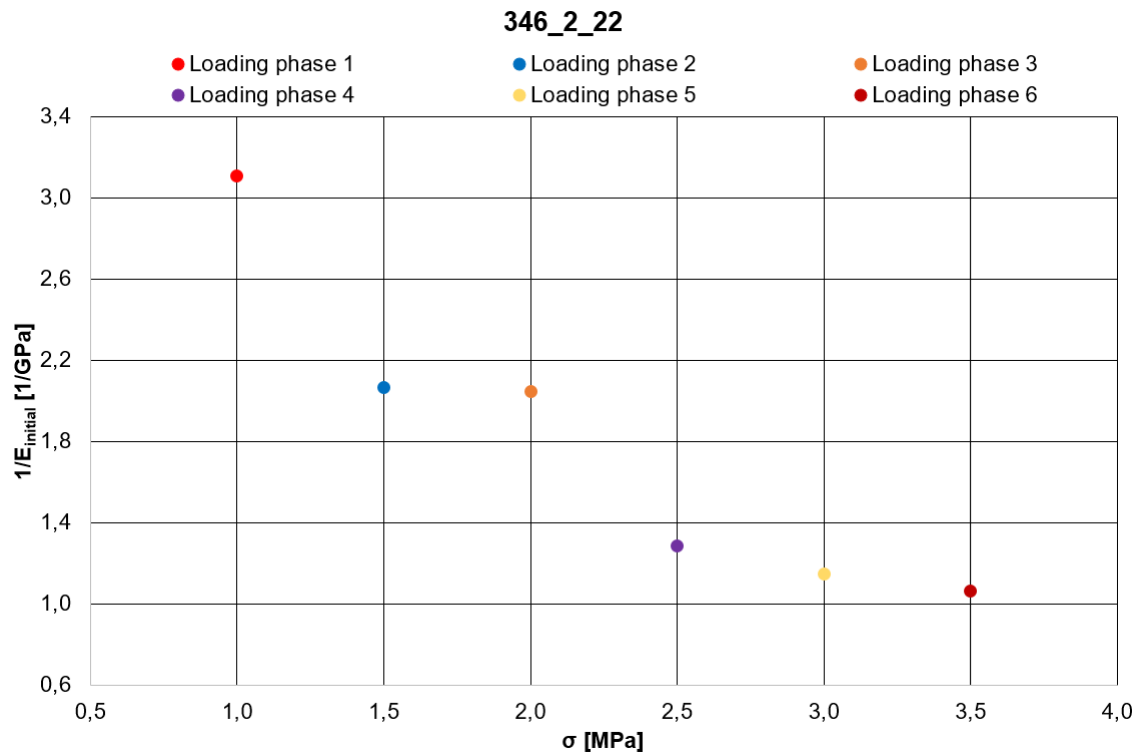
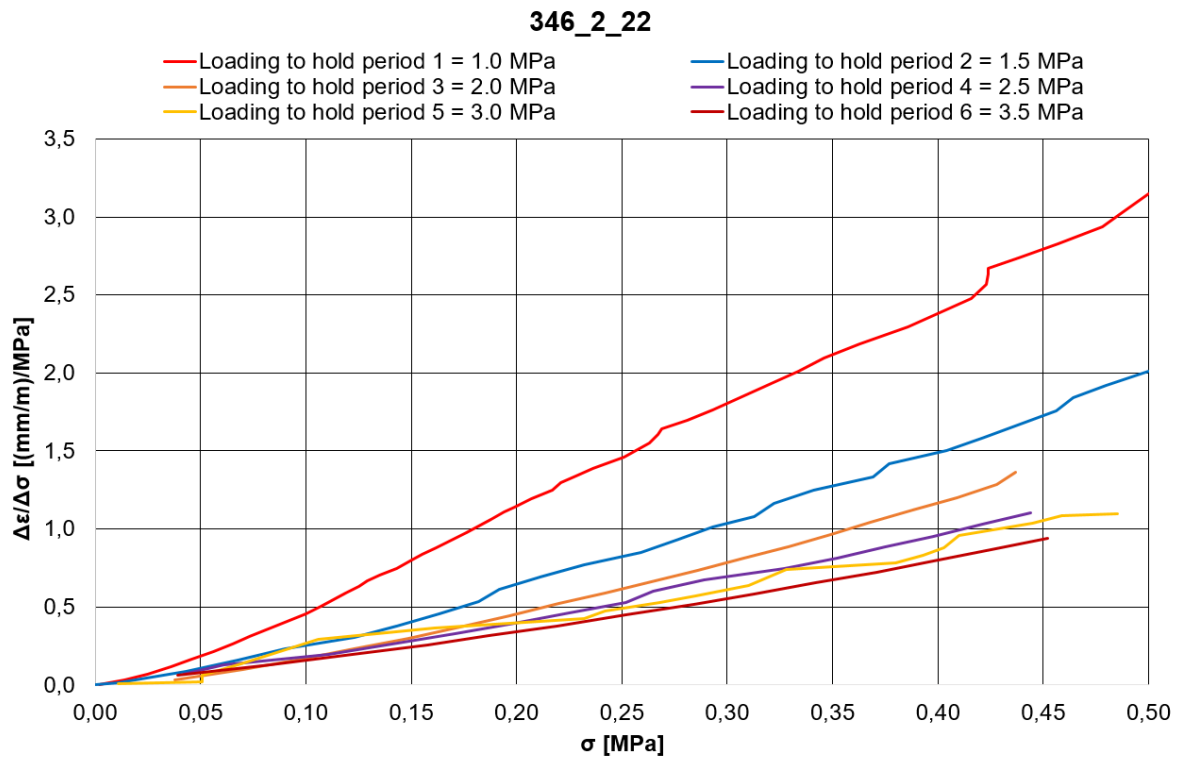


Table 7-21: Estimated values of initial stiffness for all valid loading phases.

Loading phase	$E_{initial}$ [GPa]
1	0,322
2	0,484
3	0,489
4	0,777
5	0,870
6	0,942

As seen in Table 7-21, the sample becomes stiffer throughout the test. A similar trend was found for the previous experiment in a mixture of brine and acid (346_2_21). From the start of this test to the end, the samples' initial stiffness has increased approximately 66%. Later, the values of $E_{initial}$ was used together with equations (7.2)-(7.7) (pp.96-97) to further investigate how the consolidation times are possibly affected by variation in the rocks' stiffness. Like earlier, the dynamic viscosity of the fluid was assumed constant while the initial porosity of Pierre shale 346_2 and Poisson ratio was set to 20.8% and 0.7 respectively. The obtained results are presented in Table 7-22.

Table 7-22: Investigation of how the consolidation times are possibly affected by alteration in rock stiffness.

346_2_22							
Loading phase	$\Delta\epsilon_z$	$\Delta\Phi$	Φ_{new}	k	$E_{initial}$	C_D	Relative τ_D
1	0,0015	0,00048	0,208	0,0142	0,322	4,58	1,00
2	0,0010	0,00033	0,207	0,0142	0,484	6,85	0,67
3	0,0008	0,00026	0,207	0,0141	0,489	6,89	0,66
4	0,0005	0,00016	0,207	0,0141	0,777	10,92	0,42
5	0,0005	0,00017	0,207	0,0140	0,870	12,19	0,38
6	0,0004	0,00014	0,206	0,0140	0,942	13,16	0,35

As the results illustrates, initial stiffness of the sample increases throughout the test while the permeability decreases slightly. Thus, C_D increases and the consolidation time decreases. Further, studying the relative difference in τ_D for the test (Figure 7.78), proves a declining trend. This is similar to the findings for all previous tests.

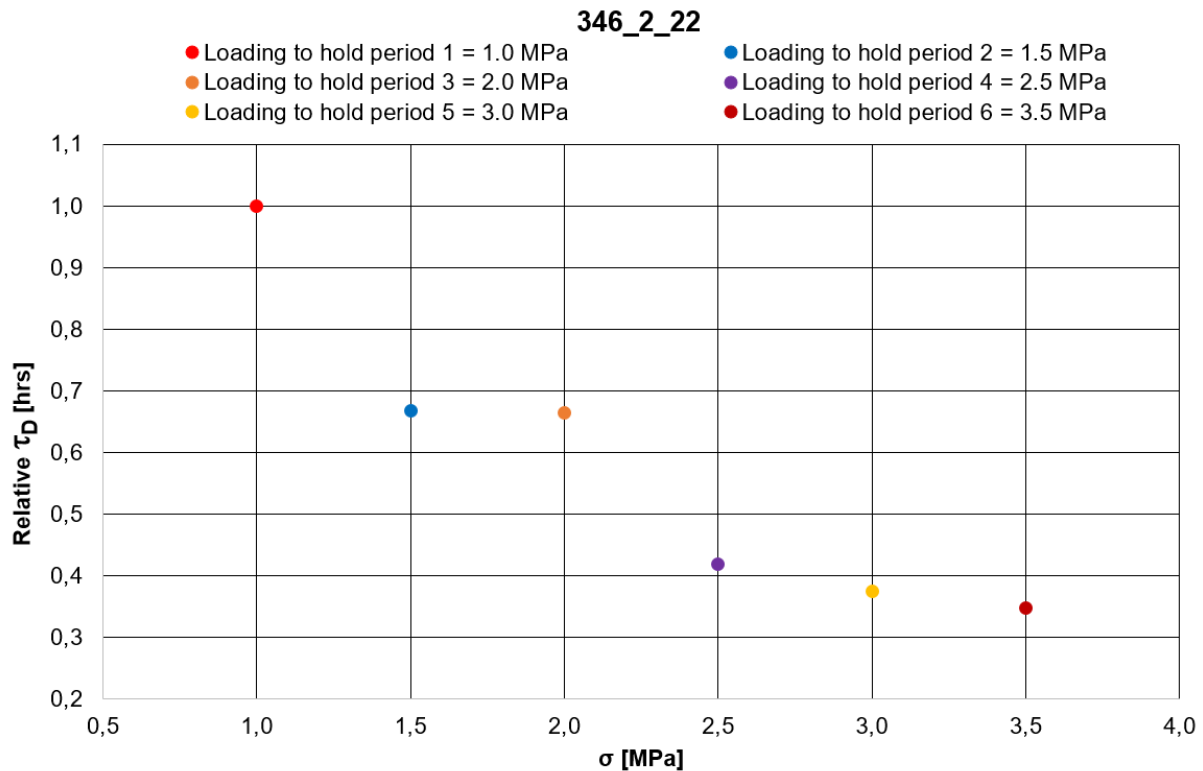


Figure 7.78: Relative difference in consolidation times versus stress throughout the test.

7.3 Comparison of the results

For comparison of results, creep experiment 346_2_20, 346_2_21, 346_2_22 and 346_2_23 will exclusively be considered. This involves two creep tests in brine and two creep tests with reduced pore fluid pH run with the same test procedure and loading path. First, some general, common trends found for the experiments will be listed. Afterwards, a discussion to identify how the creep and consolidation mechanisms were affected by alteration in porefluid pH and changes in stress conditions will be carried out.

7.3.1 Common trends

By comparing the relevant creep tests, some general and common trends were found:

- The temperature variation increased with extended test time.
- The temperature variation for all creep tests never exceeded 0.98°C, and it appeared like this value was too low to impact the deformation of Pierre shale. This is consistent with Olsen's (2015) findings for Castlegate sandstone.

- The results showed that there are two different ongoing processes in the hold periods; consolidation and creep respectively.
- The least amount of deformation was seen for the first hold period in all tests.
- Variation in stress conditions affected the maximum amount of deformation. A fluctuating trend was found and is discussed in more detail later (section 7.3.2.2, p.155).
- For all creep tests it seemed to be a stress threshold for reaching steady-state creep.
- In 3 of the tests, the first hold period did not reach steady-state creep, but approached stable behavior after transient creep phase instead.
- Deformation rates for the hold periods followed a trend; a rapid decline was seen in the beginning of all tests while more subtle rates developed towards the end.
- When using a scaling factor s to scale all hold periods down to hold period 1 in each test, different shapes of curves were seen for 3 of the tests, implying that the dissimilarity in deformation was not exclusively dependent on an amplitude factor.
- Generally, p-wave velocities were seen to increase with applied stress, but also with time for hold periods with fixed stress. This implies that the velocities are not dependent on stress exclusively. A close to linear dependency between p-wave velocities and strain was found for the hold periods, indicating that velocities are related to strain as well as stress.
- By using the graphical approach on a square root of time plot, the consolidation time was found to never be less than 0.8 hours in a hold period. This method also showed an overall trend with increasing consolidation times for ascending hold periods. In contrast, by using calculations based on $E_{initial}$ to study relative τ_D , decreasing consolidation times were detected.
- Due to a not optimal connection between the core and the pistons in the beginning of a test, the first loading phase stood out from the remaining with a different shape of deformation curve. Following loading phase 1, the amount of deformation in the other loading phases seemed to decrease for increased stress levels.
- Young's initial modulus acquired from the loading phases, $E_{initial}$, was found to increase throughout the tests, indicating stiffer samples.

In addition, due to the unfortunate lab incident for core sample 346_2_20, a significant drop in p-wave velocities was seen simultaneously as an enormous temperature increase (Figure 7.18, p.83). This indicates a correlation between the two parameters, which agrees with the results from the specialization project. Here it was revealed that increased p-wave velocities occurred for temperature drops and vice versa for a temperature variation exceeding approximately 0.80°C. Except for core sample 346_2_20, no further investigations regarding this was carried out in the master thesis due to limited time intervals in the hold periods; 4 hours was too short for obtaining significant temperature variations.

7.3.2 Identification of how creep and consolidation are affected by alteration in porefluid pH and changes in stress conditions

7.3.2.1 pH

For identifying how time-dependent mechanisms are affected by alteration in porefluid pH, creep test 346_2_23 will be compared with creep test 346_2_21 due to approximately the same amount of valid hold periods before failure. The same applies for 346_2_20 and 346_2_22.

Starting off, just to get a rough impression of how the deformation varies, one can study a plot where the relevant tests are shown in its entirety. To distinguish between different pH, the color blue is applied for creep tests performed in brine (pH=7.31) and red is used for the experiments conducted in a mixture of brine and acid (pH=3.14).

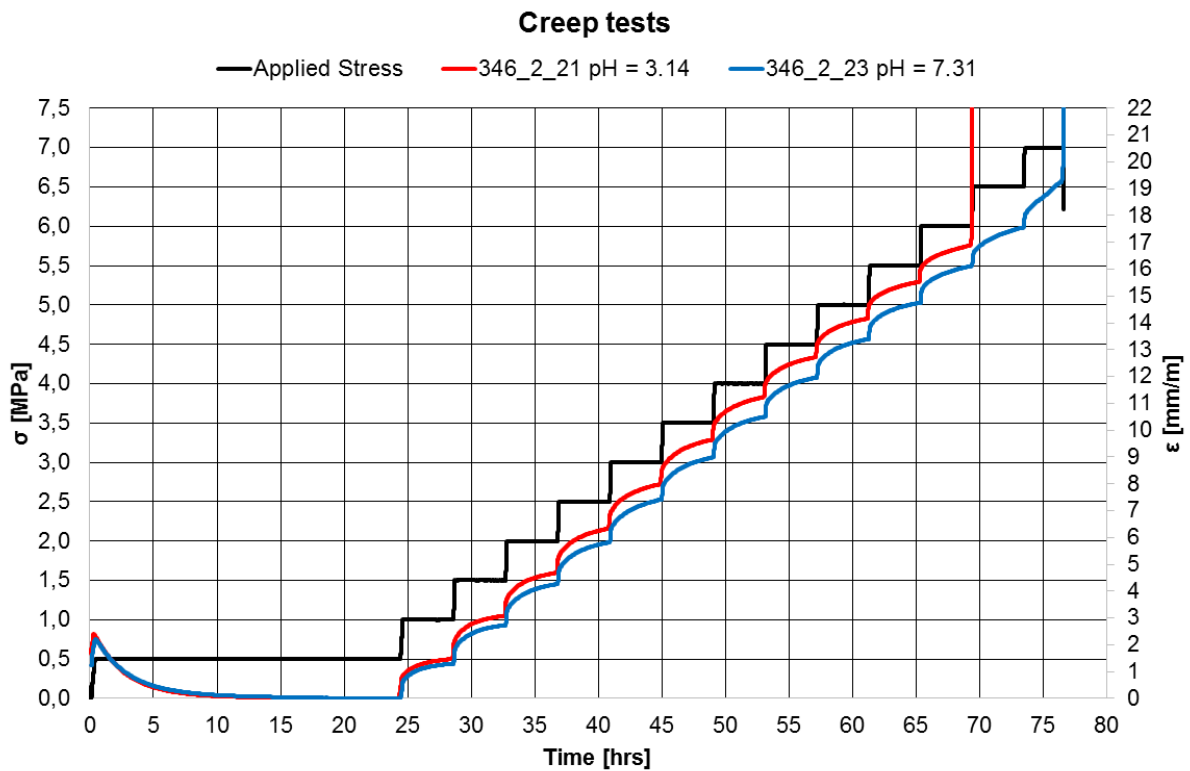


Figure 7.79: Stress and deformation for 346_2_21 versus 346_2_23.

By looking at creep test 346_2_21 versus 346_2_23, one can observe two different deformation paths. Figure 7.79 indicates that the strain is highest for the lowest pH, and it seems like the deviation accumulates throughout the test. Also, as one can see in the beginning of the experiments, the amount of swelling in the shales are approximately the same for both samples.

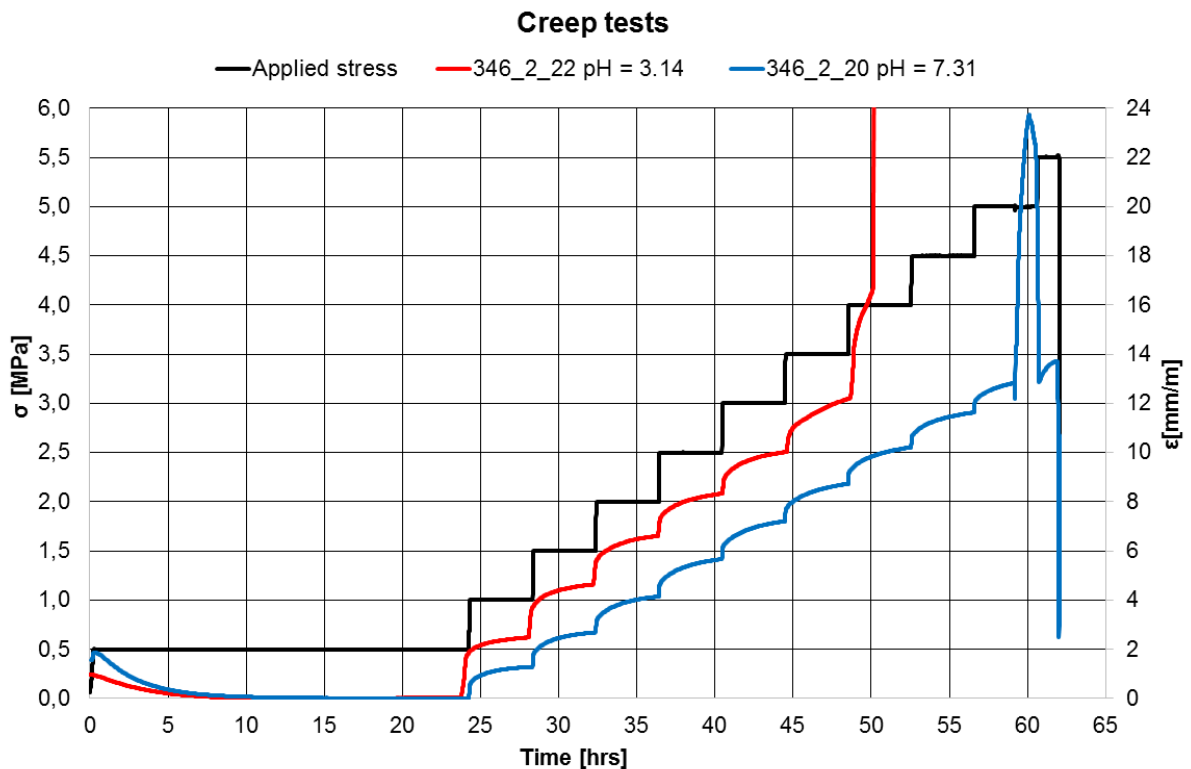


Figure 7.80: Stress and deformation for 346_2_20 versus 346_2_22.

Studying creep test 346_2_20 versus 346_2_22 demonstrates the same trend as found for the previous samples; the strain is highest for the lowest pH and the deviation accumulates throughout the test. As one can observe, a big part of the deformation takes place in the loading phases for the sample with the lowest pH, enhancing the described trend. Thus, to accurately identify how creep and consolidation are affected by change in pH, one should investigate the hold periods. Figure 7.80 also shows that the highest amount of swelling in this case appeared for the sample submerged in brine.

By examining the hold periods in detail for 346_2_21 versus 346_2_23 (Figure 7.81, Figure 7.82 and Figure 7.83), one clearly sees that the amount of strain is highest for the sample with the lowest pH. Further, it can be hard to differentiate between the two ongoing processes; creep and consolidation. As Figure 7.81 shows, the deviation between corresponding curves seems to be more or less constant at the end of a hold period. It looks like the discrepancy leading to different shapes of the curves mainly builds up in the beginning. This implies that consolidation might affect a sample saturated with acid more than a sample saturated with brine, resulting in overall higher amount of deformation for

low pH. However, one cannot draw a certain conclusion only based on this, other factors like creep rates should be investigated to potentially support the discussed observation.

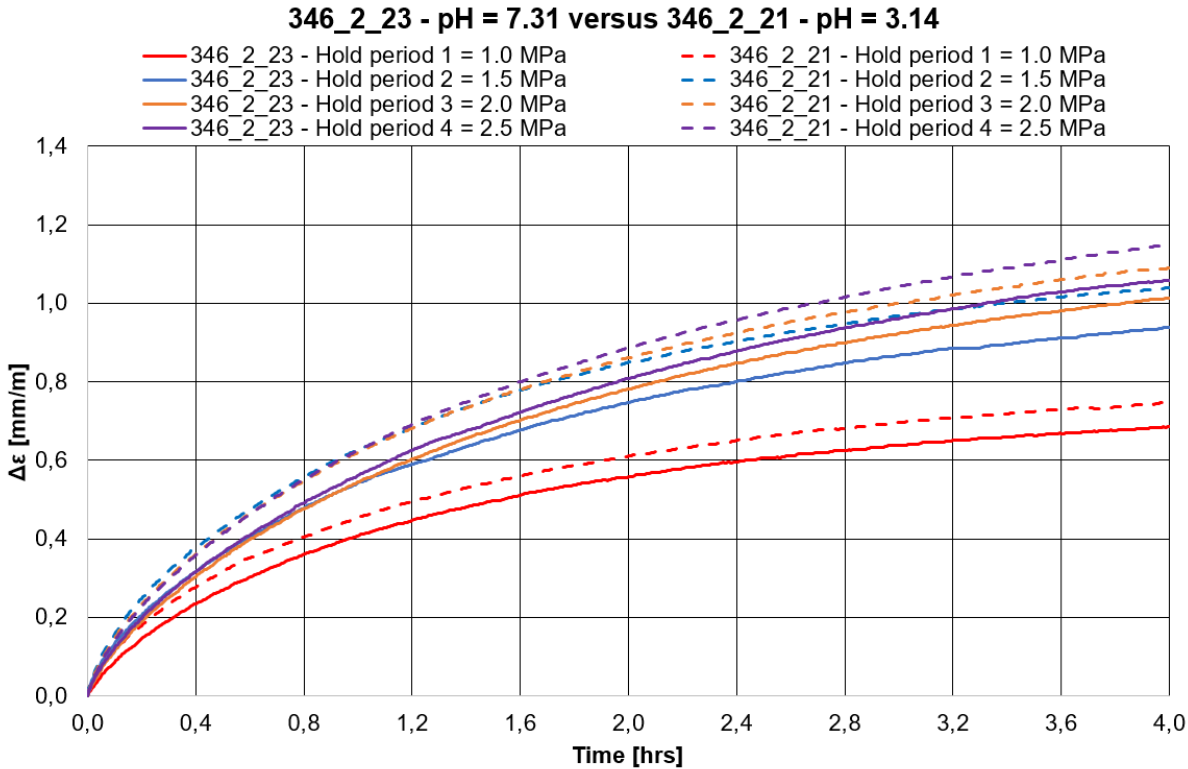


Figure 7.81: Hold periods 1-4 for 346_2_21 versus 346_2_23.

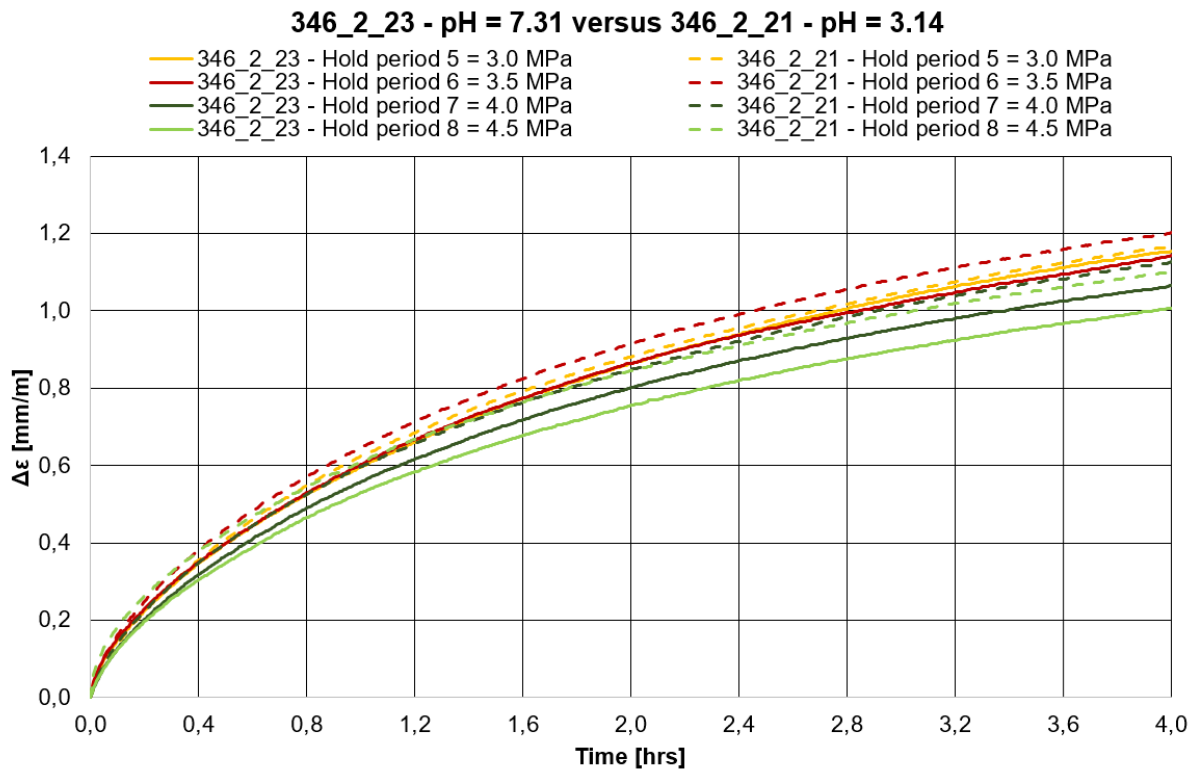


Figure 7.82: Hold periods 5-8 for 346_2_21 versus 346_2_23.

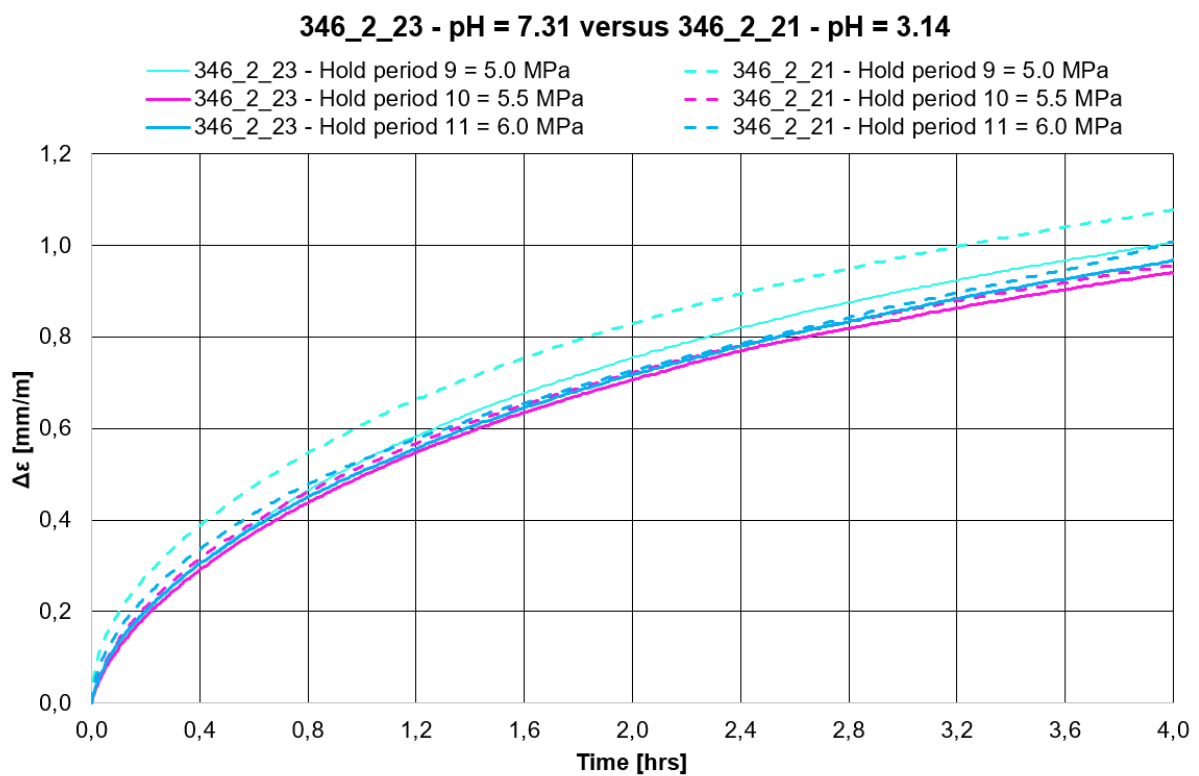


Figure 7.83: Hold periods 9-11 for 346_2_21 versus 346_2_23.

Further, Figure 7.84 presents the first three hold periods in detail for core sample 346_2_20 versus 346_2_22. As the figure demonstrates, except for hold period 2, the amount of strain is generally highest for the test with the lowest pH. This is consistent with previous findings.

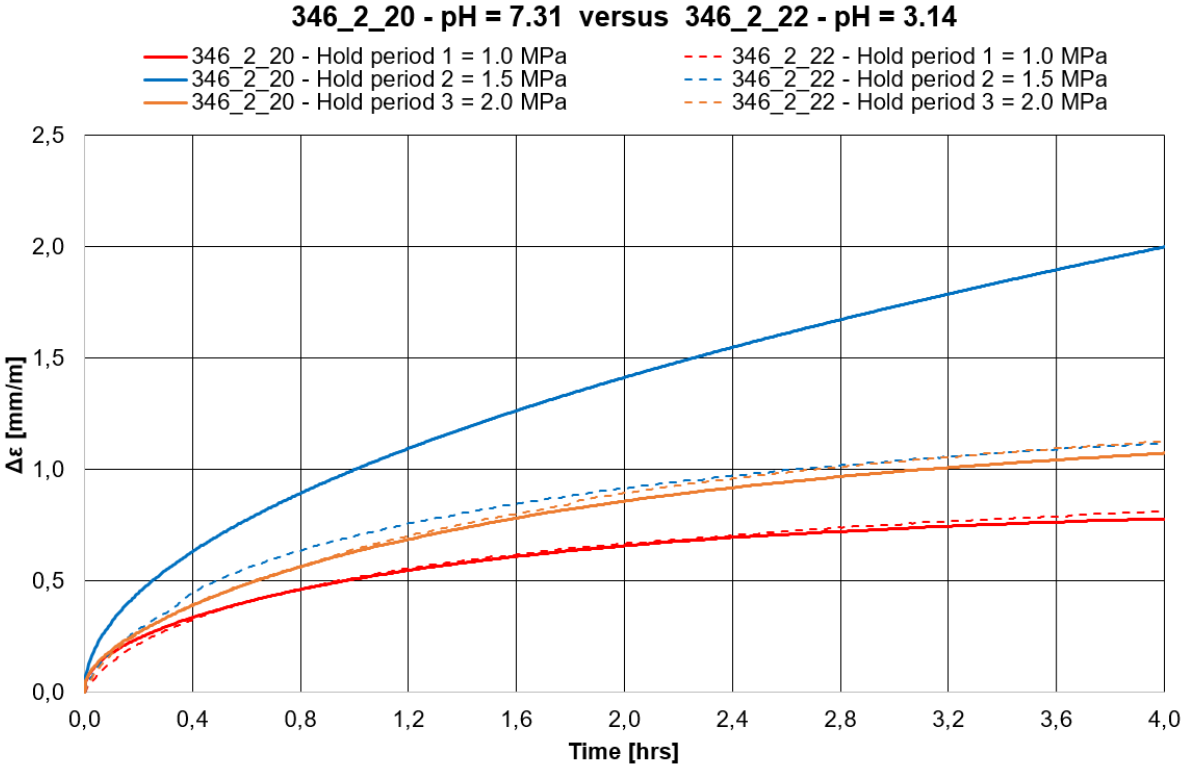


Figure 7.84: Hold periods 1-3 for 346_2_20 versus 346_2_22.

By looking at the final hold periods in Figure 7.85, one can observe that the amount of deformation in period 4 and 5 are more or less similar for the different pH-values. However, hold period 6 clearly agrees with previous findings; the amount of strain is highest for the lowest pH value.

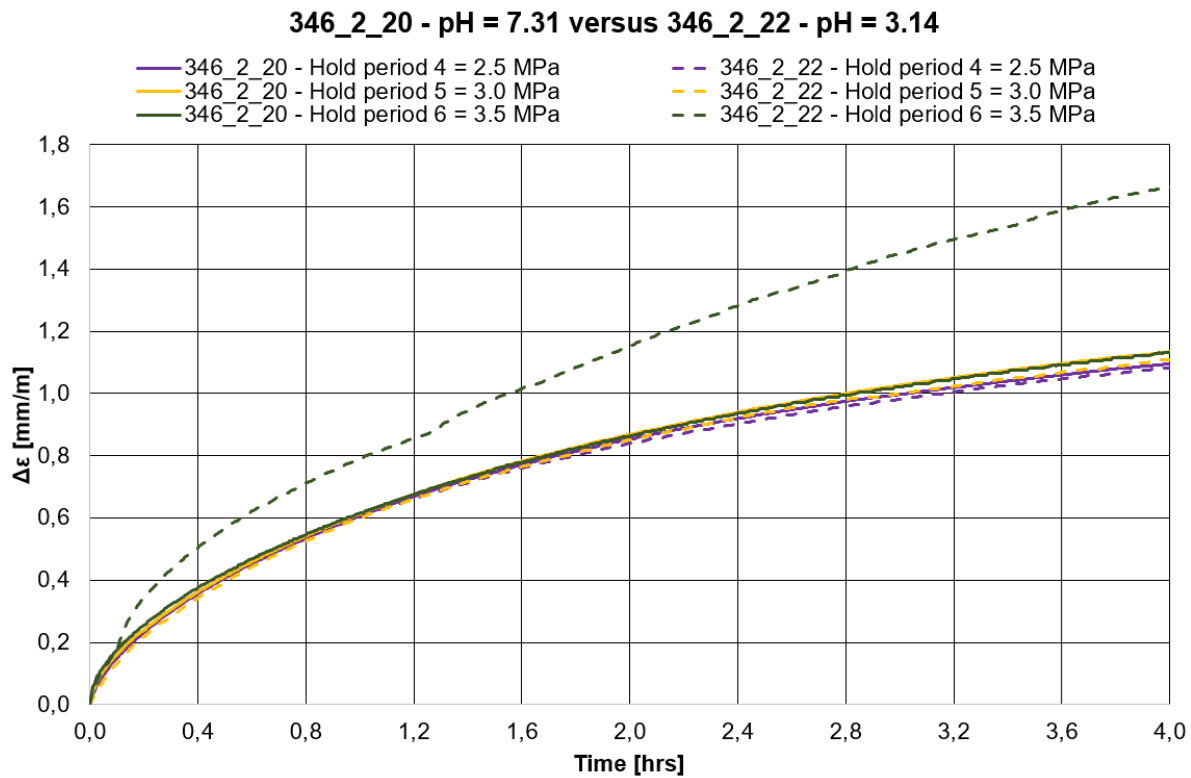


Figure 7.85: Hold periods 4-6 for 346_2_20 versus 346_2_22.

When using the same basis of comparison as above, one can see that the samples saturated with brine fails at higher stress levels than the corresponding cores saturated with acid (Figure 7.79 and Figure 7.80). Since creep in general weakens the rock, and the tests with the lowest pH value showed overall more creep, it is natural that they failed earlier than the samples in brine. The samples with low pH could potentially also have been weakened by chemical weathering due to acid. As a side note, core sample 346_2_20 is believed to have failed prematurely in brine due to the unfortunate lab incident.

Looking at change in initial stiffness throughout the tests (Table 7-23) illustrates that the samples with lower pH becomes stiffest at the end compared to the beginning. However, the samples in brine generally have the highest values of the parameter, implying overall stiffer samples. Fjær et al. (2008) states that the amount of consolidation is inversely proportional

to stiffness. Generally, considering this in conjunction with the findings above where the samples saturated with brine were found to have the least amount of deformation in the hold periods, one can speculate that stiffer shale creep less. This is consistent with the research of Li and Ghassemi (2012).

Table 7-23: Increase in initial stiffness from first to final loading phase.

Initial stiffness	346_2_20	346_2_21	346_2_22	346_2_23
First loading phase	0,9	0,7	0,3	0,8
Final loading phase	1,5	1,3	0,9	1,3
Increase in $E_{initial}$	38 %	44 %	66 %	36 %

As mentioned earlier, to further examine what can be characterized as consolidation effects and creep behavior for each hold period, one can look at deformation rates. One can assume that the consolidation process has more or less terminated at the end of a hold period. Hence, studying the last 15 min of fixed stress should presumably represent the creep phenomenon exclusively. Looking at the *average* creep rates for the brine tests and the acid tests separately for the last 15 min (Table 7-24 and Figure 7.86), demonstrates that the rates increase with applied stress as expected up to 3.5 MPa. After this a decline is seen before the rates go up again at the end. Overall, the plot indicates that the creep rates for a sample saturated with acid is generally higher than for brine. Even though the effect is not severe, it is still noticeable, and implies that low pH initiates more creep. This does not agree with the prediction based on the conducted literature study (section 3.2, p.35) where reduced pore fluid pH was assumed to result in less creep compared to a near-neutral environment. However, the relevant research was not based on shale, indicating that one should not anticipate to get the exact same results.

Table 7-24: Calculated creep rates for the final 15 min of the hold periods.

Hold period	Load [MPa]	LAST 15 MIN OF THE HOLD PERIOD				Average def. rates for BRINE	Average def. rates for ACID
		Deformation rates [(mm/m)/hrs]					
		346_2_20	346_2_23	346_2_21	346_2_22		
1	1,0	0,031	0,038	0,058	0,046	0,035	0,052
2	1,5	0,054	0,064	0,066	0,060	0,059	0,063
3	2,0	0,078	0,078	0,070	0,075	0,078	0,072
4	2,5	0,082	0,066	0,100	0,092	0,074	0,096
5	3,0	0,093	0,097	0,102	0,119	0,095	0,110
6	3,5	0,101	0,126	0,098	0,168	0,114	0,133
7	4,0	0,099	0,100	0,111	-	0,100	0,111
8	4,5	0,098	0,083	0,098	-	0,091	0,098
9	5,0	-	0,099	0,096	-	0,099	0,096
10	5,5	-	0,085	0,089	-	0,085	0,089
11	6,0	-	0,114	0,159	-	0,114	0,159
12	6,5	-	0,119	-	-	0,119	-

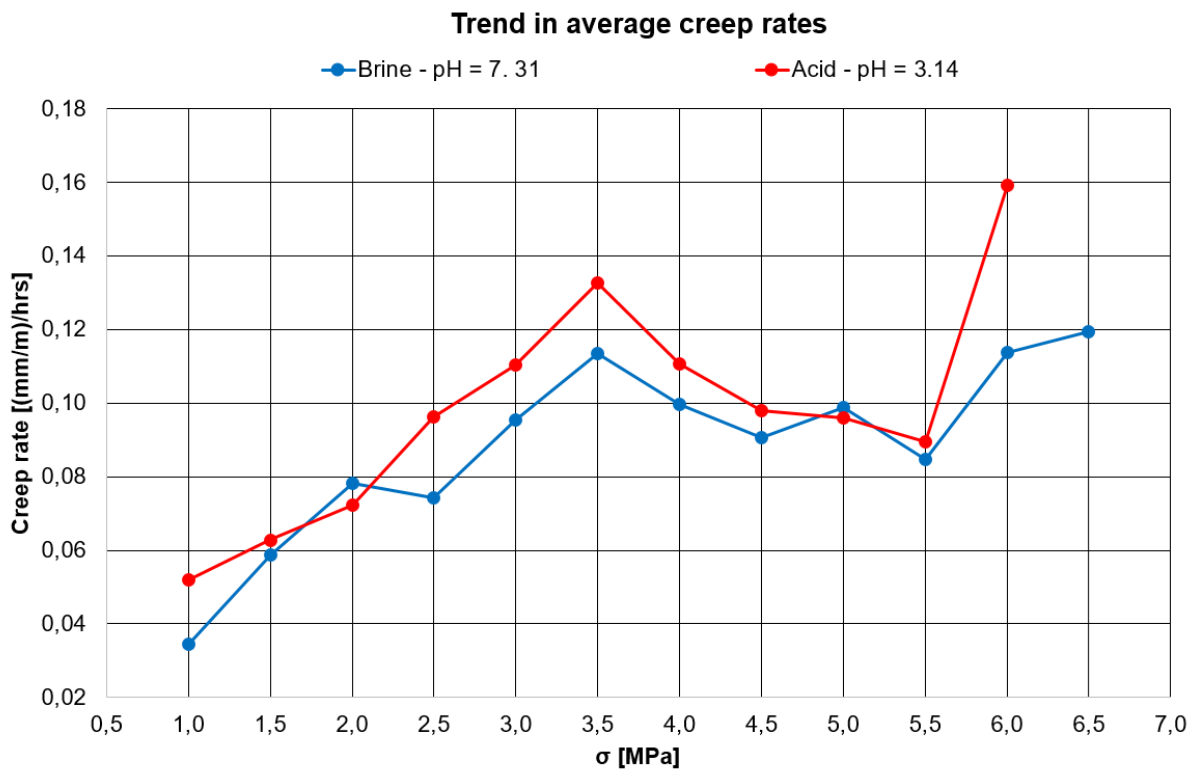


Figure 7.86: Trend in average creep rates for the final 15 min of the hold periods. Interpolation in Excel is used between the data points.

In addition to previously discussed findings, some final supplementary correlations were found:

- The magnitude of the p-wave velocities for the different chemical environments in the beginning and at the end of the tests were lowest for the samples with pH=3.14. The differences were not severe, but still worth mentioning.

Table 7-25: P-wave velocities in the beginning and at the end of the tests.

	First hold period	Final hold period
Core sample [#]	Vp-interval [m/s]	Vp-interval [m/s]
346_2_20	2520 - 2536	2648 - 2667
346_2_21	2449 - 2466	2640 - 2656
346_2_22	2432 - 2447	2527 - 2554
346_2_23	2459 - 2472	2656 - 2671

- Comparing the consolidation *times* (must not be mistaken for the consolidation amount) obtained through the graphical approach on a square root of time plot for core sample 346_2_23 and 346_2_21 (Figure 7.87), showed that the test in brine had the highest values of the parameter in general. Figure 7.88 illustrates more or less the same trend for the remaining tests, only with an exception for hold period 2 and 3 where the highest values were observed for a low pH environment.

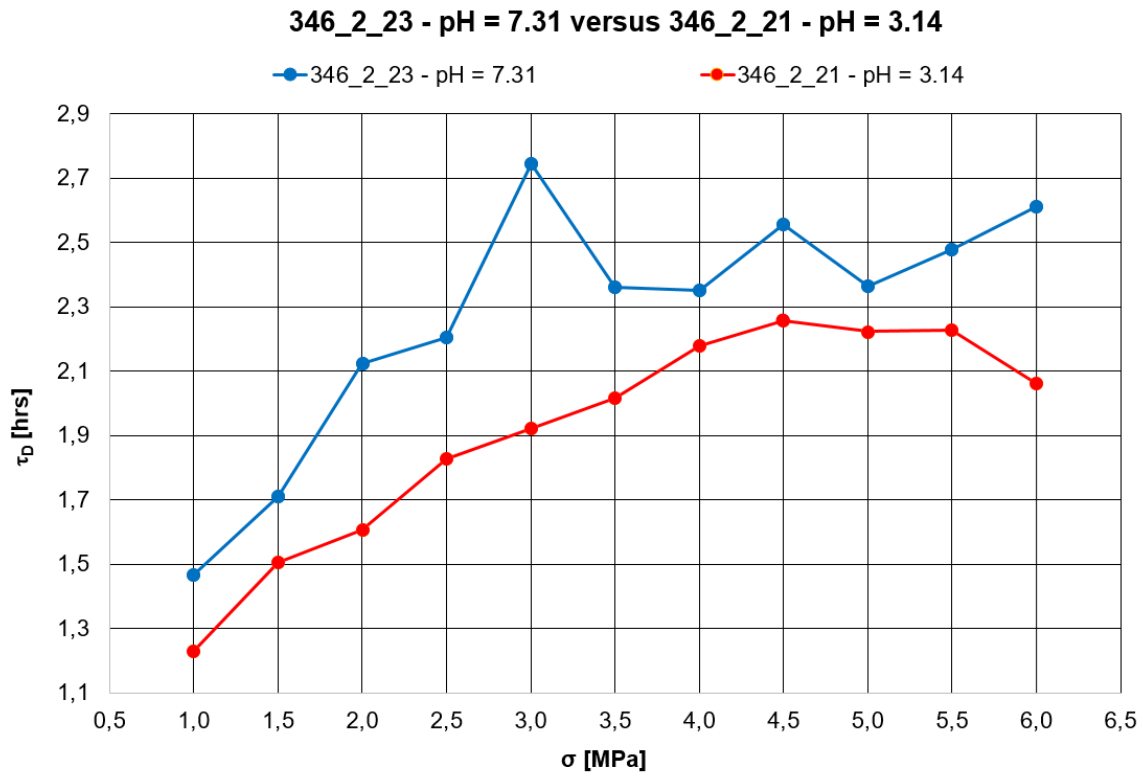


Figure 7.87: Obtained consolidation times through the graphical approach for core sample 346_2_23 and 346_2_21. Interpolation in Excel is used between the data points.

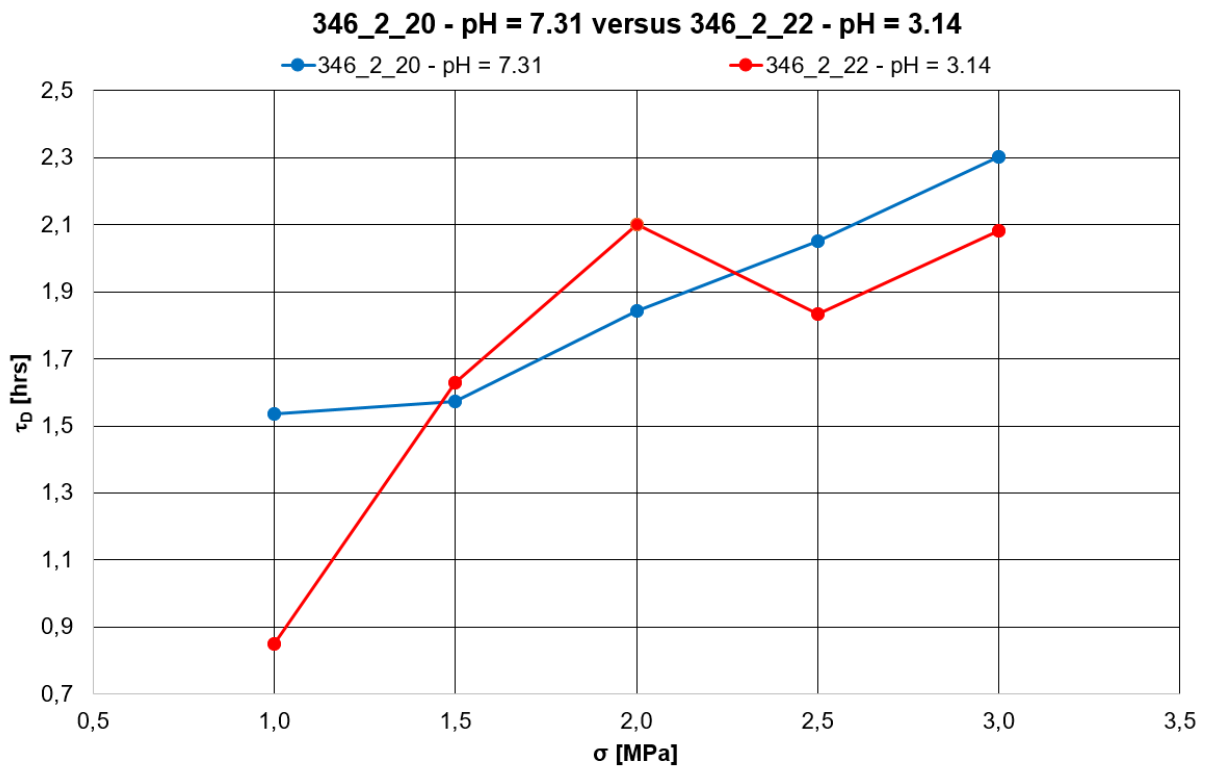


Figure 7.88: Obtained consolidation times through the graphical approach for core sample 346_2_20 and 346_2_22. Interpolation in Excel is used between the data points.

- A threshold for reaching steady-state creep phase was found for all tests (Table 7-26). It seems to be no significant difference in the parameter whether the pH value is low or near to neutral.

Table 7-26: Stress levels for reaching steady-state creep.

Threshold for reaching steady-state creep	346_2_20	346_2_21	346_2_22	346_2_23
Stress level [MPa]	2,0	2,5	2,0	1,5

7.3.2.2 Changes in stress conditions

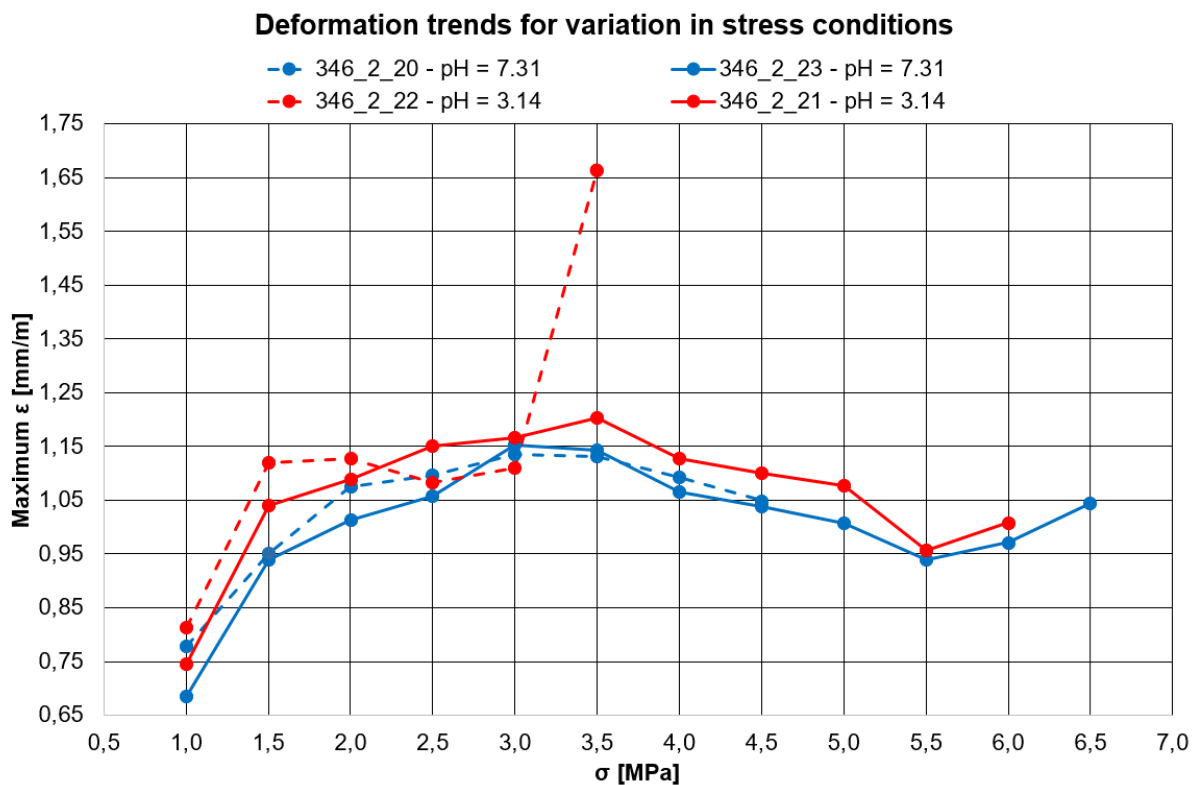


Figure 7.89: Deformation trends for variation in stress conditions. Interpolation in Excel is used between the data points.

Comparing all tests demonstrates a trend where the amount of deformation increases with applied stress up to a certain level before it declines and once again rises towards failure at the end (Figure 7.89). The stress level where the trend *shifts* varies for the different tests. This tendency was also observed for creep rates in Figure 7.86. Naturally, one assumes that deformation increases with load, but as found by Chang and Zoback (2008) the shale can behave slightly different above and below a certain stress level. They experienced an increase in strain prior to reaching this level, and a decrease after passing it. Studies showed

that this was due to a stiffening effect of the shale. Since an increase in $E_{initial}$ was also found for the relevant tests, one can assume that the behavior seen here might be explained by the same reason. A theoretical explanation of why it declines can be recognized as a consequence of a model described in Fjær et al. (2014). When applying load to a sample stepwise, it is not the load itself that promotes creep explicitly, deformation obtained from the loading phases also affects this mechanism. As previously demonstrated, a sample becomes stiffer for each ascending loading level, resulting in gradually less amount of deformation compared to the first loading phase of the test. Figure 7.90 demonstrates this exact effect for the relevant tests; initial deformation decreases for increased stress levels. When the rock becomes stiffer for ascending load levels, a certain part of the increase in load between the hold periods transition into a pure elastic deformation. This reduces the overall basis for creep, possibly causing the decline seen in Figure 7.89. Based on the theory, one could potentially prevent this reduction by applying gradually more load between the ascending hold periods to obtain the same amount of deformation for all loading phases. Overall, this theory might not be sufficient to explain the decline in its entirety, but one can presume that it probably has an impact. In addition, it is natural that the strain rises towards the end of the tests as the samples reach accelerating creep phase and eventually failure under a sufficiently high stress. This agrees with findings by Chu and Chang (1980).

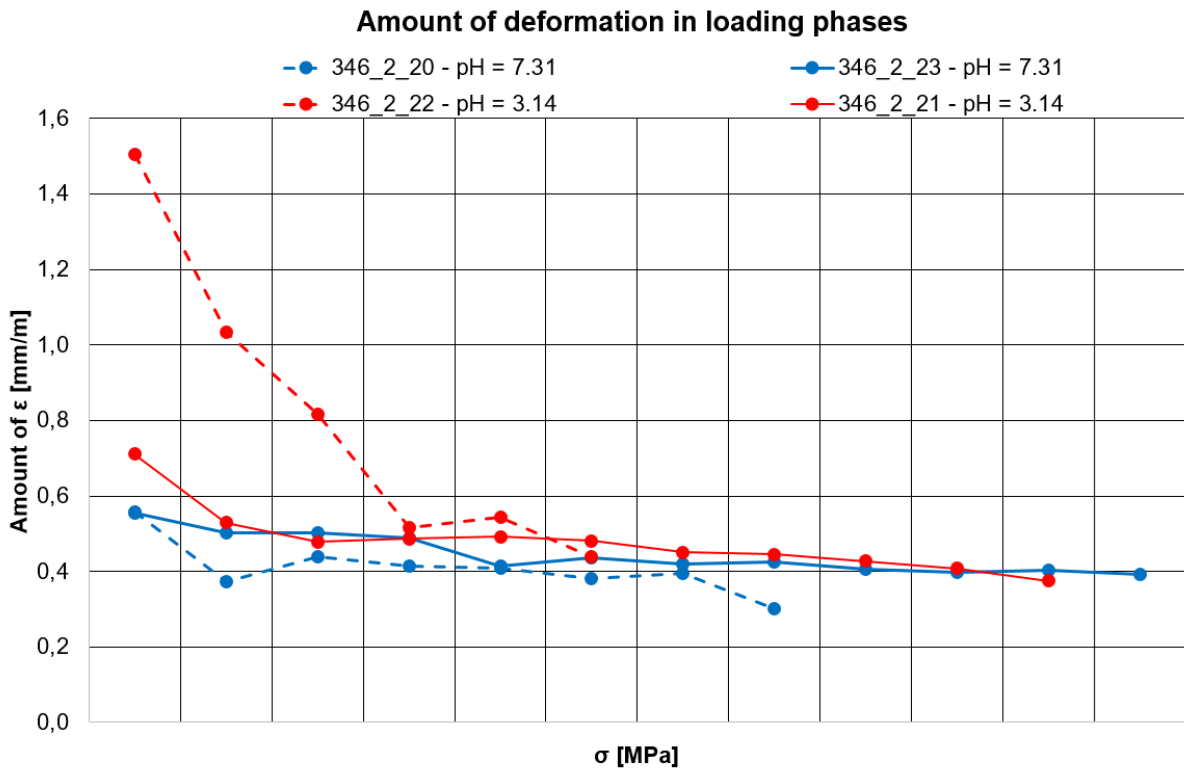


Figure 7.90: Decline in amount of deformation during the loading phases. Interpolation in Excel is used between the data points.

To identify the turning point between increasing and decreasing strain one can look at the deformation peak in conjunction with failure for the different tests (Figure 7.89). Table 7-27 shows that the samples reach approximately 43-55% of maximum load before the strain declines. Optimally, this correlation could have been exploited to approximately predict the stress level of failure if one had the opportunity to study the amount of deformation live during a test.

Table 7-27: Correlation between maximum strain and level of failure.

	346_2_20	346_2_21	346_2_22	346_2_23
Load level for maximum strain [MPa]	3,00	3,50	2,00	3,00
Load level for failure [MPa]	5,50	6,50	4,00	7,00
Load level at maximum amount of strain as percentage of load level at failure	54,5 %	53,8 %	50,0 %	42,9 %

Finally, variation in load levels initiate different phases of creep. Table 7-28 compares the creep phases for the relevant tests in the end of the hold periods (all data is extracted from earlier results). No clear correlation between load level and creep phase can be found.

Table 7-28: Creep phases in the last 15 min of each hold period. The periods where the samples failed are excluded.

Load [Mpa]	Creep phases			
	346_2_20	346_2_21	346_2_22	346_2_23
1,0	Stable	Stable	Transient	Stable
1,5	Stable	Stable	Transient	Steady-state
2,0	Steady-state	Transient	Steady-state	Steady-state
2,5	Transient	Steady-state	Steady-state	Transient
3,0	Transient	Transient	Accelerating	Transient
3,5	Steady-state	Transient		Not Defined
4,0	Steady-state	Steady-state		Steady-state
4,5	Steady-state	Steady-state		Transient
5,0		Steady-state		Steady-state
5,5		Steady-state		Transient
6,0		Accelerating		Not Defined
6,5				Steady-state

8 Potential sources of error

When conducting experiments in the laboratory, it is important to consider the possible sources of error that might impact final results.

8.1 Measurement of core dimensions

A slide caliper was used for measuring the cores' dimensions (described in section 5.2, p.51). Their diameter and length can vary throughout the sample depending on where measurements are performed. Taking several measurements of the same core to determine average diameter and length limits the inaccuracy. Also, since the measurements can depend on the person executing them, one should have the same person performing this task to obtain continuity.

8.2 Drying of shale samples

Rock properties of shale can drastically change if the sample dries out. For instance, a dry specimen will be weakened and reach failure much quicker. A sample can dry out rather quickly, thus it is important to keep it saturated with fluid at all times. Drying will most likely have the highest chance of happening when it is photographed before a test, due to heat emission from the studio lights. To avoid this one should act quickly and put the core sample right back into a fluid container after taking the required photos.

8.3 Loose grains

In the start of a test, there might be small, loose grains on top/bottom of the core/pistons that can potentially influence acquired strain data. Increasing the load on the setup will crush these small grains and the LVDTs will register this as axial deformation response. However, this should not be seen as a big issue for most of the conducted creep experiments since the essential data are collected after the ion diffusion process has completed (after 24 hours).

8.4 LVDTs

8.4.1 Calibration

To collect the most accurate data from an experiment, it requires that the LVDTs are correctly calibrated before startup. By doing this properly one can prevent imprecise results.

8.4.2 Noise

For a high LVDT sampling rate, the magnitude of axial displacement response becomes small for several stress steps in the beginning of an experiment. In this case, the CatMan software registers some noise of a magnitude higher than the total displacement response in the raw data. This is shown as a V-valley when plotting the deformations. To cancel out the noise, raw measured data can be averaged resulting in clear trends for the deformation.

8.5 Influence of room temperature

The room temperature at the lab varies during a test. People walk in and out of the door close to the setup all day long, and in addition, the air-condition switches on and off. As temperature variation can greatly impact deformation and creep behavior (as presented in section 3.1, p.31) it is important that it remains close to constant. To eliminate this potential problem a heating element was used to override the influence of the room temperature.

8.6 Heating element

In addition to providing a more or less constant temperature on the core sample in the experimental setup, the heating element also causes expansion of the steel equipment around it. The latter will influence the applied force on the system. To reduce the impact from this problem before startup, it is crucial to let the setup stabilize after turning on the heating element. For most of the creep tests, the first 24 hours involved a stabilization period to deal with this and in addition complete the ion diffusion process.

8.7 Setup of the experiment

In the experimental setup, there are different aspects to be aware of in terms of eliminating potential sources of errors. For instance it is essential that all LVDTs are screwed on tightly so they only measure relevant deformation in the system. Also, it is important that the container is placed directly under the center point of the loading frame to avoid uneven

distribution of the force through the sample. This is crucial because it can lead to increased local stress in parts of the sample and generate higher creep in these particular areas causing earlier failure.

8.8 Ion diffusion time

Based on calculations and performed experiments (described in section 4.4.3, p.45), the ion diffusion time was assumed to have a time frame between 12 hours and 2.8 days. These values were both rough estimates, thus it was impossible to know the exact value for this parameter. However, as the ion diffusion experiments showed time periods of 12-15 hours, it was decided to submerge the cores in the desired solution for 24 hours prior to the creep experiments, to ensure completion of the ion diffusion process.

8.9 pH meter

When screening brine and $HCl(aq)$ mixtures (described in section 4.4.2, p.44), a pH meter was used. This device is supposed to provide accurate pH-values for a solution when it is calibrated prior to usage. However, if it is not properly neutralized before or in-between measurements this might affect the accuracy of the device. Fortunately, as the required pH measurements for this laboratory work only aimed to distinguish between neutral and low pH trends and not specific values, this potential inaccuracy was not of great significance.

8.10 Equilibrium relative humidity measurements

To calculate chemical activity for different mixtures of brine and hydrochloric acid (described in Appendix IV, p.189), equilibrium relative humidity (ERH) was measured by placing fluid inside an ERH-cabinet. To get accurate results, it was important to make sure that the sensor performing the measurements was not covered with any vapor. This could potentially cause incorrect data as the sensor would not be able to operate correctly through the undesired coating. Also, to avoid other inaccuracies, it was significant to keep the fluid inside the cabinet until the measurement was stable. This could take from 1.5-24 hours and was indicated by flattening of a measured curve (ERH versus time) given in the display of the device. A leak in the cabinet was also suspected since some of the results showed lower values than established references, thus it was important to be aware of it and keep it in mind when processing the data.

9 Conclusion

By conducting uniaxial experiments on Pierre shale one is able to reveal genuine creep characteristics in addition to consolidation effects. The laboratory work in this master thesis resulted in 4 successful creep experiments where two of the tests were carried out for samples saturated with brine (pH=7.31) while the remaining tests concerned samples saturated with a mixture of brine and acid (pH=3.14).

Generally, it was seen that the temperature variation increased with extended test time for the conducted experiments. However, it appeared like the maximum temperature variation in the relevant creep tests (0.98°C) was too low to impact the deformation of Pierre shale.

Further, it was observed that p-wave velocities increased with applied stress, and a close to linear dependency between velocities and strain was found for all hold periods. Based on this, one can assume that p-wave velocities are dependent on strain as well as stress. Overall, the lowest velocities were seen for a low pH environment. In addition, the creep tests indicated a correlation between p-wave velocities and temperature; a significant drop in velocities was discovered for an enormous temperature increase.

Experimental results also demonstrated that creep behavior of Pierre shale is sensitive to applied stress. Changing the stress conditions affected the maximum amount of deformation in the hold periods and it appeared like the shale behaved differently before and after a certain test dependent stress level. Creep was found to increase with load as expected up to a certain level, before it declined slightly and eventually rised again towards failure at the end of a test. It is believed that this behavior can be related to a stiffening effect of the shale.

Finally, one of the main conclusions from the laboratory work is that the pH value of the pore fluid impacts consolidation and creep properties. Compared to brine, saturating a sample with a mixture of brine and acid reduced the overall stiffness and strength, resulting in more consolidation. A lower pH value showed generally more creep deformation of the samples and increased creep rates compared to a near-neutral pH environment.

10 Recommendations

10.1 Self-reflection

To share some of our own thoughts and learning points from completing this master thesis we decided to include a self-reflection section at the end. It has been inspiring and highly educational for us to be part of a SINTEF project investigating creep in shale formations. Our general knowledge concerning rock mechanics has increased greatly and we have gained valuable experience by working in a laboratory. It has been engaging to participate in work concerning creep tests with hydrochloric acid as this had never previously been done at the SINTEF Petroleum Research lab. We also learned that the topic had not been thoroughly investigated by others either as it was challenging to find relevant literature concerning creep in shale with alternating pore fluid pH. Hence, as our studies could potentially reveal new science, our motivation for working with this subject has been high. Hopefully, some of our obtained results will be helpful for SINTEFs further research.

In regards to working in the laboratory, we have truly learned the hard way that not everything will always go as planned. There was a lot of trial and error in the lab before a successful procedure and loading path could finally be established for the creep experiments. We were struggling with unwanted failure of the core samples during loading or hold periods with constant stress. Generally, working with shale in the lab is recognized as being challenging. We personally experienced that when completing the specialization project during the fall semester. However, introducing brine and hydrochloric acid to the creep experiments seemed to cause even more challenges than when previously working with marcol. Brine leads to swelling of the shale while acid causes weathering. This made the shale samples extra challenging to work with, thus it took some time and experimenting before a successful test procedure and loading path was developed. Looking back, it would probably have been wise to directly start the creep experiments with a stepwise loading path following increase of small stress increments. In this case, the UCS tests would not have been necessary and one would have ensured a greater collection of creep data from the beginning. This would have opened up for a chance to run more creep tests in general.

Overall, we are pleased with our work, but it would have been desirable with more time in the laboratory conducting additional creep experiments to support our conclusions. The

unfortunate lab incident with core sample 346_2_20 caused a delay in the lab work as new equipment had to be acquired before proceeding in addition to waiting for other students to finalize their work with the same apparatus. However, we believe that our master thesis has formed a good foundation and basis for a possible continuation of the work concerning creep and alternating pore fluid pH. We have confidence in that the presented work can be further developed with the advantage of learning from our shortcomings. As challenging chemical concepts were a part of this master thesis, cooperation between a chemical master student and a petroleum master student could be ideal for proceeding further with these studies.

10.2 Future work

In order to further investigate creep in shale with alternating pore fluid pH it will be essential to conduct additional creep tests in general to obtain more measured data. This way one will be able to draw more certain conclusions. In addition, one should also run the tests with more than two different pH-values; additional variation will clearer unveil which effect changing it has on the creep phenomenon. In regards to the loading path, it is believed to be a good idea to continue using a stepwise increase of small stress increments with hold periods in-between to obtain high quality measured data. It could be valuable to extend the time frame of the hold periods, and it might also be relevant to implement a small decrease in applied stress after a hold period to see what that generates. In addition, testing samples with differently drilled bedding planes could be significant. Generally, it would also be beneficial to apply established creep models when analyzing the obtained data.

For future laboratory work it will be ideal to use a container in the experimental setup that is fit for drainage and pumping of fluids. Further, it is significant to place the thermocouple data logger and the temperature controller at an elevated height in the experimental setup to avoid potential capillary suction of brine resulting in short circuiting of any equipment. Also, it is important to use molded temperature sensors and set an upper safety temperature value for when the temperature controller should disable during tests. Finally, as deformation is highly dependent on temperature, one should have focus on trying to achieve an even more stable temperature during future creep experiments.

List of abbreviations

EDXS	Energy Dispersive X-ray Spectroscopy
ERH	Equilibrium relative humidity
FE-SEM	Field-Emission Scanning Electron Microscope
LVDT	Linear variable differential transformers
NCS	Norwegian Continental Shelf
NORSOK	Norsk Søkkelts Konkurransesjisjon
NTNU	Norwegian University of Science and Technology
PEEK	Polyether ether ketone
pH	“Power of hydrogen”
PP&A	Permanent plug and abandonment
PSA	Petroleum Safety Authority of Norway
SEM	Scanning Electron Microscope
TOC	Total organic content
UCS	Uniaxial compressive strength
US	United States
USA	United States of America

Chemical terminology

Al	Aluminum
Ca	Calcium
CaCl ₂	Calcium chloride
CaCO ₃	Calcium carbonate

CO ₂	Carbon dioxide
Fe	Iron
H	Hydrogen
HCl	Hydrogen chloride
HCl (aq)	Hydrochloric acid
H ₂ O	Water
K	Potassium
KOH	Potassium hydroxide
Mg	Magnesium
Na	Sodium
NaCl	Sodium chloride
NaCl (aq)	Brine
NaOH	Sodium hydroxide
NH ₄ OH	Ammonium hydroxide
O	Oxygen
Si	Silicon

Nomenclature

a_{kj}	Chemical activity
a_A	Chemical activity of component A
A	Surface area
A_c	Cross section area
B	Skempton parameter
C	Biot's C-parameter
C_0	Unconfined compressional strength
C_D	Pore pressure diffusion constant
C_I	Ionic diffusion coefficient
E	Young's modulus
E_{dyn}	Dynamic Young's modulus
$E_{initial}$	Initial Young's modulus
E_{stat}	Static Young's modulus
f_A	Activity coefficient for component A
F	Additional non-elastic deformation caused by shear loading
F_n	Normal force
F_m	Force that represents the spontaneous tendency of molecules to disperse
F_p	Parallel force
g	Gravity constant
G	Shear modulus
G_{fr}	Shear modulus of the rock frame
h	Height difference

H	Uniaxial compaction modulus
H^+	Hydrogen ions
k	Permeability
k_0	Shape factor in the Carman-Kozeny equation
K	Bulk modulus
K_{dyn}	Dynamic bulk modulus
K_{fr}	Bulk modulus of the rock frame
K_s	Bulk modulus of the solid part of the rock
K_{stat}	Static bulk modulus
l_D	Pore pressure diffusion length
l_I	Ionic diffusion length
L	Length
$\left(\frac{L_e}{L}\right)^2$	Hydraulic “tortuosity factor” in the Carman-Kozeny equation
M	Biot’s M-parameter
P	Pressure
P_i	Non-elastic compliance (inverse of stiffness)
p_f	Pore pressure
Q	Flow rate of fluid
r	Radial direction
R^2	Coefficient of determination
S_0	Cohesion of the material
S_A	Specific surface area based on a solid’s volume
t	Time

T	Temperature
T_0	Tensile strength
T_{cp}	Threshold value for distinguishing between transient and steady-state creep phase at the end of a hold period
v_p	P-wave velocity
x	Position of ion
x_A	Molar concentration of a given ion
z	Axial direction

Greek symbols

σ	Stress
σ_{ij}	Total external stress
σ'_{ij}	Effective stress
τ	Shear stress
τ_D	Pore pressure diffusion time/Consolidation time
τ_I	Ionic diffusion time
\mathcal{E}_{vol}	Volumetric strain
\mathcal{E}	Elongation
$\Delta\mathcal{E}_z$	Vertical change in deformation during the loading phase in a creep test
η	Viscosity of the fluid
η_f	Dynamic viscosity of the fluid
ρ	Density
ζ	A strain parameter for the fluid part
ν	Poisson's ratio
α	Biot coefficient

α_T	Coefficient of linear expansion
β	Orientation of the failure plane
ϕ	Porosity
φ	Friction angle
λ	Lamé 1 st coefficient
μ	Chemical potential
π	Osmotic pressure
γ	Shear strain
ψ	The change in angle between two initially orthogonal directions

Bibliography

Almon, W. R., & Davies, D. K. (1981). Formation damage and the crystal chemistry of clays. Short course in clays and the resource geologist: Montreal, Mineralogical Association of Canada, 7, 81-102.

Askew, J. (2012). Chemistry class 21. pH and the pH Scale, Crecent High School, Oklahoma. Last visited 22.01.2016: <http://crescentok.com/staff/jaskew/isr/chemistry/class21.htm>

Atkins, P. & De Paula, J. (2006) Atkins` physical chemistry, 8th edition.

Balashov, V. N., Guthrie, G. D., Lopano, C. L., Hakala, J. A., & Brantley, S. L. (2015). Reaction and diffusion at the reservoir/shale interface during CO₂ storage: Impact of geochemical kinetics. *Applied Geochemistry*, 61, 119-131.

Birkeland, P.W. (1974). *Pedology, Weathering, and Geomorphological Research*. Oxford University Press, New York.

Cath, T.Y., Childress, A.E., Elimelech, M. (2006). Forward osmosis: Principles, applications, and recent developments, *Journal of Membrane Science*, Volume 281, Issues 1–2, Pages 70-87, ISSN 0376-7388.

Cauvain, S. P., & Young, L. S. (2009). *Bakery food manufacture and quality: water control and effects*. John Wiley & Sons.

Chang, C. and M. D. Zoback (2008). Creep in unconsolidated shale and its implication on rock physical properties, American Rock Mechanics Association.

Chermak, J. A. (1992). Low temperature experimental investigation of the effect of high pH NaOH solutions on the Opalinus Shale, Switzerland. *Clays and Clay Minerals*, 40, 650-650.

Chigira, M., Oyama, T. (1999). Mechanism and effect of chemical weathering of sedimentary rocks. *Engin. Geol.* 55, 3-14.

Chong, K.P, Smith, J.W, Khaliki, B.A (1978). Creep and relaxation of oil shale. Proc 19th US Symposium on Rock Mechanics, Stateline, Nevada, 1–3 May 1978, V1, P414–418. Publ Reno: University of Nevada, 1978.

Christensen, N. I. (1982). Seismic velocities. In: Carmichael, R.S (Ed.), *Handbook of Physical Properties of Rocks*. Vol. II. CRC Press, pp.2-228.

Chu, M.S, Chang, N.Y (1980). Uniaxial creep of oil shale under elevated temperatures. Proc 21st US Symposium on Rock Mechanics, Rolla, Missouri, 28–30 May 1980, P207–216. *International Journal of Rock Mechanics and Mining Sciences and Geomechanics Abstracts*, 18(4), 67.

Cogan, J. (1976). "Triaxial creep tests of Opohonga limestone and Ophir shale." *International Journal of Rock Mechanics and Mining Sciences & Geomechanics Abstracts* 13(1): 1-10.

Detournay, E., Cheng, A.H.-D. (1993). Fundamentals of poroelasticity, Chapter 5 in *Comprehensive Rock Engineering: Principles, Practice and Projects*, Vol. II, Analysis and Design Method, ed. C. Fairhurst, Pergamon Press, pp.113-171.

- Dullien, F.A.L. (1992) Porous media: fluid transport and pore structure. Academic press.
- Egeland, E. S., (2015). Store norske leksikon. "I kjemisk Analyse". Last visited 11.02.2016: <https://snl.no/aktivitet%2Fkjemi>.
- Fjær, E. (1999). Static and dynamic moduli of weak sandstones. In: Amadei, B., Kranz, R.L., Scott, G.A., Smeallie, P.H. (Eds.), Rock Mechanics for Industry. Balkema, pp. 675-681.
- Fjær, E. (2006). Modeling the stress dependence of elastic wave velocities in soft rocks. The 41st U.S. Symposium on Rock Mechanics (USRMS): 50 Years of Rock Mechanics – Landmarks and Future Challenges. Golden, CO: ARMA.
- Fjær, E., Holt, R., Horsrud, P., Raaen, A., & Risnes, R. (2008). Petroleum Related Rock Mechanics 2nd Edition. Oxford: Elsevier B.V.
- Fjær, E., Larsen, I., Holt, R. M., & Bauer, A. (2014, August). A creepy model for creep. In 48th US Rock Mechanics/Geomechanics Symposium. American Rock Mechanics Association.
- Fooks, J. C., & Dusseault, M. B. (1996). Strength of Pierre I Shale As Function of Moisture Content. International Society for Rock Mechanics.
- Geertsma, J. (1957). A remark on the analogy between thermoelasticity and the elasticity of saturated porous media, J. Mech. Phys. Solids, 6, 13-6.
- Ghassemi, A., and Suarez-Rivera, R. (2012). Sustaining fracture area and conductivity of shale gas reservoirs for enhancing long-term production and recovery. Research Partnership to Secure Energy for America, 08122-48, College Station, TX.
- Goldich, S.S. (1938). A study in rock weathering. J. Geol. 46, 17-58.
- Hangx, S. J. T., Spiers, C. J., & Peach, C. J. (2010). Creep of simulated reservoir sands and coupled chemical-mechanical effects of CO₂ injection. Journal of Geophysical Research: Solid Earth, 115(B9).
- Hillewaert, H., (2007. February) Osmose. Last visited 02.02.2016: <https://commons.wikimedia.org/wiki/File:Osmose.svg>
- Holt, R. (2013). Poroelasticity, Lecture in TPG4185.
- Horsrud, P., Holt, R.M., Sonstebo, E.F., Svano, G., Bostrom, B. (1994). Time dependent borehole stability: Laboratory studies and numerical simulation of different mechanisms in shale. SPE 28060.
- Jaeger, J. C., Cook, N. W., & Zimmerman, R. W. (2007). *Fundamentals of Rock Mechanics*. Malden, MA: Wiley-Blackwell.
- Jensen, William B. (2004). The Symbol for pH. Department of Chemistry, University of Cincinnati, J. Chem. Educ., 2004, 81, 21.
- Lal, M. (1999). Shale Stability: Drilling Fluid Interaction and Shale Strength. Society of Petroleum Engineers. doi:10.2118/54356-MS.

- Li, Y., & Ghassemi, A. (2012). Creep Behavior of Barnett, Haynesville, And Marcellus Shale. American Rock Mechanics Association.
- Lim, Kieran F. (2006). Negative pH Does Exist. *Journal of Chemical Education* 83(10): 1465
- Liu, J. and R. Zhou (2000). Mechanical Effects of Water Content in the Creep Parameters, American Rock Mechanics Association.
- Lo, K., & Lee, Y. (1990). Time-dependent deformation behaviour of Queenston shale. *Canadian Geotechnical Journal*, 27(4), 461-471.
- Mamo, M. (2016). Department of Agronomy and Horticulture , University of Nebraska-Lincoln, USA. 2.3 Types of weathering – Chemical. Last visited 22.02.16:
<http://passel.unl.edu/pages/informationmodule.php?idinformationmodule=1124303183&to picorder=4&maxto=7>
- Mese, A. I., & Tutuncu, A. N. (1996). An Experimental Investigation For Relationship Between Physicochemical And Acoustic Properties of Pure Kaolinite And Pierre Shale. Society of Exploration Geophysicists.
- Meyers and Chawla (1999): "Mechanical Behavior of Materials", 98-103.
- Mishra, B. and P. Verma (2015). "Uniaxial and triaxial single and multistage creep tests on coal-measure shale rocks." *International Journal of Coal Geology* 137: 55-65.
- Mungan, N. (1965). Permeability Reduction Through Changes in pH and Salinity. Society of Petroleum Engineers.
- Muniz, A. and Abildsnes, K. (2009). Cappelen Damm, Helsefremmende arbeid – 10 (9) Transport i kroppen: Respirasjon og sirkulasjon. Last visited 12.02.16:
<http://helseogsosialfag.cappelendamm.no/c562052/artikkel/vis.html?tid=101126>
- Nakken, S.J, Christensen, T.J, Marsden, R., Holt, R.M. (1989). Mechanical behavior of clays at high stress levels for wellbore stability applications.
- Norris, A. (1992). On the correspondence between poroelasticity and thermoelasticity, *J. Appl. Phys.*, 71, 1138-41.
- NORSOK Standard D-010, rev. June 2013
- NPD, Fakta 2014 Norsk Petroleumsverksemd
- NPTEL (2015). E-learning course "Introduction to soil mechanics". Last visited 01.02.2016:
<http://nptel.ac.in/courses/105103097/web/chap9final/s7.htm>
- Olabode, A., & Radonjic, M. (2013). Experimental investigations of caprock integrity in CO₂ sequestration. *Energy Procedia*, 37, 5014-5025.
- Olabode, A., & Radonjic, M. (2014). Diagenetic Influence on Fracture Conductivity in Tight Shale and CO₂ Sequestration. *Energy Procedia*, 63, 5021-5031.

- Olsen, R. A. (2015). Investigation of Creep Characteristics for Stresses close to Failure (*Unpublished master thesis*). Norwegian University of Science and Technology, Trondheim, Norway.
- Petsch, S. T., Berner, R. A., & Eglinton, T. I. (2000). A field study of the chemical weathering of ancient sedimentary organic matter. *Organic Geochemistry*, 31(5), 475-487.
- Pool, J., (2008 August) Example of diffusion. Last visited 09.02.2016:
http://faculty.southwest.tn.edu/jiwilliams/diffusion_of_a_dye_in_water.htm.
- Pruess, K. and Bodvarsson, G.S. (1984). Thermal effects of reinjection in geothermal reservoirs with masjon vertical fractures, *J. Petrol. Tech.*, 36, 1567-78.
- Rogers, D.V. (2015). Image from <http://allshookup.org/quakes/wavetype.htm>. Last visited 01.02.2016.
- Rongzun, H., Zuhui, Z., & Jingen, D. (1987). The Creep Characteristics of Shale Formation And the Analysis of Its Loading On the Oil Well Casing. *International Society for Rock Mechanics*.
- Samson, E., Marchand, J. and Snyder, K.A. (2003) *Materials and Structures* Vol. 36, pp 156-165
- Sangesland, S., et. al. (2012). "An Introduction to Well Integrity", *Compendium*, Rev 0.
- Savage, W. Z. and W. A. Braddock (1991). "A model for hydrostatic consolidation of Pierre shale." *International Journal of Rock Mechanics and Mining Sciences & Geomechanics Abstracts* 28(5): 345-354
- Schultz, L.G, Tourtelot, H.A, Gill, J.R, Boerngen, J.G. (1980). *Composition and Properties of the Pierre Shale and Equivalent Rocks, Northern Great Plains Region*. Geological survey professional paper 1064-B, United States Government Printing Office, Washington.
- Skalle, P. (2014). *Drilling Fluid Engineering*, 5th Edition.
- Somiya, Shigeyuki (2013). *Handbook of Advanced Ceramics: Materials, Applications, Processing, and Properties*. Academic Press.
- Sone, H. and M. D. Zoback (2010). *Strength, Creep And Frictional Properties of Gas Shale Reservoir Rocks*, American Rock Mechanics Association.
- Sone, H. and M. D. Zoback (2014). "Time-dependent deformation of shale gas reservoir rocks and its long-term effect on the in situ state of stress." *International Journal of Rock Mechanics and Mining Sciences* 69: 120-132.
- Steward, H.E., Cripps, J.C. (1983). *Quarterly Journal of Engineering Geology and Hydrogeology*, 16, 281-289.
- Sørensen, S. P. L. (1909). *Enzyme Studies II. The Measurement and Meaning of Hydrogen Ion Concentration in Enzymatic Processes*. *Biochemische Zeitschrift* 21, p.131-200.

Tuttle, M. L., & Breit, G. N. (2009). Weathering of the New Albany Shale, Kentucky, USA: I. Weathering zones defined by mineralogy and major-element composition. *Applied Geochemistry*, 24(8), 1549-1564.

Villamor Lora, R., & Ghazanfari, E. (2015). Creep Behavior of Shale Formations in Shale Gas Development. In *IFCEE 2015* (pp. 2024-2033). ASCE.

Wang, J., Kalinichev, A. G., & Kirkpatrick, R. J. (2006). Effects of substrate structure and composition on the structure, dynamics, and energetics of water at mineral surfaces: A molecular dynamics modeling study. *Geochimica et cosmochimica acta*, 70(3), 562-582.

Williams, S. M., Carlsen, T., Constable, K. C., & Guldahl, A. C. (2009). Identification and Qualification of Shale Annular Barriers Using Wireline Logs During Plug and Abandonment Operations. Society of Petroleum Engineers, SPE-119321-MS. Presented at SPE/IADC Drilling Conference and Exhibition, 17-19 March, Amsterdam, The Netherlands

Wu, W., & Sharma, M. M. (2015). Acid Fracturing Shales: Effect of Dilute Acid on Properties and Pore Structure of Shale. In SPE Hydraulic Fracturing Technology Conference. Society of Petroleum Engineers.

Zumdahl, Steven S. (2009). *Chemical Principles*, Sixth Edition, Brooks/Cole, Cengage Learning.

Appendix I. Calculations of expected consolidation time

As described in section 4.4.1 (p.44), the calculations for estimating the expected consolidation time in Pierre shale will be presented here. Some of the parameters used for the calculations were obtained from Table 2-2 (p.29) showing approximate values for properties of Pierre shale, while others, like permeability and viscosity, were assumed. Overall, a summary of the chosen parameters are presented below.

Table I- 1: Parameters used in calculations.

Diameter [m]	l_D [m]	Poisson ratio [-]	Bulk modulus [GPa]	Viscosity [Pa·s]	Permeability [m ²]
0.0254	0.0127	0.36	1	10 ⁻³	3.95·10 ⁻²⁰

As described in section 2.3.2 (p.17), the consolidation time τ_D can be calculated through the following equation;

$$\tau_D = \frac{l_D^2}{C_D} \quad \text{Appendix I-1}$$

The diffusion length l_D is already given in the table above, and to determine the pore pressure diffusion constant C_D , one can apply equation (2.19) (p.20). As previously mentioned in section 2.3.2 (p.17), there are generally several equations to choose from when estimating C_D , but this equation was suggested by supervisor Erling Fjær. Ahead of using the equation one needs to calculate the shear- and bulk modulus of the rock frame;

$$G_{fr} = \frac{E}{2(1+\nu)} = \frac{1.0 \text{ GPa}}{2(1+0.65)} = 0.37 \text{ GPa} \quad \text{Appendix I-2}$$

$$K_{fr} = \frac{E}{3(1-2\nu)} = \frac{1.0 \text{ GPa}}{3(1-2 \cdot 0.36)} = 1.19 \text{ GPa} \quad \text{Appendix I-3}$$

Eventually, this results in the following pore pressure diffusion constant

$$C_D \rightarrow \frac{k}{\eta_f} \left(K_{fr} + \frac{4}{3} G_{fr} \right)$$

$$= \frac{3.95 \cdot 10^{-20} m^2}{1 \cdot 10^{-3} Pa \cdot s} \left(1.19 \cdot 10^9 Pa + \frac{4}{3} \cdot 0.37 \cdot 10^9 Pa \right) = 6.63 \cdot 10^{-8} \frac{m^2}{s}$$

Appendix I-4

Finally, equation (Appendix I-1) gives the approximate consolidation time for Pierre shale

$$\tau_D = \frac{0.0127^2}{6.63 \cdot 10^{-8} \frac{m^2}{s}} = 2432.19s \approx 40.5 \text{ min} \approx \underline{\underline{0.68 \text{ hrs}}}$$

Appendix I-5

Appendix II. Estimation of ion diffusion time

Summary of experimental settings

Table II- 1: Summary of experimental settings for the ion diffusion tests.

Core sample [#]	Submerged in fluid	Crosshead speed [mm/min]	Average running speed [MPa/hrs]	Time before stable [hrs]
346_2_10	Brine	0,0075	1,56	12
346_2_11	Brine	0,0075	1,62	15
346_2_14	Mixture of brine and HCl	0,0075	1,45	14

All ion diffusion tests were performed at 30°C and at a load level of 0.5 MPa.

Core sample 346_2_10

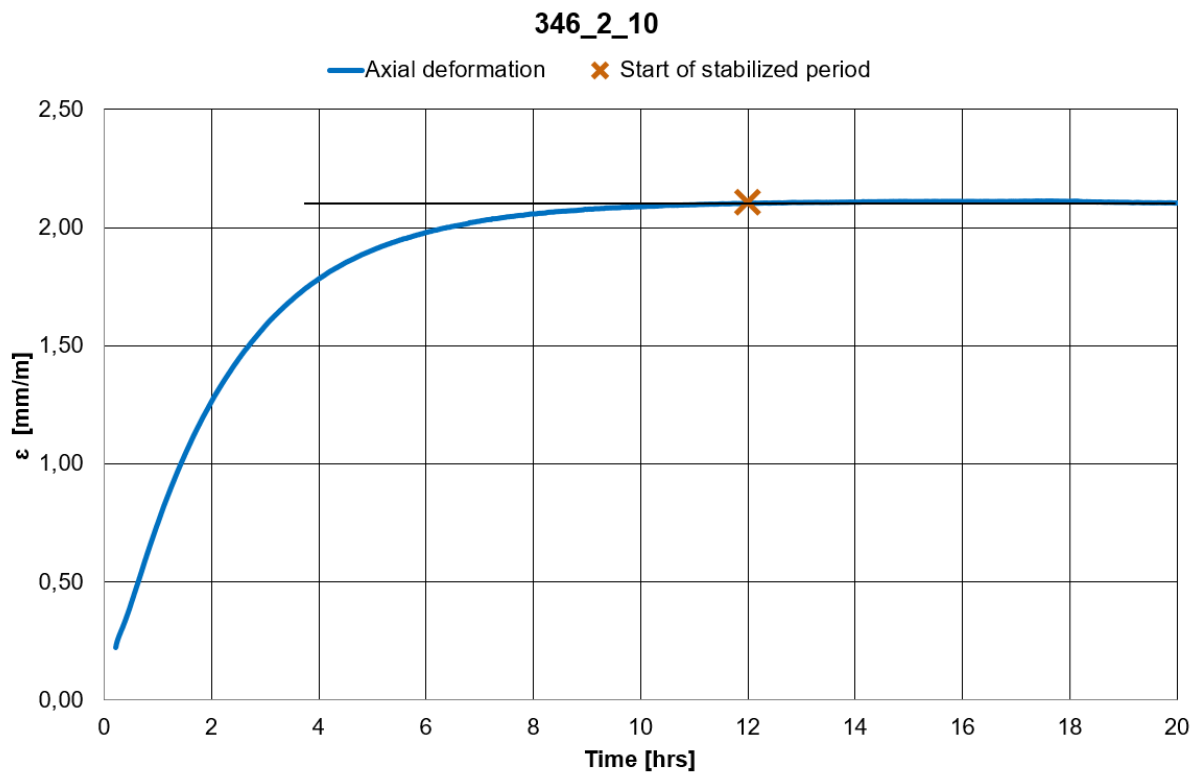


Figure II- 1: Strain vs. time for core sample 346_2_10.

As Figure II-1 shows, the deformation of the sample was stable after approximately 12 hours in brine.

Core sample 346_2_11

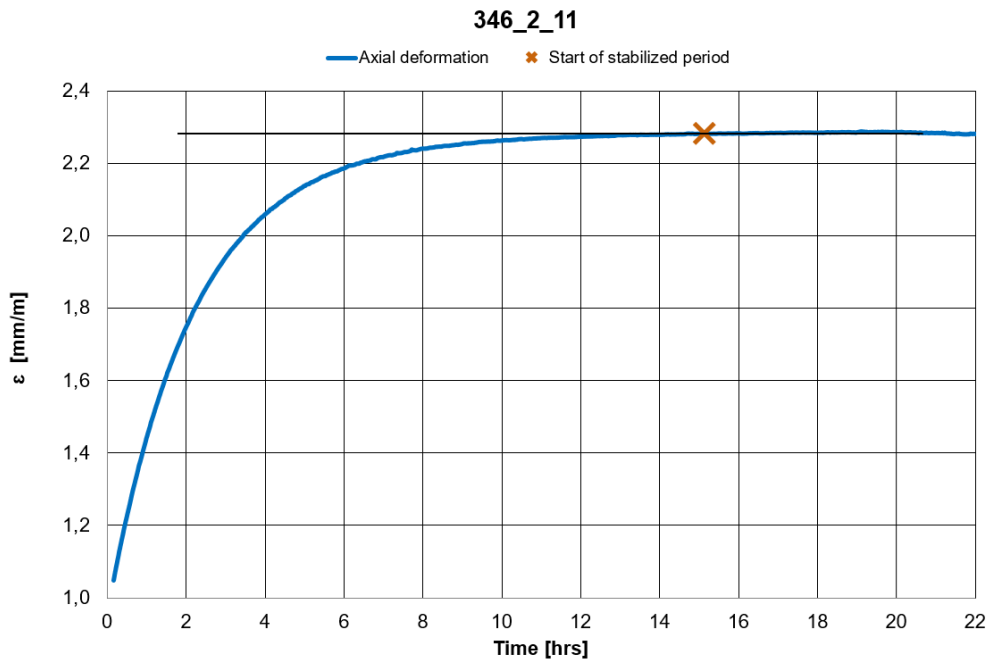


Figure II- 2: Strain vs. time for core sample 346_2_11.

As Figure II-2 demonstrates, the deformation of the sample was stable after approximately 15 hours in brine.

Core sample 346_2_14

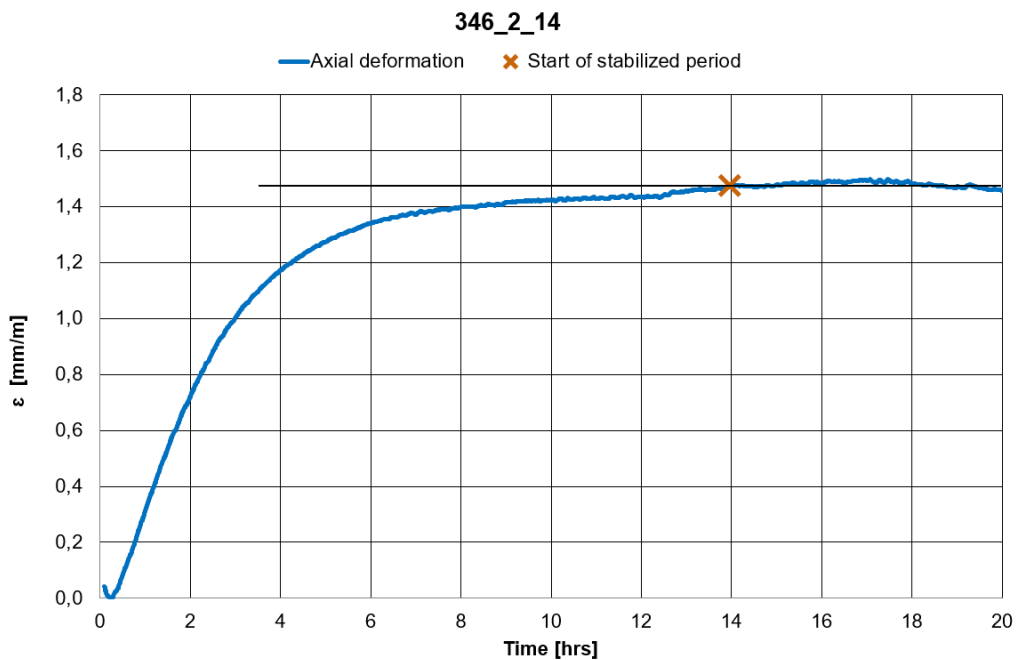


Figure II- 3: Strain vs. time for core sample 346_2_14.

As Figure II-3 shows, the deformation of the sample was stable after approximately 14 hours in a mixture of brine and $HCl(aq)$.

Appendix III. Defining uniaxial compressive strength

Summary of experimental settings

Table III- 1: Summary of experimental settings for the UCS tests.

Core sample [#]	Submerged in fluid	Pre-load [MPa]	Crosshead speed [mm/min]	Average running speed [MPa/hrs]	UCS [MPa]
346_2_10	Brine	0,5	0,0030	1,04	9,2
346_2_11	Brine	0,5	0,0030	1,09	9,2
346_2_14	Mixture of brine and HCl	0,5	0,0030	0,96	7,7
346_2_16	Brine	-	0,0030	0,70	3,6

All UCS tests were run at 30°C. The first three UCS tests were all extensions of ion diffusion experiments, and the crosshead speed was based on experience from the performed laboratory work in the specialization project. As the optimal running speed was desired to be approximately 1.0 MPa/hr, the crosshead speed in the final UCS test was set identical to the previous UCS experiments since they had more or less obtained the preferred value.

Core sample 346_2_10

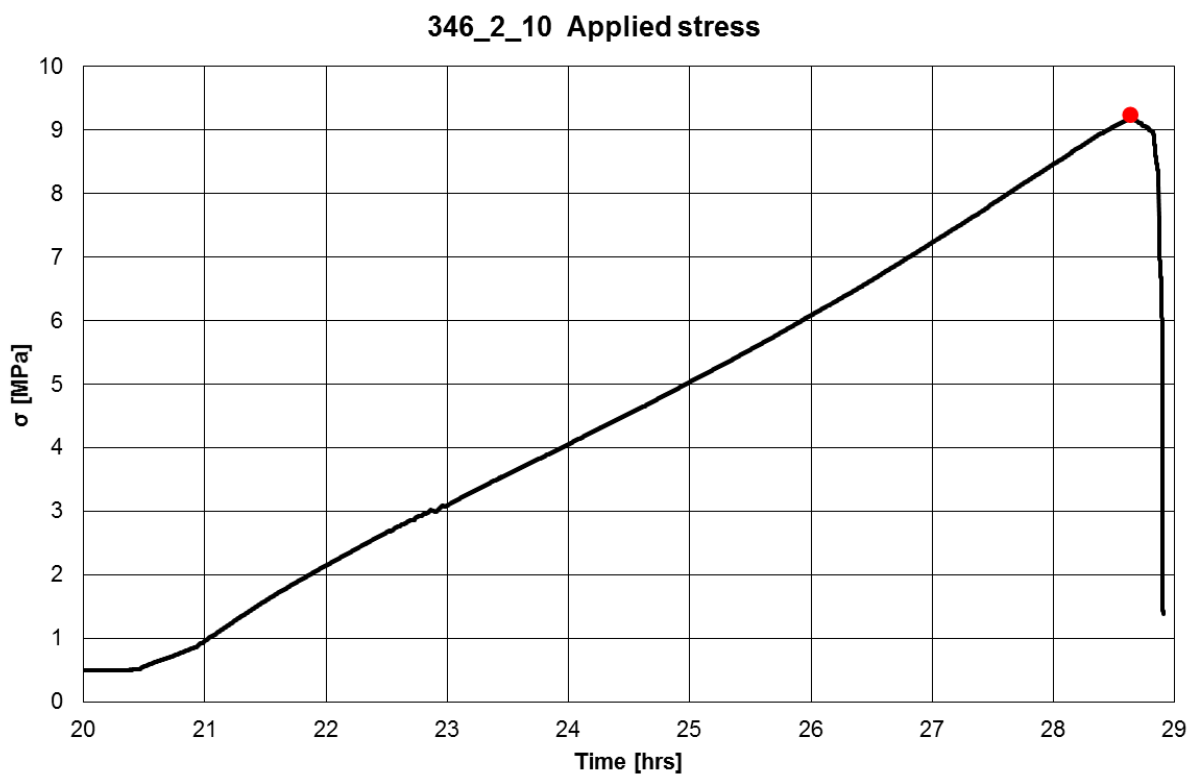


Figure III- 1: Stress versus time for core sample 346_2_10.

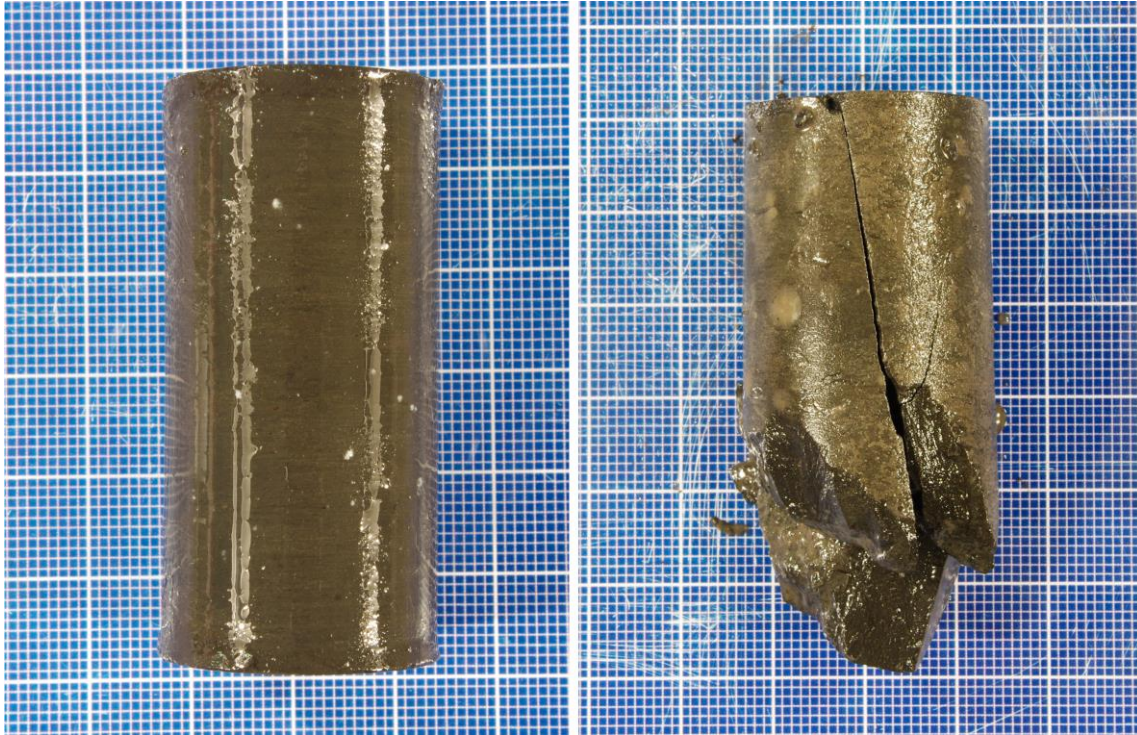


Figure III- 2: Core sample 346_2_10 before and after failure.

Core sample 346_2_11

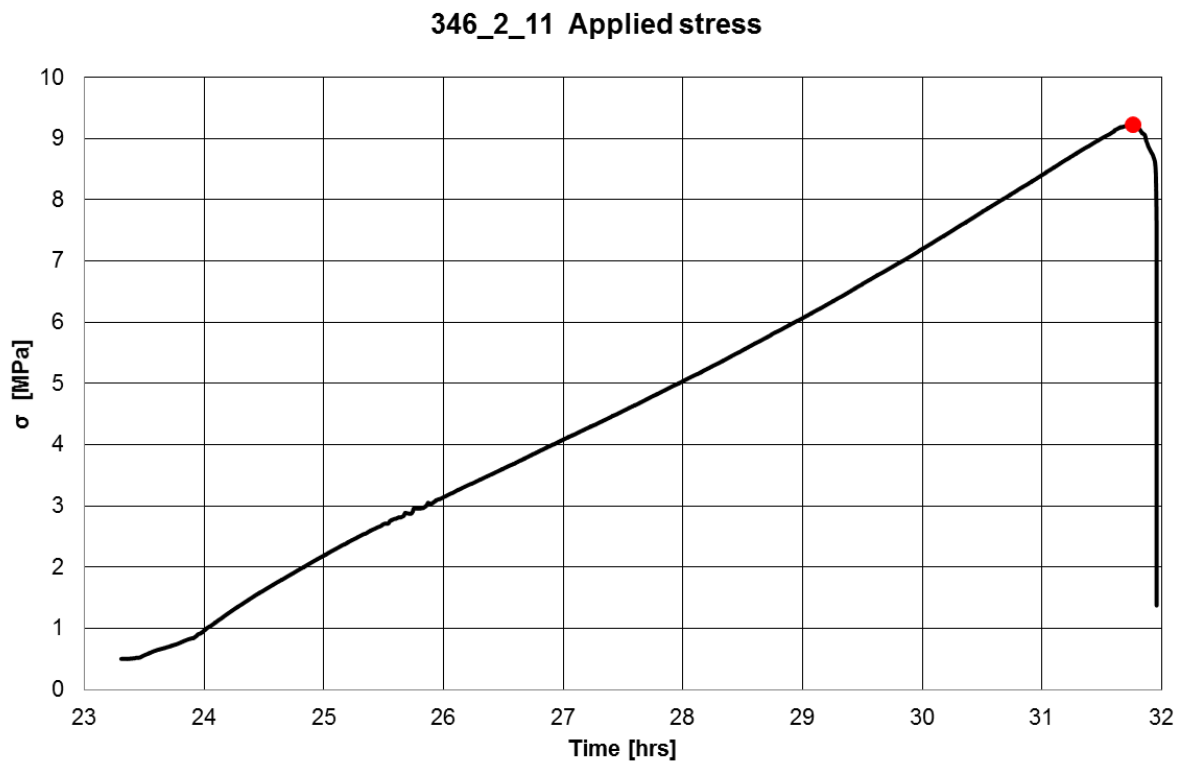


Figure III- 3: Stress versus time for core sample 346_2_11.

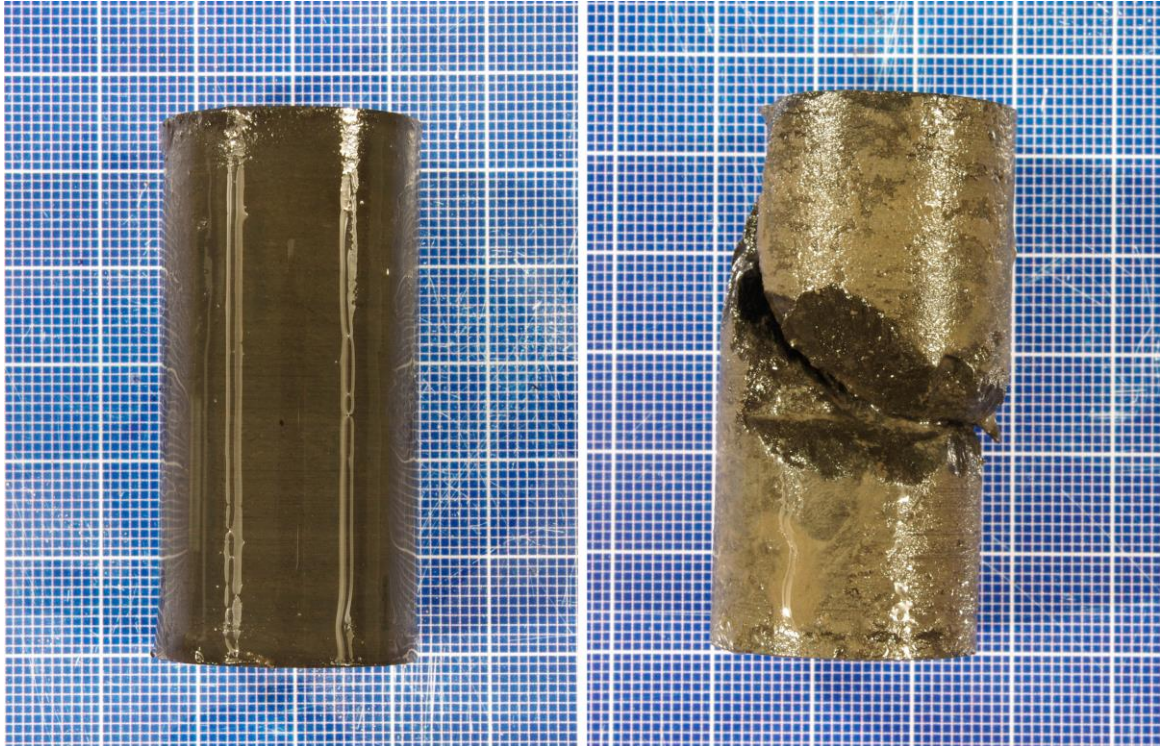


Figure III- 4: Core sample 346_2_11 before and after failure.

Core sample 346_2_14

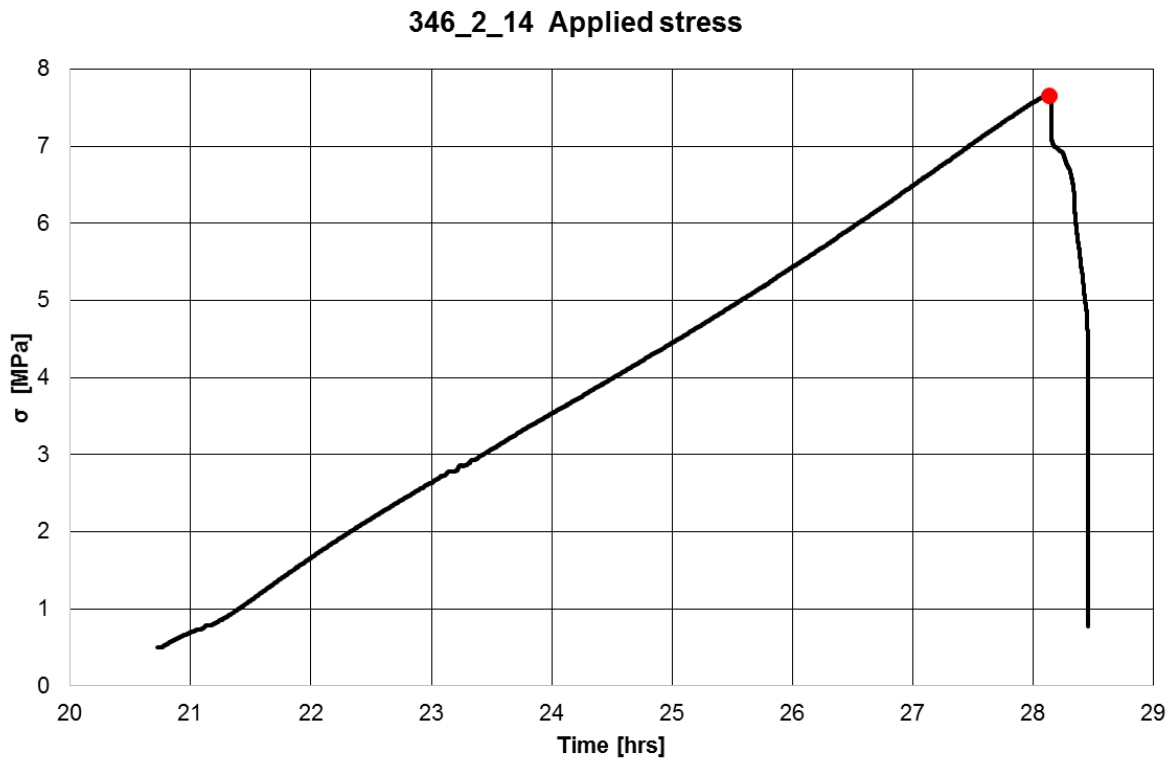


Figure III- 5: Stress versus time for core sample 346_2_14.



Figure III- 6: Core sample 346_2_14 before and after failure.

Core sample 346_2_16

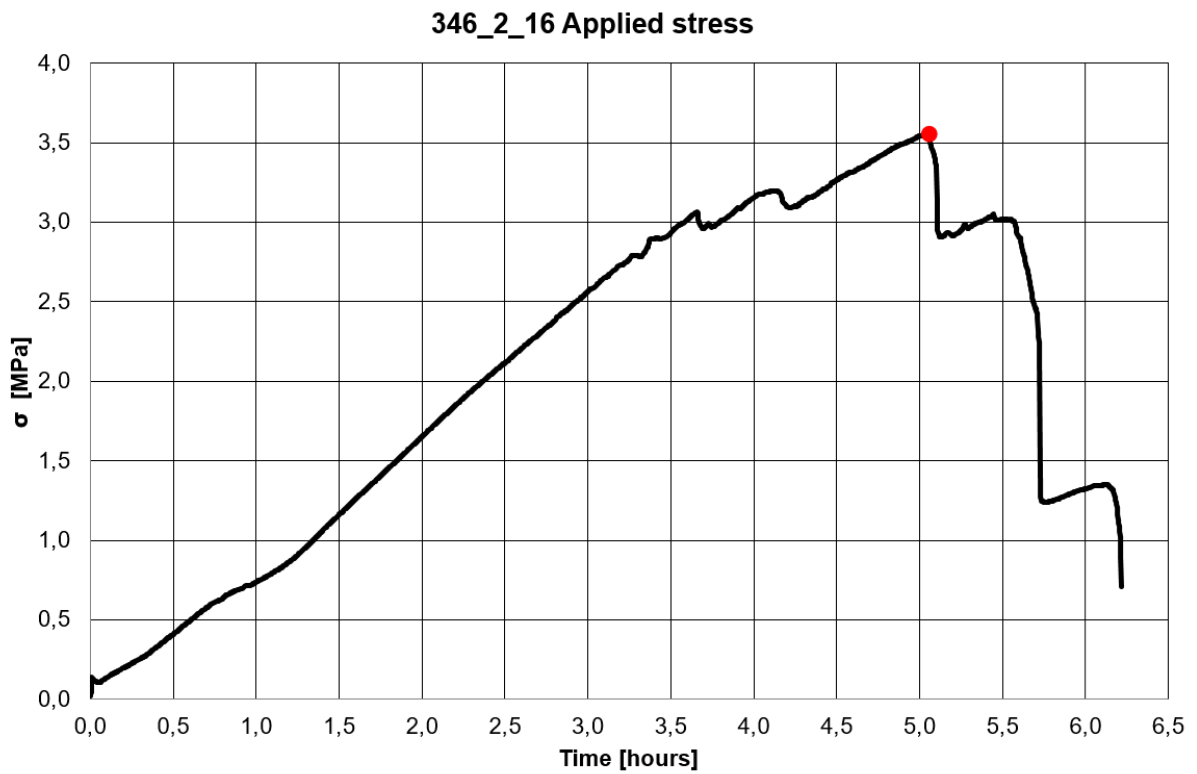


Figure III- 7: Stress versus time for core sample 346_2_16.



Figure III- 8: Core sample 346_2_16 before and after failure.

Appendix IV. Screening of brine and HCl mixtures

As described in section 4.4.2 (p.44), an initial screening of brine and $HCl(aq)$ mixtures was performed to recognize which $HCl(aq)$ concentration would provide a sufficient pH reduction in the pore fluid prior to running the creep experiments with reduced pH. The composition of the Pierre shale in question is showed in Table VI-2 (Appendix VI, p.199). Total clay content is about 69%, and as one can see, approximately 30% of the rock is chlorite which is known to be extremely sensitive to $HCl(aq)$ (section 3.2.2, p.36). Naturally, the various parts of the sample will respond differently to acid, but because the chlorite content is so high, it was recognized that the concentration of $HCl(aq)$ should be restricted in order to avoid dissolution of this clay mineral. The overall aim with the screening process was also to mix a solution with a pH-value and chemical activity that did not deviate too much from initial 3.5wt% $NaCl(aq)$ but at the same time would assumingly adequately affect the creep of the samples.

Starting off, just to get an overview of pH-values in mixed solutions, it was determined to blend both high and low concentrations of $HCl(aq)$ with brine in separate test tubes. Fortunately, $NaCl(aq)$ and $HCl(aq)$ are both miscible fluids, implying that a mixture of them should result in a single liquid phase, and thus, no continuous stirring mechanism was required. For each test tube a 100 mL mixture of 3.5wt% $NaCl(aq)$ and $HCl(aq)$ was prepared. The initial strength of $HCl(aq)$ was 25%, and by adding different volumes of brine one could manipulate the acid concentration as desired. Initially, four test tubes with different concentrations were prepared and measurements in the tubes showed the following results:

Table IV- 1: Overview of amounts and measurements for test tube 1-4.

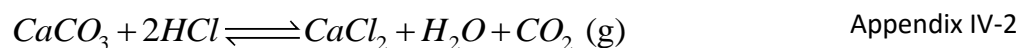
Test tube #	HCL		3.5 wt% NaCl	Mixture	Measurements		
	%	Amount [mL]	Amount [mL]	Total strength of HCl (aq) [%]	pH	ERH	Chemical activity
1	25 %	0	100	0	7,31	94,2	0,942
2	25 %	20	80	5	-0,12	72,4	0,724
3	25 %	40	60	10	-0,35	68,0	0,680
4	25 %	60	40	15	-0,73	63,7	0,637

As one can see from Table IV-1, the pH-value of brine was close to neutral while the ones containing $HCl(aq)$ showed a strong acidic environment with negative values. The prepared mixtures obviously had a too high acid concentration, so it was determined to mix new solutions. Another observation worth mentioning from the measurements was that stronger concentration of $HCl(aq)$ naturally resulted in less chemical activity and more deviation from the initial brine. The chemical activity was calculated based on its relationship to relative humidity (Cauvain and Young 2009), showing

$$a_{kj} = \frac{ERH}{100} \quad \text{Appendix IV-1}$$

where ERH is the equilibrium relative humidity.

Even though these solutions were not potential candidates to be used for the upcoming creep experiments, it was out of curiosity determined to put small samples of Pierre shale saturated with in marcol into the test tubes to observe what happened in terms of weathering (Figure IV-1 - Figure IV-4). After approximately 4 days, one could see that the fluid was to some degree contaminated. It had obtained a somewhat yellow-ish color and it was believed that this was caused by dissolved minerals. When specifically looking at the shale samples with the bare eye, one could observe that the sample submerged in the strongest acid solution (15% $HCl(aq)$) had a slightly coarser texture and some loose grains compared to the others. The sample submerged in pure brine had a visible layer of wet clay on its surface. Looking through a Scanning Electron Microscope (SEM) with Energy Dispersive X-ray Spectroscopy (EDXS) would have revealed how much the samples were actually affected by weathering on a microscopic scale. Also, the mixtures in test tubes 2, 3 and 4 were tested on core samples of chalk. This resulted in bubbles/fizzing on the surface of the chalk as acid reacted with the calcite and formed bubbles of carbon dioxide:



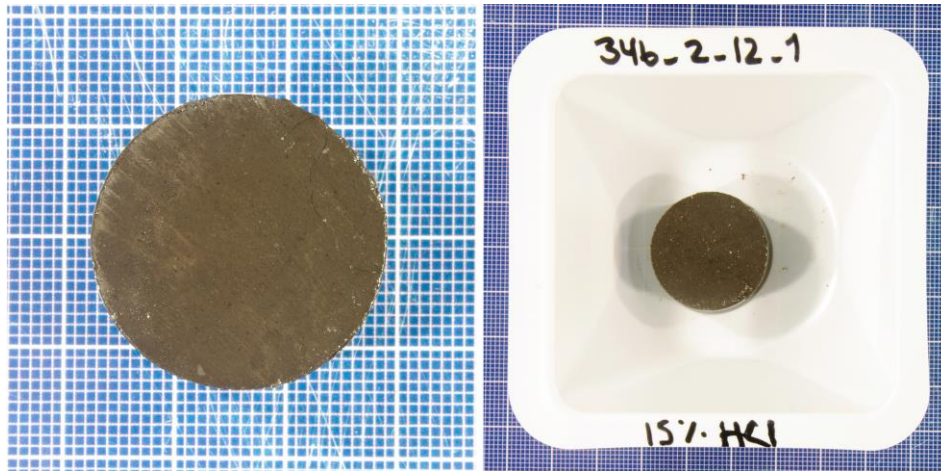


Figure IV- 1: Test tube 4. Small sample of Pierre shale before and after 4 days in an acidic environment (15% HCl).

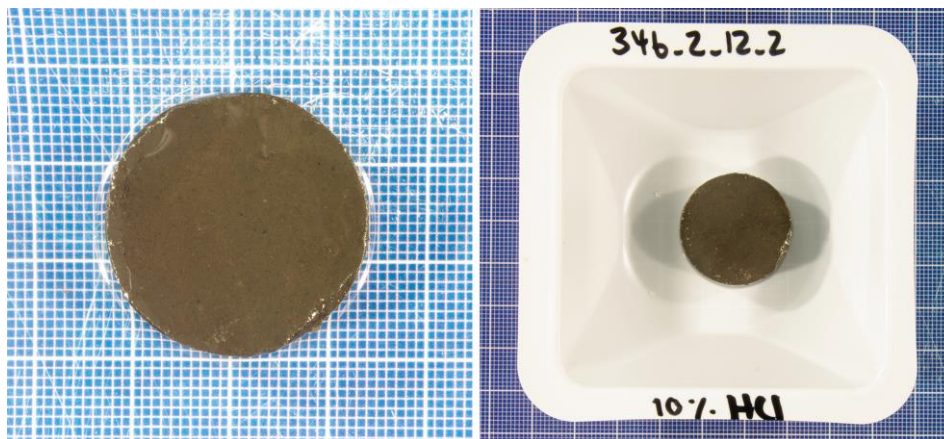


Figure IV- 2: Test tube 3. Small sample of Pierre shale before and after 4 days in an acidic environment (10% HCl).

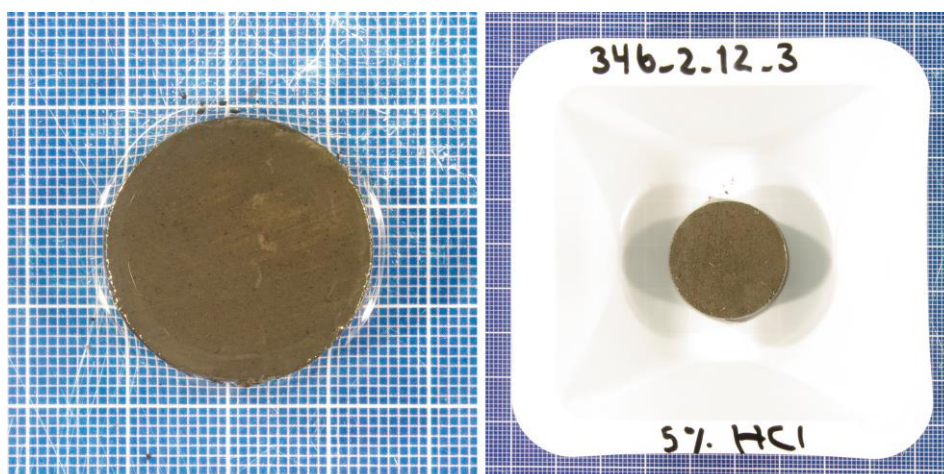


Figure IV- 3: Test tube 2. Small sample of Pierre shale before and after 4 days in an acidic environment (5% HCl).

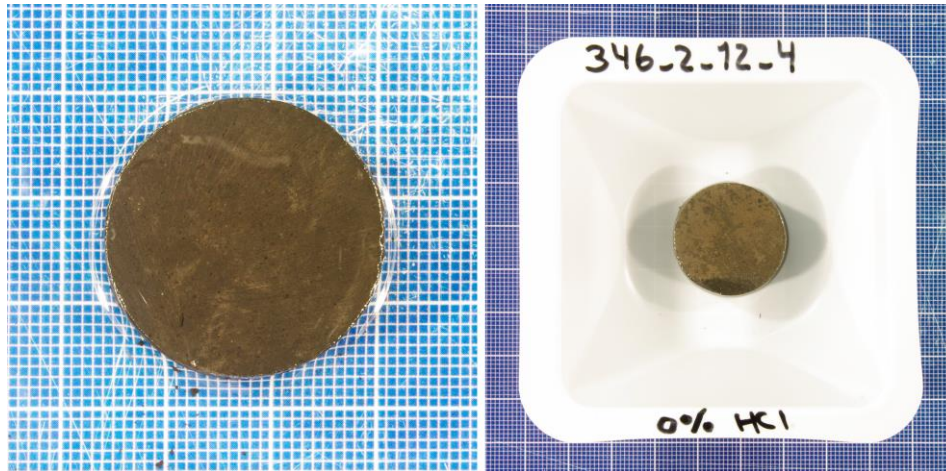


Figure IV- 4: Test tube 1. Small sample of Pierre shale before and after 4 days in brine (0% HCl).

In further investigations of finding the best fit pH-value, new mixtures were prepared, and the following results were obtained:

Table IV- 2: Overview of amounts and measurements for test tube 5-9.

Test tube	HCL		3.5 wt% NaCl	Mixture	Measurement
#	%	Amount [mL]	Amount [mL]	Total strength of HCl (aq) [%]	pH
5	25 %	4	96,0	1	0,29
6	25 %	2	98,0	0,5	0,36
7	25 %	1	99,0	0,25	0,51
8	25 %	0,5	99,5	0,125	0,75
9	25 %	0,1	99,9	0,025	1,36

As one can see from Table IV-2, the mixtures still had a high deviation in pH-value from the initial brine. Due to already low amounts of added $HCl(aq)$ it was hard to prepare an even less quantity, so it was determined to dilute the $HCl(aq)$ concentration with more brine by mixing 1L of solution instead of 100 mL. Thus, starting off, 1L solution of 0.0025% $HCl(aq)$ concentration was prepared with a measured pH-value of 2.91. This mixture was then diluted with more brine into bulks of 100 mL test tubes, and the following results were obtained:

Table IV- 3: Overview of amounts and measurements for test tube 10-14.

Test tube	HCL		3.5 wt% NaCl	Mixture	Measurements		
	#	%	Amount [mL]	Amount [mL]	Total strength of HCl (aq) [%]	pH	ERH
10	0,0025 %	50,000	50,0000	0,0012500	3,14	93,8	0,938
11	0,0025 %	25,000	75,0000	0,0006250	3,84		
12	0,0025 %	12,500	87,5000	0,00031250	4,17		
13	0,0025 %	6,2500	93,7500	0,00015625	4,92		
14	0,0025 %	1,5625	98,4375	0,00003906	6,23		

As seen from Table IV-3, test tubes nr.13 and 14 showed promising pH-values that could potentially qualify for the final solution mix of brine and $HCl(aq)$. Thus, small samples of Pierre shale submerged in brine were put inside the tubes for approximately 3 days (Figure IV-5 and Figure IV-6). No significant weathering could be observed.

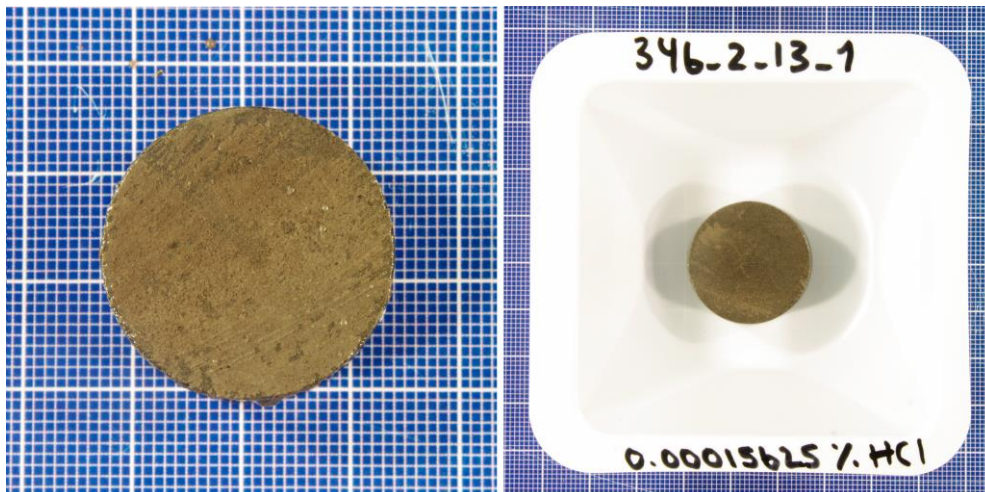


Figure IV- 5: Test tube 13. Small sample of Pierre shale before and after 3 days in an acidic environment (0.00015625% HCl).

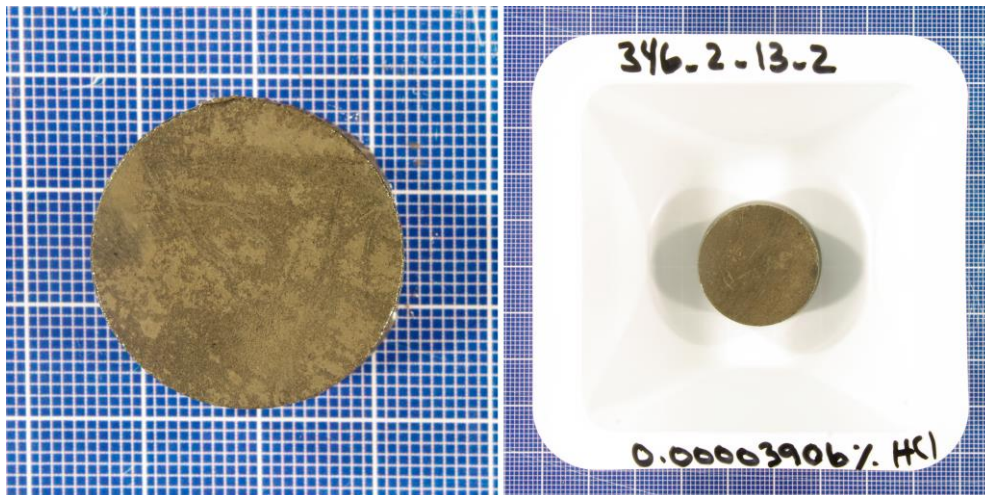


Figure IV- 6: Test tube 14. Small sample of Pierre shale before and after 3 days in an acidic environment (0.00003906% HCl).

Eventually, after discussion with the supervisor, it was decided to proceed further with test tube nr.10 for the creep experiments. This solution had a chemical activity of 0.938 and a pH-value of 3.14.

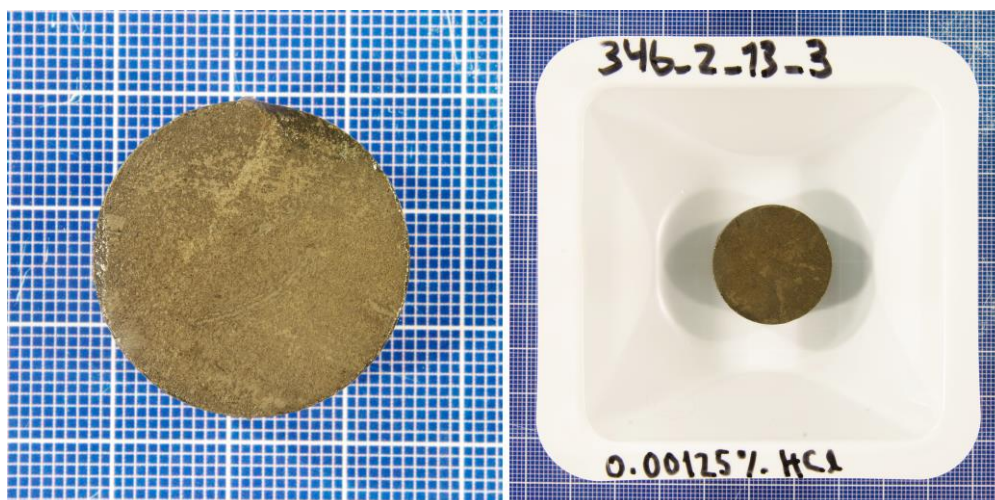


Figure IV- 7: Test tube 10. Small sample of Pierre shale before and after 3 days in an acidic environment (0.00125% HCl).

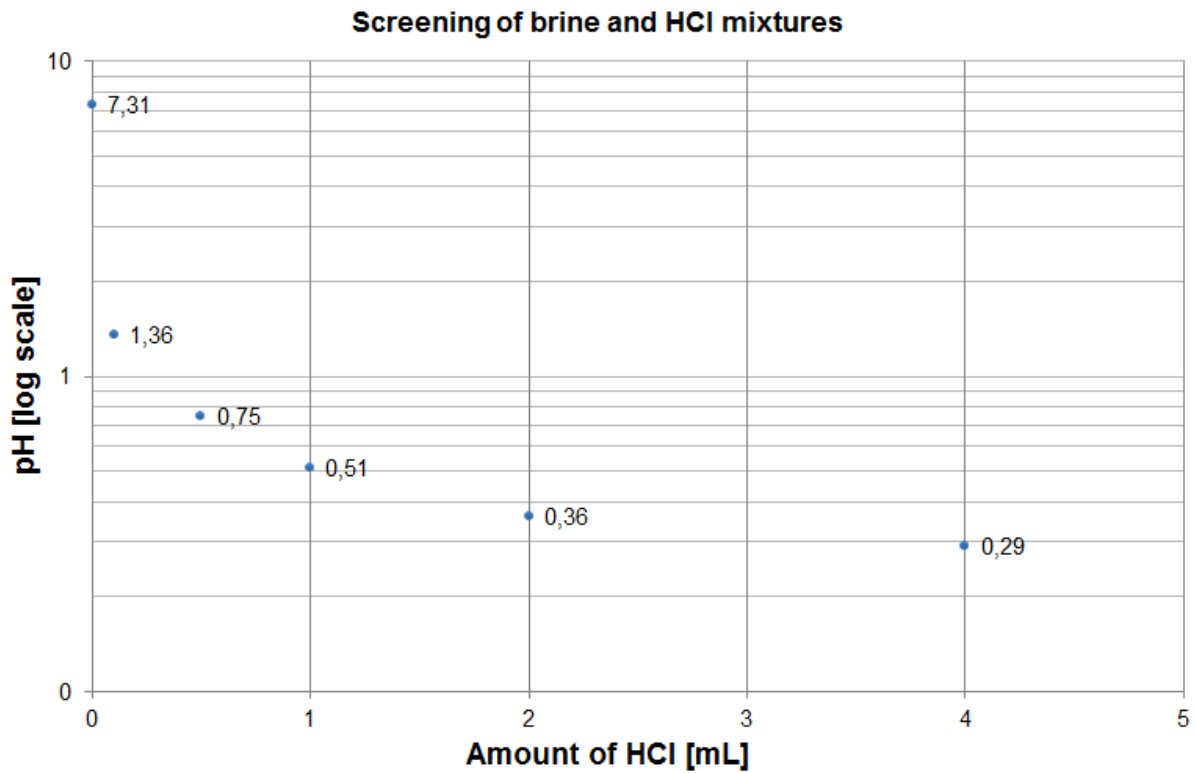


Figure IV- 8: Obtained pH-values by diluting 25% HCl (aq) concentration with 3.5wt% brine. Total amount of mixture equals 100 mL. Negative pH-values are excluded from the plot.

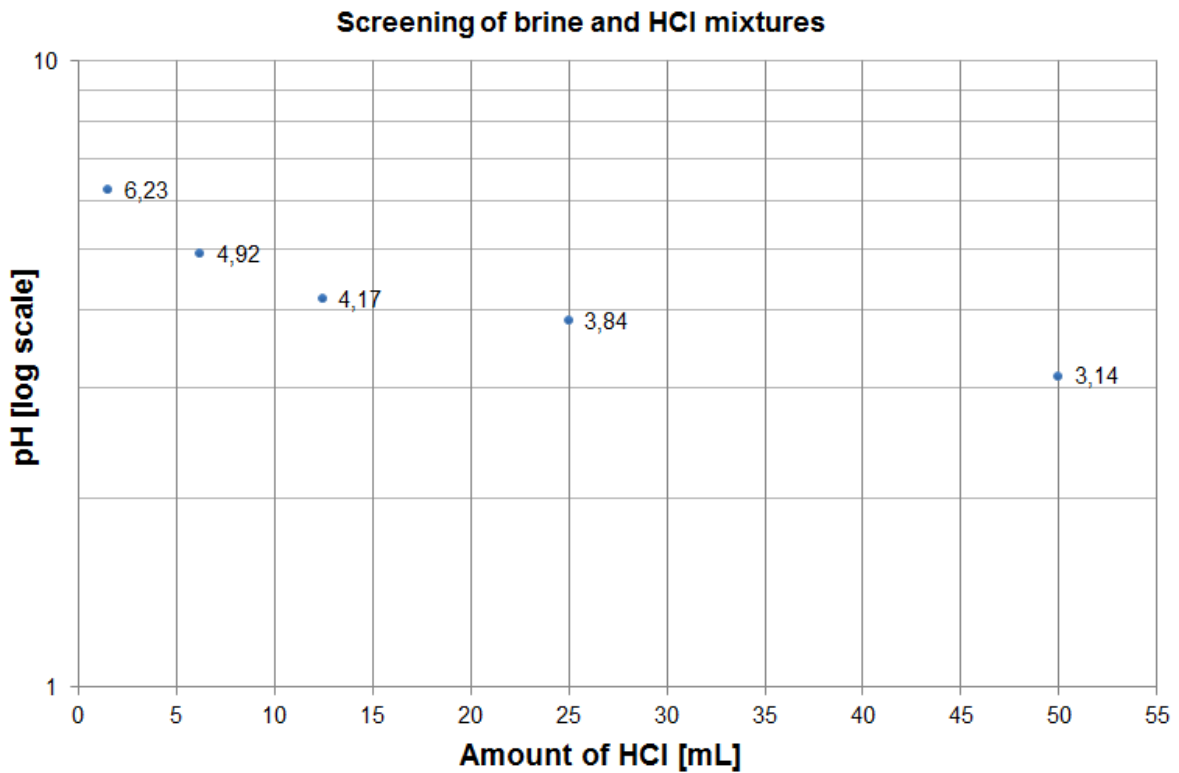


Figure IV- 9: Obtained pH-values by diluting 0.0025% HCl (aq) concentration with 3.5wt% brine. Total amount of mixture equals 100 mL.

Appendix V. Relations between elastic moduli

Table V- 1: Known relations between elastic moduli (Fjær et al. 2008).

$E = 3K(1 - 2\nu)$	$K = \lambda \frac{1 + \nu}{3\nu}$	$\frac{\lambda}{\lambda + G} = 2\nu$
$E = 2G(1 + \nu)$	$K = \frac{2}{3}G \frac{1 + \nu}{1 - 2\nu}$	$\frac{G}{\lambda + G} = 1 - 2\nu$
$E = \frac{9KG}{3K + G}$	$K = \lambda + \frac{2}{3}G$	$\frac{\lambda + 2G}{\lambda + G} = 2(1 - \nu)$
$E = G \frac{3\lambda + 2G}{\lambda + G}$	$K = \frac{GE}{9G - 3E}$	$\frac{3\lambda + 2G}{\lambda + G} = 2(1 + \nu)$
$E = \frac{\lambda}{\nu}(1 + \nu)(1 - 2\nu)$	$\frac{\lambda}{G} = \frac{2\nu}{1 - 2\nu}$	$\frac{3\lambda + 4G}{\lambda + G} = 2(2 - \nu)$
$H = \lambda + 2G$	$H = K + \frac{4}{3}G$	$\nu = \frac{3K - 2G}{2(3K + G)}$
$H = E \frac{1 - \nu}{(1 + \nu)(1 - 2\nu)}$	$H = 2G \frac{1 - \nu}{1 - 2\nu}$	$H = 3K \frac{1 - \nu}{1 + \nu}$

Appendix VI. Additional tables

Table VI- 1: Measured data for all core samples.

Core sample [#]	Average diameter [mm]	Average length [mm]	Wet weight [g]	Density [g/mm ³]	Used in test
346_2_10	25,29	52,55	63,54	2,41	Ion diffusion test + UCS
346_2_11	25,29	52,58	63,93	2,42	Ion diffusion test + UCS
346_2_12_1	25,24	10,17	11,61	2,28	Put in 15% HCl solution for screening
346_2_12_2	25,24	10,13	11,55	2,28	Put in 10% HCl solution for screening
346_2_12_3	25,24	10,23	11,65	2,28	Put in 5% HCl solution for screening
346_2_12_4	25,24	10,18	11,57	2,27	Put in 0% HCl solution for screening
346_2_13_1	25,27	10,24	11,87	2,31	Put in 0,00015625% HCl solution for screening
346_2_13_2	25,27	10,16	11,72	2,30	Put in 0,00003906% HCl solution for screening
346_2_13_3	25,27	10,21	11,84	2,31	Put in 0,00125% HCl solution for screening
346_2_14	25,37	52,50	63,93	2,41	Ion diffusion test + UCS
346_2_15	25,25	52,47	63,53	2,42	Creep test brine
346_2_16	25,39	52,33	63,43	2,39	UCS test
346_2_17	25,40	52,66	63,79	2,39	Not used in any test
346_2_18	25,28	52,13	63,06	2,41	Creep test brine
346_2_19	25,30	52,14	63,36	2,42	Creep test brine
346_2_20	25,30	51,93	62,48	2,39	Creep test brine
346_2_21	25,28	52,59	63,61	2,41	Creep test with reduced pore fluid pH
346_2_22	25,25	51,66	62,13	2,40	Creep test with reduced pore fluid pH
346_2_23	25,25	51,50	62,14	2,41	Creep test brine

Table VI- 2: Mineralogy composition of Pierre shale, block 346_2 (given by the lab at SINTEF Petroleum 2015).

Fine analysis Pierre shale 346_2					
Mineral	%	Reacts with HCl			Comment
		Slight	High	Stable	
Quartz	16,0			x	
Plag.	8,55	x			
Chlorite	29,6		x		Dissolves
Illite	19,9	x			May dissolve
Smectite	19,8	x			Might swell in presence of fresh water
Calcite	1,54		x		Dissolves
Sid	1,43	x			
Dol/Ank	2,63	x			
Pyrite	0,63	x			

Table VI- 3: Overview of the first three creep experiments.

Creep tests overview															
Core sample [#]	Submerged in fluid	Test procedure [#]	Loading path [#]	Crosshead speed 1 [mm/min]	Average running speed 1 [MPa/hrs]	Load level 1 [MPa]	Percentage of UCS [%]	Hold time [hrs]	Crosshead speed 2 [mm/min]	Average running speed 2 [MPa/min]	Load level 2 [MPa]	Percentage of UCS [%]	Hold time [hrs]	Maximum temperature variation [°C]	Comment
346_2_15	Brine	1	1	0,0030	0,94	7,8	85	1,56	-	-	-	-	-	0,37	Sample failed after 1.56 hrs on loading level 1.
346_2_18	Brine	2	2	0,0030	0,89	7,8	85	-	-	-	-	-	-	N/A	Sample failed before reaching loading level 1.
346_2_19	Brine	2	3	0,0030	0,93	5,2	57	48	0,018	0,28	5,7	62	1,89	N/A	Sample failed after 1.89 hrs on loading level 2.

Table VI- 4: Overview of the remaining creep experiments.

Creep tests overview					
Test procedure: 2					
Loading path: 4					
Core sample [#]	Submerged in fluid	Crosshead speed loading [mm/min]	Average running speed loading [MPa/min]	Maximum temperature variation [°C]	Comment
346_2_20	Brine	0,018	0,23	N/A	Successful test, failure on loading level 10 (5.5 MPa)
346_2_21	Mixture of brine and HCl	0,009	0,10	0,83	Successful test, failure on loading level 12 (6.5 MPa)
346_2_22	Mixture of brine and HCl	0,009	0,06	0,47	Successful test, failure on loading level 7 (4.0 MPa)
346_2_23	Brine	0,009	0,10	0,98	Successful test, failure on loading level 13 (7.0 MPa)

Appendix VII. Calibration of LVDTs

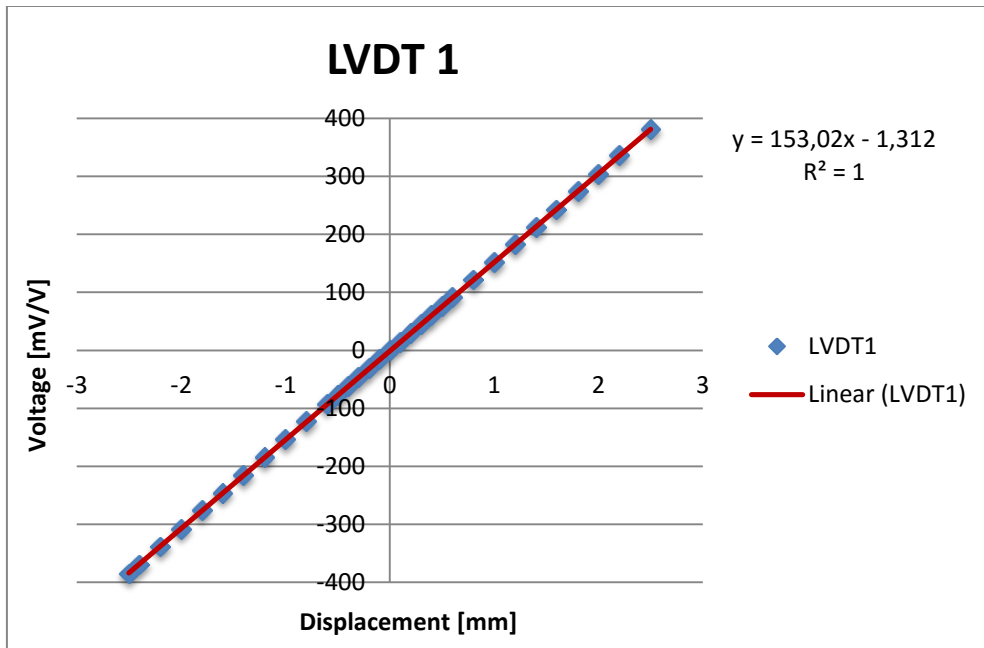


Figure VII- 1: Calibration for LVDT 1

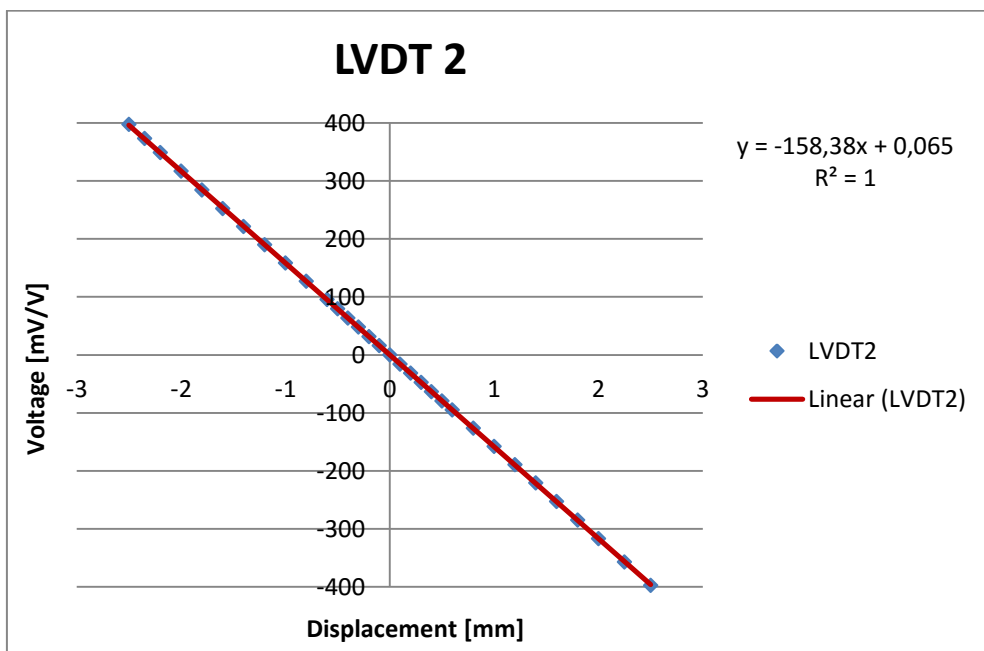


Figure VII- 2: Calibration for LVDT 2.

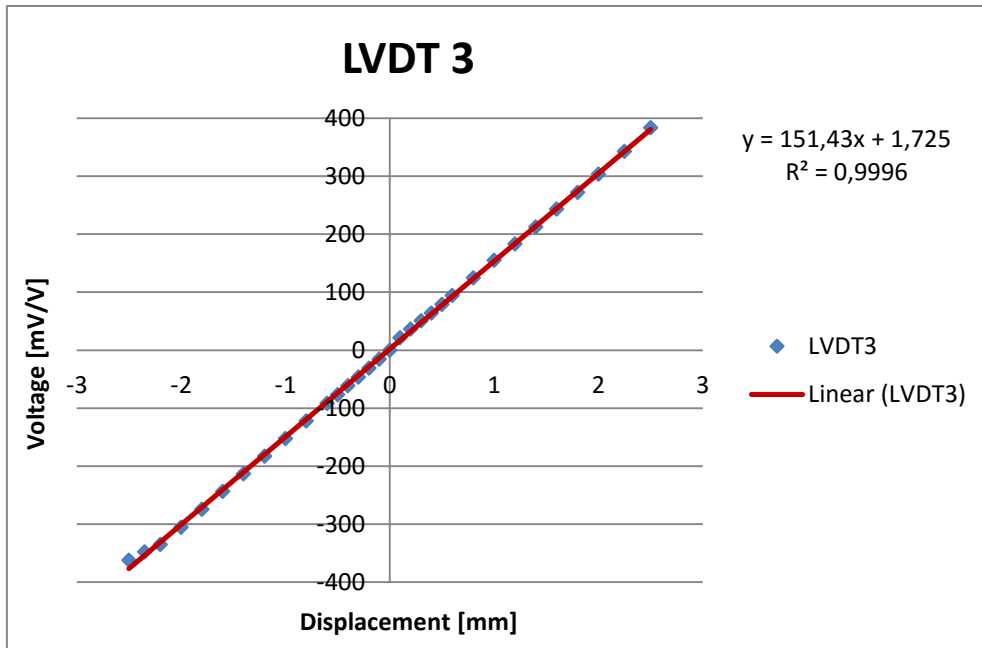


Figure VII- 3: Calibration for LVDT 3.

Appendix VIII. Calculations of system correction factor

Length of PEEK sample: 0.0508 m

PEEK velocity: 2563 m/s

Total travel time through PEEK:

$$\frac{0.0508 \text{ m}}{2563 \text{ m/s}} \cdot 10^6 = 19.82 \mu\text{s}$$

Appendix VIII-1

PEEK arrival time: 3.40 μs

System correction factor:

$$19.82 \mu\text{s} - 3.14 \mu\text{s} = \underline{\underline{14.18 \mu\text{s}}}$$

Appendix VIII-2

Appendix IX. Sampling rates during experiments

Ion diffusion tests

Table IX- 1: Sampling rates during ion diffusion tests.

Test period	LVDTs [Hz]	Load frame [Hz]	Temperatur sensors [Hz]	Acoustic [Hz]
Loading phase	1,0	1,0	0,001	0,0167
Hold period	0,05	0,01	0,001	0,00167

Unfortunately, the equipment for acoustic measurements was not available for the ion diffusion test performed on the sample submerged in a mixture of brine and $HCl(aq)$ (core sample 346_2_14).

UCS tests (extensions of ion diffusion tests)

Table IX- 2: Sampling rates during UCS tests (extensions of ion diffusion tests).

Test period	LVDTs [Hz]	Load frame [Hz]	Temperatur sensors [Hz]	Acoustic [Hz]
Loading phase	1,0	1,0	0,001	0,0167

UCS test (independent UCS test, core sample 346_2_16)

Table IX- 3: Sampling rates during independent UCS test.

Test period	LVDTs [Hz]	Load frame [Hz]	Temperatur sensors [Hz]	Acoustic [Hz]
Loading phase	0,05	0,1	0,001	0,03

Creep tests

Table IX- 4: Sampling rates during creep experiments.

Test period	LVDTs [Hz]	Load frame [Hz]	Temperatur sensors [Hz]	Acoustic [Hz]
Loading phase	0,050	0,10	0,001*	0,0167**
Hold period	0,050	0,01	0,001*	0,0167**


*Temperature measurements for core sample 346_2_21, 346_2_22 and 346_2_23 were set to 0.0033 Hz

**Core sample 346_2_18 had an acoustic sampling rate of 0.0083 Hz while core sample 346_2_22 and 346_2_23 were run with 0.0056 Hz.

Unfortunately, no temperature measurements could be carried out for core sample 346_2_20 due to damaged equipment.

Appendix X. Risk assessment

Id	Activity	Possible unwanted incident	Existing barriers	Risk with existing measures				Risk reducing measures	Risk with new measures			
				Human	Environment	Reputation	Economy		Human	Environment	Reputation	Economy
1	Adjusting loadframe	Damage to equipment	Emergency breaks on loadframe	A1	A1	A1	B3	Exercise caution when adjusting loadframe, use slow speed when controlling it up/down.	A1	A1	A1	B2
2	Adjusting loadframe	Damage to hand	-	C2	A1	A1	A1	Exercise caution when adjusting loadframe, do not stick your fingers too close to the apparatus.	C1	A1	A1	A1
3	Wrong use of equipment	Damage of expensive equipment	User manual for the equipment	A1	A1	A1	C3	Get sufficient instructions on how to use the equipment. Take the time that is needed for each activity.	A1	A1	A1	C2
4	Wrong use of equipment	Damage to personnel	Protective gear	C3	A1	A1	A1	Always use recommended protective gear.	C2	A1	A1	A1
5	Use of heating element	Damage to personnel and short circuiting	Copper frame between liquid and heating element	B1	A1	A1	A1	Get sufficient instructions on how to use the equipment. Take the time that is needed for each activity.	A1	A1	A1	A1
6	Moving around inside the lab	Damage to personnel due to slippery floor	Stay inside marked guidelines when leaving your work station and use of proper shoes	A3	A1	A1	A1	Exercise caution to your walking path, and use proper shoes. Clean up spills on the floor immediately.	A2	A1	A1	A1
7	Handling HCl	Damage to personnel and equipment	Protective gear, safety data sheet for HCl	D2	A1	A1	A1	Exercise caution when handling HCl and perform all operations in a ventilated environment. Use protective gear.	D1	A1	A1	A1
8	Use of temperature controller	Electricity shock in personnel	Protective container around the temperature controller	C3	A1	A1	A1	Plug all cables before starting the temperature controller. Have no loose wires.	C2	A1	A1	A1


 Unit: IPT/SINTEF
 Building: PTS 2
 Room/Equipment: Formasjonsfysikk 10 kN loading frame
 Date: 25.02.2016
 Participants: Marita Laukeland Kleiven og Elisabeth Lund
 Lab manager: Jørn Stenebråten
Elisabeth Lund

MATRISSE FOR RISIKOVURDERINGER I SINTEF

KONSEKVENNS	Svært alvorlig	E1	E2	E3	E4	E5
	Alvorlig	D1	D2	D3	D4	D5
	Moderat	C1	C2	C3	C4	C5
	Liten	B1	B2	B3	B4	B5
	Svært liten	A1	A2	A3	A4	A5
		Svært liten	Liten	Middels	Stor	Svært stor
		SANNSYNLIGHET				

Prinsipp over akseptkriterium. Forklaring av fargene som er brukt i risikomatriksen.

Farge	Beskrivelse
Rød	Uakseptabel risiko. Tiltak skal gjennomføres for å redusere risikoen.
Gul	Vurderingsområde. Tiltak skal vurderes.
Grønn	Akseptabel risiko. Tiltak kan vurderes ut fra andre hensyn.

Sannsynlighet		
1	Svært liten	Sjeldnere enn en gang hvert 50. år.
2	Liten	Mellom en gang hvert 10. år og en gang hvert 50. år.
3	Middels	Mellom en gang hvert år og en gang hvert 10. år.
4	Stor	Mellom en gang hver måned og en gang hvert år.
5	Svært stor	Oftere enn hver måned.

Konsekvensmatrise				
	Personskade	Skade på ytre miljø	Økonomisk tap / Materiell skade	Skade på omdømme
E	Død	Svært langvarig og ikke-reversibel skade	Tap på mer enn NOK 5 mill	Troverdighet og respekt betydelig og varig svekket
D	Alvorlig personskade/ mulig uferhet	Langvarig skade Lang restitusjonstid	Tap opp til NOK 5 mill	Troverdighet og respekt betydelig svekket.
C	Alvorlig personskade	Mindre skade og lang restitusjonstid	Tap opp til NOK 1 mill	Troverdighet og respekt svekket.
B	Medisinsk behandling	Mindre skade og kort restitusjonstid	Tap opp til NOK 250.000	Negativ påvirkning på troverdighet og respekt
A	Førstehjelp	Ubetydelig skade og kort restitusjonstid	Tap opp til NOK 50.000	Liten påvirkning på troverdighet og respekt

Appendix XI. Pictures of core samples after creep experiments



Figure XI- 1: Core sample 346_2_15 after creep test.



Figure XI- 2: Core sample 346_2_18 after creep test.



Figure XI- 3: Core sample 346_2_19 after creep test.



Figure XI- 4: Core sample 346_2_20 after creep test.



Figure XI- 5: Core sample 346_2_21 after creep test.



Figure XI- 6: Core sample 346_2_22 after creep test.



Figure XI- 7: Core sample 346_2_23 after creep test.

Appendix XII. Pictures from the unfortunate lab incident with core sample 346_2_20



Figure XII- 1: A damaged heating element.

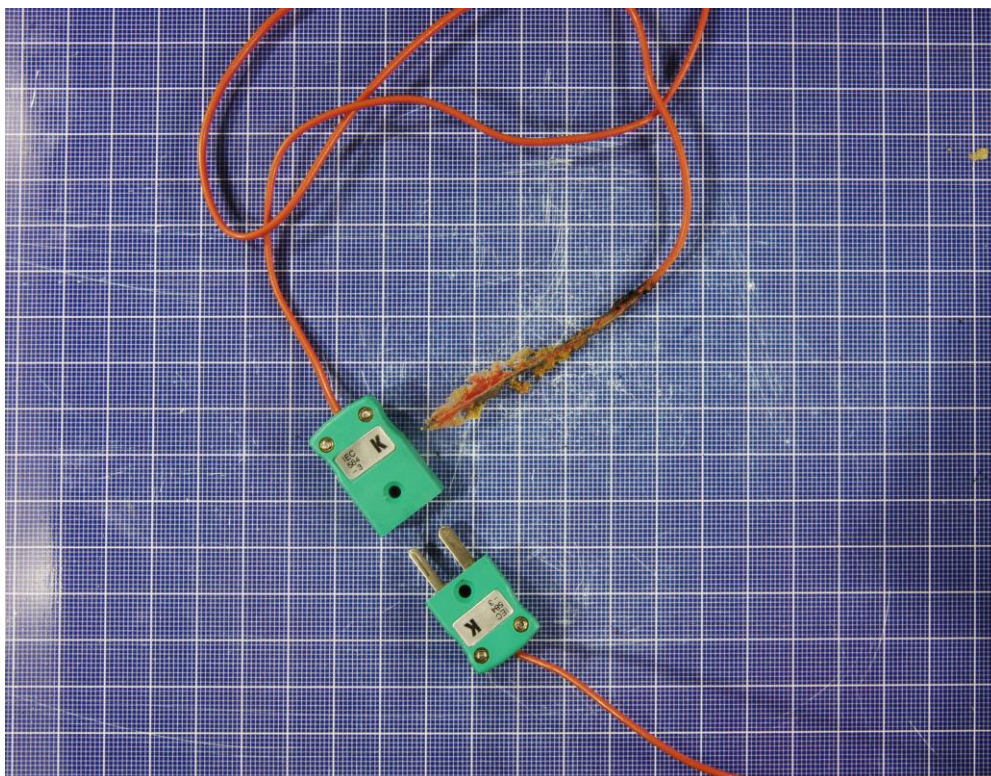


Figure XII- 2: Picture illustrating the connection point between the heating element and the temperature controller. It was believed that capillary suction lead brine into this point causing a dysfunctional device.



Figure XII- 3: Melted plastic parts from the experimental setup.



Figure XII- 4: Dried out core sample inside container due to leakage/evaporation of fluid.

Appendix XIII. Digital attachments

The following Excel files are enclosed to the master thesis:

- 346_2_10.xlsx
- 346_2_11.xlsx
- 346_2_14.xlsx
- 346_2_15.xlsx
- 346_2_16.xls
- 346_2_18.xlsx
- 346_2_19.xlsx
- 346_2_20.xls
- 346_2_21.xlsx
- 346_2_22.xlsx
- 346_2_23.xlsx
- Attempt_to_predict_failure.xlsx
- Calculations_of_relative_consolidation_times.xlsx
- Comparison_20-23.xlsx

Appendix XIV. Additional plots – creep experiments

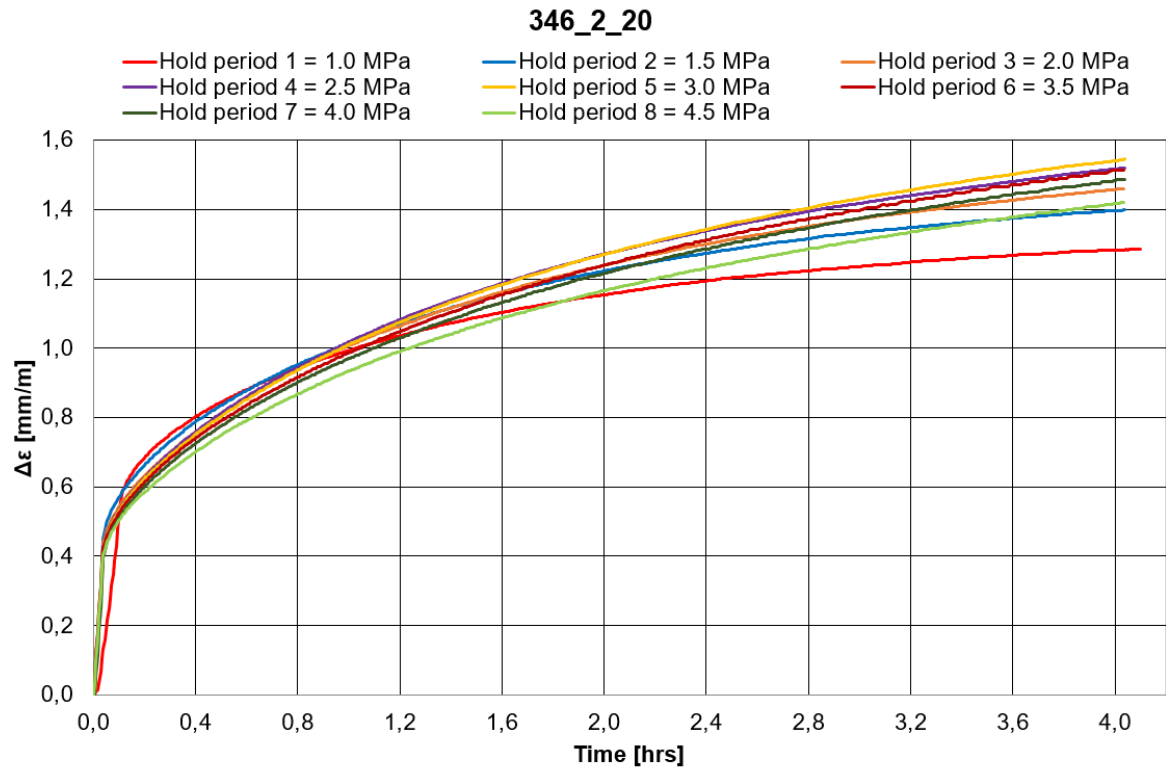


Figure XIV- 1: Strain versus time for loading phases and hold periods.

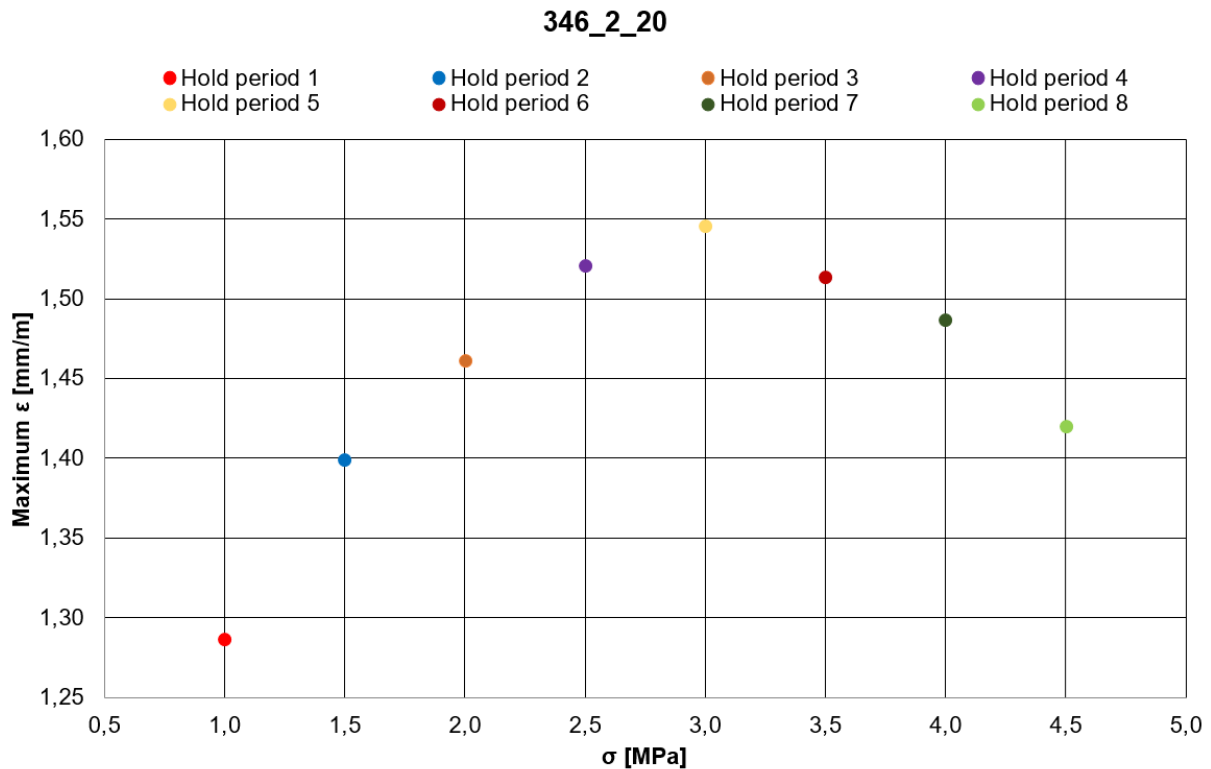


Figure XIV- 2: Maximum strain for loading phase and hold period versus stress level.

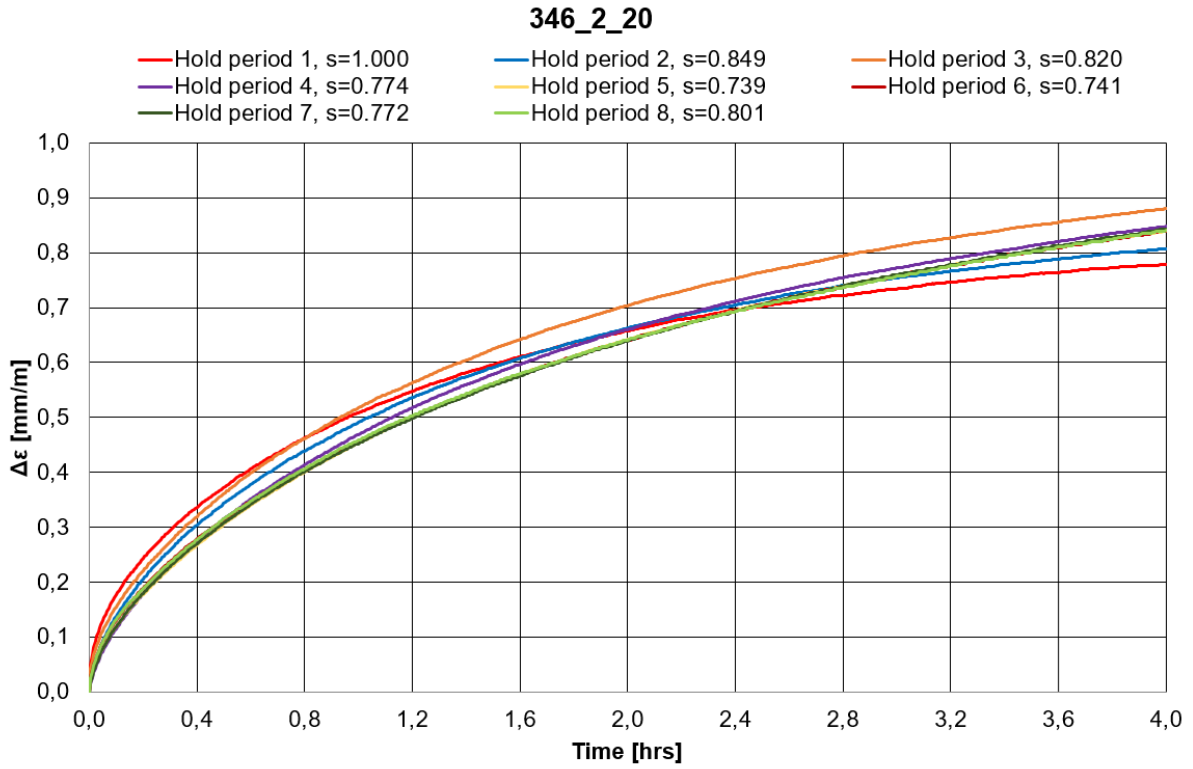


Figure XIV- 3: An attempt to scale the other hold periods down to hold period 1 with a scaling factor s . Scaling factors are included in the legend.

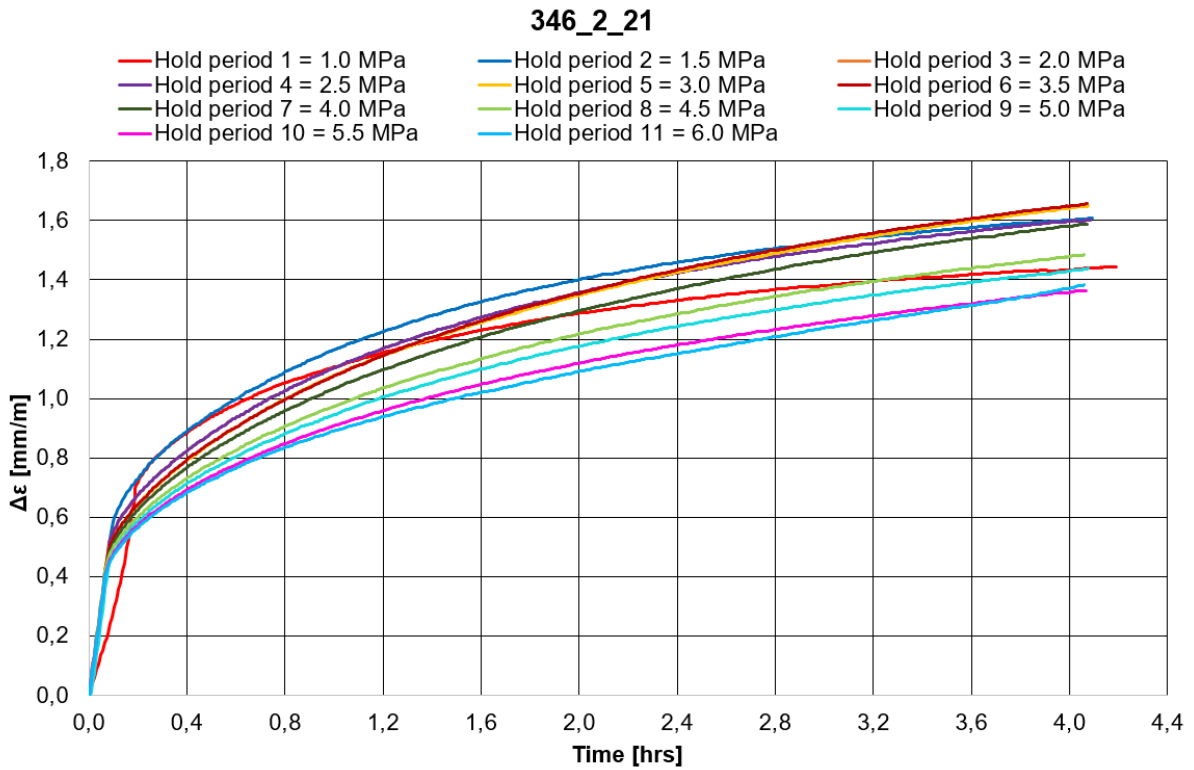


Figure XIV- 4: Strain versus time for loading phases and hold periods.

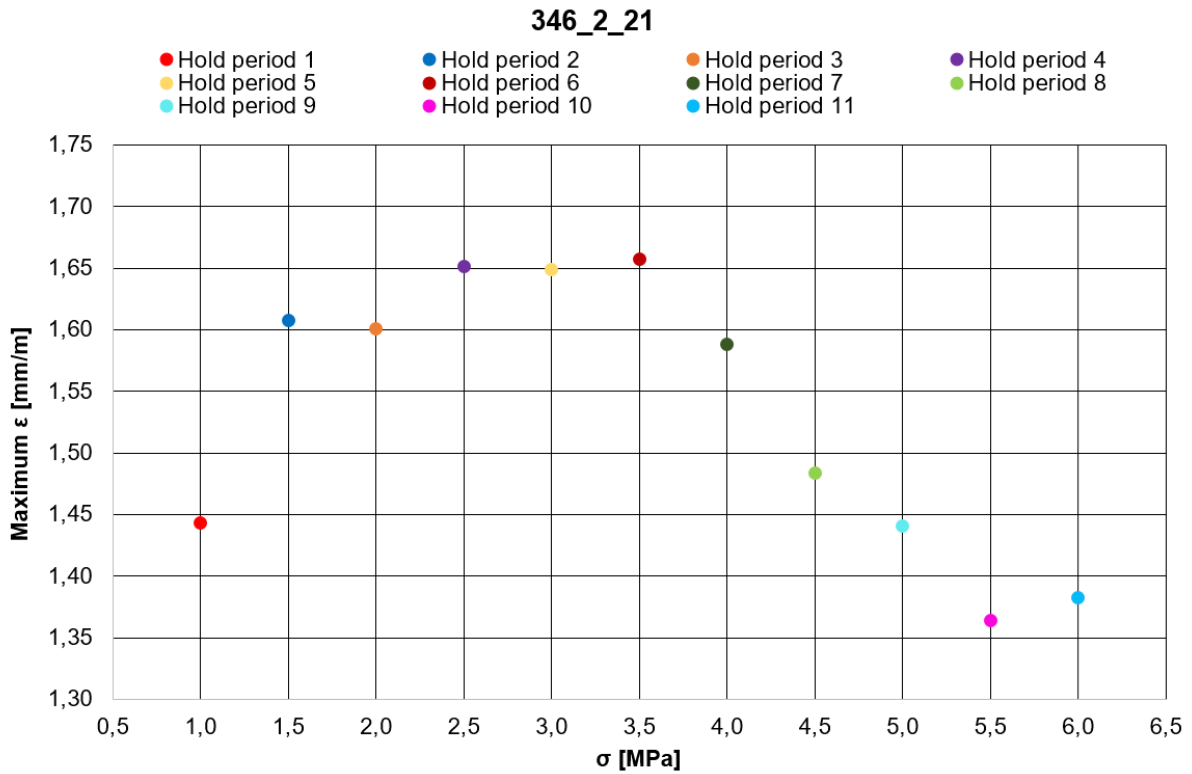


Figure XIV- 5: Maximum strain for loading phase and hold period versus stress level.

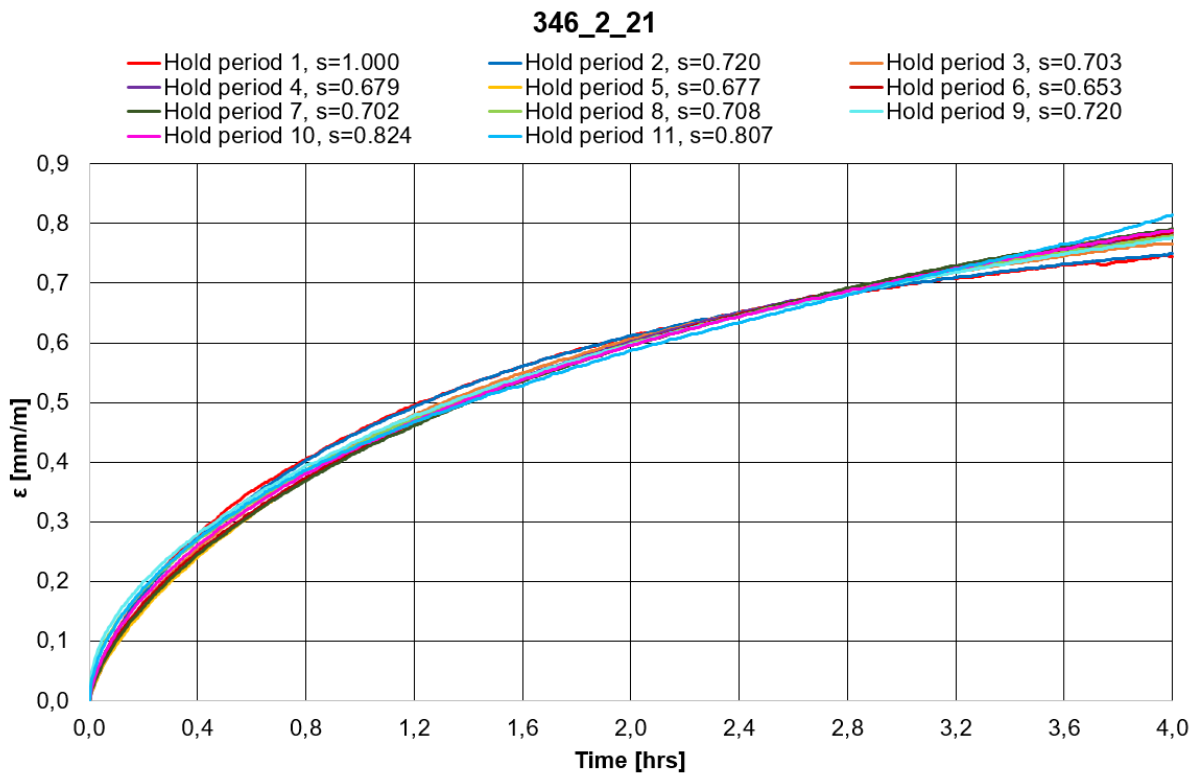


Figure XIV- 6: An attempt to scale the other hold periods down to hold period 1 with a scaling factor s . Scaling factors are included in the legend.

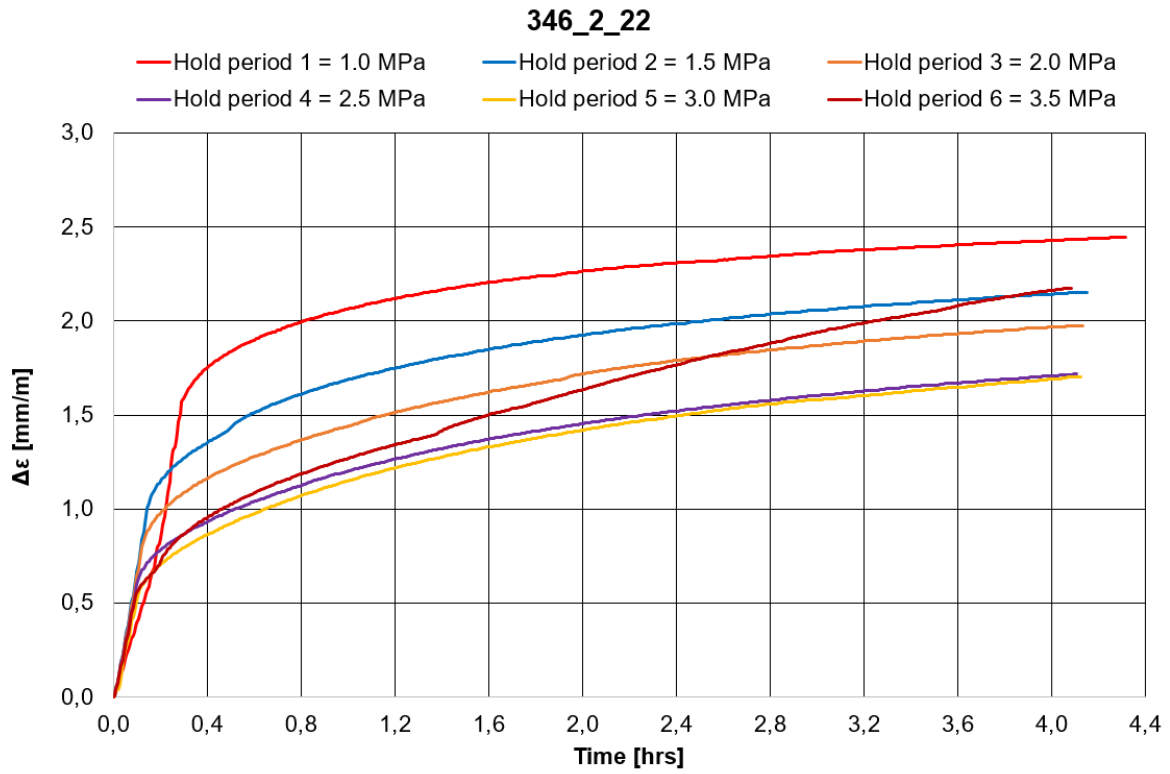


Figure XIV- 7: Strain versus time for loading phases and hold periods.

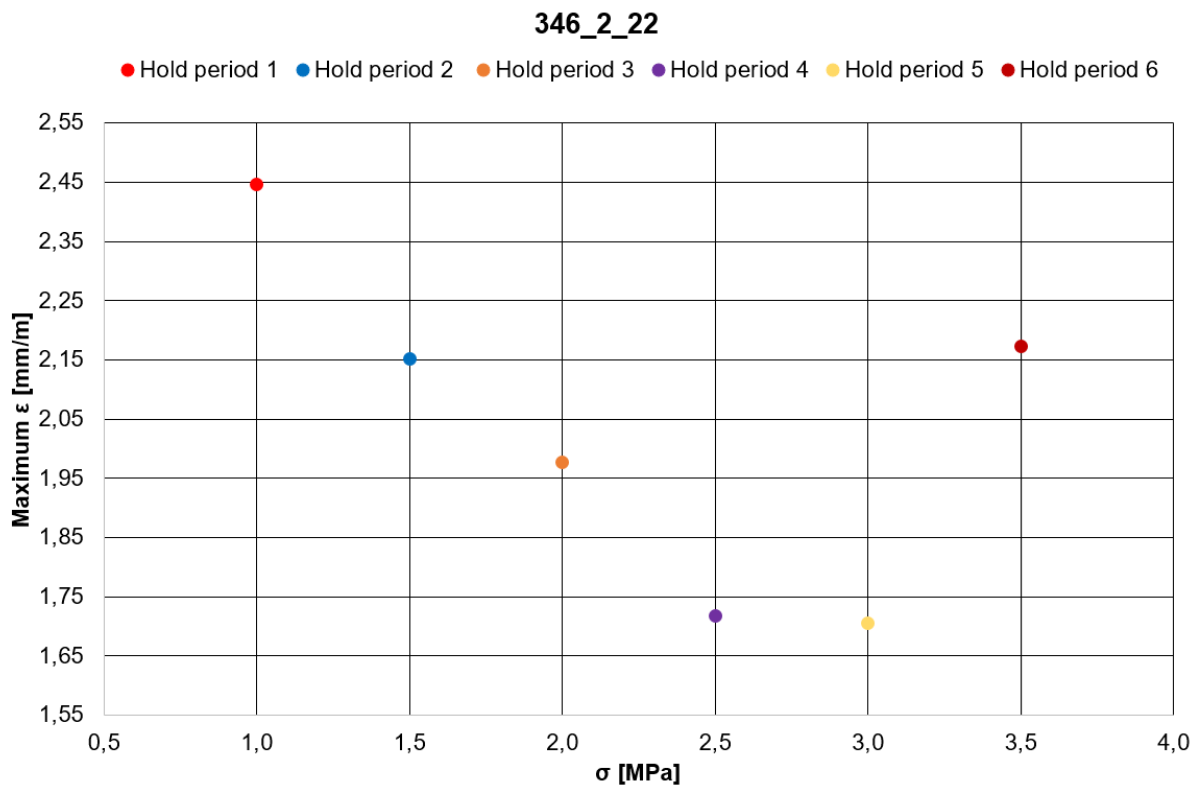


Figure XIV- 8: Maximum strain for loading phase and hold period versus stress level.

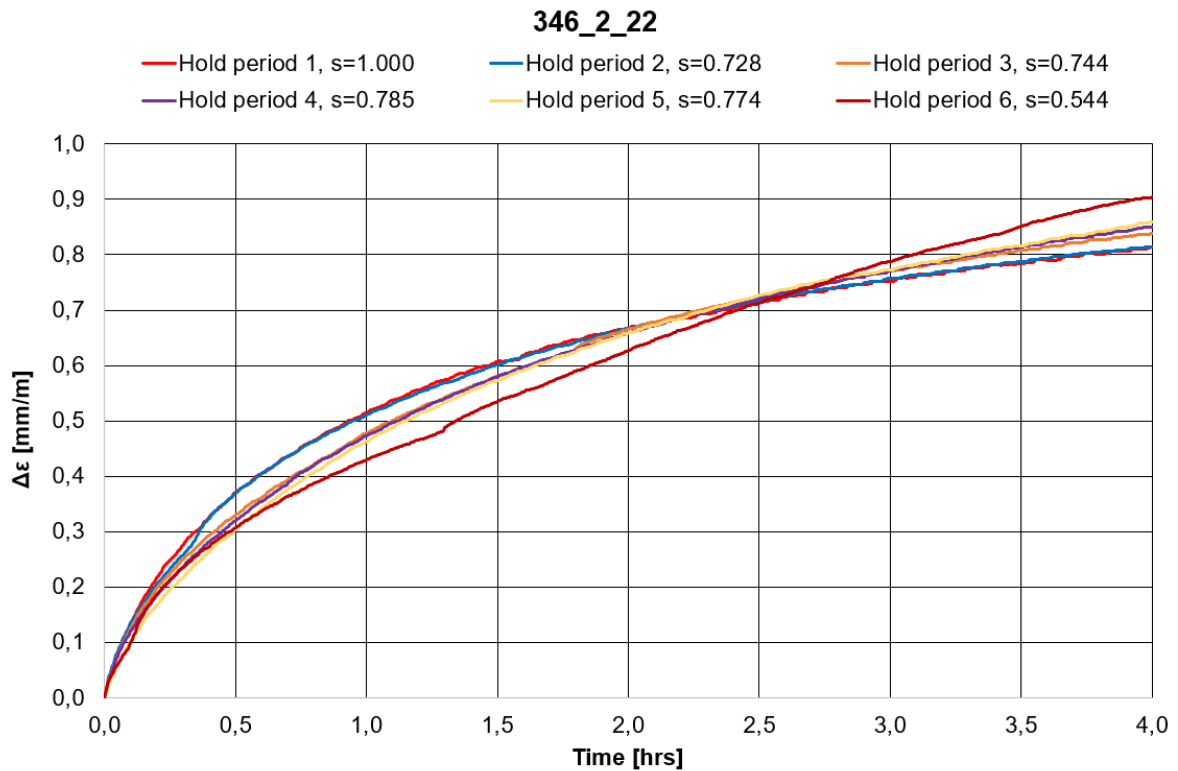


Figure XIV- 9: An attempt to scale the other hold periods down to hold period 1 with a scaling factor s . Scaling factors are included in the legend.

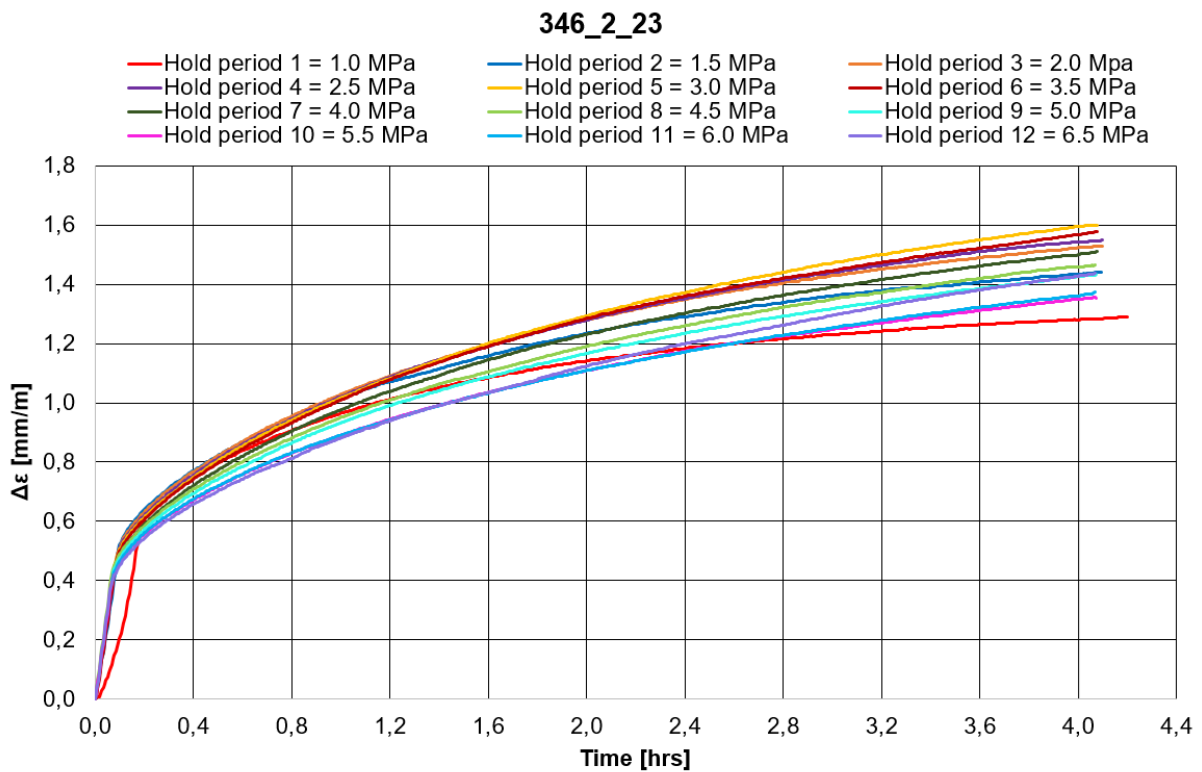


Figure XIV- 10: Strain versus time for loading phases and hold periods.

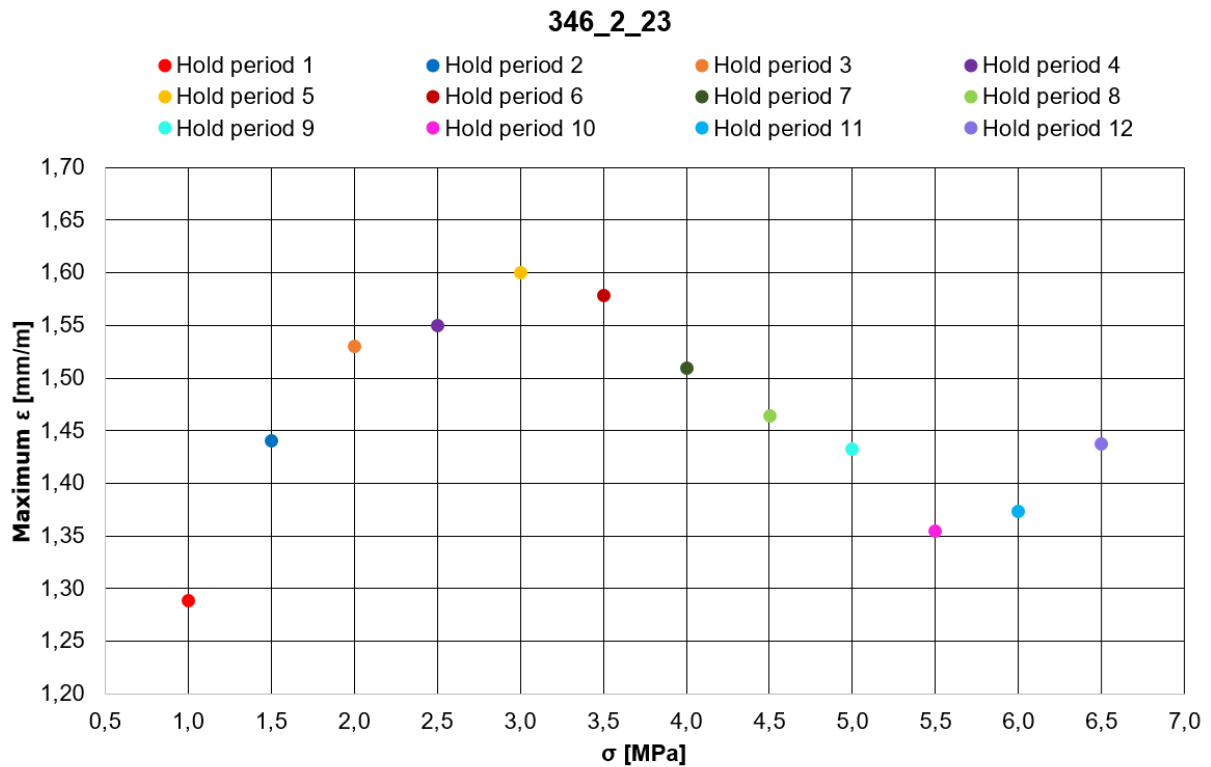


Figure XIV- 11: Maximum strain for loading phase and hold period versus stress level.

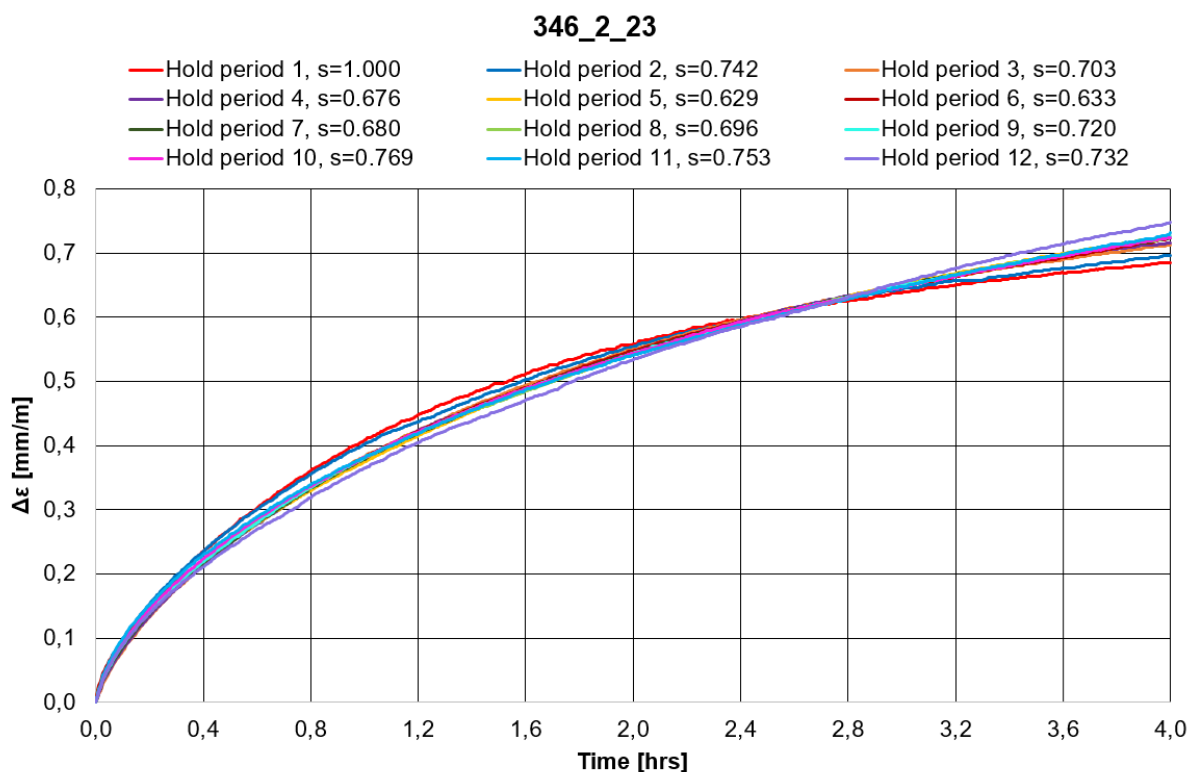


Figure XIV- 12: An attempt to scale the other hold periods down to hold period 1 with a scaling factor s . Scaling factors are included in the legend.